ISSN 2423-9992

JAEA R&D Review 2015

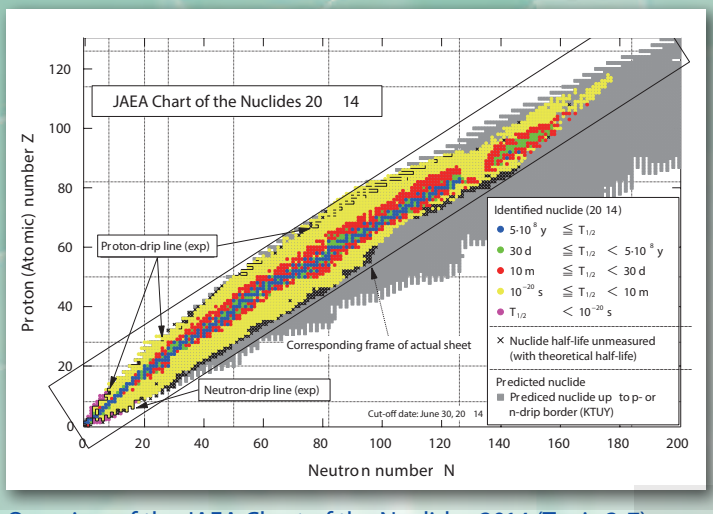

Overview of the JAEA Chart of the Nuclides 2014 (Topic 3-7)

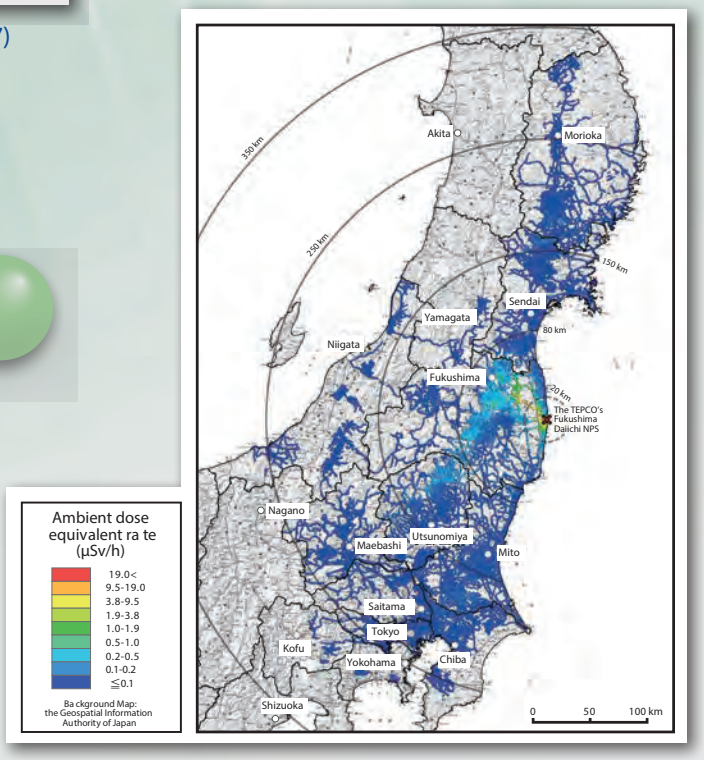

A map of ambient dose equivalent rates through the eighth vehicle-borne survey (Topic 1-1)

Message from the President

児玉敏雄

President Toshio KODAMA

We sincerely thank you for your understanding and continued support of our research and development (R&D) activities. This publication has been issued annually since the foundation of the Japan Atomic Energy Agency (JAEA), with the intention of informing you of the agency's day-to-day achievements.

JAEA is the sole comprehensive R&D institute dedicated to nuclear energy in Japan, and our mission is to contribute to the welfare and prosperity of human society through nuclear science and technology. In accordance with our 3rd medium- and long-term goals set in April 2015, JAEA has focused on issues such as the response to the accident at the Fukushima Daiichi Nuclear Power Station of Tokyo Electric Power Company, Incorporated which is our highest priority, research for safety improvement in the field of nuclear energy, R&D toward the establishment of nuclear fuel cycle technology, and the development of technology for the treatment and disposal of radioactive waste. In addition, to support these R&D and create new technologies, we have implemented basic nuclear science and engineering research and human resources development.

In particular, restarting the operation of the "Monju" fast breeder reactor is the urgent task. We will devote the utmost effort.

In carrying forward our R&D activities, we will continue the steady reform of JAEA and make an effort to foster a culture of safety. We will fulfill our responsibilities as a R&D institution by creating excellent outcomes, whilst remaining aware of our mission as mandated by society.

We are pleased that you will gain further understanding of JAEA's accomplishments through this publication, and we expect your continued encouragement and guidance in our R&D activities.

2 Nuclear Safety Research

3 Advanced Science Research

4 Nuclear Science and Engineering Research

5 Quantum Beam Science Research

6 HTGR Hydrogen and Heat Application Research

7 Research and Development of Fast Reactors

8 Research and Development Related to the Backend of the Nuclear Fuel Cycle and the Reprocessing of Spent Nuclear Fuel

9 Nuclear Fusion Research and Development

10 Computational Science and E-Systems Research

11 Development of Science & Technology for Nuclear Nonproliferation

About This Publication and the Outline of the Organization of JAEA

This publication introduces our latest research and development (R&D) results in each field. Each chapter presents the activities of one R&D Sector. The various R&D Sectors perform their activities through R&D centers or institutes. Depending on the R&D activities, some of these centers or institutes comprise only one site, whereas others comprise two or more sites. The R&D centers and institutes are located throughout Japan, as shown on the map below. The following brief introduction outlines the research undertaken by each R&D Sector at various R&D centers and institutes.

1. **The Sector of Fukushima Research and Development** is engaged in R&D, aimed at recovery from the accident at the Fukushima Daiichi Nuclear Power Station of Tokyo Electric Power Company, Incorporated (TEPCO). To contribute to the realization of a secure environment for residents, the Fukushima Environmental Safety Center has been conducting environmental radiation monitoring and R&D for monitoring radiocesium behavior in the environment and for developing decontamination and volume reduction technologies. The Collaborative Laboratories for Advanced Decommissioning Science (CLADS) has been conducting R&D ranging from basic research to applied studies, such as understanding of the properties of fuel debris, analysis of the situation inside the reactors, and processing and disposal of radioactive waste, in line with the "Mid-and-Long-Term Roadmap towards the Decommissioning of TEPCO's Fukushima Daiichi Nuclear Power Station Units 1-4". Moreover, the Fukushima Research Infrastructural Creation Center has been preparing R&D facilities such as the "Naraha Remote Technology Development Center" and the "Okuma Analysis and Research Center" as indispensable research bases for promoting the decommissioning of TEPCO's Fukushima Daiichi Nuclear Power Station.
2. **The Nuclear Safety Research Center, Sector of Nuclear Safety Research and Emergency Preparedness,** is in charge of safety research that supports the national nuclear safety bodies that regulate nuclear power plants, nuclear fuel cycle facilities, and radioactive waste-disposal facilities. This work is being conducted at the Nuclear Science Research Institute.
3. **The Advanced Science Research Center, Sector of Nuclear Science Research,** explores yet-undiscovered disciplines and studies advanced atomic energy sciences via the Nuclear Science Research Institute to develop new theories and investigate novel phenomena, materials, and technologies. In particular, six research themes have been organized under the two divisions "advanced actinides science" and "advanced nuclear materials science".
4. **The Nuclear Science and Engineering Center, Sector of Nuclear Science Research,** is engaged in key and basic research on various fundamental technologies that support nuclear power use. These efforts are being conducted mainly at the Nuclear Science Research Institute and the Oarai Research and Development Center.
5. **The Quantum Beam Science Center, Sector of Nuclear Science Research,** is engaged in research using neutrons at the Nuclear Science Research Institute and Japan Proton Accelerator Research Complex (J-PARC). Work using electron beams, gamma rays, and ion beams is being conducted at the Takasaki Advanced Radiation Research Institute. Research using lasers and synchrotron radiation is being performed at the Kansai Photon Science Institute.

Japan Atomic Energy Agency -Outline of Organization-

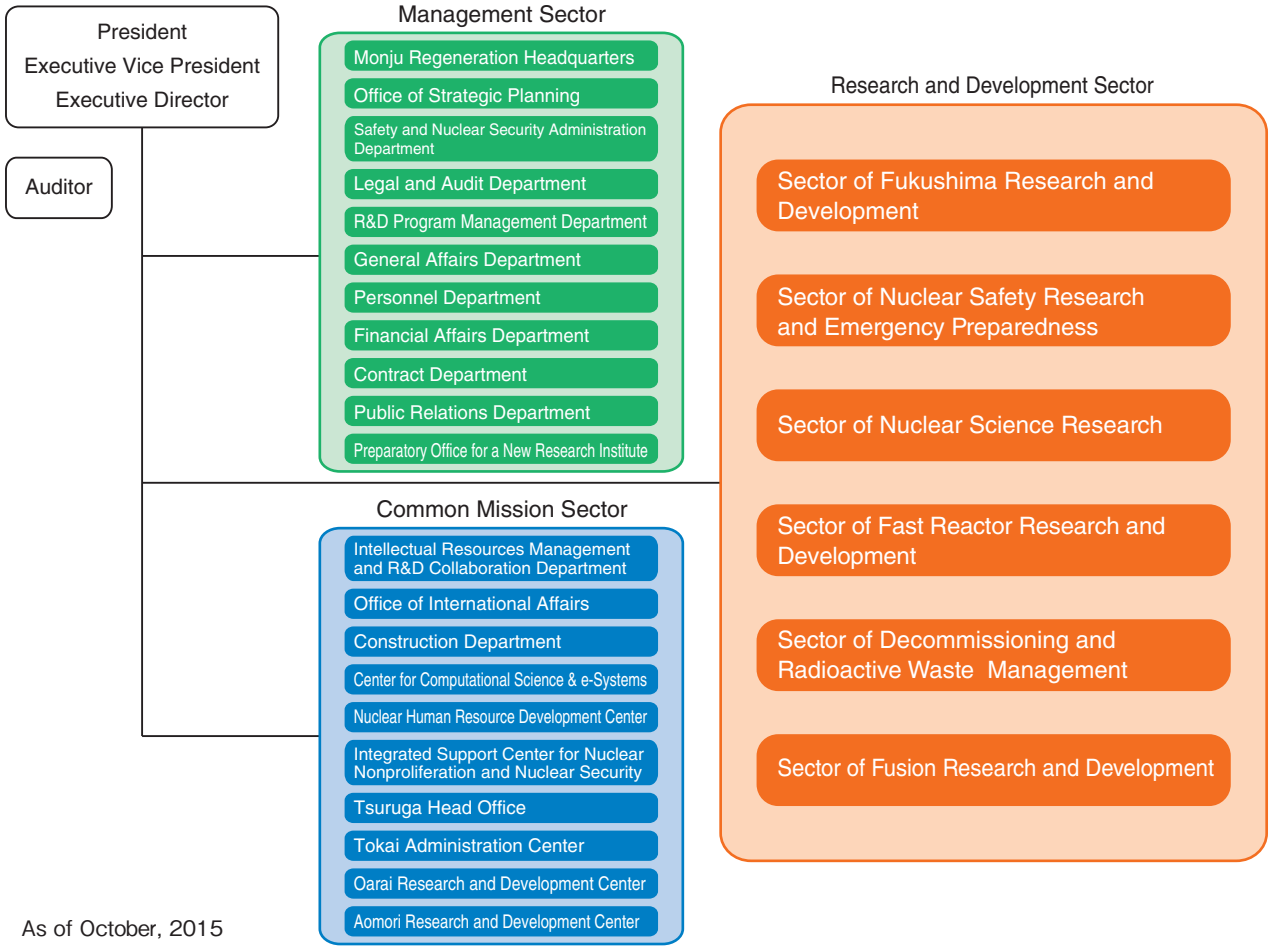

As of October, 2015

6. **The HTGR Hydrogen and Heat Application Research Center, Sector of Nuclear Science Research,** conducts R&D on technologies for high-temperature gas-cooled reactors (HTGRs) and thermochemical hydrogen production at the Oarai Research and Development Center.
7. **The Sector of Fast Reactor Research and Development** is conducting R&D toward the establishment of fast reactor (FR) cycles to address long-term energy security and global environmental issues. In Tsuruga, staff at the Prototype Fast Breeder Reactor Monju and the Monju Project Management and Engineering Center are conducting R&D on "MONJU". R&D activities are also aimed at enhancing the safety of the FR system at the Oarai Research and Development Center and at manufacturing plutonium fuel and reprocessing spent FBR fuel at the Nuclear Fuel Cycle Engineering Laboratories.
8. **The Sector of Decommissioning and Radioactive Waste Management** develops technologies for the safe and rational decommissioning of nuclear power facilities as well as measures for processing and disposing of radioactive waste in their R&D centers or institutes. This sector also conducts multidisciplinary R&D aimed at improving the reliability of geological isolation of high-level radioactive waste in Japan. A particular focus involves establishing techniques for investigating the deep geological environment through R&D at the Tono Geoscience Center and the Horonobe Underground Research Center. At the Nuclear Fuel Cycle Engineering Laboratories, the focus is on improving the technologies for disposal facility design and safety assessment. Additionally, ongoing work is focused on the development of a next-generation knowledge management system based on the above R&D activities. Furthermore, the development of nuclear fuel cycle technology for LWRs is in progress at the Nuclear Fuel Cycle Engineering Laboratories.
9. **The Sector of Fusion Research and Development** is performing fusion R&D as a domestic agency of the International Thermonuclear Experimental Reactor (ITER) project and as an implementing agency of the Broader Approach (BA) activities. The procurement activity of the ITER project, upgrade of JT-60 into a superconducting machine as a BA activity, fusion plasma research, and R&D on various elemental technologies are being conducted at the Naka Fusion Institute. Moreover, the International Fusion Energy Research Center project and the Engineering Validation and Engineering Design Activities of the International Fusion Material Irradiation Facility as a BA activity are mainly being performed at the Rokkasho Fusion Institute.
10. **The Center for Computational Science & e-Systems** performs research on advanced simulation technology and on basic technology in computational science, and also operates and maintains computer systems. These efforts are mainly conducted at the Nuclear Science Research Institute and the Kashiwa Office.
11. **The Integrated Support Center for Nuclear Nonproliferation and Nuclear Security** plays an active role in technology development in the field of nuclear nonproliferation and nuclear security in international organizations, such as IAEA, and each country, activities to contribute nuclear material management and peaceful uses on ensuring transparency, and policy research. And ISCN continues human capacity development support projects which contribute the capacity building in Asian countries. These efforts are carried out mainly at the Head Office and the Nuclear Science Research Institute.

R&D Institutes/Centers of JAEA

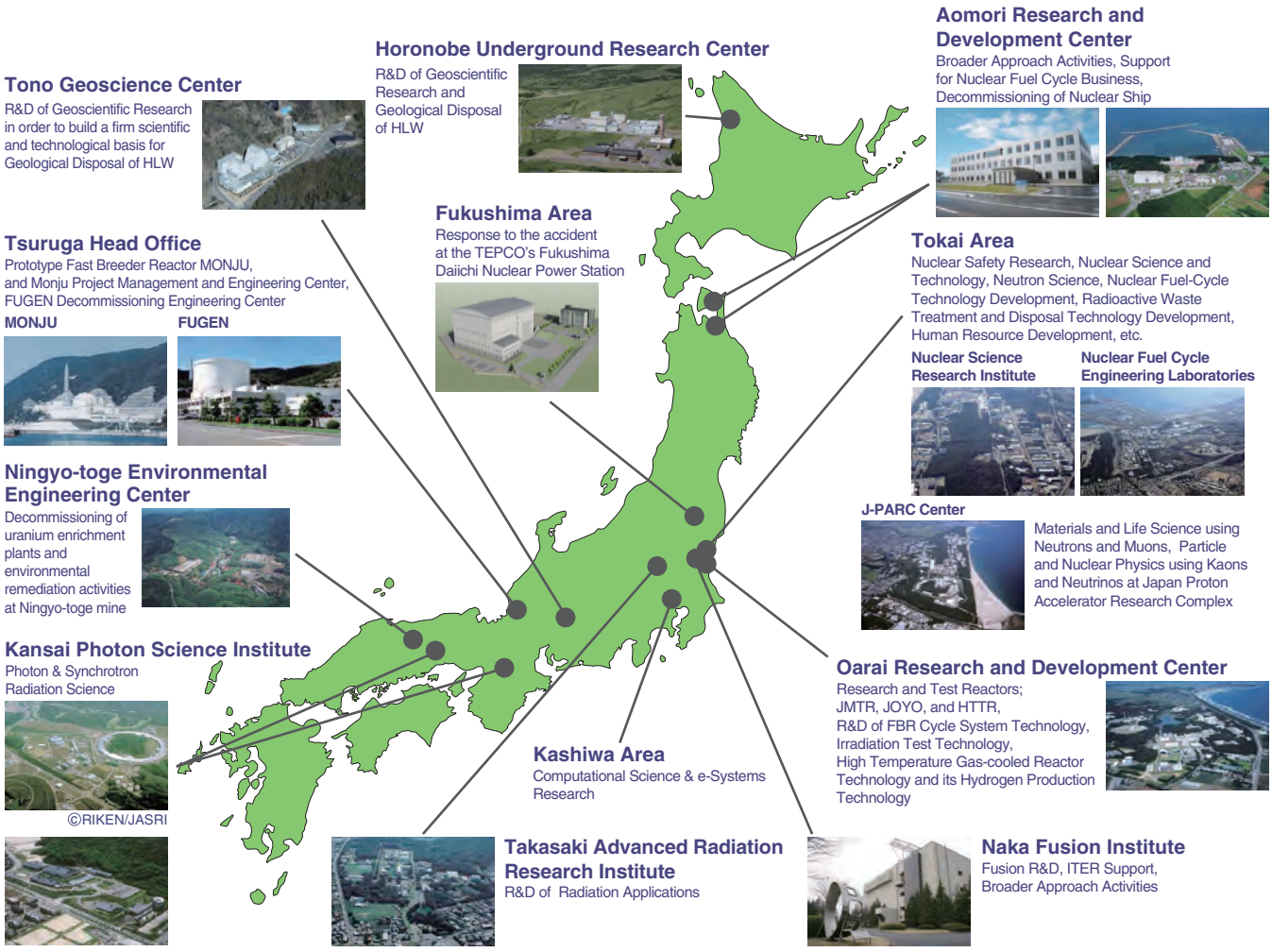

1 Research and Development Related to the Accident at TEPCO's Fukushima Daiichi NPS

Aiming to Provide Research and Development Results to Promote Reconstruction and Decommissioning

Fukushima Prefectural Centre for Environmental Creation
Miharu Town facility

Fukushima Prefectural Centre for Environmental Creation
Minamisoma City facility

Fig.1-1 Fukushima Prefectural Centre for Environmental Creation, which will open in the FY 2015
The Miharu Town facility has four functions: monitoring, research, information collection/dissemination, and education/training/communication. We will conduct research on environmental dynamics and others in this facility and promote research and development in cooperation with Fukushima Prefecture and the National Institute for Environmental Studies. The Minamisoma City facility has the function of monitoring the vicinities of nuclear power plants. We will cooperate with the Beach Local Agriculture Reproduction Research Center (tentative name) and Fukushima Off-site Center (tentative name) to perform research and safety monitoring. We will also develop advanced radiation-measurement technology in this facility.

Contributing to the Safety and Security of Residents through Research and Development toward Environmental Recovery

To proceed with the activities lined out in the "Basic Act on Reconstruction in Response to the Great East Japan Earthquake (Cabinet Decision, July, 2012)" as well as the "Fukushima Prefectural Centre for Environmental Creation Policy for Medium- and Long-term Initiatives" formulated by the Fukushima Prefectural Centre for Environmental Creation Management Strategy Conference, we researched and developed technologies related to environmental recovery for the safety and security of residents (Fig.1-1).

We developed environmental monitoring and mapping technology capable of evaluating individual doses by monitoring living areas dose rates in forest, river, coastal, and sea areas.

We evaluated the half-lives of actual spatial dose rates under the migration behavior present in the actual environment through means such as artificial impact assessment while excluding the impact of the physical decay of radioactive cesium (Cs). This collective evaluation method is known as determining the "ecological half-life of Cs". We assessed the dose rate changes under different land uses by utilizing the simulation model considering this ecological half-life (Topic 1-1). We have developed an analytical method to evaluate the exposure dose due to radioactive Cs deposited over a wide range of soils by the accident at the Fukushima Daiichi Nuclear Power Station (1F) of Tokyo Electric Power Company, Incorporated (Topic 1-2).

Each municipality asks for the release of the government's evacuation order, and promotes the return of evacuated residents. The JAEA obtains technical information by studying environmental assessments and provides this information as needed for the release of evacuation orders upon municipalities. The technical information is obtained by studying a long-term assessment of the transport of radioactive contaminants in the environment of Fukushima.

Lichen is an index of radioactive Cs because it is a simple, slow-growing plant that typically forms a low, crust-like, leaf-like, or branching growth on rocks, walls, and trees. Slow-growing plants contain radioactive Cs over the long-term. Thus, we research the Cs concentration of lichen as a radioactive index of the accident at 1F (Topic 1-3). Radioactive strontium has a low concentration in fresh water. To accurately measure the radioactivity, it is necessary to concentrate the large-volume (over 100 ℓ) water samples . We have found an efficient analytical method, which will help in providing detailed exposure assessment and environmental monitoring of radionuclide migration(Topic 1-4). Furthermore, to understand the 1F accident's effect on the marine environment in detail, we measured the concentration of radioactive materials in the seabed soil taken on the Ibaraki Prefecture coast (Topic 1-5).

To contribute to reducing the burden related to the storing of soil generated from the decontamination, we studied the transition mechanisms of radioactive Cs in soil and used these mechanisms to reasonably reduce the volume of Cs-contaminated soil or to reuse the soil (Topic 1-5). A decontamination activities support system (called RESET: Restoration Support System for the Environment) was developed for the purpose of supporting the implementation of efficient and effective decontamination procedures. RESET is used in decontamination planning by national and local governments (Topic 1-6). Cs in the soil is mainly strongly adsorbed by mica such as that present in clay minerals. In separating the Cs from the mica clay mineral, it is possible to reduce the volume of the waste soil that occurs in decontamination. Using the computational science technique called a first-principles calculation method, we clarified the form of adsorption (Topic 1-7). We found that vermiculite, a clay mineral distributed widely in Fukushima, was easily adsorbed to radioactive Cs. Thus, we observed a mechanism for Cs adsorption in this mineral at the nanometer level (Topic 1-8). A large amount of sewage sludge incineration ash, contaminated with radioactive Cs, was generated. For appropriate treatment, we examined how to reduce the volume of sludge incineration ash (Topic 1-9).

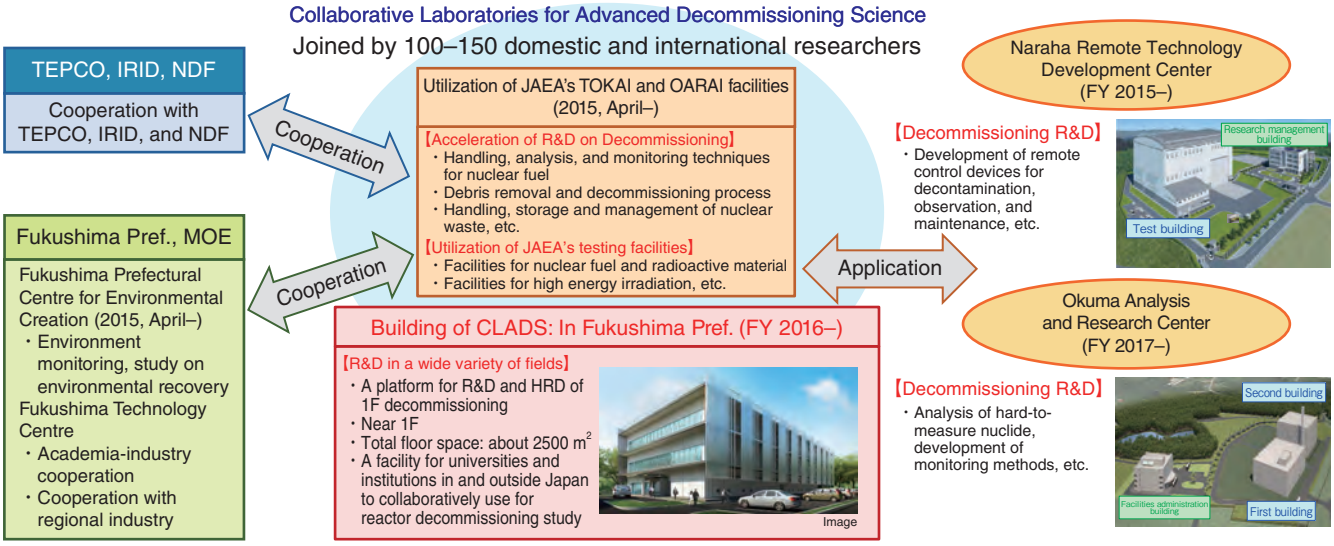

Fig.1-2 Function of CLADS
JAEA established CLADS as an R&D center for the decommissioning of reactors in April 2015. JAEA utilizes existing facilities in Tokai and Oarai and is preparing R&D facilities in Fukushima Prefecture. R&D is promoted by cooperation with Tokyo Electric Power Company, Incorporated (TEPCO), International Research Institute for Nuclear Decommissioning (IRID), Nuclear Damage Compensation and Decommissioning Facilitation Corporation (NDF), the Ministry of the Environment (MOE), and Fukushima Prefecture.

The Challenge of Decommissioning

JAEA has constructed international R&D centers to integrally promote R&D and human resource development (HRD) by industry, academia, and government, forming an interacting human resource network of universities, research institutions, and industries at home and abroad. In particular, JAEA has established "Collaborative Laboratories for Advanced Decommissioning Science (CLADS)" in April 2015 for R&D towards decommissioning (Fig.1-2). The objectives of CLADS include the following: "Gathering the wisdom of experts from home and abroad"; "Enhancement of support for domestic and overseas decommissioning research"; "Enhancement of middle- and long-term HRD"; and "(performing a) Role of information transmission". It is charged with a role of a core of R&D for the decommissioning reactors. Although JAEA is utilizing existing facilities in the Tokai and Oarai area for the time being, it will launch other collaborative research projects based on R&D facilities in Fukushima, such as the "Naraha Remote Technology Development Center (FY 2015–)" and the "Okuma Analysis and Research Center (FY 2017–)". JAEA will develop an "International Collaborative Research Building (tentative)" in Fukushima Prefecture as the base institute utilized by many diverse researchers. This institute is to be used as a platform for basic R&D and cooperation at the 1F site with universities for HRD.

Pool Fuel and Debris-Unloading Preparation

Because a great deal of seawater was poured into the reactor to cool used fuel following the 1F accident, there is a fear that the constituent materials of a fuel aggregate will be corroded. We study soundness about strength and corrosion to storage the used fuel in common pool (Topics 1-10 and 1-11).

For safely removing fuel debris from the nuclear reactor, it is very important to know the state of the debris. This information must be known beforehand, so that removing tools or equipment can be correctly selected. We tested to determine the differences in the fuel hardness according to changes in the components of the cladding (Topic 1-12) and the extended period immersion in cooling water in a nuclear reactor (Topic 1-13).

Accident Progress Evaluation

To understand in detail how the core meltdown progressed, we performed analyses and experiments to study the fracture process and damage to the pressure vessel damage by the lower parts of the fuel rods at the time of the accident. (Topics 1-14, 1-15, 1-16, and 1-17). In addition, we evaluated the properties of the radioactive material that was released during the accident (Topic 1-18).

Processing and Disposal of Radioactive Waste

The safe storage, processing, and disposal of waste generated by the 1F accident is a very important initiative, and we need to know the states of the waste generated by the accident. At present, it is difficult to obtain samples and analyze all of the wastes; thus, data is not uniformly accurate. However, we have investigated a method of estimating the radioactivity by indirect analysis (Topic 1-19). It is well-known that hydrogen is generated by radiolysis in high-radiation moisture waste; we experimentally evaluate the amount of generated hydrogen (Topic 1-20). The result shows that it is safe to store these wastes.

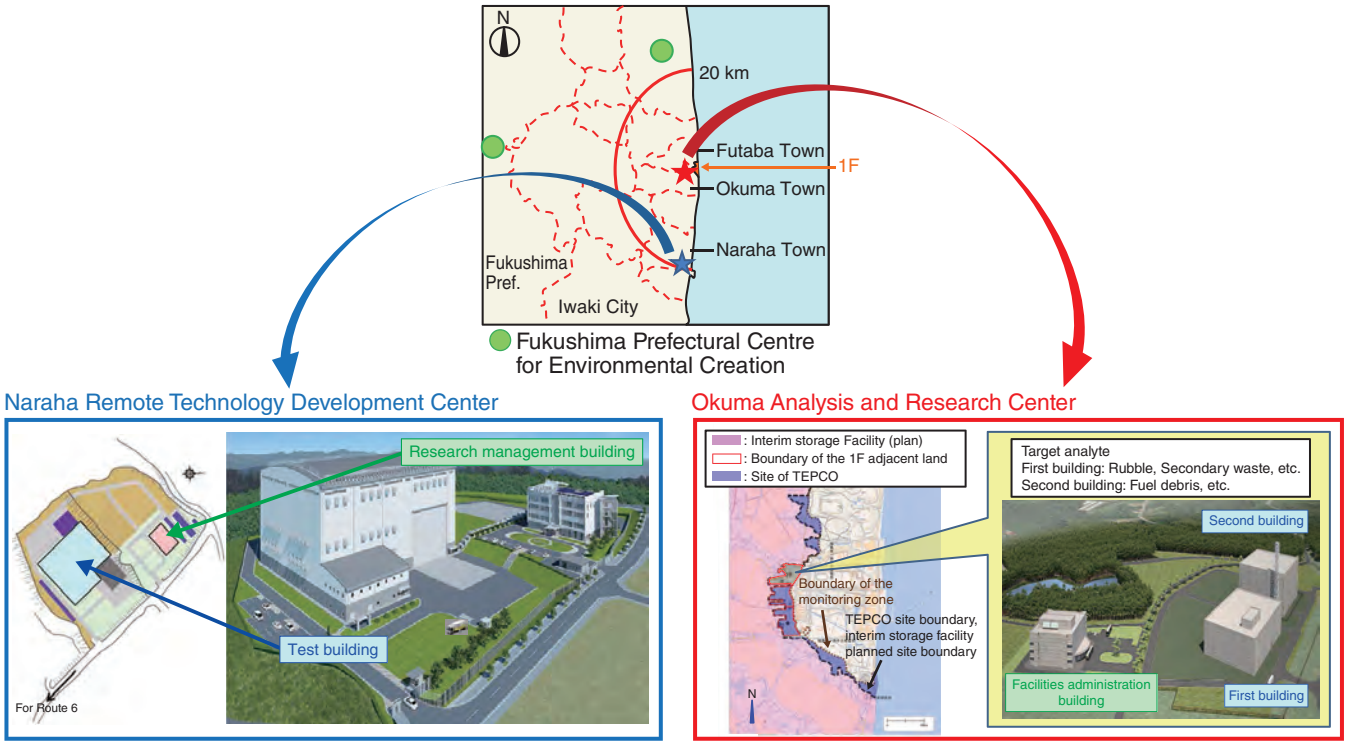

Fig.1-3 Locations of Naraha Remote Technology Development Center and Okuma Analysis and Research Center
The Naraha Remote Technology Development Center comprises a research management building (4-story bldg.: width 35 m, length 25 m, height 20 m) and a test building (1-story bldg.: width 60 m, length 80 m, height 40 m) and will commence operation in FY 2016. The Okuma Analysis and Research Center comprises 3 buildings: "Administrative building", "Laboratry-1", and "Laboratory-2". Laboratry-1 treats debris and secondary waste from water treatment with a low radiation dose rate. Laboratry-2 treats fuel debris and secondary waste from water treatment with a high radiation dose rate. The center is planned to commence operation in FY 2017.

The Fukushima Research Infrastructural Creation Center is now establishing two research bases for technological development toward the decommissioning of 1F. These bases are to assume roles in the preparation of removal of fuel debris from nuclear reactors and in the treatment and disposal of radioactive wastes generated from the decommissioning work. As Fig.1-3 shows, the "Remote-controlled Equipment and Device Development Facility" (hereafter, Naraha Remote Technology Development Center) is being constructed in the Naraha Town, in Fukushima Prefecture, and the "Radioactive Material Analysis and Research Facility" (hereafter, Okuma Analysis and Research Center) is being constructed in the Okuma Town, also in Fukushima Prefecture. Their outlines and situations are described below.

Naraha Remote Technology Development Center

A research management building is intended for administrative work and meetings as well as development and installation of an immersive virtual reality (VR) system. The VR system will provide a virtual reality space in which we can check the feasibility of the planned procedure and train workers and operators of remote-controlled equipment by simulating motions in places that cannot safely be accessed by humans. In the First Building, development and demonstration of new technologies such as techniques for stopping water leaks at the lower part of the reactor containment vessel, and the remote-controlled equipment necessary for investigation and decontamination in the 1F building, will be conducted. Installation of the equipment is almost complete, and all preparations for starting operation in FY 2016 will be ready soon.

Okuma Analysis and Research Center

For disposal and treatment of radioactive wastes in 1F, isotropic composition and physical property analysis of radioactive materials, safety evaluation of radioactive wastes storage, tests of radioactive waste conditioning, and technologies for safety-evaluation of disposal are needed. Some efforts such as establishing an advisory commission with outside experts have been accelerated, keeping in mind the points listed below.

- Simultaneous execution of routine work and R&D for analysis;
- Flexibility for various tests;
- Promotion of facility utilization;
- Quickness and high reliability of measurement and evaluation.

Now, we are steadily designing the Okuma Analysis and Research Center, with a view to scheduling a "Mid-and-long-Term Roadmap toward the Decommissioning of 1F".

The Goal of the Research Base

To concentrate domestic and world expertise, our research base aims to organically actuate R&D resources. Domestically, we promote the construction of an innovation hub that realizes cooperation with universities and industry. Internationally, we have signed a memorandum with Texas A&M University for future cooperation in the demonstration of remote-control equipment, as well as a cooperative agreement that provides for international network and facility use. This is the sole research base located within 20 km off 1F. By conducting R&D and delivering results, we aim to establish an attractive research base and promote the use of facilities, and by so doing, contribute to the re-creation of regional industry.

1–1 Changes in Ambient Dose-Equivalent Rates Dependent on Land Use

— Evaluation of Ecological Half-Lives for Decreasing Trends of Ambient Dose-Equivalent Rates —

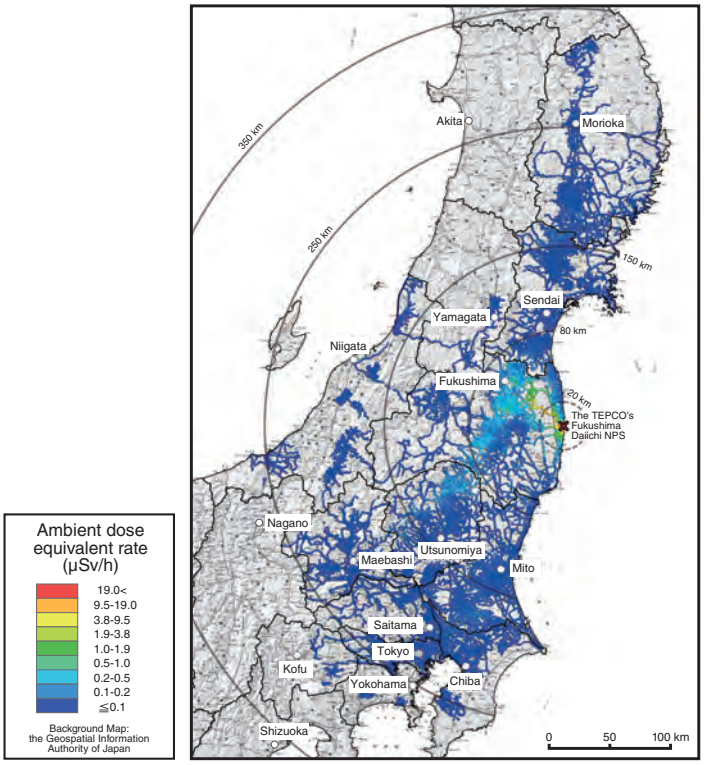

Fig.1-4 A map of ambient dose equivalent rates through vehicle-borne surveys
(The eighth survey was conducted from June 23 to August 8, 2014)

Table 1-1 Ecological half-lives for the fast elimination component (median)
The median values of the ecological half-lives of the fast elimination component for each land use are listed in this table.

Land use	Ecological half-lives for the fast elimination component (year)
Water	0.56
Urban	0.60
Paddy	0.55
Crop	0.63
Grass	0.58
Deciduous forest	0.66
Evergreen forest	0.94
Bare surface	0.62

To support a rehabilitation program after the accident at the TEPCO's Fukushima Daiichi NPS, prediction models have been developed to assess how ambient dose-equivalent rates obtained from the radioactive cesium (Cs) deposited on the ground might change in future. The prediction models were expressed using calculation formulae characterized by ecological half-lives for the fast/slow elimination components. The prediction models can provide information on the time-variation of the ambient dose-equivalent rates for land use. The ecological half-life is defined as the time for the ambient dose-equivalent rate to be halved due to natural removal phenomena and human activities.

In Western countries, ecological half-lives were evaluated after atmospheric nuclear tests and the accident at the Chernobyl Nuclear Power Plant. However, it is not clear yet whether these ecological half-lives are applicable in Japan. We evaluated ecological half-lives for the fast elimination component using ambient dose-equivalent rates through eight vehicle-borne surveys conducted from June 2011 to August 2014 (Fig.1-4). The ecological half-lives for land use were analyzed on the basis of a statistical method. The ecological half-life for the slow elimination component was assumed to be the same regardless of land use as it is well-known to be 45–135 year and is not easily evaluated using the data obtained within several years after the accident.

We found that the ecological half-lives for the fast elimination component in deciduous and evergreen forest areas are longer than those in other areas. In many areas other than deciduous and evergreen forests, the ecological half-lives were found to be approximately 0.55–0.63 year (Table 1-1). Our findings indicate that radioactive Cs in forest areas is unlikely to flow out into surrounding areas. Hence, a rehabilitation program in forest areas is an important issue as there are large forest areas in Fukushima Prefecture.

The present study was sponsored by the Secretariat of the Nuclear Regulation Authority (NRA).

References

Kinase, S. et al., Development of Prediction Models for Radioactive Caesium Distribution within the 80-km Radius of the Fukushima Daiichi Nuclear Power Plant, Radiation Protection Dosimetry, vol.160, no.4, 2014, p.318–321.
Kinase, S., Development and Validation of Prediction Models for Ambient Dose Equivalent Rates, Report on Establishment of Evaluation Methods for Long-Term Consequences due to Radioactive Substances Released by the Accident at the TEPCO's Fukushima Daiichi NPS, Commissioned by the Nuclear Regulation Authority in FY2014, Japan Atomic Energy Agency, 2014, p.217-238 (in Japanese), http://fukushima.jaea.go.jp/initiatives/cat03/entry07.html

1–2 Predicting the Doses to Residents Exposed to Radiations from Radioactive Cesium

— Calculation of Age-Dependent Dose Conversion Coefficients for External Exposure —

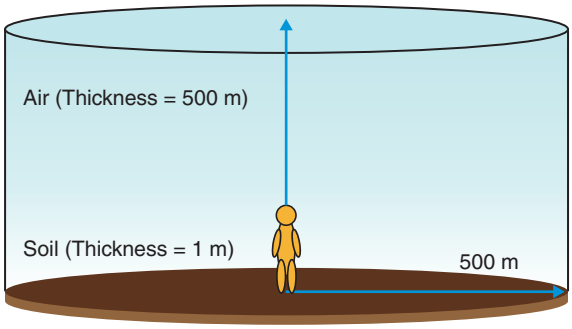

Fig.1-5 Schematic of the geometry used to calculate dose-conversion coefficients
The absorbed doses of tissues and organs inside a computational phantom were calculated by transporting the γ-rays emitted from the radioactive Cs in the soil through the geometry that models the environment in PHITS.

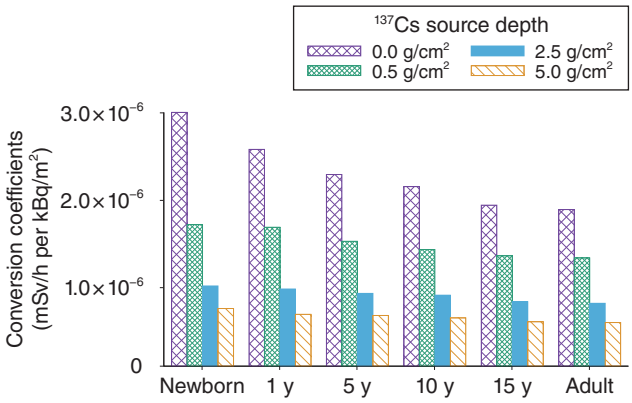

Fig.1-6 Dose conversion coefficients of ^{137}Cs
The coefficients convert the activity concentration of a ^{137}Cs planar source into the effective dose rate for each age. The depth of the planar source is expressed in units of g/cm^2 to apply the present results to various soil densities.

Dose estimation for radioactive cesium (^{134}Cs and ^{137}Cs) distributed in soil because of the accident at the TEPCO's Fukushima Daiichi NPS (1F) is important for establishing action plans to ensure the radiological safety of the residents. While spatial dose rates have been monitored continuously, time-dependent changes of the radioactive Cs should be considered in predictions of radiation doses over the middle- to long-term. We have developed a method for predicting the human doses as a function of time after the accident at 1F by calculating age-dependent conversion coefficients from the activity concentration of the Cs to the effective doses that indicate the human dose.

The conversion coefficients were calculated for six age groups within the public (newborns; 1-, 5-, 10-, and 15-year-old children; and adults). We used the radiation transport code PHITS and computational phantoms representing the anatomical structure of human bodies. The size of the geometry depicted in Fig.1-5 was equivalent to approximately five times an average flight path of γ-rays through air without interactions. This size is adequate for treating the contributions of distant radioactive Cs to the dose. The behavior of the γ-rays from a planar source of ^{134}Cs or ^{137}Cs was traced in the calculation geometry, and the absorbed doses of tissues and organs were calculated using computational phantoms centered on the ground.

The effective dose was computed from the results of the absorbed doses according to the 2007 Recommendations by the International Commission on Radiological Protection (ICRP), and the coefficients for converting activity concentrations into effective dose rates were obtained. In addition, we evaluated the conversion coefficients for volumetric sources by means of a weighted integration for the results of the planar sources. The decays of ^{134}Cs and ^{137}Cs were also considered along the time course after the accident at 1F.

Fig.1-6 shows the age-dependent dose conversion coefficients of ^{137}Cs. The conversion coefficients of the effective dose rate increase for younger subjects because the tissues and organs inside younger subjects are closer to the radiation source in the soil than those inside adults. As the depth of the source in the soil increases, the effective dose rates decrease because of the shielding effect of the soil.

Based on the present results, the effective dose rates for various age groups can be estimated considering the time-dependent changes of radioactivity and the depth profile of the Cs. These data are very useful for predicting the doses of the residents who return to the areas where the evacuation orders have been lifted after remediation.

Reference

Satoh, D. et al., Age–Dependent Dose Conversion Coefficients for External Exposure to Radioactive Cesium in Soil, Journal of Nuclear Science and Technology, vol.53, issue 1, 2016, p.69–81.

1–3 Application of Lichens for the Record of Fukushima Fallout
— A Potential Indicator for the Estimation of Initial Fallout Amount —

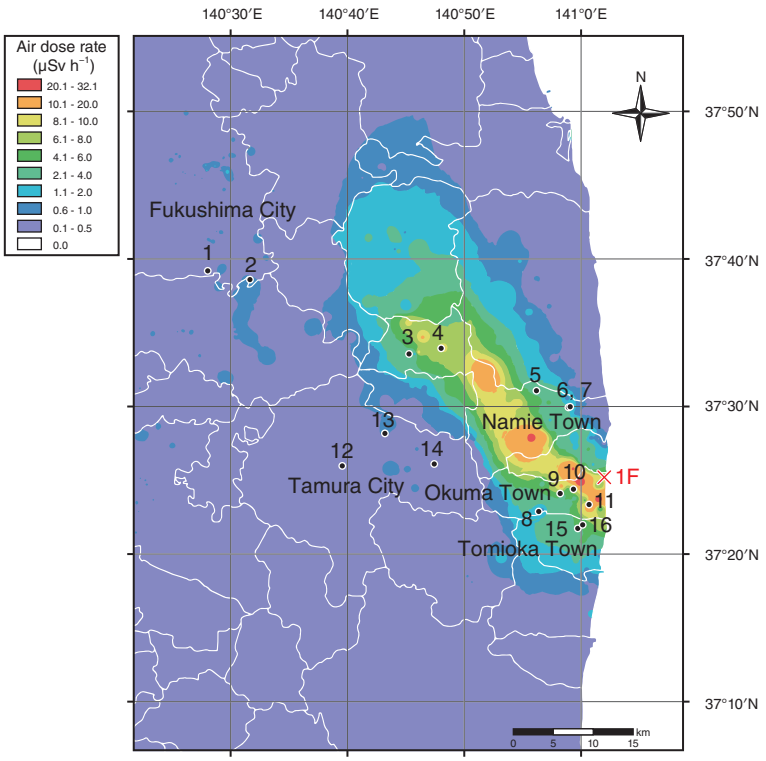

Fig.1-7 Locations of lichen sampling points superimposed on a distribution map of the air dose rate
The air dose rate was measured by MEXT in June and July 2011. A number of lichen samples were collected at each sampling point.

Fig.1-8 Parmelioid lichens growing on *Prunus* spp., Japanese cherry
Parmelioid lichens can be found commonly in Japan.

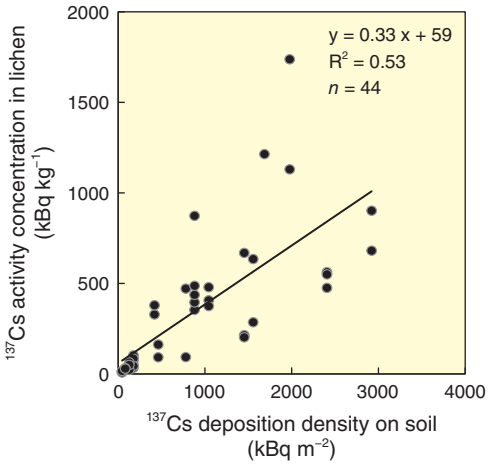

Fig.1-9 The relationship between the ^{137}Cs activity concentration in all 44 lichen samples and the ^{137}Cs deposition density on soil at each sampling point
The relationship between the activity concentration of ^{137}Cs in lichens and the ^{137}Cs inventory in soil shows a significant positive correlation.

Lichens are symbiotic organisms consisting of fungi and algae, and they are found in almost all terrestrial habitats, e.g. on rocks, tree bark, and soil. Lichens have been used for understanding and monitoring radioactive fallout contamination in high-latitude regions caused by atmospheric nuclear weapons testing and the Chernobyl Nuclear Power Plant accident of 1986. The merits of lichens for such investigations are especially because of their longevity (more than several decades) and direct absorption of water and airborne through their entire thallus without a root system.

We are working on a research project for estimating the initial fallout amounts of radiocaesium from the accident at the TEPCO's Fukushima Daiichi NPS (1F) using the radiocaesium activity in lichens as an index value. For the application of a lichen species as an indicator, the following conditions are necessary: ① it has a wide distribution in the study area; ② it shows significant positive correlation between radiocaesium activity concentration in lichens and fallout amounts; and ③ it grows stably enough for long-term monitoring. We have conducted field investigations at 16 points within a radius of 60 km from the 1F since December 2012 (Fig.1-7). We focused on parmeliod lichens which commonly grow on the trunks of *Prunus* spp. (Japanese Cherry trees) planted on public places, e.g., parks, schools, and river banks (Fig.1-8). The activity concentrations of ^{134}Cs and ^{137}Cs in lichen samples were measured by γ-ray spectrometry using a CsI scintillation detector coupled to a multichannel analyzer. The relationship between radiocaesium activity concentration in lichen samples and the ^{137}Cs deposition density on soil was examined. The ^{137}Cs inventory in soil at each sampling point was estimated based on data collected by the Ministry of Education, Culture, Sports, Science and Technology (MEXT) three months after the 1F accident.

The relationship between the activity concentration of ^{137}Cs in nine species of parmelioid lichens collected two years after the accident and the ^{137}Cs inventory in soil shows a significant positive correlation (Fig.1-9). This result suggests the possibility that lichens could hold radiocaesium on their thalli for at least two years after the accident. We are focusing on especially *Flavoparmelia caperata* and *Parmotrema clavuliferum*, which are dominant in the study area and show good correlations with radiocaesium inventory in soil. Further research on the half-life of radiocaesium would contribute to improving our estimation of initial fallout amount.

The present study was accomplished in collaboration with the National Museum of Nature and Science.

Reference

Dohi, T. et al., Radiocaesium Activity Concentrations in Parmelioid Lichens within a 60 km Radius of the Fukushima Dai-Ichi Nuclear Power Plant, Journal of Environmental Radioactivity, vol.146, 2015, p.125–133.

1–4 Efficient In situ Pre-Concentration of Strontium from Water Samples using Ion Exchange Resin
— Development of Low-Level Radiostrontium Analysis in a Freshwater Sample —

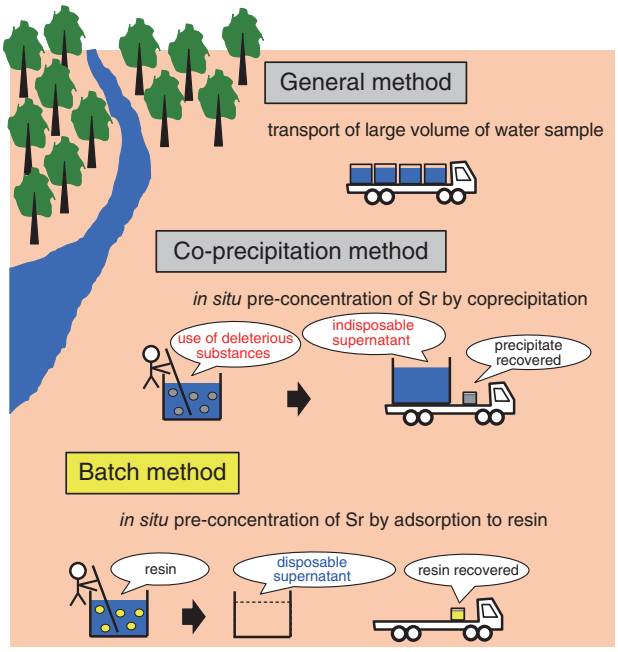

Fig.1-10 Comparison of operations at sampling sites
In most cases, large-volume water samples required for analysis are directly transported to the laboratory. Co-precipitation and batch methods are also used for *in situ* pre-concentration of specific components.

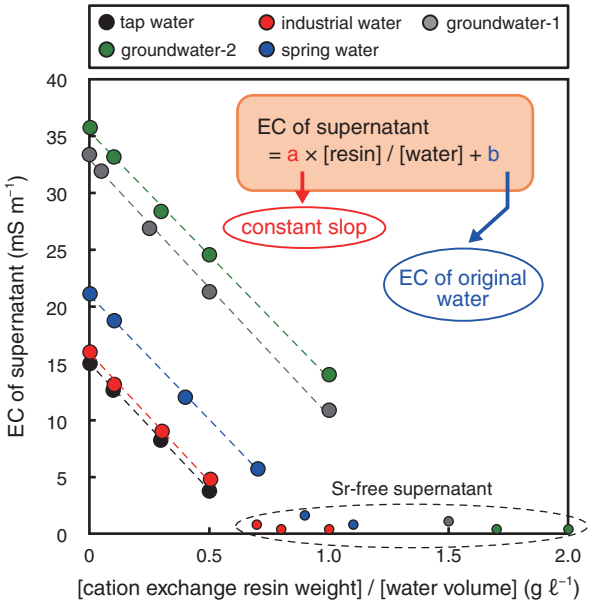

Fig.1-11 Relationship between EC value of supernatant and [cation exchange resin weight] / [water volume] ratio obtained by the batch method
The EC values of supernatant decreased from those of the original water samples with constant slopes among all water samples when [cation exchange weight] / [water volume] ratios increased.

A large volume (over 100 ℓ) is required for precise determination of the low-level radiostrontium activities of freshwater samples. The difficulty of transporting such samples to the laboratory limits the number that can be analyzed. A co-precipitation method using deleterious substances is also undesirable because of the disposal of the waste liquid in the field. In this study, an improved analytical method for low-level radiostrontium in a freshwater sample, which enables sample-collection from many locations, was developed. Emphasis was placed on the *in situ* pre-concentration of Sr by a batch method using Powdex resin to efficiently reduce the sample volume without using deleterious substances in the field (Fig.1-10).

The batch method used here refers to the operation used to adsorb specific components to resin added into the container of a large water sample under stirring. The challenge of this study was to estimate the amount of resin required for quantitatively adsorbing Sr from water samples with various dissolved solid contents. The results of batch experiments using various environmental water samples indicated that the electric conductivity (EC) of supernatant could be determined by the EC of the original water sample, the amount of cation exchange resin, and the water volume. Because the EC of supernatant was assumed to be zero under complete adsorption of Sr, the amount of cation exchange resin required could be empirically determined by the EC of the original water and the water volume (Fig.1-11). Keeping the pH of supernatant neutral by the simultaneous addition of the anion exchange resin enabled both efficient *in situ* reduction of sample volume and sampling from multiple locations.

The resin adsorbing Sr was brought back to the laboratory. The Sr was then chemically and radiochemically separated from Ca and interference nuclides of radiostrontium (i.e., radioactive Pb and Ra isotopes) for β-ray measurement after extraction from the resin.

Analysis of tap water samples by this method gave high chemical recoveries (88% on average) of Sr. Some water samples (170 ℓ) incorporating known amounts of ^{90}Sr with different salinities were prepared for validation assessment. The ^{90}Sr activities determined by this analytical method were in good agreement with those added, and validation was confirmed. The detection limit of ^{90}Sr activity with 170 ℓ water samples was estimated to be approximately 0.1 mBq ℓ$^{-1}$.

The analytical method developed in this study enabled the precise evaluation of internal exposure, and can contribute to ensuring the safety and security of residents.

Reference

Tomita, J. et al., Determination of Low-Level Radiostrontium, with Emphasis on *in situ* Pre-Concentration of Sr from Large Volume of Freshwater Sample using Powdex Resin, Journal of Environmental Radioactivity, vol.146, 2015, p.88–93.

1–5 Investigation of the Concentrations of Radionuclides in Seabed Sediments

— The Spatial Distribution of Radionuclides in Seabed Sediments off the Ibaraki Coast —

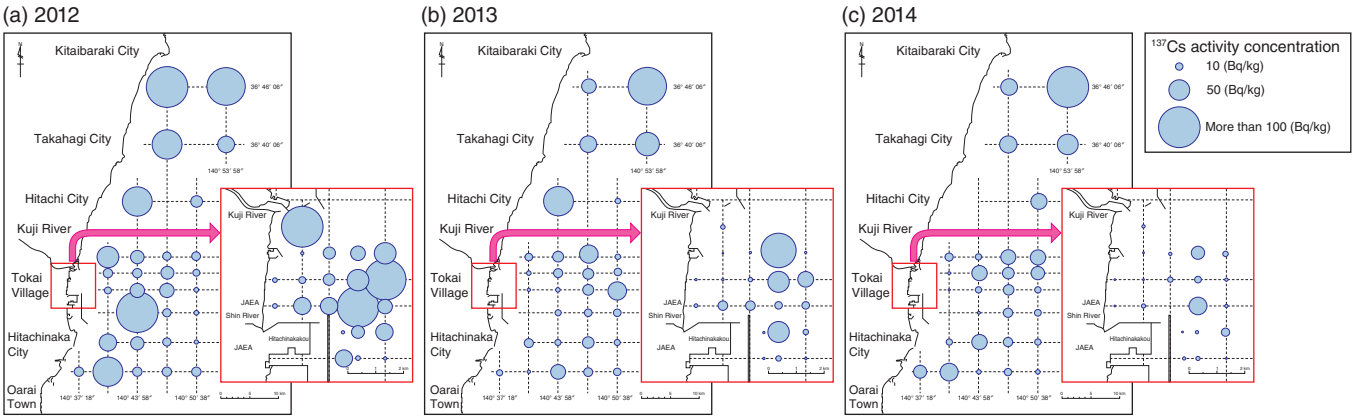

Fig.1-12 Time series of ^{137}Cs concentrations in seabed sediments off the Ibaraki coast
Starting in 2012 and continuing for the next two years, we collected 51 seabed sediment samples in coastal regions from Kitaibaraki City to Oarai Town in Ibaraki Prefecture, spreading approximately 50 km north to south and approximately 20 km offshore. ^{137}Cs radioactivity concentrations are indicated in 2012 (a), 2013 (b), and 2014 (c) by circle size. Thus, we could understand the distributions and time series of the ^{137}Cs radioactivity concentrations.

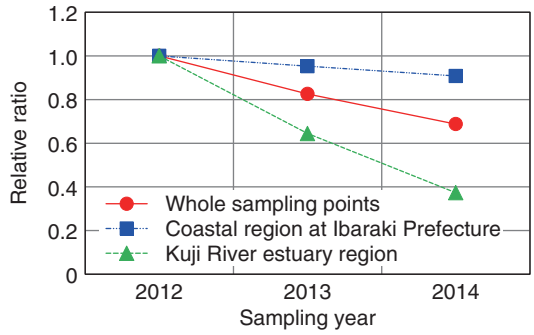

Fig.1-13 Time series of ^{137}Cs concentrations in seabed sediments
Time series of radioactivity concentrations in 2013 and 2014 are indicated, and are normalized to unity for the concentrations in 2012. Concentrations were averaged using the whole data of sampling points and two divided datasets for the coastal region at Ibaraki Prefecture and the Kuji River estuary region.

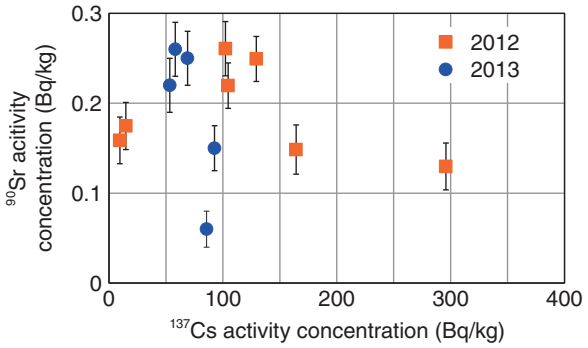

Fig.1-14 The relationship between ^{137}Cs and ^{90}Sr concentrations in seabed sediments
We investigated the correlation between ^{137}Cs and ^{90}Sr concentrations in seabed sediments collected in 2012 and 2013 using samples with higher ^{137}Cs concentrations.

Various radionuclides were discharged into the environment by the accident at the TEPCO's Fukushima Daiichi NPS (1F). We have continuously investigated the radioactivity concentrations in seabed sediment, seawater, and marine organisms on the Ibaraki coast from before the accident to the present time, and confirmed that the concentrations were influenced by the accident at 1F. Therefore, to estimate the influence in detail, we studied the radioactivity concentrations of cesium-134 (^{134}Cs), cesium-137 (^{137}Cs), strontium-90 (^{90}Sr), and plutonium (^{238}Pu and ^{239,240}Pu) in 51 dried seabed sediment samples collected in the coastal regions of Ibaraki Prefecture.

We collected seabed sediment at the same points for three years during May–July 2012, June–July 2013, and May–July in 2014 and determined ^{134}Cs and ^{137}Cs concentrations. Then, ^{90}Sr and Pu were analyzed using seabed sediments with higher ^{137}Cs concentrations.

Fig.1-12 shows time series of ^{137}Cs concentrations over three years. Most concentrations decreased overall with time. The highest ^{137}Cs concentration in 2012 was approximately 100 times higher than the values (about 1 Bq/kg) observed before the accident but decreased to several tens of times higher than those values in 2013 and 2014. Some ^{137}Cs concentrations decreased to the level they had had prior to the accident in 2014. We investigated the decreasing tendency of ^{137}Cs concentrations for three years and found that there were different tendencies among the sampling points, especially between the coastal region (30 points) at Ibaraki Prefecture and the Kuji River estuary region (21 points), as shown in Fig.1-13. We suggest that the difference could have been caused by influence of geographical features and particle size in the sediment and so on.

The ^{90}Sr-concentrations ranged from ND (not detected) to 0.26 Bq/kg in 2012 and 2013. Moreover, we found no correlation between ^{137}Cs and ^{90}Sr concentrations in this study (Fig.1-14). Therefore it seemed that the influence of ^{90}Sr concentration was smaller than those of the ^{134}Cs and ^{137}Cs concentrations because of the accident in the seabed sediments off the Ibaraki coast. Moreover, Pu concentrations were very low and no influence of the accident was recognized in this study.

We will continue to investigate the influence of the accident on environmental monitoring in the regions.

Reference

Nagaoka, M. et al., Spatial Distribution of Radionuclides in Seabed Sediments off Ibaraki Coast after the Fukushima Daiichi Nuclear Power Plant Accident, Journal of Radioanalytical and Nuclear Chemistry, vol.303, issue 2, 2015, p.1305–1308.

1–6 Prediction and Visualization of the Decontamination Effect

— Support for Decontamination Projects in Fukushima using the Restoration Support System for the Environment, "RESET" —

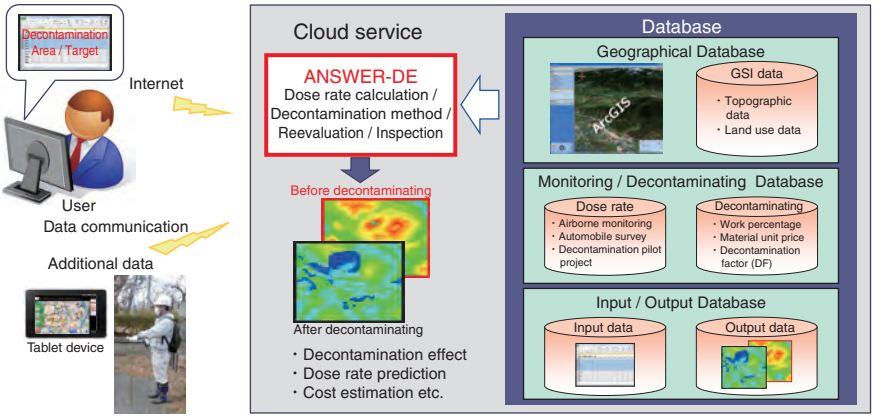

Fig.1-15 Restoration support system for the environment, "RESET"

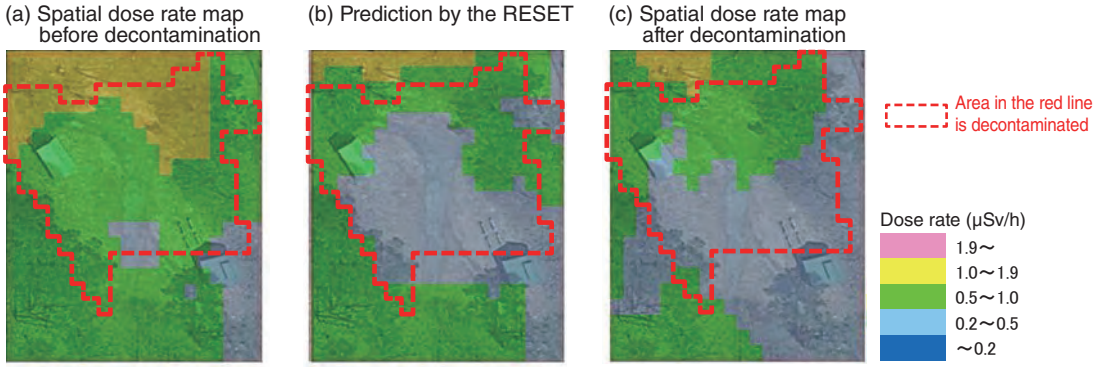

Fig.1-16 Comparison of decontamination results and prediction by RESET
Reduction of the spatial dose rate after decontamination can be confirmed from comparison of (a) the measured spatial dose rate before decontamination and (b) the predicted spatial dose rate by RESET. Good agreement of the prediction by RESET with the actual dose rate could be confirmed from comparison of (b) the predicted spatial dose rate by RESET and (c) the measured spatial dose rate after decontamination.

To restore the environment polluted by the accident at the TEPCO's Fukushima Daiichi NPS, energetic decontamination has been implemented in the communities within 11 special decontamination areas (comprising the 20 km restricted area and the evacuation areas) and 97 intensive contamination survey areas (with radiation backgrounds of 1 mSv/year or more). We constructed an office in Fukushima City and have been technically supporting the Ministry of the Environment (MOE) and local governments in decontamination of the areas since June 2011.

RESET (Fig.1-15) was developed to support MOE and local governments for planning and efficient and effective implementation of decontamination. Since RESET is constructed on a cloud computer, users who can connect to the Internet using a WEB browser can perform a quick and highly precise prediction calculation. RESET has a database that has the airborne monitoring and the automobile survey data published by the Nuclear Regulation Authority (NRA) Japan, electronic topographic data, and land-use data of the Geospatial Information Authority of Japan (GSI). We can easily input data using the database. After inputting the spatial dose rate at a height of 1 m measured before decontamination into RESET, the surface pollution density and spatial dose rate at a 1 m height after decontaminating are calculated by considering 3-dimensional geographic effects using ANSWER-DE, which is a spatial dose rate calculation program included in RESET.

We introduce a simulation result for decontamination of a campsite in the Fukushima Prefecture as an example. Fig.1-16 shows a comparison of the spatial dose rate maps measured before decontamination, as predicted by RESET and measured after the fact. Since the effect of decontamination can be visualized for ease of understanding, as in these figures, it can be used to study efficient decontamination methods and risk communication for residents in the area.

RESET is now used by MOE, the Fukushima prefectural office, and 12 towns and villages, and we are using RESET in responding to requests by local and national governments for advice and technical guidance on the implementation of effective decontamination, predicting dose rates in the future, and studying effective decontamination methods for an area. We are planning to apply RESET to higher-dose rate areas such as resident restricted areas and areas to which return is difficult, as well as forests, which accounts for 70% of the area of Fukushima Prefecture.

References

Tagawa, A.,Yamashita, T. et al., Decontamination Estimate and Demonstration Test Results on Road in the Return Difficult Area, Proceedings of 10th Annual Conference of Japan Society of Maintenology, Suita, Japan, 2013, p.699-702 (in Japanese).
Verification of the Decontamination Effects on Different Objects in the Decontamination of Houses, Report of the Decontamination Technique Support Business Operation for Cities and Villages in Fukushima Prefecture in FY2014, Social Affairs and Environment Department, Fukushima Prefecture Office, 2014, p.57-77 (in Japanese), http://www.pref.fukushima.lg.jp/uploaded/attachment/116502.pdf

1–7 Investigation of the Mechanism of Cesium Adsorption into the Soil using a Supercomputer
— Singular Adsorption of Cesium Revealed by First Principles Calculations —

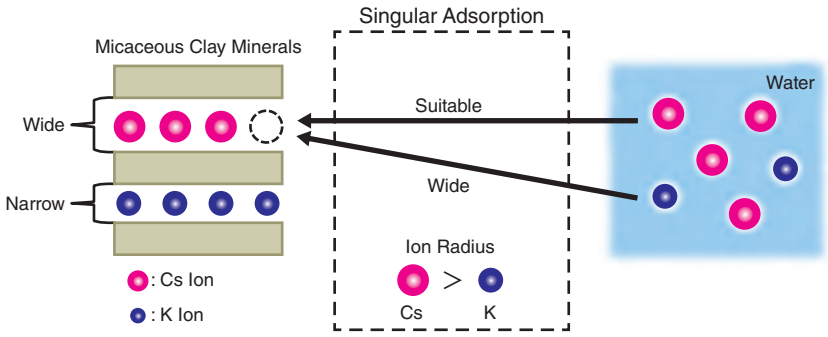

Fig.1-17 Model of ion-exchange reaction between micaceous clay mineral and water and the mechanism of singular adsorption
This schematic figure shows adsorption of hydrated Cs ions onto micaceous clay minerals modeled by supercomputer calculations. Micaceous clay minerals have a stacked layer structure. The interlayer distances are varied by the radii of the contained ions. Due to this property, the affinity of clay minerals for Cs ions becomes stronger as the interlayer Cs ions increase.

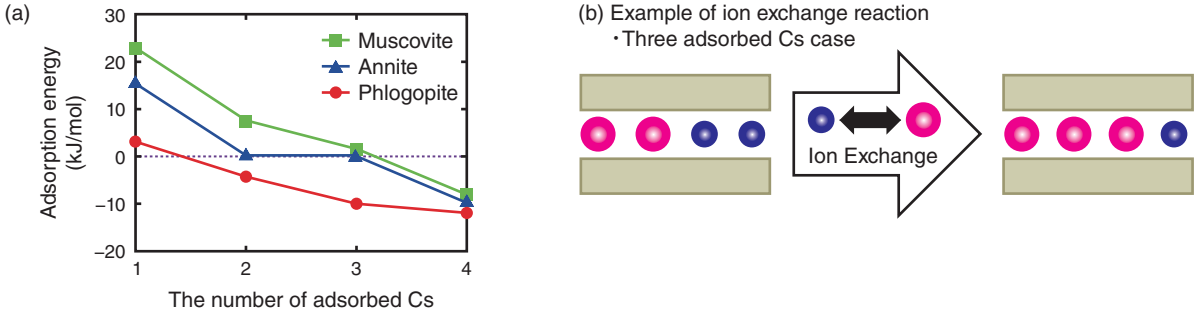

Fig.1-18 Cs adsorption energy of micaceous clay minerals
(a) Result of a first-principles calculation. Adsorption energy represents the energy change over an ion-exchange reaction. The reaction proceeds spontaneously when the value is negative, and smaller values imply the final states are more stable. (b) An example of an adsorption process.

The accident at the TEPCO's Fukushima Daiichi NPS in 2011 released many radioactive nuclides into the environment. In particular, radioactive cesium (Cs) has been the main γ-ray emitter because it has a long half-life and has been retained by surface soil. The Japanese government has performed large-scale decontamination, which has reduced radiation. However, a new issue arose: treatment of huge amounts of waste soil.

It is known that Cs in soils is adsorbed by micaceous clay minerals. The waste volume can be reduced if the Cs is desorbed from them. However, there is no economical or effective technique for this reduction owing to lack of knowledge about adsorption sites at an atomic scale. Therefore, it is necessary to reveal the mechanism of the strong adsorption of Cs to the micaceous clay minerals for development of the desorption techniques.

It is expected that Cs released into the environment would have been dissolved into water as an ion and then adsorbed to micaceous clay minerals by ion-exchange reaction with potassium (K) ions preoccupying the clay minerals. Recently, a singular Cs adsorption to a clay mineral has been observed: Cs ions are accumulated by biotite.

Therefore, we made models of muscovite, phlogopite, and annite, which are end members of biotite, on a supercomputer (Fig.1-17). We simulated ion-exchange reactions and evaluated their energy using a first-principles calculation (Fig.1-18). We obtained the result that serial adsorption increases the affinity of clay minerals for Cs. In particular, phlogopite and annite show stronger affinity than muscovite. In addition, this tendency is explained by a simple model: matching of ion radius and interlayer distance (Fig.1-17). This result shows that the singular adsorption observed is a general phenomenon in the environment. We continue our study to develop a technique for waste volume-reduction, which contributes to the reduction of environmental damage.

Reference
Okumura, M. et al., Energetics of Atomic Level Serial Ion Exchange for Cesium in Micaceous Clay Minerals, Clay Science, vol.18, no.3, 2014, p.53–61.

1–8 Selective Adsorption of Radioactive Cesium onto Weathered Biotite
— Successive Adsorption Mechanism of Cesium like "Domino Toppling" —

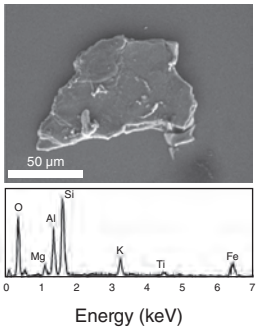

Fig.1-19 A microscope picture of radioactive fine particles (upper), and the chemical compositions of these particles determined by the X-ray emission spectrum (lower)

Fig.1-20 Widely seen clay mineral in Fukushima, vermiculite

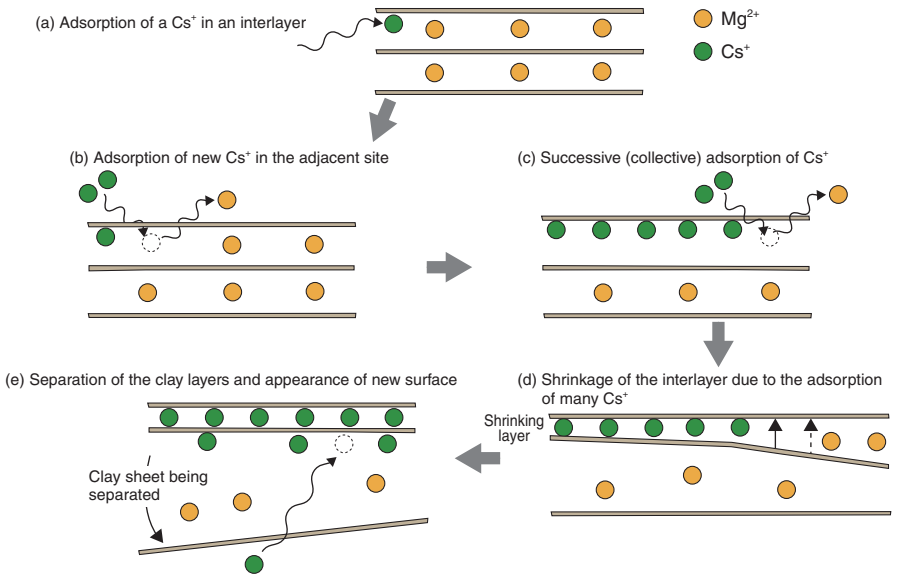

Fig.1-21 Successive adsorption of Cs^+ like "domino toppling" and schematics of the structural change of vermiculite
This image expresses the exchange process of Mg^{2+} with Cs^+ in a swelling interlayer of clay minerals like vermiculite. This process would promote an environment to help further Cs^+ penetration into the layer and work for neutralization of the interlayer charge.

The accident at the TEPCO's Fukushima Daiichi NPS has caused serious contamination of the surrounding environment. We have found the selective adsorption of radioactive cesium (Cs) onto weathered biotite (or vermiculite, Figs.1-19 and 1-20), which commonly occurs in Fukushima, and have clarified its successive adsorption mechanism (Fig.1-21), using a radiation-recording medium, an imaging plate (IP), electron microscope techniques, and small-angle X-ray scattering.

Weathered biotite has been considered to be a promising absorbent for radioactive Cs in real soil in Fukushina. We first collected soil contaminated with radioactive Cs at Iitate Village, Fukushima. The soil particles were put on IP and the radiation from each particle was recorded. On the basis of the images, the particles including radioactive Cs were then transferred to an electron microscope (SEM), and the structures and chemical composition were investigated. Consequently, we found that the particles containing radioactive Cs are categorized into the several types. After slicing the particulates into thin sections, we further analyzed the detailed micro-structures inside of the particulates using an electron microscope (TEM) with a higher resolution. Consequently, it became clear that most radioactive Cs was immobilized on the weathered biotite. In addition, the Cs ion (Cs^+) in the real soil of Fukushima was not concentrated in the edge area of the micaceous particles but distributed homogeneously in this mineral, in contrast to the previous sorption-experimental results in the laboratory. In fact, much weathered biotite, deriving from the granite in the east part of Fukushima, occurs in Fukushima soil. Thus, there is a high possibility that a large amount of radioactive Cs in the soils of forests and rice fields is strongly trapped in this mineral.

We investigated the adsorption behavior of radioactive Cs and the structural changes in vermiculite clay with an increase in Cs^+ concentration in dipping solution. Consequently, once one Cs^+ adsorbed at a specific point of the vermiculite interlayer, the Cs^+ and other ions with similar chemical properties tended to occupy the neighboring site in the same interlayer space. Finally substantial Cs^+ adsorbed collectively in the selective interlayer spaces. Furthermore, there were electrostatic interactions in the clay interlayer space because of the Cs^+ adsorption. The direct bonding of substantial positive Cs^+ with oxygen atoms of the clay sheet, locally compensated for the layer charge of the clay sheet. Thus, the attractive interaction between the clay sheets on opposite sides of the interlayer was weakened. Consequently, the two clay layers were separated, and the newly formed surface of the separated layer potentially could work as an adsorption site of the other Cs^+. Therefore, substantial amounts of Cs^+ were adsorbed in the layer of vermiculite one after another like "domino toppling". In order to investigate this mechanism at the atomic/molecular scale, the research group employed a method called "small angle X-ray scattering". Consequently, it was found that the structure had changed, as shown in Fig.1-21.

These detailed results for a concentrated mineral and adsorption mechanism of radioactive Cs in Fukushima are expected to provide useful information for the Fukushima environmental recovery.

References

Motokawa, R., Yaita, T. et al., Collective Structural Changes in Vermiculite Clay Suspensions Induced by Cesium Ions, Scientific Reports, vol.4, 2014, p.6585–1–6585–6.
Mukai, H., Yaita, T. et al., Speciation of Radioactive Soil Particles in the Fukushima Contaminated Area by IP Autoradiography and Microanalyses, Environmental Science & Technology, vol.48, issue 22, 2014, p.13053–13059.

1–9 Removal of ^{137}Cs from Sewage Sludge Ash by Dissolving Iron Oxide

— Success in Removing ^{137}Cs Efficiently through Elucidation of the Chemical States of ^{137}Cs —

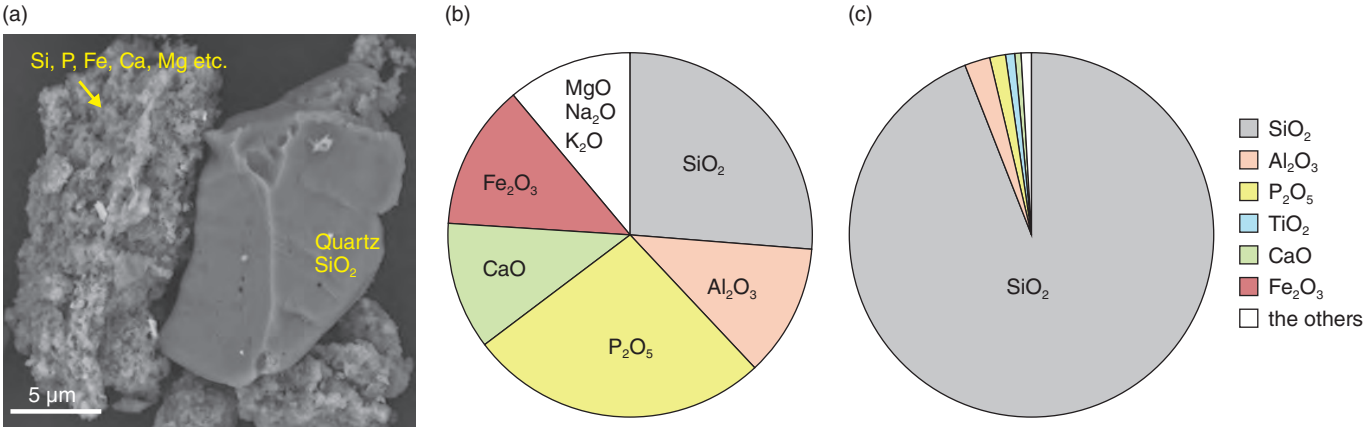

Fig.1-22 SEM image of SSA (a), elemental composition of SSA on oxide basis (b), and elemental composition of residue after SSA was pulverized and treated with a hydrochloric acid aqueous solution (c)
Iron is contained in aggregates of numerous fine particles (the left particle shown with a yellow arrow in (a)). By dissolving all of the iron, the radioactivity concentration of ^{137}Cs in SSA, 23000 Bq/kg, was decreased to 4800 Bq/kg.

After the accident at the TEPCO's Fukushima Daiichi NPS (1F), a huge amount of sewage sludge ashes (SSAs) contaminated with radioactive cesium (Cs) (hereafter Cs) was produced at sewage treatment plants in east Japan. Most of them have been stored at those sewage treatment plants. The SSAs containing Cs above 8000 Bq/kg (radioactivity criterion) have been strictly stored as designated waste. Because this was the first case of radioactive contamination of SSA in the world, no scientific knowledge was available to develop a strategy for treatment and disposal of contaminated SSAs.

Si and P were the most abundant elements contained in SSAs, followed by Al, Ca, and Fe (Fig.1-22(a)). SSAs consisted of two main types of particles (Fig.1-22(b)). The first type was natural quartz and feldspar; the second type was a dense aggregate of numerous fine particles thought to be formed during incineration of sewage sludge. These aggregates mainly contained iron oxides, phosphate minerals, and silicon-bearing minerals supposed to be silicon dioxides (hereafter silicon dioxide). We collected SSAs containing Cs of 1F origin above the radioactivity criterion and investigated the relationships among elements such as Cs and iron dissolved from SSAs in acid solution to elucidate the chemical states of Cs, *i.e.*, the solid phase retaining Cs. We found that a significant percentage of Cs was contained as water-soluble salt; approximately 10% was in silicates (quartz, feldspar, and silicon dioxide); and the remainder was in iron oxides. A portion of the iron oxides was not easily dissolved in acid solution, and the Cs concentration in the acid-treatment residue containing iron was not lowered to below the radioactivity criterion because such iron oxide was present inside densely sintered aggregates of numerous nanoparticles with a silicate-framework. Hydrochloric acid solution did not reach the depths of these aggregates. Accordingly, we pulverized the SSAs down to several-hundred nanometers and then dissolved them in hydrochloric acid. Consequently, we succeeded in dissolving almost all of the iron oxides in the SSAs (Fig.1-22(c)). The Cs concentration in the acid-treatment residue of pulverized SSAs was lowered to below the radioactivity criterion. Long-term leaching tests confirmed that the Cs contained in the acid-treatment residue was not leacheable to pure water and seawater at the raised temperature.

We expect that these findings will contribute to the development of a strategy for appropriate treatment of the designated waste containing radionuclides released from 1F and reducing its volume.

Reference

Kozai, N. et al., Radioactive Fallout Cesium in Sewage Sludge Ash Produced after the Fukushima Daiichi Nuclear Accident, Water Research, vol.68, 2015, p.616–626.

1–10 Evaluation of the Integrity of a Fuel Cladding Tube after Seawater Injection
— Investigation of the Pitting Potential —

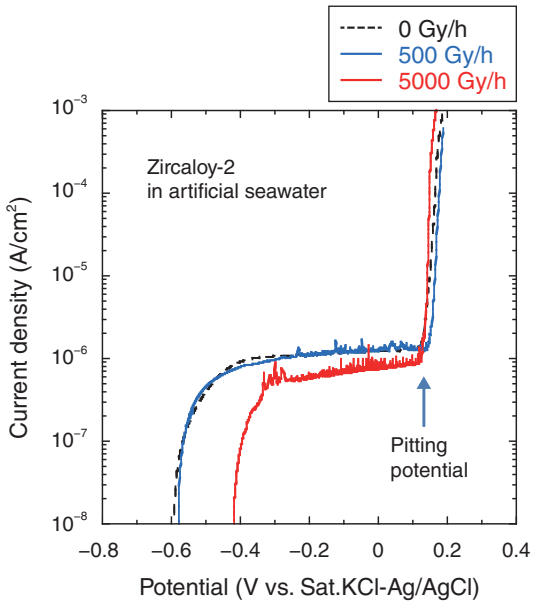

Fig.1-23 Polarization curves of Zircaloy-2 immersed in artificial seawater at ambient temperature
The pitting potential of Zircaloy-2 was measured by electrochemical techniques. Pitting potential where a fast current rise occurs is similar with and without γ-ray radiation.

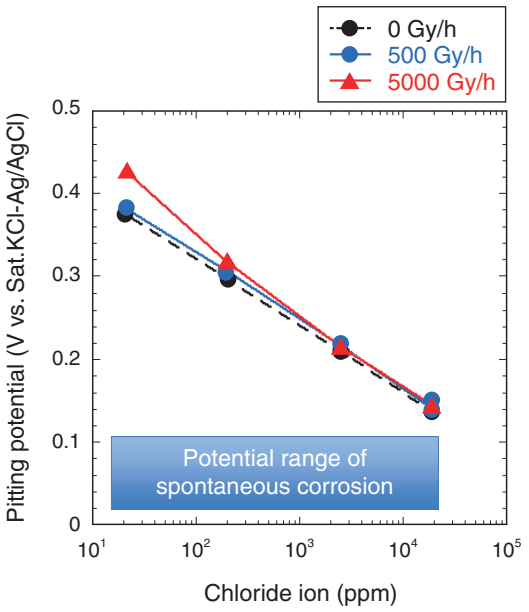

Fig.1-24 Pitting and spontaneous potentials of Zircaloy-2 as functions of the chloride concentration of diluted artificial seawater
The pitting corrosion and spontaneous potentials of Zircaloy-2 were measured in diluted artificial seawater. The pitting potential was higher than the spontaneous potential. This result indicates that pitting corrosion could not occur spontaneously in the tested solutions.

At the TEPCO's Fukushima Daiichi NPS (1F), the cooling function of the spent fuel pools (SFPs) failed with the loss of the electrical power supply, so seawater was injected into the SFPs of Units 2–4 as an emergency measure for avoiding fuel exposure to air. Corrosion troubles are not a concern under circulation of purified water in SFP, but they are under circulation of water contaminated by seawater. Chloride ions, which originate from seawater. can lead to pitting corrosion of fuel cladding tubes (Zircaloy-2) and radioactive substances are leaked from the pitting position. To avoid a leakage risk, TEPCO has been removing seawater components from contaminated water, and fuel rods are cooled by water containing less than 10 ppm of chloride ions.

There are many corrosion survey data for Zircaloy-2 in a clean water environment at high-temperature, but very few data are available in water with a high radioactivity and chloride ion-concentration at ambient temperature. The corrosion data of Zircaloy-2 in the latter environment is needed to evaluate the integrity of Zircaloy-2 cladding tubes in SFPs after accidents. Therefore, we have investigated the electrochemical corrosion behavior of Zircaloy-2 in diluted artificial seawater under γ-ray irradiation at ambient temperature. Pitting and spontaneous potentials of Zircaloy-2 were measured as the electrochemical corrosion data.

Fig.1-23 shows polarization curves of Zircaloy-2 immersed in artificial seawater at ambient temperature. The potential at which the apparent rise of current density occurs is called the pitting potential. There is no difference in the pitting potentials under the tested dose rate conditions (0, 500, 5000 Gy/h). This result suggests that pitting potential is not affected by γ-ray irradiation. Fig.1-24 shows the relationship between the pitting and the spontaneous potentials of Zircaloy-2 and the chloride ion-concentration of diluted artificial seawater. It is known that pitting corrosion can occur if pitting potential is less than spontaneous potentials. Pitting potentials are higher than spontaneous potentials in all cases, indicating that pitting corrosion of Zircaloy-2 hardly occurs in the tested solution.

At present, the chloride ion-concentration of circulation water is maintained at less than 10 ppm in SFPs and the common pool of 1F. It is believed that Zircaloy-2 is not subject to pitting corrosion in the above mentioned environments.

Reference

Motooka, T. et al., Effect of Gamma Radiolysis on Pit Initiation of Zircaloy–2 in Water Containing Sea Salt, Journal of Nuclear Science and Technology, vol.51, issues 7–8, 2014, p.987–995.

1–11 Integrity Assessment of a Fuel Assembly

— Mechanical Property-Evaluation of a Fuel Cladding Tube Immersed in Seawater —

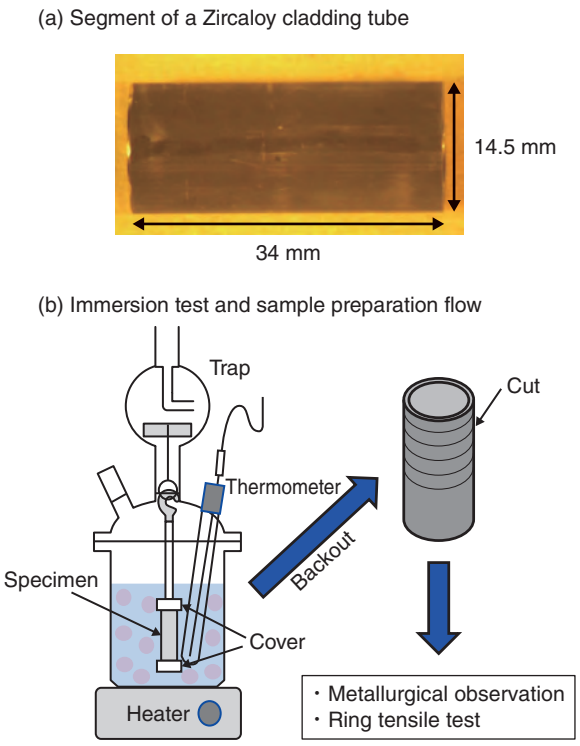

Fig.1-25 Immersion test procedure and sample preparation
Using a Zircaloy cladding tube (after fuel removal), a seawater-immersion test was conducted at 80 °C for 1051 hours. After the immersion test, the cladding tube was cut and metallurgical observations and tensile tests were performed.

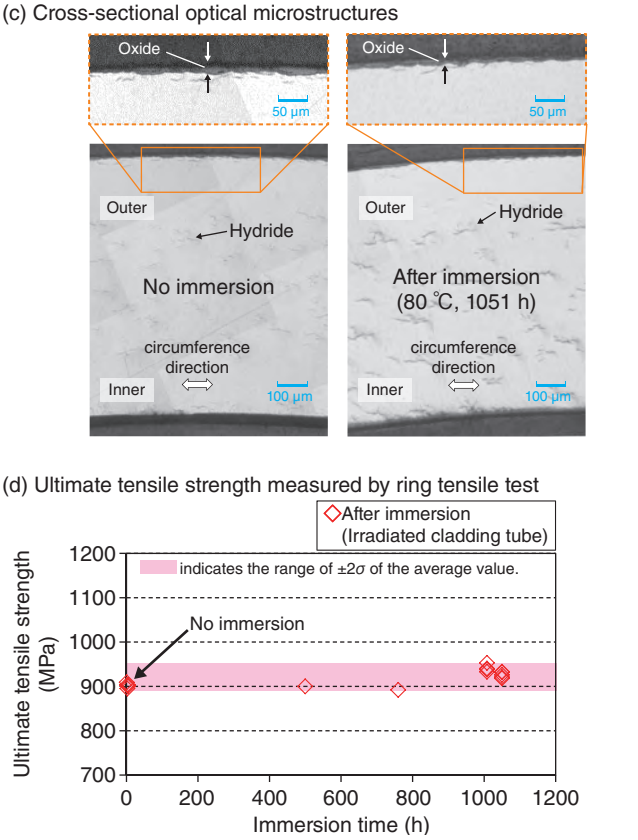

Fig.1-26 Optical microstructures and tensile properties of the cladding tubes without immersion and after seawater immersion
Metallurgical observation and ring tensile tests were conducted for ring specimens cut from the cladding tube after seawater immersion. Consequently, not only was there no change in oxide film and hydride formation but also no degradation of ultimate tensile strength was observed.

In the accident at the TEPCO's Fukushima Daiichi NPS (1F), seawater was temporarily injected into the spent fuel pools (SFPs). Then, new and spent fuel assemblies in the SFPs were temporary immersed in seawater at high temperatures (70–90 °C). There are plans to transport the fuel assemblies in the SFPs to a common pool set up on the 1F site, where they will be stored for a long time. Therefore, during storage, the integrity of the fuel assemblies must be maintained, and fuel failure should not occur. However, for those assemblies that experienced seawater immersion, surface corrosion because of seawater constituents such as chloride ions and the resultant degradation of mechanical properties are of concern. It is necessary to assess the integrity of the fuel assemblies, especially the cladding tubes that act as the most important boundaries for containing radioactive fission products inside the fuel rods. Therefore, using the irradiated Zircaloy cladding tubes that were obtained from a spent fuel assembly of the advanced thermal reactor "FUGEN" (which is similar to the type of BWRs used at the 1F plant), a seawater immersion test was conducted under the assumed environment of the SFPs in the early stage of the 1F accident. After that, a ring tensile test was evaluated for the cladding tube specimens (Fig.1-25).

The typical cross-sectional optical microstructures of the cladding tubes without immersion and after seawater immersion are shown in Fig.1-26(c). Focusing on the outer surfaces, there was no change between the non-immersed and immersed tube specimens. Neither pitting corrosion nor uniform corrosion had been caused. No obvious change in the oxide formation induced during reactor operation would not influence the mechanical properties in the circumferential direction. In addition, there were no visible changes in the hydride distribution (such as reorientation) in the matrix of the cladding tube. This meant that the hydride distribution in the radial direction, which would affect the mechanical properties in the circumference direction, had not progressed during the time of the immersion test. The ultimate tensile strength measured by a ring tensile test is shown in Fig.1-26(d). This indicates that no significant degradation in the ultimate tensile strength in the circumferential direction was confirmed in this immersion condition and the ultimate tensile strength was independent of the immersion time.

Therefore, it was considered that the influence of seawater immersion on the corrosion behavior and mechanical properties of irradiated Zircaloy-2 cladding tubes was negligible under this immersion condition. As future work, mechanical property evaluations after various immersion conditions, as well as evaluations of other parts of the fuel assembly or the real cladding tubes of Units 1-4, will be conducted.

Reference

Fukushima Project Team et al., Influence Evaluation of Corrosion on Long-Term Integrity of Spent Fuel Assembly Component Materials Exposed to Unusual Corrosive Environment at Unit 1-4 Spent Fuel Pools of Fukushima Dai-Ichi Nuclear Power Stations, JAEA-Technology 2014-020, 2014, 52p. (in Japanese).

1–12 Evaluation of the Mechanical Properties of the Fuel Debris
— Relationship between Fuel Debris and the Cladding Tube Components —

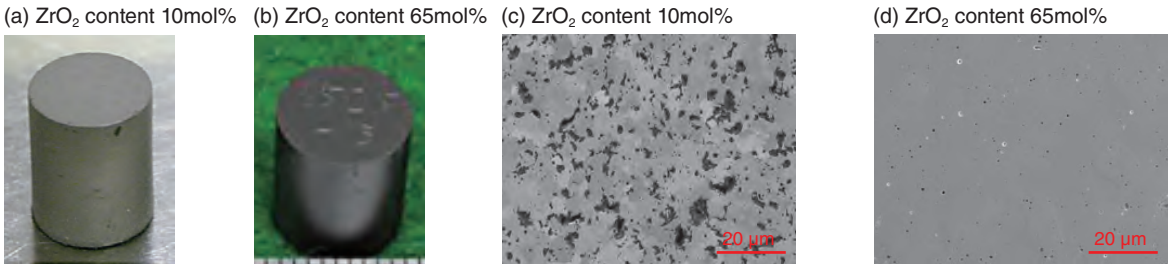

Fig.1-27 External appearance and cross section of the simulated debris
Photos (a) and (b) show the appearance of simulated debris samples with ZrO_2 contents of 10 and 65mol%, respectively. Photos (c) and (d) show the respective cross-sectional images of these samples. ZrO_2 content represents the cladding tube component. There are no defects, such as cracks in the external surface. The portion that is visible in the spotty pattern shows the grain boundary in the cross section. These grain sizes are 10–40 μm.

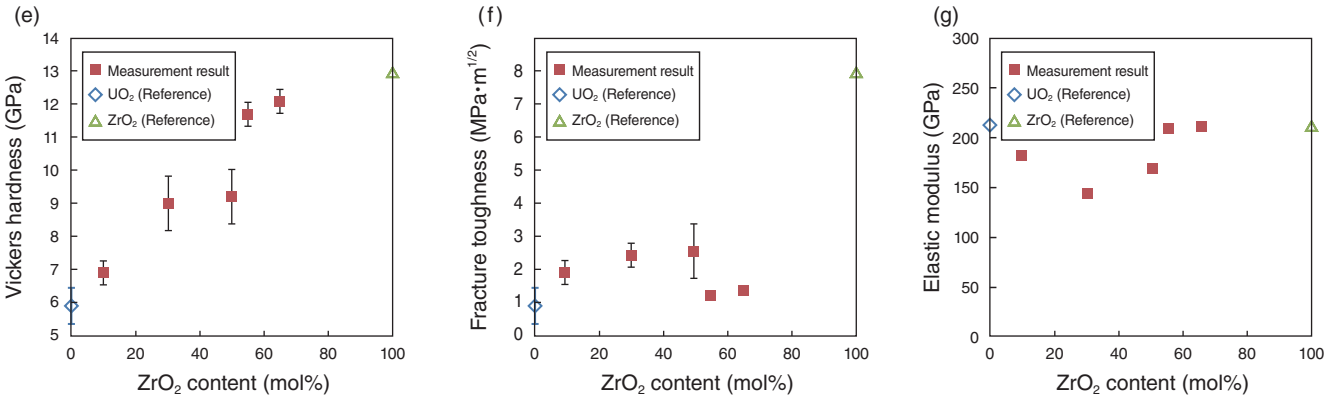

Fig.1-28 Relationship between mechanical properties and ZrO_2 content
These figures show the relationship between (e) Vickers hardness, (f) fracture toughness, and (g) elastic modulus and ZrO_2 content. In particular, ZrO_2 content affects the Vickers hardness significantly and hardness increases with ZrO_2 content.

In the decommissioning of TEPCO's Fukushima Daiichi NPS (1F), one important issue is to perform safe and steady defueling work. Before defueling in 1F, it is necessary to evaluate fuel debris for properties related to defueling procedures and technology. While defueling after the Three Mile Island Unit 2 (TMI-2) accident in the U.S., a core-boring system played an important role. Considering the working principle behind core-boring, hardness, elastic modulus, and fracture toughness were found to be important fuel debris properties that had a profound effects on the performance of the boring machine. It is speculated that uranium and zirconium oxide solid solution ($(U,Zr)O_2$) is one of the major constituents of fuel debris in 1F, according to the TMI-2 accident experience and the results of past severe accident studies. In addition, the zirconium (Zr) content of 1F fuel debris is expected to be higher than that of TMI-2 debris because the 1F boiling-water reactors (BWRs) had a high Zr rate in their constituent materials.

In this report, the mechanical properties of $(U,Zr)O_2$ made with an electric furnace are evaluated in the zirconium dioxide (ZrO_2) content range from 10mol% to 65mol% (Fig.1-27). The hardness, elastic modulus, and fracture toughness were measured by Vickers testing, the ultrasonic pulse echo method, and the indentation fracture method, respectively (Fig.1-28).

In the ZrO_2 content range under 50mol%, the Vickers hardness (e) and fracture toughness (f) of $(U,Zr)O_2$ increased, and the elastic modulus (g) decreased slightly with ZrO_2 content. In the case of 55mol% and 65mol% ZrO_2, all of those measures increased slightly with ZrO_2 content. Summarizing these results, ZrO_2 content affected the mechanical properties significantly in the case of low ZrO_2 content. Higher Zr content (exceeding 50mol%) had little effect on mechanical properties.

In the future, nonradioactive surrogate debris will be necessary for small-scale functional and large-scale mockup tests of various defueling technologies. These results are useful for selecting the material for surrogate debris.

This topic includes a part of the results of "Establishment of basic technology for decommissioning and safety of nuclear reactors for power generation" in FY 2013 that was entrusted to IRID from METI and conducted by JAEA as a member of IRID.

Reference

Hoshino, T. et al., Mechanical Properties of Fuel Debris for Defueling Toward Decommissioning, Proceedings of 23rd International Conference on Nuclear Engineering (ICONE 23), Chiba, Japan, 2015, ICONE23–2111, 6p., in DVD–ROM.

1–13 How do Microscopic Particles of Debris Change in Water?

— To Understand the Chemical Effects of Hydrogen Peroxide and Boric Acid —

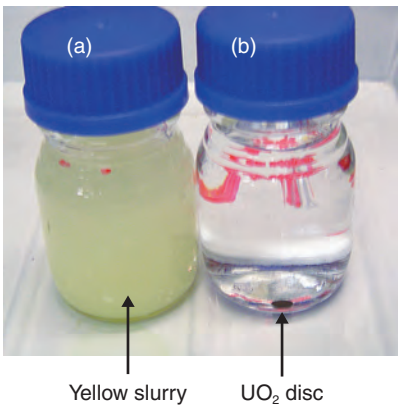

Fig.1-29 Yellow slurry of $UO_4{\cdot}4H_2O$ and a UO_2 disc in water
(a) Yellow slurry of $UO_4{\cdot}4H_2O$ given by the immersion of a UO_2 disc in 10wt% H_2O_2 aqueous solution, (b) UO_2 disc immersed in pure water over a period corresponding to (a). UO_2 discs as well as powders are fully oxidized and pulverized into microscopic particles by H_2O_2.

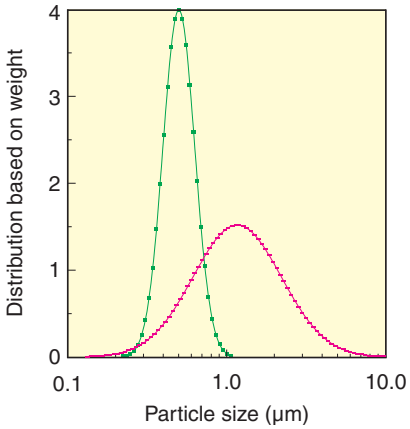

Fig.1-30 Particle size distribution of $UO_4{\cdot}4H_2O$
particle size distribution of the $UO_4{\cdot}4H_2O$ given by the immersion of UO_2 in 10wt% H_2O_2 aqueous solution (pH 5.6), the distribution after hydrochloric acid (HCl) has been added to the slurry (pH 2.8). As the acidity of the aqueous solution is stronger, the particles are flocculated; consequently, the particle size becomes larger. This property means that the slurry is mesocolloidal.

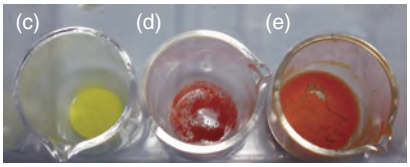

Fig.1-31 Uranium trioxide hydrate
(c) Uranium trioxide dihydrate ($UO_3{\cdot}2H_2O$), (d) uranium trioxide monohydrate ($UO_3{\cdot}H_2O$), and (e) UO_3. $UO_3{\cdot}2H_2O$ are formed by the moisture-absorption of UO_3; in contrast, a perfect dehydration of $UO_3{\cdot}2H_2O$ cannot be accomplished by heating at 300 °C. Under this condition, $UO_3{\cdot}H_2O$ is formed.

During the accident at the TEPCO's Fukushima Daiichi NPS, the nuclear fuels melted together with the structural materials of the nuclear reactors and became debris. It is supposed that a portion of the debris may have dropped into the cooling water. In such a quenching condition, the debris could be pulverized into small particles. In addition, the particle size would become smaller by oxidation. Small powders of the debris will also be produced by cutting under the removal operations of the debris from the nuclear reactors. However, the chemical behaviors of the small particles of the debris in water are not understood.

Therefore, to investigate the chemical change and pulverization of debris immersed in cooling water for a long time, uranium dioxide (UO_2), a component of the debris, was immersed in pure water as well as sodium chloride (NaCl), hydrogen peroxide (H_2O_2), and boric acid (H_3BO_3) aqueous solutions for a month at 50 °C. As shown in Fig.1-29, UO_2 reacted perfectly with H_2O_2; consequently, yellow particles of uranium peroxide tetrahydrate ($UO_4{\cdot}4H_2O$) were formed. It was found that the average particle size was smaller than 1 μm, as shown in Fig.1-30, and that the slurry showed mesocolloidal properties. In contrast, UO_2 did not show notable chemical changes in the other aqueous solutions.

The chemical bonding of the UO_2 and H_3BO_3 was investigated by infrared spectroscopy. From the result, H_3BO_3 was predicted not to accompany the debris under removal operations from the H_3BO_3 aqueous solution. The influence of heating temperature and humidity on the hydration number of uranium peroxide hydrates was investigated. It was found that although $UO_4{\cdot}4H_2O$ changed to orange anhydrous uranium trioxide (UO_3) under heating at 300 °C, UO_3 absorbed the moisture and easily suffered the hydration. Please see Fig.1-31.

This topic includes a part of the results of "Establishment of basic technology for decommissioning and safety of nuclear reactors for power generation" in FY 2013 that was entrusted to IRID from METI and of the subsidy program "Project of Decommissioning and Contaminated Water Management" in the FY 2013 supplementary budget and conducted by JAEA as a member of IRID.

Reference

Otobe, H. et al., Corrosion of Uranium and Plutonium Dioxides in Aqueous Solutions, Proceedings of 2014 Nuclear Plant Chemistry Conference (NPC 2014), Sapporo, Japan, 2014, paper 10173, 11p., in USB Flash Drive.

1–14 Investigating the Effects of Seawater on the Cooling Performance of a Reactor Core

— Evaluation of the Thermal-Hydraulic Behavior of Seawater using a Model Fuel Rod —

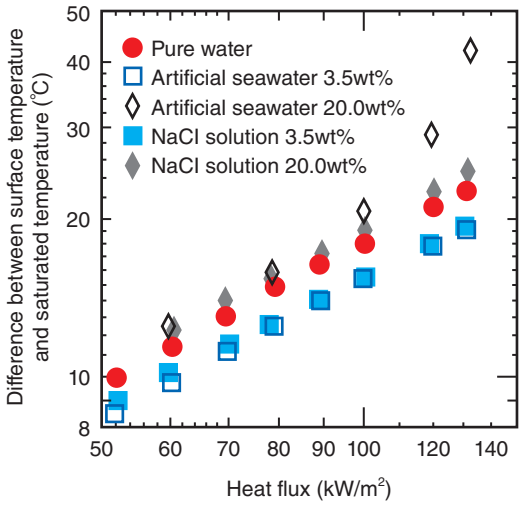

Fig.1-32 Heat transfer characteristics of saturated boiling
As in pure water, the temperature differences in the NaCl solution and the artificial seawater of 3.5wt% are proportional to a power of the heat flux. However, the surface temperature in the artificial seawater of 20wt% becomes higher than the correlation for higher heat flux.

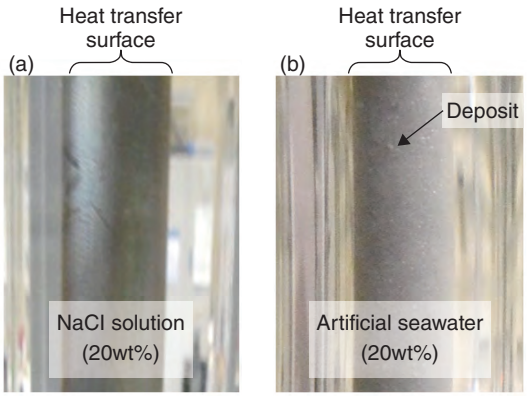

Fig.1-33 Photographs of the heat transfer surface after experiments
(a) and (b) show the heat transfer surface after experiments with the NaCl solution and the artificial seawater of 20wt%, respectively. The white crystals have been deposited to cover the heat transfer surface in the artificial seawater of 20wt%.

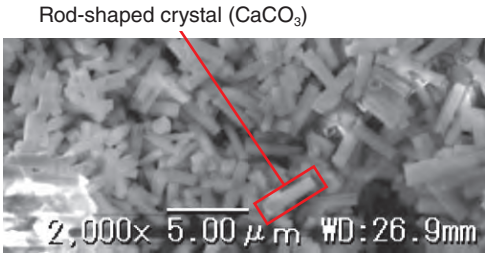

Fig.1-34 SEM images of the deposited crystals
The rod-shaped objects are the deposited crystals. By quantitative analysis with XRD, it has been confirmed that the crystal is calcium carbon dioxide ($CaCO_3$).

In the accident at the TEPCO's Fukushima Daiichi NPS, seawater was injected into reactor cores instead of pure water because core cooling systems were lost in a station blackout. However, the physical properties of seawater are different from those of pure water. Moreover, minerals are included in seawater. These minerals may influence the cooling performance because these deposits may change the heat transfer surface and block the flow.

We conducted an experiment with an internally heated annulus modeled on a fuel rod to estimate the effects of seawater on the cooling performance. The working fluid was artificial seawater modeled on real seawater. In addition, we used pure water and sodium chloride (NaCl) solution as comparison fluids. The concentration ranged from 3.5wt%, like the seawater around Japan, to 20wt%, like the seawater concentration in a core.

Fig.1-32 shows a double-logarithmic graph of the difference between the temperature on the heat transfer surface and the saturated temperature as a function of the heat flux (heating power per unit area). In the pure water, the artificial seawater of 3.5wt%, and the NaCl solutions of 3.5wt% and 20wt%, these temperature differences are proportional to the power of the heat flux. However, in the artificial seawater of 20wt%, the surface temperature increases more than linearly predicted from the condition of higher heat flux. This result indicates deterioration in the cooling performance. One of the causes is crystal deposition on the heat transfer surface. Fig.1-33 shows photographs of the heat transfer surface after the experiments in the artificial seawater and the NaCl solution of 20wt%. Although the surface condition in the NaCl solution has not changed from its condition before the experiment, white crystals have covered the surface in the artificial seawater. The deposition is observed in only the artificial seawater of 20wt%. Fig.1-34 shows scanning electron microscopy (SEM) images of the crystals. Many rod-shaped crystals with sizes of 3–4 μm are observed. By quantitative analysis with X-ray diffraction (XRD), the crystal was found to be calcium carbonate ($CaCO_3$). Therefore, it has been confirmed that the cooling performance deteriorated when the $CaCO_3$ crystals covered the heat transfer surface. In future, these results will be reflected in numerical simulations to grasp the condition of the reactor core.

This topic includes a part of the results of "Establishment of basic technology for decommissioning and safety of nuclear reactors for power generation" in FY 2013 that was entrusted to IRID from METI and of the subsidy program "Project of Decommissioning and Contaminated Water Management" in the FY 2013 supplementary budget and conducted by JAEA as a member of IRID.

Reference

Uesawa, S. et al., The Thermal–Hydraulic Behavior of Seawater in an Internally Heated Annulus, Proceedings of 23rd International Conference on Nuclear Engineering (ICONE 23), Chiba, Japan, 2015, ICONE23–1367, 8p., in DVD–ROM.

1–15 Calculation of the Melting Behavior of Fuel Rods in Severe Accidents
— Development of a Numerical Method Based on the Particle Method —

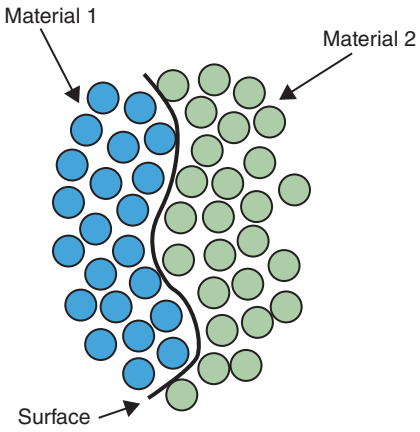

Fig.1-35 Surface in the particle method
This figure shows a surface between different materials. Friction and surface tension forces act at the surface. A model that could calculate these forces was introduced to the POPCORN code, making it possible to calculate the interaction at the surface.

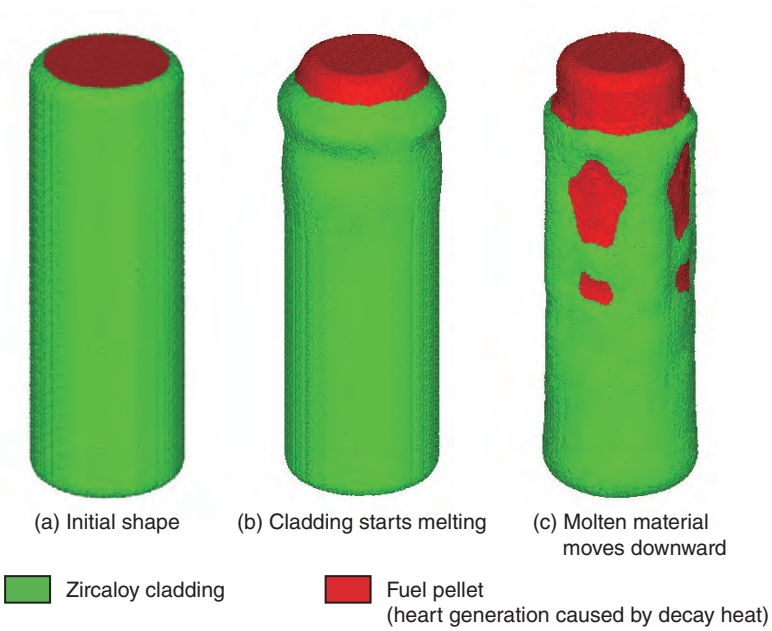

Fig.1-36 Melting behavior of a fuel rod
These figures show the calculation results for the melting behavior of a fuel rod. (a) The fuel rod consists of zircaloy cladding and fuel pellets; (b) zircaloy cladding starts melting because of decay heat; (c) melting zircaloy relocates to the bottom, and UO_2 remains in a solid phase because of the high melting temperature compared with the melting point of zircaloy.

Many numerical simulations are performed using severe accident codes for safety assessment of nuclear power plants. In severe accident codes, complex and diverse phenomena are simplified using the experimental results and numerical models because the calculation load is very high if these complex phenomena are calculated directly. Therefore, the accuracy of the calculation results is decreased in unexpected situations, because the models are not adequate to handle them. Experiments concerning severe accidents are not easy to perform because the experimental cost is very high and radioactive materials are difficult to use in such experiments. Therefore a detailed numerical simulation that can calculate a wider range of phenomena than severe accident codes plays an important role in evaluating the phenomena involved in a severe accident.

Thus, we are developing a numerical simulation code (POPCORN) for the melting behavior of fuel rods in severe accidents. In melting processes, it is expected that various types of phenomena will occur, including phase change, oxidation of zircaloy cladding and failure of fuel rods. To calculate the melting behavior of a fuel rod, we chose the particle method as a basis for developing the numerical code. In the particle method, fluid and solid materials are represented by groups of small particles, and not only fluid but also solid behavior can be calculated, with many types of materials being treated in a pressure vessel.

For the melting process, a large viscosity is set for molten materials to represent the fact that the molten materials have difficulty flowing, and interaction models are introduced to the POPCORN code at surfaces between different materials (Fig.1-35). Fig.1-36 shows the results of test calculations for the melting of fuel rods caused by decay heat. Zircaloy cladding melted because of decay heat, and molten zircaloy was relocated to bottom part.

In future work, chemical reactions and eutectic models will be introduced to the POPCORN code, and will be validated with experimental results.

Reference

Nagatake, T. et al., Development of POPCORN Code for Simulating Melting Behavior of Fuel Element: Fundamental Validation and Simulation for Melting Behavior of Simulated Fuel Rod, Proceedings of 23rd International Conference on Nuclear Engineering (ICONE 23), Chiba, Japan, 2015, ICONE23–1914, 6p., in DVD–ROM.

1–16 Estimation of the Failure Time and Location of the Pressure Vessel Lower Head in Severe Accidents

— Development of Failure Evaluation Methods for the Pressure Vessel Lower Head —

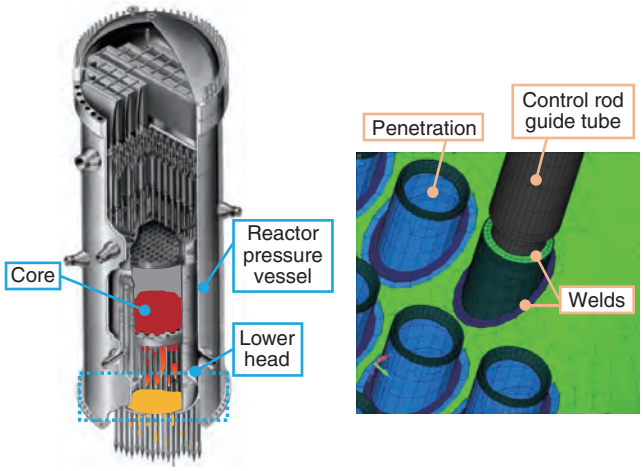

Fig.1-37 Analysis model of RPV lower head
The RPV lower head of a BWR, similar to 1F, has a complicated geometry since there are many penetrations and welds for connecting the control rod guide tubes. It is expected that failure location and time of the lower head after relocation of molten fuel are affected by this complicated geometry. We have developed a 3D model that includes these welds to assess the rupture behavior of the lower head during the accident in detail.

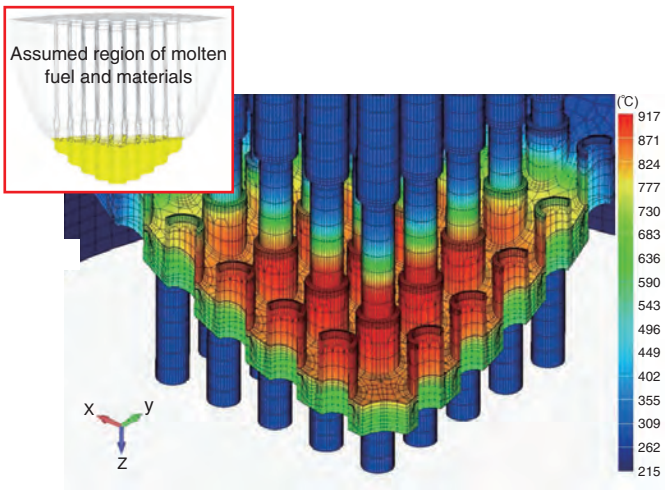

Fig.1-38 An example of the temperature distribution
This figure illustrates an example of temperature distribution obtained from thermal-hydraulic analyses with a detailed 3D model. The yellow region in the top left figure corresponds to relocated molten fuel and materials. Through this region is heated up, the temperatures of the materials comprising the RPV lower head are also raised, resulting in creep deformation of the lower head.

To gain better awareness of the situation within the reactor pressure vessel (RPV) of the TEPCO's Fukushima Daiichi NPS (1F) and improve the current severe accident (SA) analysis codes, e.g. THALES2 developed by JAEA, we are conducting research and development to assess the rupture behavior of the RPV lower head due to relocation of the molten core. Since simple evaluation methods and models are used for rupture evaluations in the current SA analysis codes, failure time and location obtained from the current codes may include a large uncertainty (scatter). For more accurate evaluations of the rupture behavior of the lower head of boiling water reactors (BWRs) like 1F, it is necessary to develop methods to estimate local failure by considering geometrically complicated structures (Fig.1-37).

In this study, we are developing a coupled analysis method of thermal-hydraulics (TH) and structural analyses, which are to be applied to the behavior of a molten core and to the thermal-elastic-plastic-creep behavior of the structures, respectively. We are also developing methods for evaluating the failure time and locations of the RPV lower head due to creep-deformation.

Fig.1-38 illustrates an example of analysis results obtained by using a three-dimensional (3D) model that considers the penetrations of a BWR (Fig.1-37). As an initial condition, we assumed that 10% of the reactor core has been melted and relocated to the lower head, and that the coolant water in the reactor is completely evaporated. Here, this scenario differs from the accident at 1F. The relocated core is heated by decay heat and the temperature of the lower head also increases. Using the developed failure-evaluation methods considering creep-deformation, we estimated that ruptures would occur at the penetrations because the damage index showed maximal values at those points.

In future, through experiments whose details are described in Topic 1-17, we will improve the failure-evaluation methods and contribute to the estimation of rupture time and the location of RPV in 1F and the improvement of SA analysis codes.

Reference

Katsuyama, J. et al., Development of Failure Evaluation Method for BWR Lower Head in Severe Accident; (3) Creep Damage Evaluation Based on Thermal–Hydraulics and Structural Analyses, Proceedings of 23rd International Conference on Nuclear Engineering (ICONE 23), Chiba, Japan, 2015, ICONE23–1534, 7p., in DVD–ROM.

1–17 Estimation of the Failure Time and Location of the Pressure Vessel Lower Head in Severe Accidents
— High-Temperature Creep Test and Investigation of Creep Constitutive Laws —

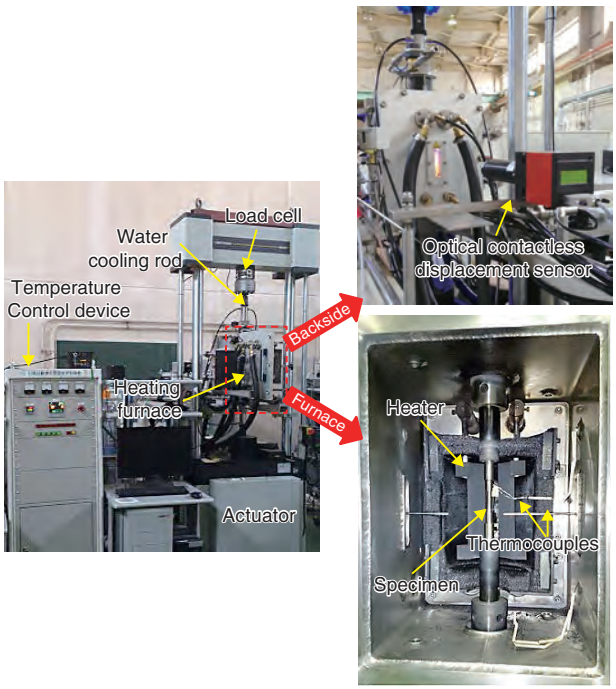

Fig.1-39 High-temperature tensile- and creep-testing equipment
Tensile- and creep-testing equipment with temperatures ranging up to 1600 °C have been developed to measure material properties near the melting point. Using an optical contactless displacement sensor, the elongation of gauge length could be continuously measured.

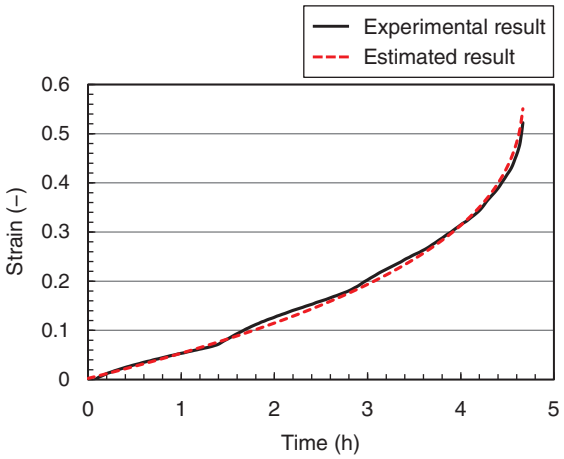

Fig.1-40 An example of a high-temperature creep test and estimation results using a creep constitutive law
As an example, a typical creep test result at 1300 °C and an estimated result based on a creep constitutive law proposed in this study are represented. We confirmed that a creep constitutive law that considers the creep damage mechanism can simulate the tendency by which the strain rate rapidly increases at approximately 4.5 hours before a rupture.

Following the accident at the TEPCO's Fukushima Daiichi NPS, we are performing various studies using numerical analysis to estimate the rupture behavior of reactor pressure vessel (RPV) lower heads because of relocation of the molten core. It is necessary to obtain the mechanical properties near the melting points for materials at the lower head to analyze the mechanical behavior during a severe accident. Especially in the case that high-temperature, high-pressure loadings are applied, we need a creep constitutive law that can simulate creep deformation. However, since there is little data regarding the mechanical properties (such as tensile and creep properties) in the high-temperature region beyond 1100 °C, we developed uniaxial tensile- and creep-testing equipment, as shown in Fig.1-39, and obtained data about the mechanical properties. We expanded the database of tensile and creep properties to a temperature of 1300 °C.

—— in Fig.1-40 represents a creep strain curve obtained experimentally at 1300 °C by a creep test. The specimen ruptured approximately 4.5 hours after it achieved 50% elongation. The strain rate rapidly increased just before the rupture, and this behavior is remarkable at high temperature. A creep constitutive law was investigated based on the obtained experimental data with consideration of such a tendency of the strain rate. Consequently, it was confirmed that a creep constitutive law considering material damage due to creep deformation can simulate the deformation to high accuracy, as well as the rupture time of the test specimens (– – – – in Fig.1-40). To apply this creep constitutive law to numerical analysis, we confirmed its applicability to different temperatures and materials, and a database of parameters for the creep constitutive law including the high-temperature region up to 1300 °C was developed. Through the above investigation, we showed a prospect for estimating the rupture time of the lower head due to creep deformation when the temperature and loading at a certain time were determined based on numerical analysis.

The creep constitutive law investigated in this study will be applied to failure analyses for RPV lower heads with the details being described in Topic 1-16, and will contribute to the estimation of rupture time and location of RPV.

Reference

Yamaguchi, Y. et al., Development of Failure Evaluation Method for BWR Lower Head in Severe Accident; (1) High Temperature Creep Test and Creep Damage Model, Proceedings of 23rd International Conference on Nuclear Engineering (ICONE 23), Chiba, Japan, 2015, ICONE23–1533, 7p., in DVD–ROM.

1–18 Prediction of the Characteristics of Radioactive Materials Released from Nuclear Fuel during Nuclear Power Plant Accidents

— Evaluation of the Effects of Boron Released from BWR Control Rods on the Chemical Behavior of Fission Products —

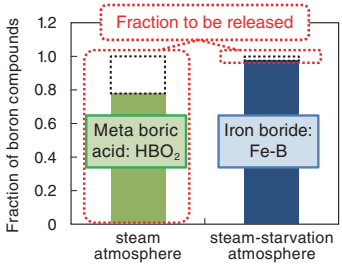

Change in boron, cesium, and iodine compounds formation, due to the decrease in boron release (calculation)	
Cesium metaborate: $CsBO_2$	–97%
Cesium iodine: CsI	+17%
Hydrogen iodide (gaseous): HI	–30%
Iodine (volatile): I	–30%

Fig.1-41 Prediction of boron compounds and release fractions in different atmospheres and their effects on cesium and iodine chemical forms
Cesium metaborate is formed by the reaction between the released boron and cesium iodine, resulting in generation of gaseous/volatile iodine compounds from the excess iodine. The calculation shows that the formation of gaseous/volatile iodine can be suppressed under a steam-starvation atmosphere because of a lower boron release. This lower release of boron is caused by the possible formation of boron-stainless steel reaction products during the degradation of BWR control rods.

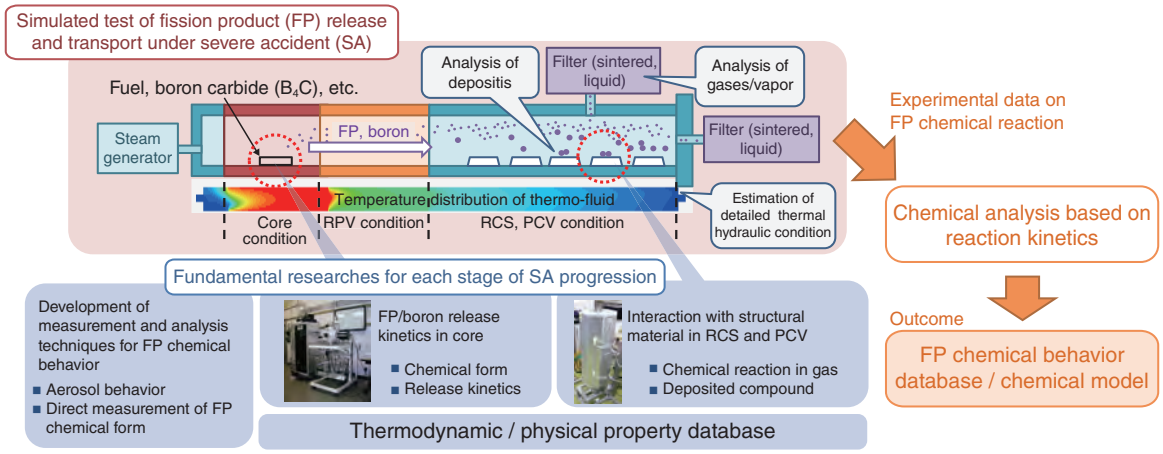

Fig.1-42 Research approach for the evaluation of FP chemical behavior
Data on the chemical reaction of fission products (FPs) are acquired by experiments simulating FP release and transport in a reactor during a severe accident as well as by fundamental studies on the FP chemical behavior for each stage of accident progression. A database on FP chemical behavior will be constructed from analyses with the reaction kinetics evaluated based on the obtained data. This database is available for improvements of FP chemical models in severe accident analysis codes.

We are conducting fundamental research on improving fission product (FP) release and transport analysis methods under severe accident (SA) conditions to contribute to the development of technologies for decommissioning work on TEPCO's Fukushima Daiichi NPS and to enhance LWR safety. During SAs, FPs are released from nuclear fuel with temperature escalation, transported to the primary containment vessel from the damaged reactor pressure vessel and reactor coolant system, and finally released into the environment. Since the FP release and transport behavior is governed by the chemical behavior (such as chemical changes of FP compounds and interactions with control materials), the primary target of our research is to evaluate FP chemical behavior.

Although FP release and transport behavior has been widely studied, uncertainties still remain in, for example, the formation of gaseous iodine, which is potentially changed by reaction with boron carbide (B_4C) control material in BWRs. In this research program, therefore, we will focus on the degradation of BWR control rods and the steam starvation atmosphere caused by decompression boiling and evaluate FP chemical behavior under these conditions. So far, we have analyzed boron (B) compounds in different atmospheres and release fractions from boron–stainless steel reaction products (Fig.1-41), which are assumed to form during the degradation of BWR control rods. The thermodynamically stable iron boride is formed under a steam-starvation atmosphere, leading to the decrease of the B release fraction. It is also shown that the decrease in the B release results in a 30% decrease in the generation of gaseous/volatile iodine. Consequently, the change of the B release fraction could significantly affect the FP chemical behavior.

In our future experiments, we will attempt to validate these calculation results by acquiring data on the B release fraction. Concurrently, we will conduct simulated tests on FP release and transport in a severe accident and fundamental research on FP chemical behavior for each stage of the accident progression. Then, we will construct a database of FP chemical behavior by analyzing the obtained data based on the reaction kinetics to improve the FP chemical models (Fig.1-42).

Reference

Miwa, S. et al., Research Program for the Evaluation of Fission Product and Actinide Release Behaviour, Focusing on Their Chemical Forms, Energy Procedia, vol.71, 2015, p.168–181.

1–19 Accurate Estimation of the Amount of Radioactivity in Accident Waste

— Estimation Method for the Samples and Nuclides that are Difficult to Analyze —

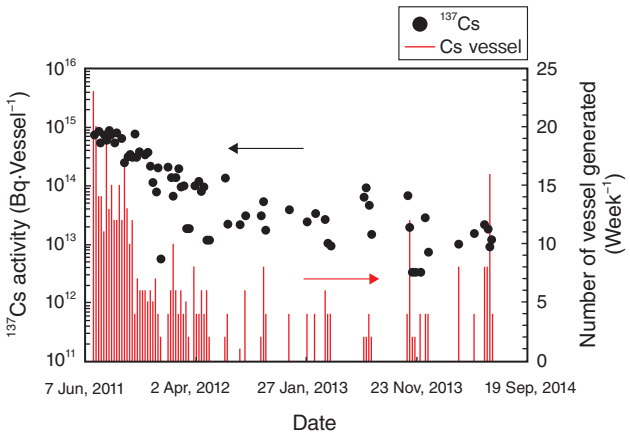

Fig.1-43 Inventory estimation of Cs adsorption vessels
The ^{137}Cs activity in 514 Cs adsorption vessels generated between the date on which contaminated water treatment commenced and August 2014 was estimated. Many vessels that contain high concentrations of Cs were generated in the early stages of operation. Afterward, the treatment of accumulated water progressed, and the number of vessels generated as well as the Cs concentration in them decreased.

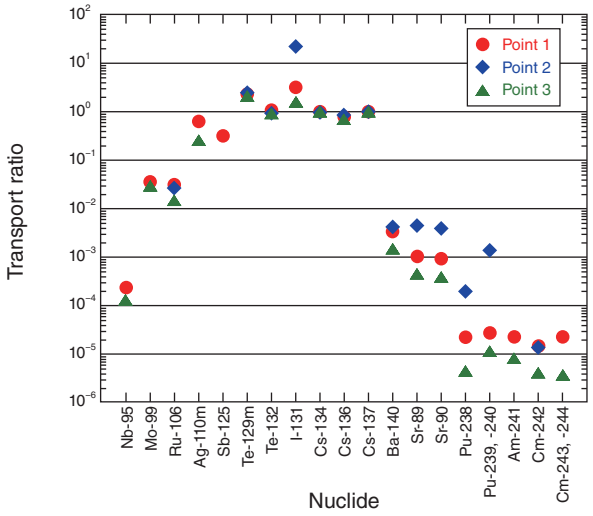

Fig.1-44 Relative extent of transport from the damaged fuel to the soil inside the nuclear power station
"The transport ratio" was calculated by supposing ^{137}Cs to be a standard nuclide and using the analytical concentration and the calculated activity in the fuel (sum of units 1 through 3). Isotopes present an identical value. A value greater than unity indicates a greater transport (of elements, not of activity) from the fuel to the soil compared with Cs.

Operations for reactor decommissioning and fuel debris retrieval are progressing at the TEPCO's Fukushima Daiichi NPS. A radioactive inventory is necessary as basic information for appropriate waste treatment and disposal. Accurate inventory estimation is an important development task because it allows more efficient decommissioning. However, the activity of the waste cannot be determined with direct analysis in case sampling waste is difficult, the concentration of activity is very low or other factors inhibit analysis. It is necessary to establish a method for estimating activity in the waste. We are going to introduce achievements based on two approaches.

Cesium (Cs) adsorption vessels, a secondary waste generated from contaminated water treatment, is the first example of waste that is difficult to sample. The contaminated water accumulated in the reactor buildings is decontaminated by devices such as the Cs adsorption device; then, the Cs adsorption vessels or sludge containing radioactivity are generated. These products cannot be analyzed because of their high doses. Therefore, the ^{137}Cs inventory was estimated using the concentrations in the contaminated water upstream and downstream of the Cs adsorption device (Fig.1-43). The sludge inventory was also estimated in a similar way. The analytical values and operational information of the devices were used, and the evaluation period was from the start date of device operation to August 2014. The ^{137}Cs inventory of a weekly-generated Cs adsorption vessel is useful to estimate the total amount of ^{137}Cs decontaminated from the accumulated water. Consequently, it was found that approximately 37% of the ^{137}Cs contained in the reactor fuels of units 1–3 was decontaminated by contaminated water treatment.

Concerning the latter approach for the case of difficult detection, a method based on considering the chemical similarities of elements has been investigated. To obtain basic knowledge about the relationship between contamination behavior and chemical properties radioactivity concentrations analytically determined were investigated for the contamination behavior of some radionuclides. Differences between elements are important and should be quantified; therefore, the ratio of analytical concentrations to the fuel inventory was obtained for normalization, and the resulting ratio was divided by that for the standard nuclide, as defined in the following equation and referred to as a "transport ratio":

Transport ratio = Ratio of radioactivity concentration for the nuclide of interest and of ^{137}Cs
/Ratio of calculated radioactivity in the fuel for the nuclide of interest and of ^{137}Cs

Transport ratios were calculated for the data in the soil (Fig.1-44). The values for some isotopes were almost identical and it was concluded that the transport ratio indicates elemental behavior. It was found that the order nuclides from greatest to least extent of transport from the damaged fuel was iodine, Cs, silver, strontium, and actinides including plutonium, and that the release of nuclear material was considerably smaller than that of volatile fission products.

These methods will be further investigated and applied to estimating a radioactivity inventory with more reliability.

This topic includes a part of the results of "Establishment of basic technology for decommissioning and safety of nuclear reactors for power generation" in FY 2013 that was entrusted to IRID from METI and conducted by JAEA as a member of IRID.

References

Kato, J. et al., Inventory Estimation of ^{137}Cs in Radioactive Wastes Generated from Contaminated Water Treatment System in Fukushima Daiichi Nuclear Power Station, E-Journal of Advanced Maintenance, vol.7, no.2, 2015, p.138–144.
Koma, Y., Transfer of Radionuclides to Soil at Fukushima Daiichi Nuclear Power Station, JAEA-Data/Code 2014-015, 2014, 23p. (in Japanese).

1–20 Safe Storage of Spent Cs-Adsorbents after Decontamination of Radioactive Water

— Estimation of H_2-Generation in Spent Vessels from the Latest "Small-Scale Experiments" —

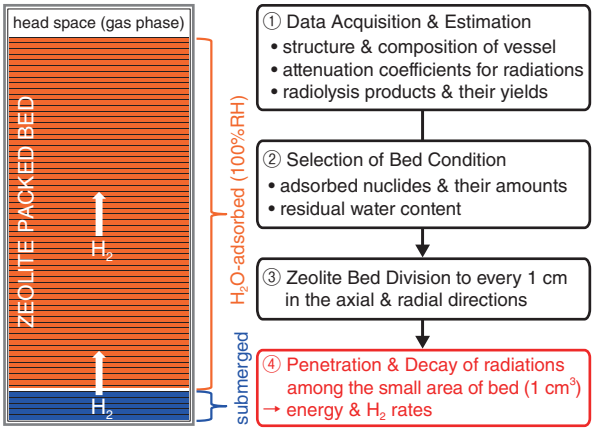

Fig.1-45 Schematic distribution of residual water and the estimation procedure for H_2-generation in spent adsorption vessels
Water content partially remained in spent vessels, even when the zeolite bed in the vessel was dewatered after the decontamination process. The bed can be sequentially separated into damp and submerged parts.

Table 1-2 Decontamination of radioactive water after the accidents at 1F and TMI-2

	1F	TMI-2
decontamination apparatus	Cs adsorption vessel (KURION & SARRY)	SDS vessel (Submerged Demineralizer System)
operation start after the accident	*ca.* 3 months later	*ca.* 2 years later
seawater content in radioactive H_2O	YES	NO
zeolite adsorbents	single use of zeolite for radioactive Cs	mixing use of two zeolites for radioactive Cs & Sr
decay heat after processed	maximum 504 W per one vessel	lower than 300 W per one vessel

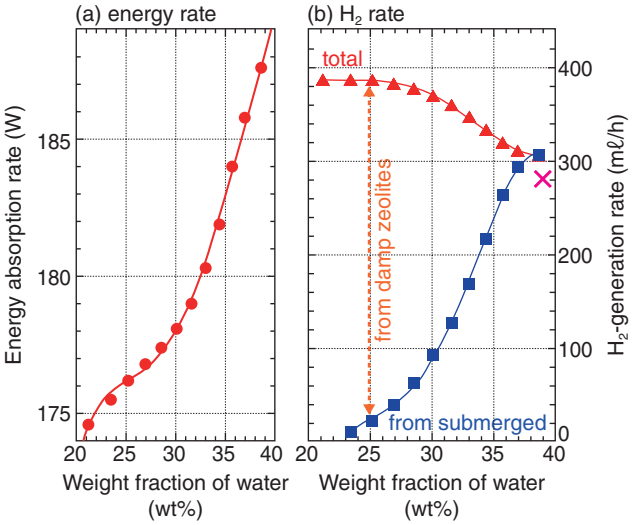

Fig.1-46 A typical example of estimated rates of energy-absorption (a) and subsequent H_2-generation (b) in the spent SDS vessel
These results were obtained by changing the water content from the damp zeolite bed at 100% RH to the submerged one in the vessel with a decay heat of 225 W at ambient temperature.

To attain long-term safe storage of spent Cs adsorption apparatuses (KURION and SARRY) with zeolite adsorbents used in the decontamination of radioactive water emitted after the accident at the TEPCO's Fukushima Daiichi NPS (1F), energy-absorption of radiations from radioactive nuclides adsorbed onto the zeolites, as well as subsequent H_2-generation by water radiolysis in the adsorption vessels, have been estimated on the basis of the latest experimental data obtained from adsorption and radiolysis occurring in "small-scale" zeolite-water mixtures. This was done using the estimation procedure (1) to (4) illustrated in Fig.1-45.

Two years after Three Mile Island Unit 2 (TMI-2) accident in 1979, radioactive water without seawater content had been processed through a Submerged Demineralizer System (SDS) with two types of zeolites to remove radioactive nuclides of Sr, Cs, and their daughter nuclides (Table 1-2). During and after this process, H_2-generation was monitored directly in the "large-scale" of a spent SDS vessel, together with the amount of adsorbed nuclides and the residual water content (whose measured and analyzed data are open and available in reports) as well as the size and geometry of the vessel.

In this work, the re-estimation of H_2-generation in spent SDS vessels from the TMI-2 accident was conducted on the basis of publicly available information about the vessel, and of the latest experimental data from small-scale zeolite-water mixtures like in the spent vessels from the 1F accident. The latest estimated data was compared with that previously reported.

A typical example of the estimated results is shown in Fig.1-46. The energy rate (a) absorbed in the vessel increased with increasing water content and was found to be 74%–84% of the decay heat, of which the rest was given to SUS and leakage out of the vessel. According to the H_2-generation rate (b) obtained from the energy rate, the partial rate at the submerged part of the zeolite bed increased with increasing water content, while the total rate decreased, leading to a "liquid depth effect" corresponding to the size effect of the bed. Directly monitored H_2 data has been reported for the completely submerged condition of the bed, and the reported data (× in Fig.1-46) was found to agree well with the estimated one in this work.

Finally, the estimation method for H_2-generation in spent vessels from "small-scale experiments" performed in this work was validated. To estimate this generation more accurately, the temperature distribution of the spent zeolite bed because of its long-term storage, and radiolysis behavior in complicated systems containing solids and/or solutes are being further studied.

Reference
Nagaishi, R. et al., Revaluation of Hydrogen Generation by Water Radiolysis in SDS Vessels at TMI-2 Accident, Proceedings of 2014 Nuclear Plant Chemistry Conference (NPC 2014), Sapporo, Japan, 2014, paper 10224, 9p., in USB Flash Drive.

2 Nuclear Safety Research

Implementing Continuous Improvements in Safety

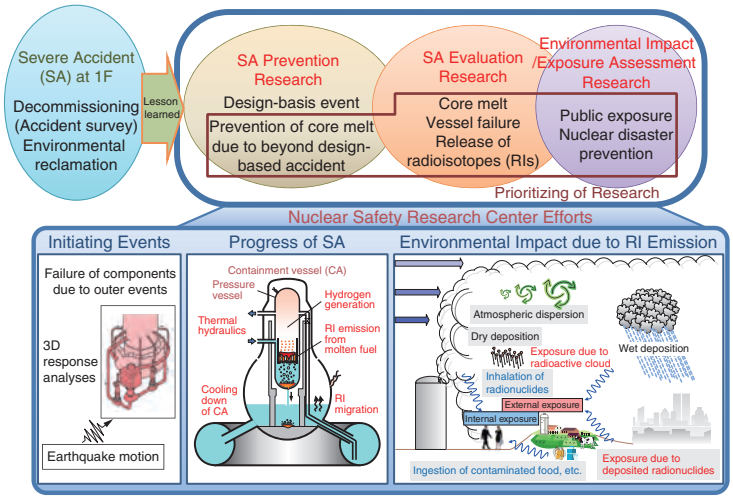

Fig.2-1 Directions of nuclear safety research
In accordance with the lessons learned from the accident at 1F, we have promoted studies on severe accident (SA) prevention efforts and nuclear emergency preparedness activities such as environmental impact assessments in addition to safety assessments within design basis events.

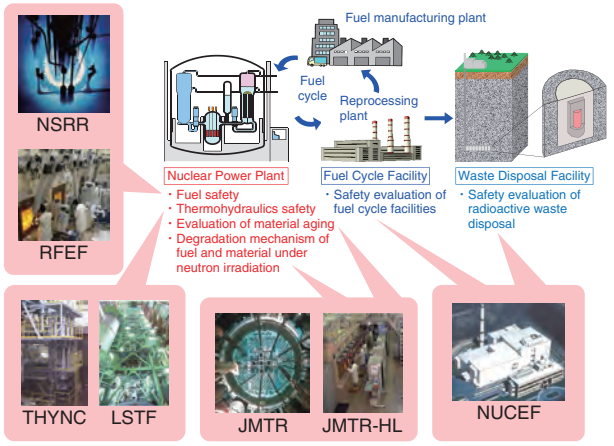

Fig.2-2 Nuclear safety research areas and related JAEA facilities
The NSRC acquires experimental data from various Japan Atomic Energy Agency (JAEA) facilities. These data, used for risk assessment and safety evaluation of nuclear facilities, contribute to international efforts to develop evaluation methods and criteria.

To ensure the safe use of current nuclear facilities, the Nuclear Safety Research Center (NSRC) is studying the possibility of serious accidents at nuclear installations and their consequences. A massive and severe accident (SA) occurred at the Fukushima Daiichi Nuclear Power Station (1F) of Tokyo Electric Power Company, Incorporated as a result of the Great East Japan Earthquake and Tsunami. The NSRC has been collaborating with the Japanese government to institute appropriate emergency response procedures. The specialists at the NSRC regret that they were unable to prevent the accident.

Continuous efforts should be made to avoid serious damage while we utilize nuclear energy. A proper understanding of the situation is important for making the best and safest use of such technologies. In fact, the International Atomic Energy Agency, which investigated the accident at 1F, highlighted the importance of “continuous improvement”. To contribute to “continuous improvement aimed at the highest level of safety”, we have promoted studies on SA prevention and evaluation to reduce the risk of accidents at nuclear facilities and to improve nuclear disaster prevention using analyses such as environmental impact assessments, as shown in Fig.2-1.

We are committed to safety research and have devoted various facilities to this cause, as shown in Fig.2-2. These special facilities allow for the handling of radionuclides and the simulation of accident conditions.

This chapter presents the results of recent research on the following topics: strength evaluation of fuel cladding, which is tested under the simulated conditions of a loss-of-coolant accident, by bend experiments (Topic 2-1); development of an uncertainty analysis method on the source term in SA analyses (Topic 2-2); evaluation of the precautionary action zone using a probabilistic consequence analysis (Topic 2-3); improvement for the estimation of peak power during criticality accidents at nuclear reprocessing plants (Topic 2-4); evaluation of the sorption distribution coefficients of radioactive iodine to rocks using sorption tests (Topic 2-5); and evaluation of radioactivity concentration for site release by the application of the Kriging method (Topic 2-6).

The following topic, solicited by the NSRC and related to the accident at 1F, is described in Chapter 1: Evaluation of Failure at Pressure Vessel Lower-head Based on the Creep Test and the Creep Damage Model (Topic 1-17).

2–1 Investigation of the Fracture Resistance of Zircaloy Cladding under a Post-LOCA Condition
— Evaluation of Ruptured and Quenched Cladding by Four-Point-Bend Tests —

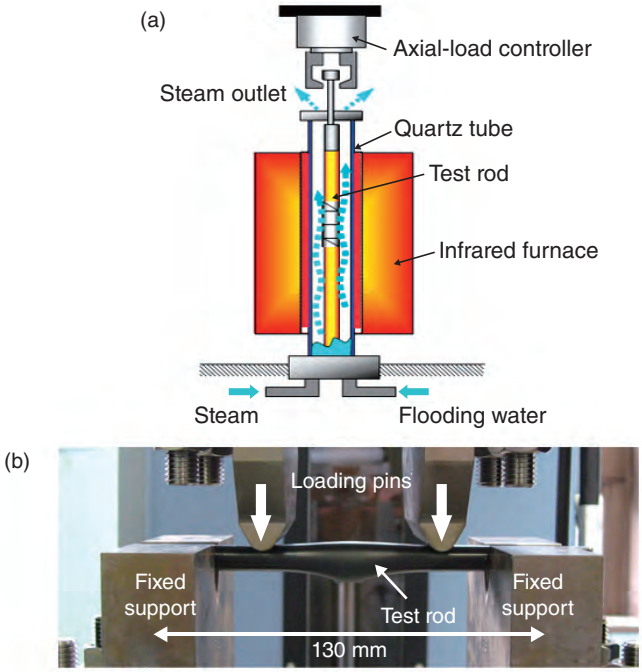

Fig.2-3 (a) Schematic of oxidation and quench test used to simulate a LOCA condition
(b) Ruptured cladding specimen mounted in a four-point-bend test jig
(a) A test rod is heated in the furnace in steam flow. During the heat-up phase, the cladding balloons and ruptures due to rod-inner-pressure increase and cladding strength deterioration. After the isothermal oxidation phase, the test rod is quenched by water injected from the bottom.
(b) A four-point-bend test apparatus is designed to apply a uniform bending moment to the rupture region and to generate tensile stress on the rupture side.

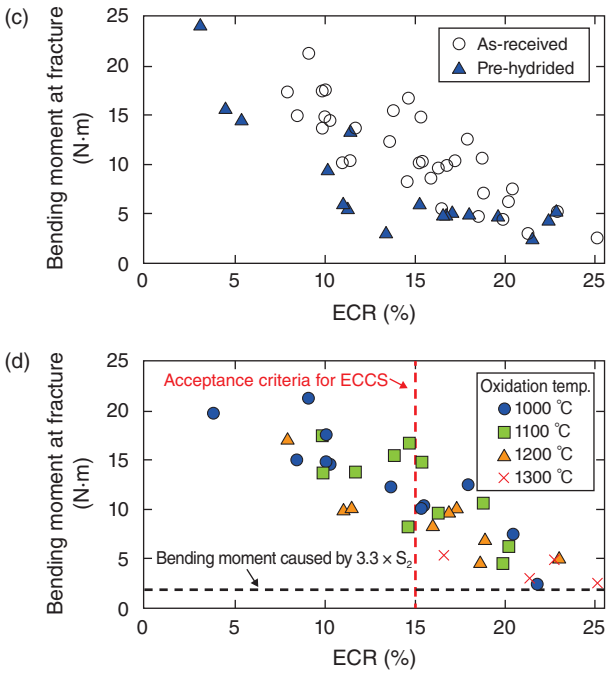

Fig.2-4 Results of four-point-bend-tests on the cladding specimens tested under simulated LOCA conditions
Bending moments at fracture decreased with increasing ECR and pre-hydriding (~800 ppm). The results showed that fuel cladding should not fracture when the PCT and the ECR are below 1300 °C and 15%, respectively, even if there is a seismic load corresponding to 3.3 times as much as S_2 during the LTC following a LOCA.

A loss-of-coolant accident (LOCA) is one of the accidents postulated in the safety design of a nuclear power plant. During a LOCA, fuel cladding is exposed to high-temperature steam until cooling water from the emergency core cooling system (ECCS) is injected into the reactor core. The material used for fuel cladding is zirconium-based alloy; in the case where the cladding is exposed to high-temperature steam in the core for a long time during a LOCA, the cladding is severely oxidized and embrittled. The oxidized and embrittled cladding may fracture due to its quench following the water injected from ECCS.

Regarding the fracture prevention in the cladding oxidized during a LOCA, the current Japanese ECCS regulatory criteria directs that the peak cladding temperature (PCT) and the maximum amount of oxidation of cladding should not exceed 1200 °C and 15% equivalent cladding reacted (ECR) during a LOCA so that the oxidized cladding can survive the thermal shock at the time of quenching. However, to maintain long-term cooling (LTC) following a LOCA, it is important to maintain a sufficient mechanical strength of the cladding to withstand loads that may be caused by external forces (e.g., earthquake) during the LTC.

By conducting a mechanical strength test on the Zircaloy cladding under simulated LOCA conditions, the fracture resistance of the cladding against loads that may be caused by external forces during LTC is estimated.

A four-point-bend test apparatus (Fig.2-3(b)) is designed to evaluate the fracture-resistance of the cladding that is tested under simulated LOCA conditions.

Fig.2-4 shows the correlation between the bending moment at a fracture of the cladding specimen and ECR. It is found that the bending moment at the fracture decreases due to hydrogen absorption, which simulates high burnup fuel cladding conditions and decreases as ECR increases. The bending moment generated in the fuel cladding during an earthquake is estimated from a design basis seismic ground motion (S_2) defined by the previous guideline and is compared with the four-point-bend test results. The results show that, if the PCT and ECR are kept below the limits of the current Japanese ECCS regulatory criteria, it is considered that the cladding can survive a seismic load corresponding to 3.3 times the value of S_2 during LTC following a LOCA.

This study provides useful information for maintaining the geometry of reactor core during LTC following a LOCA.

Reference

Yamato, M. et al., Evaluation of Fracture Resistance of Ruptured, Oxidized, and Quenched Zircaloy Cladding by Four–Point–Bend Tests, Journal of Nuclear Science and Technology, vol.51, issue 9, 2014, p.1125–1132.

2–2 Exploring Latent Uncertainties and Influential Factors in Severe Accident Analysis

— Development of an Integrated Approach to Uncertainty and Sensitivity Analyses for Source Terms —

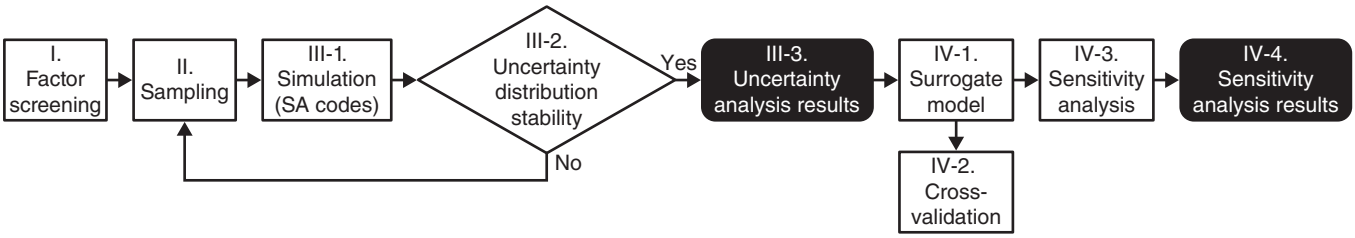

Fig.2-5 Proposed approach to uncertainty and sensitivity analyses for severe accident source terms
The proposed approach comprises four steps: I. Select the input factors that considerably affect the evaluation of source terms; II. Randomly sample the inputs based on presumed distributions; III. Iteratively execute the SA code until the uncertainty distribution becomes stable; IV. Perform a sensitivity analysis to rank the importance of the inputs. A surrogate statistical model is employed instead of the SA code to avoid unaffordable computational cost during the sensitivity analysis.

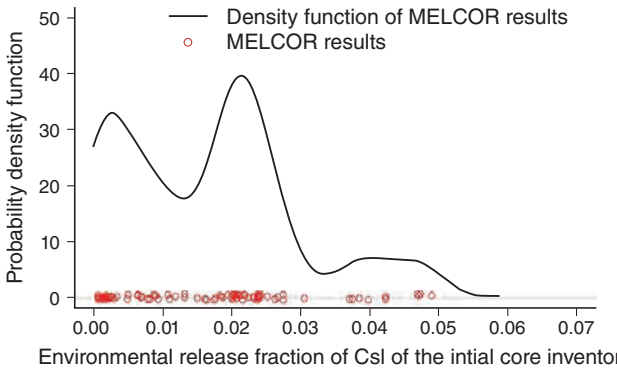

Fig.2-6 Uncertainty distribution of environmental CsI release estimated using MELCOR
Based on the 90 runs of the MELCOR code with uncertain inputs relating to fuel cladding failure, collapse of fuel rods, and radionuclide-scrubbing in the water pool, an uncertainty distribution of environmental CsI release is obtained. Although the three inputs are assumed to have uniform or normal distributions, the probability of the output shows a complicated multi-modal distribution.

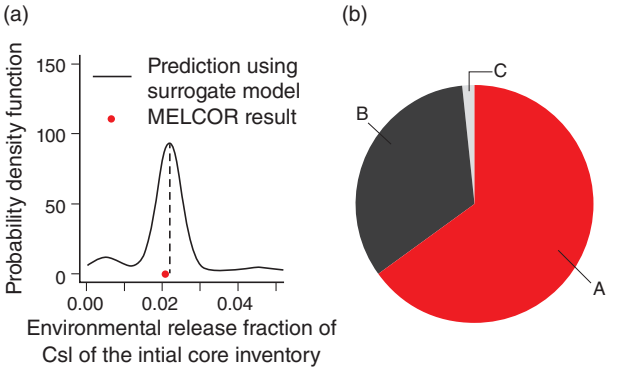

Fig.2-7 Cross-validation of the surrogate model and results of the sensitivity analysis
(a) The result of MELCOR simulation is in good agreement with the prediction using the surrogate model, whose highest-density interval perfectly contains the actual result. (b) Based on the calculation of the sensitivity indices with the surrogate model, the influence of uncertain inputs associated with fuel cladding failure (A), the collapse of fuel rods (B), and the radionuclide scrubbing in the water pool (C) on output is quantitatively estimated.

Severe accidents (SAs), such as the accident at the TEPCO's Fukushima Daiichi NPS, involve many complicated physical and chemical phenomena. In general, integrated computer codes with the models for the phenomena are applied to simulate the progression of an SA. The results, however, include uncertainties mainly due to incomplete understanding of these phenomena. To enhance the reliability of simulation results and improve SA analysis codes, evaluation of latent output uncertainties by uncertainty analyses and identification of dominant input factors by sensitivity analyses are necessary.

A novel integrated approach is illustrated in Fig.2-5. Based on the four steps, the uncertainties of the output and influential inputs can be estimated. As an example, MELCOR, an integrated SA code being developed in the United States, is applied to compute the uncertainties for the estimation of the source term (i.e., the amount and timing of environmental radioactive materials release). Fig.2-6 describes the uncertainty of source-term estimation. The environmental cesium iodide (CsI)-release fraction of the initial core inventory is almost in the range between 0 and 0.06, suggesting that the outputs should have this degree of uncertainty in the source term analyses.

To avoid the unaffordable computational cost required for the sensitivity analyses, a surrogate statistical model is constructed using statistical methods whose results can perfectly regenerate the complicated uncertainty distribution shown in Fig.2-6. The results of the sensitivity analysis after the executions of 16000 runs of the surrogate model and the cross-validation of the model are shown in Fig.2-7. Based on the results of the sensitivity analysis, it is clarified that fuel cladding failure had the greatest influence upon the output uncertainty of all the parameters tested.

The above analysis results have confirmed the applicability of the proposed approach to source term analysis during an SA. Hereafter, THALES2, an integrated SA code developed at JAEA with the advantages of simulating the chemical reactions of iodine and the capability of considering various iodine chemical forms other than CsI, will be applied to various SA scenarios for further source term uncertainty analysis. It is foreseen that the latent uncertainty could be discovered and then reduced according to the sensitivity analysis.

Reference

Zheng, X. et al., Application of Bayesian Nonparametric Models to the Uncertainty and Sensitivity Analysis of Source Term in a BWR Severe Accident, Reliability Engineering & System Safety, vol.138, 2015, p.253–262.

2–3 Evaluation of the Precautionary Action Zone for a Nuclear Emergency

— Development of an Evaluation Method using a Probabilistic Consequence Analysis —

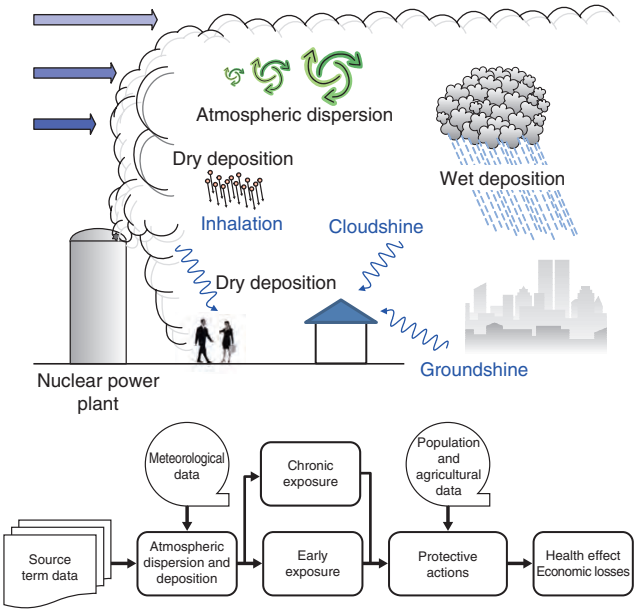

Fig.2-8 Probabilistic accident consequence assessment code OSCAAR
The off-site consequence analysis code for atmospheric release in reactor accidents (OSCAAR) evaluates the dispersion and deposition of the radionuclides released into the atmosphere, external and internal doses for the public, dose reduction by short- and long-term protective actions, and the risk of health effects.

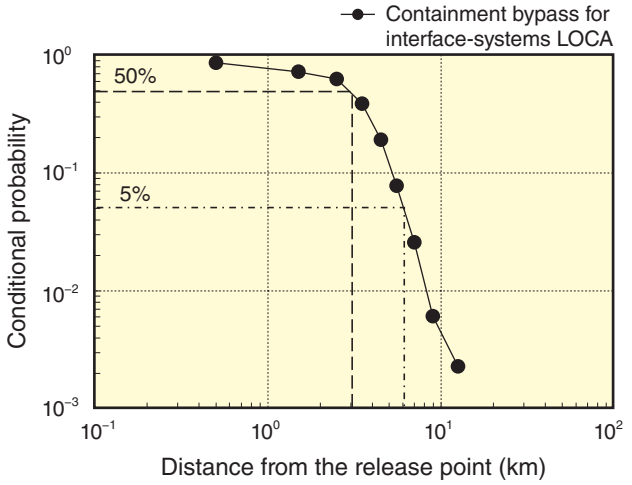

Fig.2-9 Example of evaluation results for a PAZ
In the case of the containment-bypass for the interface-systems LOCA scenario, the distances above the 50th percentile values (average weather conditions) and the 5th percentile values (severe weather conditions) for a weather occurrence are evaluated to be approximately 3 and 6 km, respectively.

The International Atomic Energy Agency (IAEA) suggested a precautionary action zone (PAZ) as a new concept for protective action zones in the case of a nuclear emergency. The PAZ is the area in which urgent protective actions (e.g., sheltering or evacuation) should be implemented before the release of radionuclides to prevent the risk of severe deterministic effects such as early death. However, the IAEA only showed the basic concept and the suggested size for the PAZ. A method for evaluating the size of the PAZ on a scientific basis needs to be introduced to Japan.

In this study, the size of the PAZ for accident scenarios was evaluated in terms of received dose using a Level 3 probabilistic risk-assessment (PRA) code, the OSCAAR (Fig.2-8). Accident scenarios were identified through a Level 2 PRA analysis for boiling water reactor (BWR) and pressurized water reactor (PWR) plants.

First, representative accident scenarios were selected in light of their frequencies of occurrence, release fractions of radionuclides, and time before release related to the implementation of the protective action. Next, the absorbed doses to red marrow, which cause severe deterministic effects, were calculated for the selected accident scenarios. The consequences of a given accidental release at a given location varied with meteorological conditions. The doses were evaluated for 8760 possible weather sequences considering one year's worth of meteorological data. The doses were calculated at each region with an (r, θ) grid system centered on the release location, and then, representative values of calculated doses at each distance from the release point were selected from the maximum values for the residential region in the corresponding annulus. After that, using the evaluation results for the doses under all possible weather sequences, the conditional probability of a weather occurrence exceeding the dose criterion of 1 Gy was calculated at each distance. Finally, the probabilistic distribution of a weather occurrence exceeding the dose criteria at each distance was shown in the form of complementary cumulative distribution functions, and the size of the PAZ was evaluated in light of the conditional probability for the weather occurrence.

Fig.2-9 shows the relation between the distance from the release point and the conditional probability of a weather occurrence exceeding the dose criteria in the case of the containment bypass for the interface-systems' loss-of-coolant accident (LOCA) scenario at the BWR plants. The distances above the 50th and 5th percentile values for a weather occurrence are evaluated to be approximately 3 and 6 km, respectively. Consequently, the size of the PAZ is estimated to be 3–6 km, and the specific evaluation method has been clarified on a scientific basis.

Reference

Kimura, M. et al., Evaluation of the Precautionary Action Zone using a Probabilistic Consequence Analysis, Journal of Nuclear Science and Technology, vol.50, issue 3, 2013, p.296–303.

2–4 Improvement of Severe Accident Assessment Method for Reprocessing Plants
— Instant Calculation of the Maximum Power in Criticality Accidents —

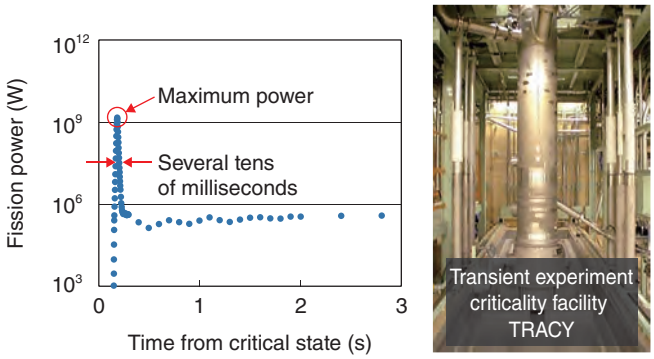

Fig.2-10 Data of a transient criticality experiment simulating a criticality accident using the transient experiment criticality facility (TRACY)
After a uranium solution is made critical by the instantaneous withdrawal of a neutron absorber at time zero, the power (i.e., the energy released from fissions per second) goes up and down in a very short period of time (about several ten ms), during which a lot of energy is released.

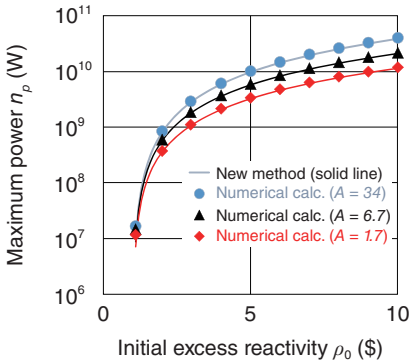

Fig.2-11 Accuracy of the new method
The maximum power calculated using the new method agrees with the numerical calculation with the one-point kinetics code for a wide range of fuel compositions, indicated by the values of "*A*".

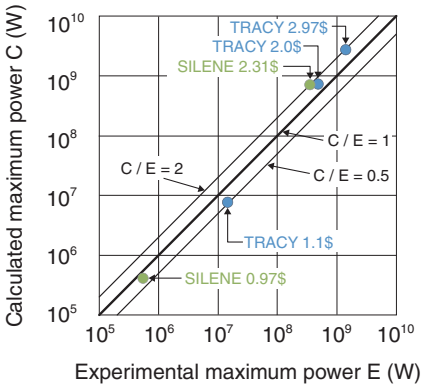

Fig.2-12 Comparison to experimental data
The maximum power calculated using the new method agrees with the experimental data. Low-enriched uranium (10%) was used in the TRACY experiment in Japan and high-enriched uranium (93%) was used in the SILENE experiment in France. "number $" shows the initial excess reactivity.

The fuel reprocessing plant was designed to keep nuclear fuel subcritical. It is also important for confirming the safety of the public and workers in a postulated criticality accident. In a criticality accident, a lot of energy and radioactive rays are instantaneously released, as shown in Fig.2-10. The released energy mainly increases the temperature of the nuclear fuel and the radioactive ray causes the exposure of workers. The maximum value of the power, fission energy per second, provides information about the maximum strength of radioactive rays needed to assess the exposure of workers. The power profile is approximately expressed by the one-point kinetics equation; this equation is not easy to analytically solve because of its complexity. Alternatively, the equation is usually solved numerically using one-point kinetics codes. Such numerical calculations require a long time because the number of calculations depends on the number of cases, wherein there are many parameters such as the initial excess reactivity.

We focused on the fact that the fission power reaches its maximum value in a very short time, causing the one-point kinetics equation to be reduced to a simple form. We have analytically solved the simple equation to obtain the solution that expresses the maximum power as a function of parameters such as the initial reactivity, ρ_0, reactivity temperature coefficients, α_1, α_2, reciprocal heat capacity, K, and delayed neutron fraction, β, as follows;

$$n_p = \frac{2\alpha_2 A^3}{3K\ell}\left(X^3 - \frac{3}{2}X^2 + \frac{1}{2}\right), \quad X = \sqrt{\frac{\rho_0 - \beta}{\alpha_2 A^2} + 1},$$

where $A = \alpha_1/(2\alpha_2)$. The maximum power calculated using this equation agrees with the numerical calculation, as shown in Fig.2-11. This result makes the calculation of the maximum power fast and easy. It also becomes easy to validate the calculation because the calculation procedure is clear. The comparison to experimental data shows good agreement for a wide range of maximum powers, as shown in Fig.2-12. The fast assessment of the dose of workers makes it possible to quickly employ countermeasures for safety.

As for the public dose, it is important to estimate the total amounts of fission products, for which the total fission energy must be estimated. We are planning to develop an expression for the released energy to make the assessment of the public dose much faster in the future.

Reference
Yamane, Y., Improvement in Estimation of First Peak Power Based on Non-Linear Temperature Feedback Reactivity in Criticality Accident with Instantaneous Reactivity Insertion, Journal of Nuclear Science and Technology, vol.52, issue 11, 2015, p.1425–1435.

2–5 Investigation of the Sorption of Radioactive Iodine onto Rocks
— Experimental Determination of the Sorption Distribution Coefficient —

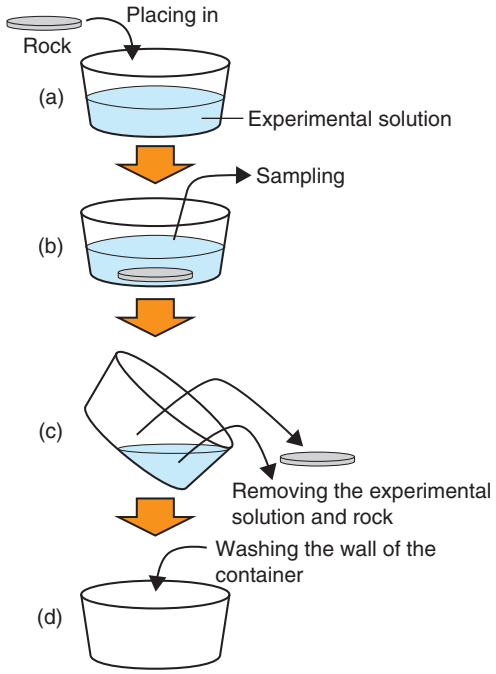

Fig.2-13 Flow of the sorption experiment
(a) The sorption experiment was commenced by immersing a rock specimen into solution in the container. (b) Sampling and concentration measurement were performed until the concentration stopped changing. (c) The experimental solution and the rock were removed from the container. (d) The amount of iodine adsorbed onto the wall was evaluated by analyzing the washing solution.

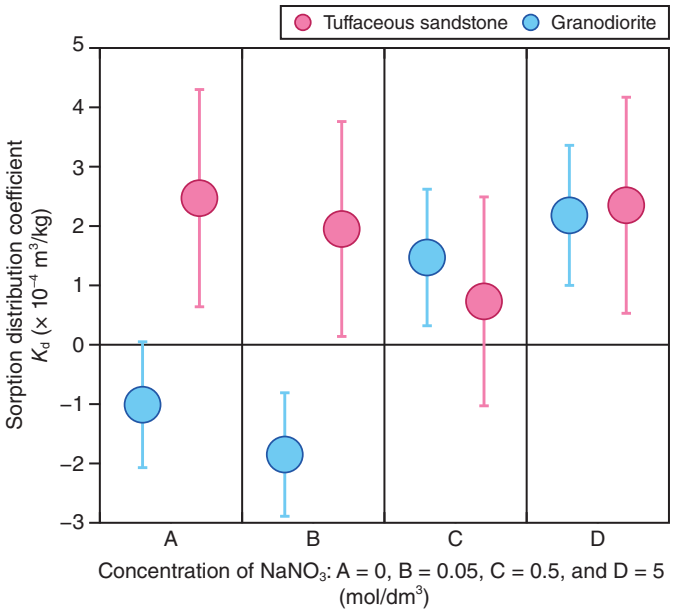

Fig.2-14 Sorption distribution coefficients of iodine on granodiorite and tuffaceous sandstone vs. concentration of $NaNO_3$
Error ranges included zero in the cases of a $NaNO_3$ concentration of 0 mol/dm^3 for granodiorite and a $NaNO_3$ concentration of 0.5 mol/dm^3 for tuffaceous sandstone, indicating that the sorption distribution coefficients (K_d) may have been zero in these cases. K_d values in other cases were found to be small but non-zero. This study showed how to judge the significance of K_d values that were close to zero.

Radioactive wastes generated from reprocessing spent fuel contain long-lived radionuclides such as iodine-129 (half-life: 1.6×10^7 year). If such wastes are disposed of into geological formations, nuclides may be eluted by groundwater and may migrate into the bedrock over a long period of time. The migration of nuclides will be delayed by the sorption of nuclides onto the bedrock. The sorption distribution coefficient, K_d, is used to evaluate this sorption.

K_d is the ratio of the element concentration in rocks to that in solution, and it never has negative values. It is difficult to directly and precisely measure the element concentration in the rock when K_d is obtained in experiments. The amount of the element sorbed onto the rock is thus determined as the difference between the element concentrations in the solution before and after contact with the rock, as shown in Fig.2-13. Either values with large errors or negative values should be obtained for the amount of the element in the rock because the measured elemental concentrations include errors due to the analysis and the handling. Such a problem is realized for low-sorptive elements (e.g., iodine) because the K_d is very small or close to zero. For such low-sorptive elements, it is essential to know whether even slight retardation of the migration in the bedrock due to sorption can be expected. It is thus necessary to clarify whether the obtained K_d values are significant by appropriately evaluating the errors.

In this study, sorption experiments of radioactive iodine onto tuffaceous sandstone and granodiorite were conducted for various sodium nitrate ($NaNO_3$) concentration conditions by considering the effect of $NaNO_3$ eluted from waste. The K_d was evaluated by subtracting the amount of iodine adsorbed onto the wall from the difference between the element concentrations in the solution before and after contact with the rock. Because the sorption of iodine onto rock was very small, various error propagations arising in the processes for the experimental solution were considered for the K_d evaluation. The experimental results showed significant values, which were non-zero under certain solution conditions, although the K_d of iodine was very small, as shown in Fig.2-14. The results showed the appropriate experimental and evaluation methods for the case where very small K_d values were expected for important nuclides involved in a safety assessment of waste disposal.

The present study was sponsored by the Secretariat of the Nuclear Regulation Authority (NRA) (formerly Japan Nuclear Energy Safety Organization, an incorporated administrative agency (JNES), formerly the Nuclear and Industrial Safety Agency (NISA), Ministry of Economy, Trade and Industry (METI), Japan).

Reference

Hemmi, K. et al., Distribution Coefficients of Iodine and Tin on Granodiorite and Tuffaceous Sandstone Specimens, Genshiryoku Bakkuendo Kenkyu (Journal of Nuclear Fuel Cycle and Environment), vol.22, no.1, 2015, p.3-10 (in Japanese).

2–6 Evaluation of Radioactivity Concentration for Site Release

— Application of Kriging to the Evaluation of Mean Radioactivity Concentration with Consideration of Spatial Correlation —

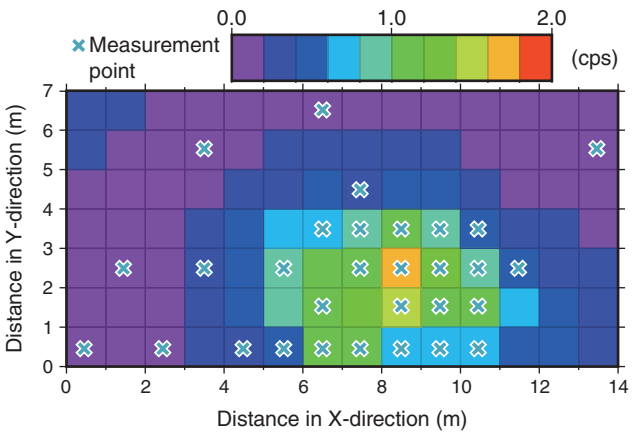

Fig.2-15 Example of the distribution of the radiation counting rate estimated by kriging
This is the distribution of the radiation counting rate including 30 measured data points (which were obtained in the region of relatively high count rates), as well as 68 data points that were estimated by kriging with consideration of spatial correlation based on the measured data. The mean counting rate estimated by kriging using all the data in the area is 0.41 cps, which is lower than that estimated by a conventional statistical method using only measured data, 0.71 cps.

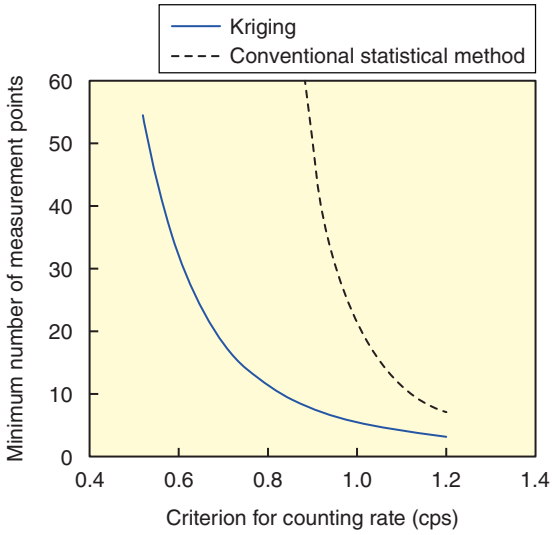

Fig.2-16 Minimum number of measurement points for the case of Fig.2-15, where the criterion for the counting rate is varied as a parameter
The minimum number of measurement points obtained by kriging is less than that obtained by a conventional statistical method. Since the difference between the estimated mean counting rate and the criterion value decreases with decreasing the criterion value, it is necessary to decrease the uncertainty in the estimated mean counting rate by increasing the minimum number of measurement points to ensure that the estimated mean counting rate including uncertainty is less than the criterion value.

After nuclear facilities are dismantled and demolished, the site (land and building) is deregulated for public use. This is called site release. A legal system regarding site release will be one of the important issues in the near future as the number of nuclear facilities such as nuclear power plants needing to be decommissioned increases. While the criterion and procedure regarding site release have not yet been established in Japan, it will eventually be necessary to confirm that significant radioactivity does not remain on the site before deciding to release it. In the United States, the standard manual of measurement and evaluation for site release has been published. It describes methods for ensuring compliance with the criterion for site release by evaluating the mean radioactivity concentration in the area of interest based on a limited amount of measured radioactivity data. In the evaluation, a conventional statistical method that does not consider spatial correlation of radioactivity concentrations between different points is applied. However, because radioactivity concentrations at the points generally have spatial correlation, it is recommended that the mean radioactivity concentration be evaluated with consideration of spatial correlation. Kriging, a geostatistics method, can estimate the value at a non-measuring point using measured data with consideration of spatial correlation.

Therefore, to support the measurement and evaluation, we studied a method of applying kriging to the estimation of the distribution of radioactivity concentration in the area of interest including non-measuring points, and the estimation of a mean concentration in the area from a limited amount of measured data. Fig.2-15 shows an example of a distribution of radiation counting rates estimated by kriging.

On the other hand, the estimated mean radioactivity concentration includes uncertainty, which may cause decision error by which the site may be judged to comply with the criterion of site release when the mean concentration actually exceeds the criterion value. The uncertainty decreases as the measurement points increase. To enhance the safety for site release, it is necessary to calculate the uncertainty and to determine a minimum number of measurement points corresponding to a given low probability of decision error. Therefore, we proposed a method to calculate the uncertainty in the estimated mean radioactivity concentration as a function of the number of measurement points and to calculate the minimum number of measurement points corresponding to a given probability of decision error.

Fig.2-16 shows the minimum number of measurement points for the case of Fig.2-15, where the criterion for the counting rate is varied as a parameter. It shows that the minimum number of measurement points obtained by kriging was less than that by a conventional statistical method.

The outcome obtained in this study will contribute to the establishment of a criterion regarding site release for nuclear facilities in the near future.

Reference

Ishigami, T., Shimada, T., Study on Application of Kriging to Evaluation of Radioactivity Concentration for Ensuring Compliance with the Criterion of Site Release, Journal of Nuclear Science and Technology, vol.52, issue 9, 2015, p.1186–1204.

3 Advanced Science Research

Pioneering the Future with Advanced Science

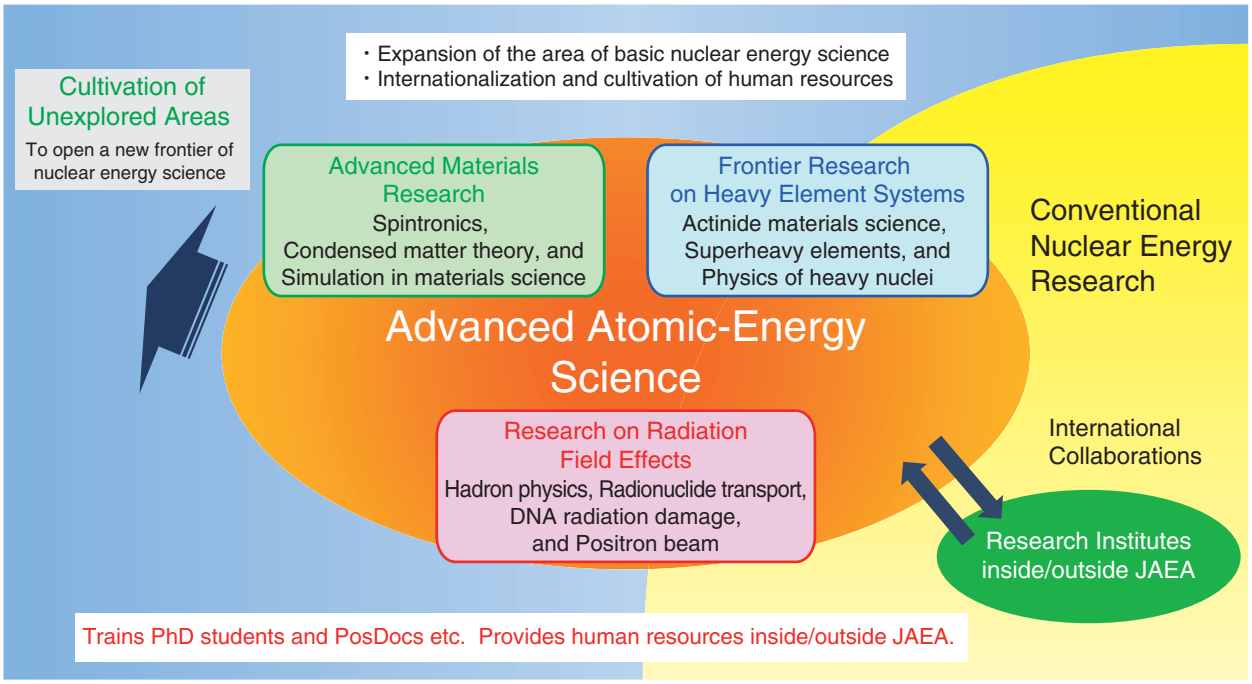

Fig.3-1 The role of advanced nuclear science research
The aim is to open a new frontier of nuclear science.

Basic research supports the greater part of nuclear-energy-related science and technology. In the development of nuclear energy research, it is particularly crucial to respond to the new phase of nuclear energy wherein we will be entering in the next few decades and to constantly seek solutions to today's energy problems.

As for the Advanced Science Research Center (ASRC), our role is to explore the unlimited possibilities of nuclear energy from the perspective of basic science. In this process, we aim to open up new research fields and strive to further develop science and technology. Beginning in FY 2010, we started our mid-term plan, focusing on three main areas: advanced materials research, frontier research on heavy element systems, and research on radiation field effects (Fig.3-1).

Advanced materials research has been conducted with the aim of creating spintronic materials and advancing the theory of solid state physics. In our research on heavy element systems, we started diverse studies on actinide compounds and the development of new materials as well as studied the nuclear science of superheavy elements. Our research on radiation field effects has included hadron physics, the study of radiation effects on bio-molecules, and the technical development and application of spin-polarized positron beams. Through interactions between the three areas and collaboration with research institutes inside and outside of the Japan Atomic Energy Agency (JAEA), we have been working on cultivating new fields of nuclear energy science (Fig.3-1).

We have made a number of highlighted achievements during FY 2014. Through advanced materials science, we achieved a theory-based outcome toward the improvement of energy-conversion efficiency, as detailed in Switching of Electric and Magnetic Flows in Metal (Topic 3-4). Substantial results have been obtained by frontier research on heavy-element systems; the successful measurement of the first ionization potential of lawrencium, element 103 (Topic 3-1), and the nuclear magnetic resonance study of a uranium compound in the world's strongest magnetic field (Topic 3-3) are marked examples. In particular, the accomplishment of the first ionization potential measurement of Lr appeared on the front cover of an issue of Nature featuring "Extreme Chemistry". Prominent results toward an explanation of the ecological effects of radiation were also acquired through research on radiation field effects. The cell cycle modification by irradiation in single cells was observed (Topic 3-6). A unique outcome using a new material surface analysis method, Surface Spin Polarization Probed by Positronium, was also a case in point (Topic 3-5). In hadron physics research at the Japan Proton Accelerator Research Complex (J-PARC), research aimed at an extreme search of the nuclear material to clarify a new form of nucleus (Topic 3-2) was performed.

A comprehensive portable nuclear decay data map, the JAEA Chart of the Nuclides 2014, has been compiled to widely distribute knowledge of the world of nuclides to the general public as part of outreach activities (Topic 3-7).

The ASRC regards it as an important issue to develop nuclear human resources with the expertise and capability of demonstrating their abilities through the aforementioned basic nuclear research.

3–1 Discrepancy in the Periodic Table Appears at Element 103

— Successful Measurement of the First Ionization Potential of Lawrencium, Element 103 —

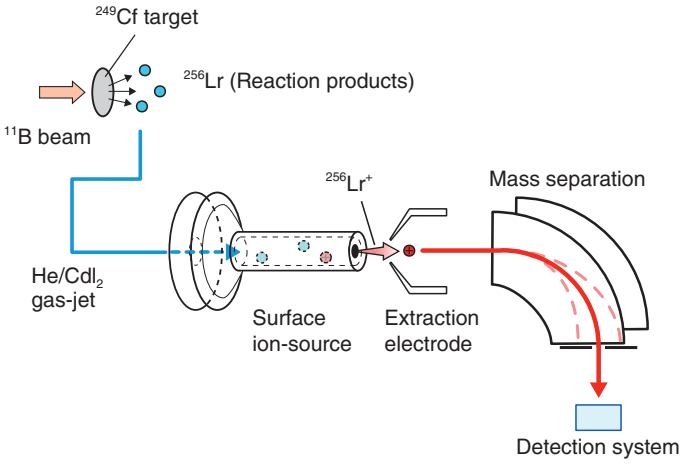

Fig.3-2 Schematic of the experimental set-up
Short-lived ^{256}Lr produced in the nuclear reaction was transported to a surface ion-source by a He/CdI$_2$ gas-jet transport system and then ionized. Produced ions were extracted and mass-separated. The amount of ions collected after the mass-separation was determined to calculate the ionization efficiency of ^{256}Lr. The first ionization potential (IP$_1$) of Lr can be calculated based on the ionization efficiency.

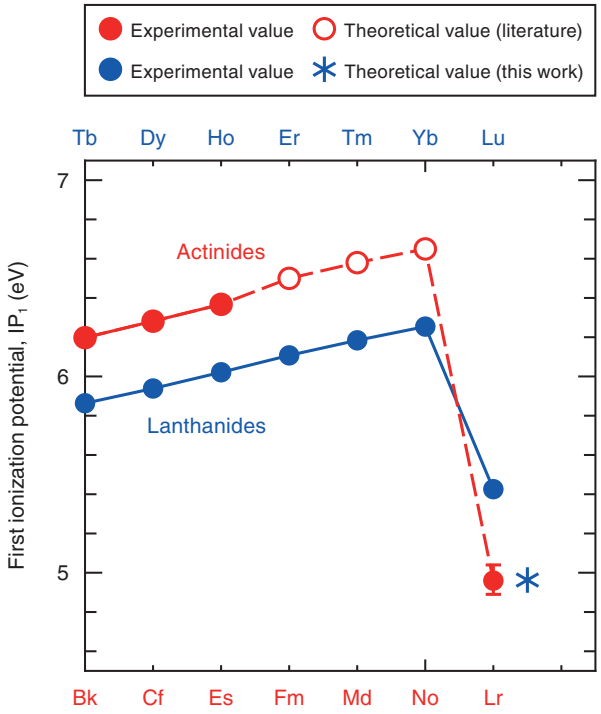

Fig.3-3 The first ionization potential (IP$_1$) of heavy lanthanides (●) and actinides (●), including our present results for Lr
Lr has the lowest IP$_1$ among actinide elements like Lu in lanthanides. This indicates that Lr is the last member of the actinide series.

The periodic table shows the periodicity of the chemical properties of elements. In the heaviest element region, however, it is expected that chemical properties may differ from those extrapolated from lighter homologs.

Heavy elements (Z > 100) can be produced in nuclear reactions using an accelerator. Their chemical properties have not been sufficiently investigated because of their low production rates and short half-lives. The first ionization potential (IP$_1$), one of the most fundamental physical and chemical properties of an element, gives direct information about the binding energy of an electron in the outermost electronic orbital of an atom. Accurate IP$_1$ values for heavy elements provide crucial tests for our understanding of their electronic structure.

In this study, we measured the IP$_1$ value of lawrencium (Lr, element 103) with a novel method we have developed based on the dependence of ionization efficiency on IP$_1$ in the surface-ionization process wherein an atom is ionized via interaction with a solid surface at a high temperature.

The isotope ^{256}Lr (half-life 27 s), produced in the reaction ^{249}Cf(^{11}B, 4n), was ionized on a tantalum surface at 2500 °C. An ionization efficiency of ^{256}Lr was determined by measuring the radioactivity of ^{256}Lr after mass separation following the ionization (Fig.3-2). This work was performed at JAEA Tandem Accelerator Facility.

From the obtained ionization efficiency, we successfully evaluated the IP$_1$ value of Lr to be $4.96^{+0.08}_{-0.07}$ eV for the first time. This IP$_1$ value is the lowest one among those of all actinide elements and comparable to that of sodium (5.1391 eV), an alkali metal. Changes of the IP$_1$ values of actinide and lanthanide elements with atomic number are shown in Fig.3-3. In the heavy lanthanide series, the IP$_1$ value increases monotonically up to ytterbium (Yb) with the atomic number and then suddenly decrease at lutetium (Lu), the last lanthanide element. Our experimental result shows that Lr has the lowest IP$_1$ like Lu. This indicates that Lr would be the last member of actinides.

A state-of-the-art theoretical calculation for Lr IP$_1$ was also performed. The theoretical value is in pretty good agreement with the experimental one. This agreement strongly suggests that the electronic configuration of the Lr atom, which characterizes the chemical properties of Lr, would differ from that expected based on the periodic table.

The results of this study are expected to yield a better understanding of the chemical properties of actinide elements.

Reference

Sato, T. K. et al., Measurement of the First Ionization Potential of Lawrencium, Element 103, Nature, vol.520, issue 7546, 2015, p.209–211.

3–2 Search for a New Type of Nuclei
— Observation of the Bound State between Kaons and Nuclei —

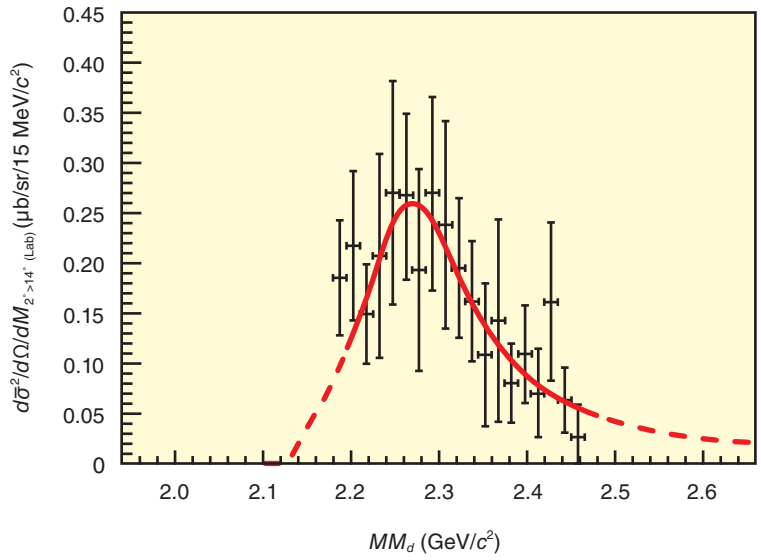

Fig.3-4 The missing-mass spectrum of the "K^-pp"-like structure
The mass distribution of the particle produced together with the K^+ meson when the π^+ beam is incident on a deuterium target. In this spectrum, a proton pair that cannot be produced from the background reaction is selected in coincidence. We observe a bump structure, which suggests that the K^-pp-like structure decays into a Σ^0 and a proton at around 2.3 GeV.

We have observed the signal of kaonic nuclei, a new type of nuclei, using the Japan Proton Accelerator Research Complex (J-PARC) Hadron Experimental Facility. Normal nuclei are composed of protons and neutrons, each of which is a kind of hadron composed of three quarks. On the other hand, kaonic nuclei are completely different because a K^{bar} meson, which is composed of a quark and anti-quark pair, is included as a component. Since the interaction between a kaon and a nucleus is strongly attractive, exotic properties, such as the possibility of forming a high density (several ρ_0) state, have been theoretically predicted. Thus, a search experiment for kaonic nuclei has been conducted recently.

In particular, the simplest kaonic nucleus, "K^-pp", which is a bound state between K^- and two protons, has been actively studied as a pathfinder for the kaonic nuclei search. The K^-pp is relatively easy to experimentally seek-out and theoretically describe because it is a three-body system. Although positive results were reported from the FINUDA and DISTO experiments, several interpretations have been put forward that can reproduce the observed spectra without assuming the existence of the K^-pp. Therefore, a new experiment is necessary to conclude the existence of the kaonic nuclei.

We have measured the missing-mass spectrum of the π^+ d $\rightarrow K^+$ X reaction, to our knowledge, for the first time. In this experiment, we used a liquid deuterium target for greater sensitivity to the K^-pp signal. Furthermore, we measured the proton pair that cannot be produced from a background reaction but only from the decay of K^-pp in coincidence; this helped reduce the background component.

By requiring the final state to comprise Σ^0 and a proton, we have observed the signal of the K^-pp-like structure, as shown in Fig.3-4. The evaluated binding energy of the K^-pp from the spectrum fitting is about ten times larger than that for normal nuclei. Such a large binding energy cannot be reproduced from a simple theoretical calculation for the K^-pp. The origin and structure of the K^-pp-like structure will be explored by further experimental and theoretical studies.

Reference

Ichikawa, Y. et al., Observation of the "K^-pp"-like Structure in the $d(\pi^+, K^+)$ Reaction at 1.69 GeV/c, Progress of Theoretical and Experimental Physics, vol.2015, issue 2, 2015, p.021D01-1-021D01-8.

3–3 Novel Magnetism in Uranium Compound Revealed by World's Strongest Magnet

— High-Field Magnetic Structure in URu_2Si_2 Observed via Nuclear Magnetic Resonance —

(a) 45 T hybrid magnet
in the National High Magnetic Field Laboratory
at Tallahassee, Florida, USA

(b) ^{29}Si enriched single crystal of URu_2Si_2

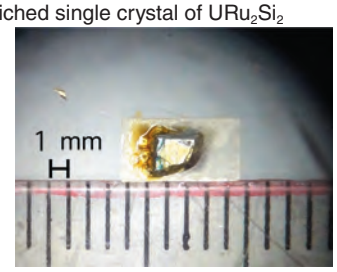

Provided by Los Alamos National Laboratory (USA)

Fig.3-5 Photos of the hybrid magnet and single crystal of URu_2Si_2 used in this study
(a) This hybrid magnet can produce the world's strongest static field at 45 T, and is composed of a superconductive magnet of 11.5 T and a water-cooling resistive magnet of 33.5 T. A large tank filled with liquid helium and cold-water pipes are seen in this photo. This magnet consumes a huge amount of energy, namely 33 MW. (b) A photo of the isotopically enriched more than 99%–^{29}Si single crystal of URu_2Si_2.

(c) Unit cell of URu_2Si_2

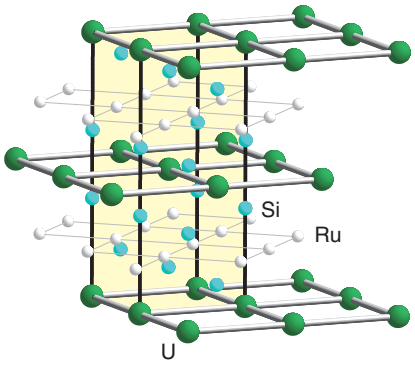

(d) The magnetic structure is schematically illustrated when the external field above 35 T is applied. The arrows represent the magnetic moments on the U sites.

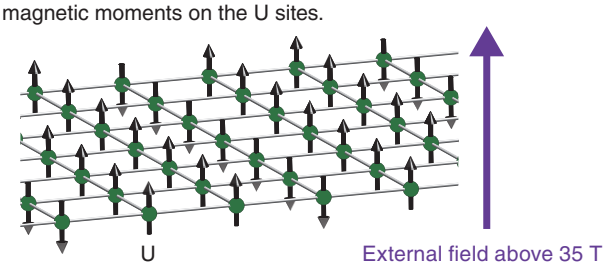

Fig.3-6 Crystal structure of URu_2Si_2 and the peculiar magnetic structure in the high field illustrated by the ^{29}Si NMR technique
(c) The unit cell is shaded yellow in color. U atoms form a square lattice. No magnetic moments on the U sites are generated even if a magnetic field of 35 T is applied. (d) Just above 35 T, a new magnetic state appears. The up and down arrows on the U sites represent the directions of the magnetic moments.

The uranium (U) material URu_2Si_2 exhibits a certain transition at 17.5 K accompanied by a large, specific heat jump, and it interestingly shows superconductivity at the low temperature of 1.5 K. This phase transition at 17.5 K is not an ordinary magnetic transition, and its origin is still unidentified after 30 years. Even now, many researchers are challenging to theoretically and experimentally identify this transition. If an external field is applied to this material, this transition temperature of 17.5 K gradually becomes lower. If the field reaches 35 T, the transition temperature becomes nearly 0 K and a new magnetic state emerges, the magnetic structure of which has not yet been determined. We have proposed a microscopic experiment to investigate the magnetic state via nuclear magnetic resonance (NMR), which is widely applied in medical research as magnetic resonance imaging. Consequently, our proposal to use the world's strongest hybrid magnet in the National High Magnetic Field Laboratory in Tallahassee, Florida, USA, was approved. Thanks to a collaboration with the Los Alamos National Laboratory, ^{29}Si nuclei enriched single crystals of URu_2Si_2 were prepared for our NMR purpose. Photos of the hybrid magnet and single crystal are shown in Fig.3-5.

As a consequence of the experiment, we have succeeded in observing ^{29}Si NMR signals in the magnetic state of URu_2Si_2 above 35 T. From the NMR spectral analysis, in this magnetic state, each U atom has a uniform magnetic moment and the moments' directions are bounded to be up or down along the external field, as shown in Fig.3-6. The propagation of the moments' array would be –up–up–down–, as if the array made striped patterns horizontally. On the other hand, below 35 T, no magnetic moment was observed; that is to say that the system is non-magnetic up to 35 T. Valence electrons of the U atom, i.e., 5f electrons, permeate site-to-site as metallic band electrons in low fields; however, if 5f electrons are bounded to the U sites suddenly above 35 T, then the generated magnetic moments are vertically aligned. Interestingly, the moments' array forms horizontal stripes with regard to the direction of the external field. Such a peculiar directional preference in the high-field metastable state is a clue to understanding the original transition below 35 T.

This study demonstrates that the nature of 5f electrons in a U atom can be highly variable with external parameters of magnetic fields or temperatures. This contributes to the knowledge for making new functional U compounds.

Reference

Sakai, H. et al., Emergent Antiferromagnetism Out of the "Hidden-Order" State in URu_2Si_2: High Magnetic Field Nuclear Magnetic Resonance to 40 T, Physical Review Letters, vol.112, issue 23, 2014, p.236401-1-236401-5.

3–4 Switching of Electric and Magnetic Flows in Metal
— A Possible Application of Spin Thermopower —

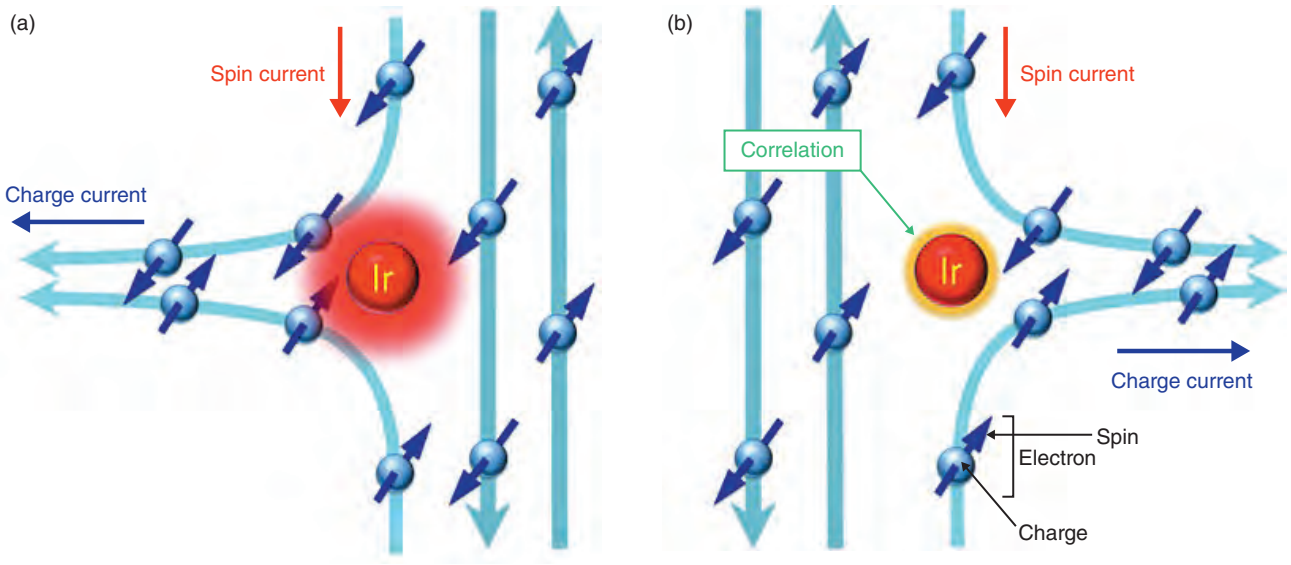

Fig.3-7 The spin Hall effect
(a) Schematic of the conversion from a charge current to a spin current. (b) The electron-electron repulsion changes the flow of the charge current. The areas shaded in red in (a) and yellow in (b) indicate the change of electron density by the correlation effect. Although the electron-electron interaction depends on the material, a similar change of the electron density could be induced by an electric field and/or light. Therefore, the charge current converted from the spin current will be controlled by an electric field and/or light. The blue circles with arrows denote electrons, wherein circles and arrows indicate charge and spin, respectively. A magnet with N and S poles is a suitable analogy for spin.

Spintronics is a rich research field not only for the wide applications to low-energy consumption and energy transformation devices but also for the new physics of interplays amongst charge, spin, orbital angular momentum, heat, etc. The spin Hall effect (SHE), which converts the injected longitudinal charge current into the transverse spin current via the spin-orbit interactions, is crucial for the development of spintronic devices (Fig.3-7).

The SHE is characterized by the ratio between the transverse and the longitudinal resistivities, called the spin Hall angle (SHA). The magnitude of SHA describes the conversion efficiency between the charge current and the spin current, whereas the sign of SHA distinguishes the scattering direction of electrons, i.e., clockwise or anticlockwise in the transverse direction.

The SHA of CuIr alloys was measured to be a small positive value in an experiment, whereas previous theories could not consistently reproduce the positive sign. Such a discrepancy inspired us to find the key physics that decide the sign of SHA. To numerically simulate the local correlation effects, we develop two specific combined methods using density functional theory (DFT) and the quantum Monte Carlo method (QMC). First, we calculate a mixing between the base material, Cu, and the impurity, Ir, via DFT, which includes the character of the material. Next, assuming the Anderson impurity model, the mixing and the correlation is solved using QMC. Using this combined method, we find that the sign of SHA changes from negative to positive with increasing magnitude of correlation.

These theoretical results are qualitatively consistent with those of the experiment, revealing the key physics that the local correlation effects are decisive on the sign of SHA in CuIr alloys. The sign of SHA of CuIr is sensitive to perturbation of the local correlations, which is favorable for the prospect of controlling the sign of the transverse spin Hall voltage, as illustrated in Fig.3-7. This may open up a way to devise a spin current switch or a spin current sensor. Furthermore, our result will be useful for the study of spin thermoelectric generation, wherein a simple bilayer of metal and magnets is used. This will contribute to the energy efficiency.

Reference

Xu, Z., Mori, M. et al., Sign Change of the Spin Hall Effect due to Electron Correlation in Nonmagnetic CuIr Alloys, Physical Review Letters, vol.114, issue 1, 2015, p.017202–1–017202–5.

3–5 Surface Spin Polarization Probed by Positronium

— Current-Induced Spin Polarization due to the Rashba Effect of the Bi/Ag Bilayer —

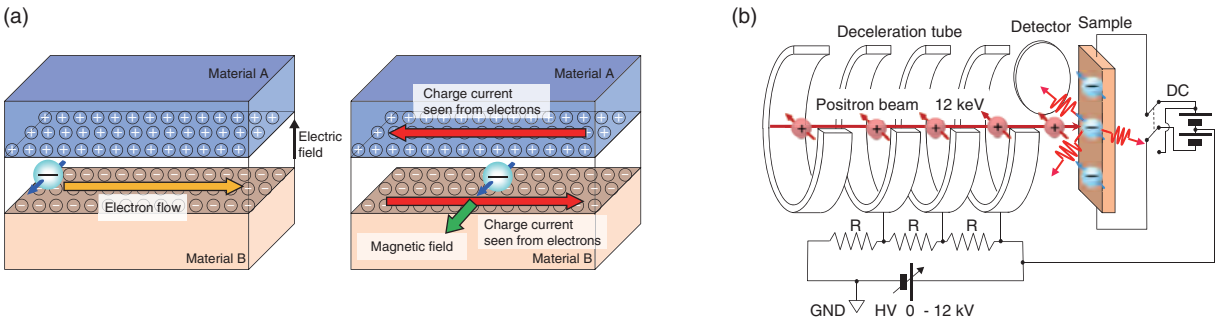

Fig.3-8 (a) Schematic of the Rashba effect and (b) schematic of the spin-polarized positron beam experiment
(a) Due to the electric field at the interface, moving electrons feel an effective magnetic field and consequently electrons are spin-polarized. (b) Spin-polarized positrons are implanted in a sample under the application of a direct current. From current-reversal asymmetry of the intensity of annihilation γ-rays from surface positronium, the spin polarization of surface electrons is determined. Incident positron energy is adjusted by a deceleration tube.

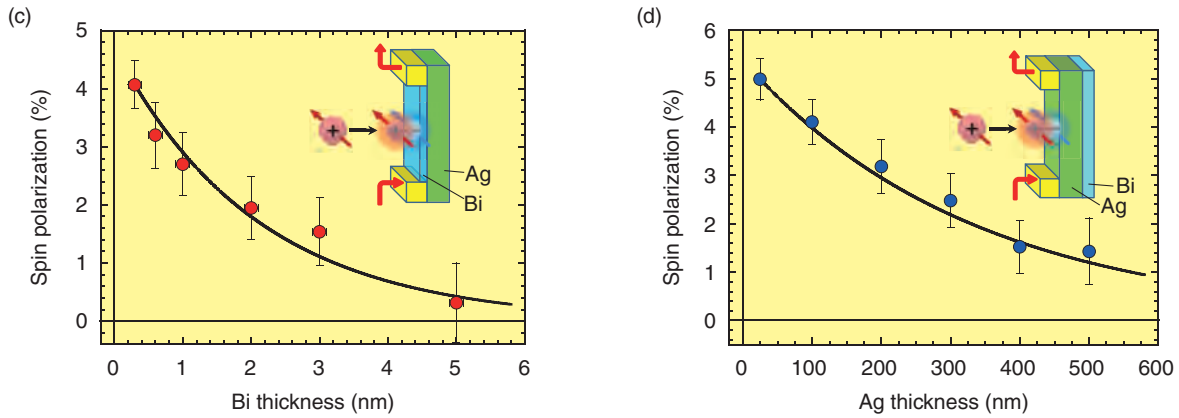

Fig.3-9 Surface spin polarizations observed for (c) Bi and (d) Ag as functions of their thicknesses
Lateral and vertical bars on data points are errors.

For energy savings by electronic devices, spintronics, which unites the charge and spin of electron, is thought to be a more promising technology than electronics based only on the charge of an electron. For the practical application of spintronics, the establishment of methods to observe and to manipulate electron spins is indispensable. In spintronics, electron spins must be manipulated without either magnetic substances or electronics. The Rashba effect is a method for electrically manipulating electron spins. Concerning applications to field effect transistors, the Rashba effect has been extensively studied. Fig.3-8(a) shows a schematic of the Rashba effect. At the interface of a bilayer system, an out-of-plane electric field is induced. Under the application of electric current, electrons see an opposite current in two materials. Consequently, an in-plane magnetic field appears; hence, electron spins are ordered in the same direction. Previous studies have suggested the occurrence of a large Rashba effect in the Bi/Ag bilayer. However, direct observation of spin-polarized electrons under a direct current has not yet been conducted so far.

In this study, we attempted to observe spin-polarized electrons in the Bi/Ag bilayer under the application of a direct current using a spin-polarized positron beam shown in Fig.3-8(b). This method enables non-destructive observation of spin-polarized electrons at the outermost surface in the natural state. In the conventional methods, the surface state may be modified because of the fabrication of electrodes on the surface to detect spin-polarized electrons.

As shown in Fig.3-9, we found that (i) electrons on the Bi and Ag surfaces are transversely spin-polarized to the applied direct current and (ii) the spin polarizations diminish as the layer thickness increases. These findings suggest that the induced spins at the Bi/Ag interface diffuse into the Bi and Ag layers and reach their surfaces. From the above results, the spin diffusion lengths can also be determined.

Thus, the spin-polarized positron beam has been demonstrated to be useful in the spintronics research.

Reference

Zhang, H. J., Kawasuso, A. et al., Charge–to–Spin Conversion and Spin Diffusion in Bi/Ag Bilayers Observed by Spin–Polarized Positron Beam, Physical Review Letters, vol.114, issue 16, 2015, p.166602–1–166602–5.

3–6 Digital Response Character of Cells Exposed to Ionizing Radiation
— Single-Cell Tracking of Cell Cycle Modulation by Ionizing Irradiation —

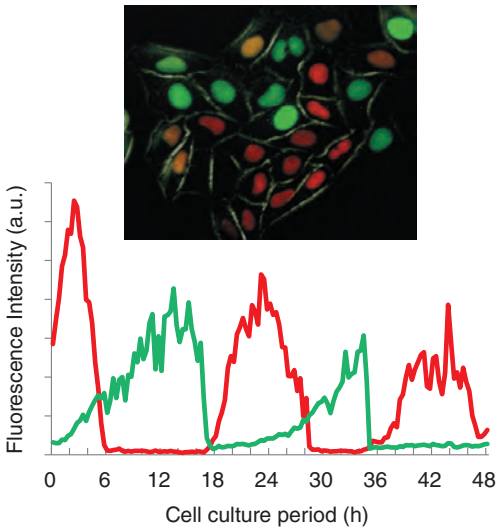

Fig.3-10 Timecourse of the fluoresce profile of HeLa-Fucci cells
A single HeLa-Fucci cell in the colony (photograph) was selected to survey the timecourse of the fluorescence intensity. Red and Green indicate that the cell was in the G1 and G2 phases, respectively. After the first cell division, as indicated by a sharp drop of the green curve around 18 h, the intensity of one of the dividing cells was plotted.

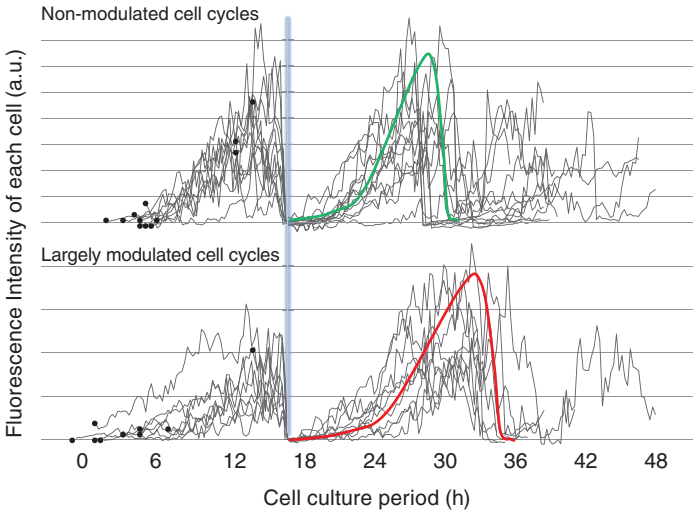

Fig.3-11 Timecourse of the fluorescence of irradiated cells relevant to cell cycle progression
Time-dependence of the green (G2) fluorescence intensity of an individual cell is shown. Irradiated cells were divided into two populations: those without (upper panel) and with (lower panel) a significant cell cycle modulation. The green curve indicates the averaged fluorescence time course of the non-irradiated cells. The red curve is the averaged intensity time course for the population showing cell cycle delay.

Recent advances in microscopic live cell imaging technologies with cell-labeling indicators have enabled us to easily observe cellular functions with dynamics. The obtained dynamic images include the information within individual cells. This is of great advantage to us because conventional methods afford only static images or statistical averages of functional molecules biochemically extracted from populations of cells, and hardly provide us with dynamic cellular functions. Using a time-lapse imaging technique, we have investigated cell cycle modulation induced by ionizing irradiation.

Cell divisions of mammalian cells, including human cells, constantly undergo a cell cycle. The exposure to ionizing radiation, however, affects the cells to cause cell cycle delay or arrest. This is thought to be controlled by the so-called “check point mechanism” with various proteins to ensure the repair time of genomic DNA damage, although the details have not yet been clarified, particularly concerning whether all cells undergo cell cycle delay over a similar period when exposed to the same dose or how the cell cycle delay recovers to its normal value.

Using HeLa-Fucci cells showing their cell cycle stages with specific colors (Fig.3-10), we have performed time-lapse observations to track individual cycles of cells on a culture dish after X-ray exposure of 5 Gy, which causes inactivation of cell division for 99% of the irradiated cells. The results show that the cells could undergo about two cell divisions within 48 h. Furthermore, tracking the cell nucleus colors for 20 cells revealed that the cells were possibly separated into two populations: those with modified and with hardly modified cell cycles (Fig.3-11). These results indicate that there is a novel mechanism underlying the appearance of the two types of cell populations by switching the cell cycle from “ON” to “OFF” states and the output to 0 or 1. Understanding such digitally cellular responses might be a breakthrough for studies on the diverging point in the loss of cell division or surviving with mutation.

A part of this study has been performed as a Joint Research Program between the graduate school of Ibaraki University and JAEA.

Reference

Kaminaga, K., Yokoya, A. et al., Visualization of Cell Cycle Modifications by X-Ray Irradiation of Single HeLa Cells using Fluorescent Ubiquitination-Based Cell Cycle Indicators, Radiation Protection Dosimetry, vol.166, issues 1-4, 2015, p.91-94.

3–7 The Newest Nuclear Data at Hand

— Completion of a Comprehensive Portable Nuclear Decay Data Map, the "JAEA Chart of the Nuclides 2014" —

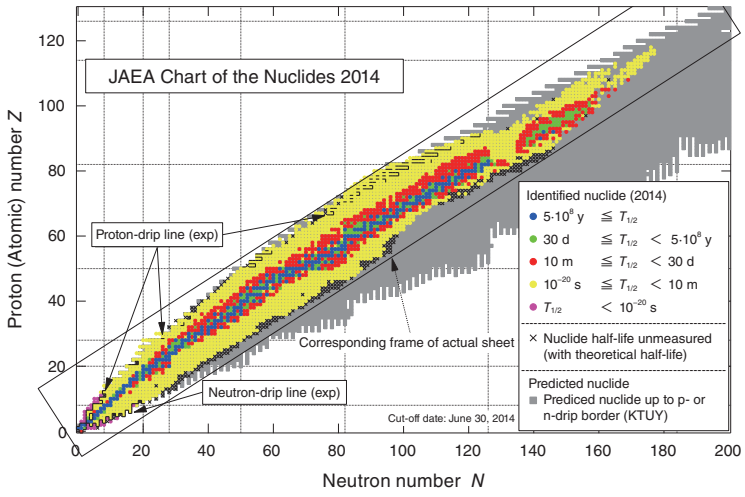

Fig.3-12 Overview of the JAEA Chart of the Nuclides 2014
Vertical axis: number of protons (atomic number); horizontal axis: number of neutrons. Colored non-gray nuclei indicate experimentally identified nuclides (3150); the region of the slanted rectangle corresponds to the main part of the chart. The gray region indicates nuclides whose existence has been theoretically predicted through calculation with the Koura–Tachibana–Uno–Yamada (KTUY) mass model, which was developed at the Advanced Science Research Center (ASRC) with collaborators.

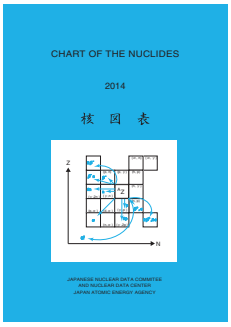

Fig.3-13 Cover page

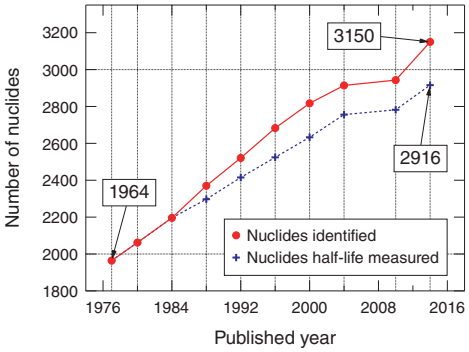

Fig.3-14 Transition of the number of identified nuclides
Vertical lines indicate publication years of the JAEA Chart of the Nuclides (1977, 1980, 1984, 1988, 1992, 1996, 2000, 2004, 2010, and 2014).

All the materials found on Earth are made of atoms, with each atom composed of electrons and a nucleus. A nucleus is ten thousand times smaller than an atom and is composed of protons and neutrons. The combination of protons and neutrons determines properties of the nuclei, such as stability and nuclear decay. What is the relation between this combination and the decay properties, and how many combinations are available?

Nuclear physicists have synthesized various nuclei with combinations of protons and neutrons and investigated nuclear properties to answer these questions. To represent the properties of various nuclei, nuclear physicists have made a chart of nuclei, where the number of protons is shown on the vertical axis and the number of neutrons is shown on the horizontal axis like a map.

We have also published such a chart on a regular basis since 1977, and we have now revised the chart as the "JAEA Chart of the Nuclides 2014", with major upgrades since the previous version in 2010 (Figs.3-12 and 3-13).

This chart includes the latest 3150 experimentally identified nuclides, and the evaluated half-lives and decay modes of 2916 of them. The number of nuclei added since 2010 is approximately two hundred, and approximately one thousand isotopes have been discovered and identified over nearly forty years (Fig.3-14).

The unique feature of this chart is that decay data for unmeasured nuclei (1578 points) have also been presented based on calculations using nuclear theory. Furthermore, nuclei with extremely short half-lives (less than 10^{-20} s) have been newly added, and neutron and proton drip lines are also drawn. These data provide useful information for nuclear experiments worldwide.

This chart has been used in high-school lectures and science cafes for the general public to understand nucleosynthesis in the universe and atomic energy related to various phenomena of nuclei such as nuclear transmutation.

Reference

Koura, H. et al., Chart of the Nuclides 2014, Japanese Nuclear Data Committee and Nuclear Data Center, Japan Atomic Energy Agency, 2015.

4 Nuclear Science and Engineering Research

Promoting Basic R&D on Nuclear Energy and Creation of Innovative Technology to Meet Social Needs

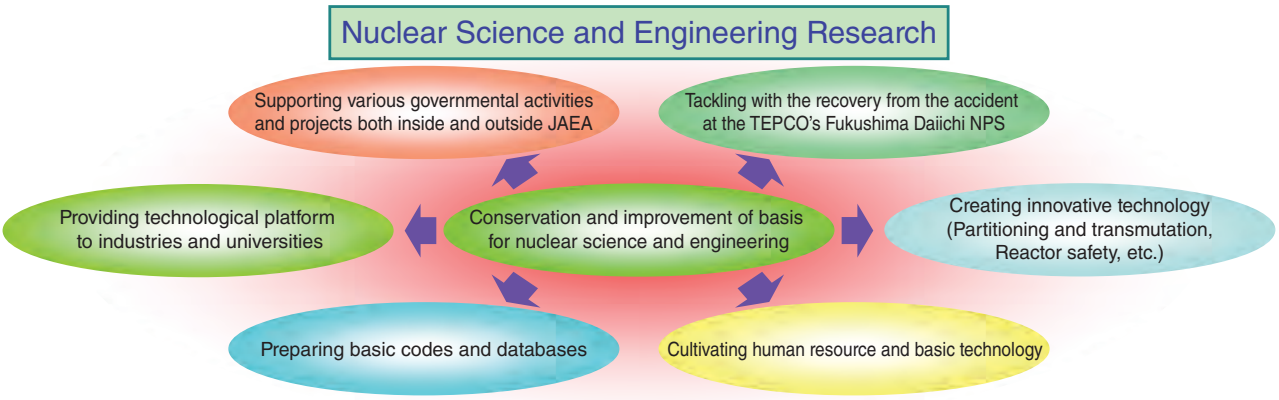

Fig.4-1 Roles of nuclear science and engineering research
We serve various roles in the conservation and improvement of the foundation of nuclear science and engineering.

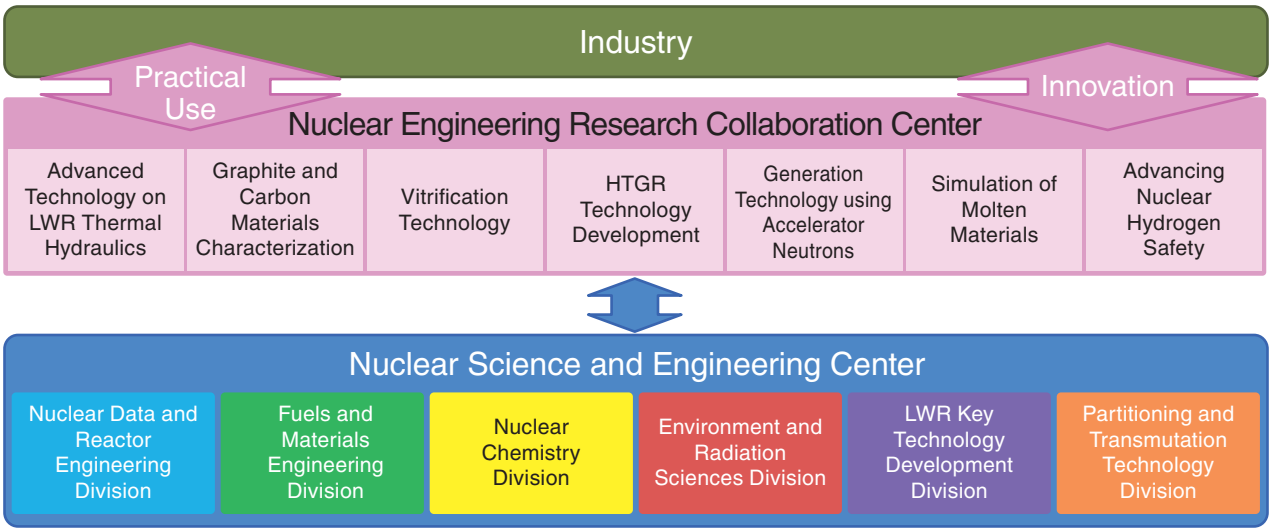

Fig.4-2 Nuclear Engineering Research Collaboration Center
To create innovative and practical products, joint research with industry and academia is being promoted.

Nuclear science and engineering research aims to promote various activities, as shown in Fig.4-1. These include recovery from the accident at the Fukushima Daiichi Nuclear Power Station (1F) of Tokyo Electric Power Company, Incorporated development of transmutation technologies for reducing the amount of long-lived radioactive waste, and Light Water Reactor (LWR) key technologies for reactor safety improvement. In the area of nuclear data and reactor engineering, for the new edition of the Japanese Evaluated Nuclear Data Library (JENDL), measurement of nuclear data and development of a methodology for nuclear reactor design are being studied using advanced theoretical, experimental, and simulation approaches (Topics 4-1 and 4-2). In the area of fuels and materials engineering, research on the nuclear fuels and materials used in reactors and fuel cycle facilities is being promoted (Topics 4-3, 4-4, and 4-5). In the area of nuclear chemistry, research is being promoted on basic data for reprocessing and detection of extremely small amounts of nuclear materials and on practical uses of the above technologies (Topics 4-6, 4-7, and 4-8). In the area of environmental and radiation science, studies of the behavior of radionuclides in the environment and the development of a database for radiation protection are being promoted (Topics 4-9, 4-10, and 4-11). Joint research with industry is also being promoted via the Nuclear Engineering Research Collaboration Center with fundamental technologies (Fig.4-2).

For the development of fundamental technologies for 1F recovery, we are studying estimation methods for doses from Cs radioisotopes considering people's age, prediction of Cs dose distributions in houses and buildings, chemical behavior of emitted radionuclides, simulation of melting fuel behavior, the effects of introducing seawater on fuels and structural materials, estimation of the reactor bottom situation after melt-down, and other topics (Chapter 1, Topics 1-2, 1-10, 1-14, 1-15, 1-16, and 1-18).

Technologies for the partitioning of minor actinide (MA) nuclides (ex. Neptunium and Americium) and fission products from spent nuclear fuel and for MA transmutation using accelerator-driven subcritical systems (ADSs) are being studied.

4–1 Highly Accurate Estimation of Nuclear Reactor Parameters

— Development of a Novel Calculation Method for Calculating Reactor Kinetics Parameters with Monte Carlo Method —

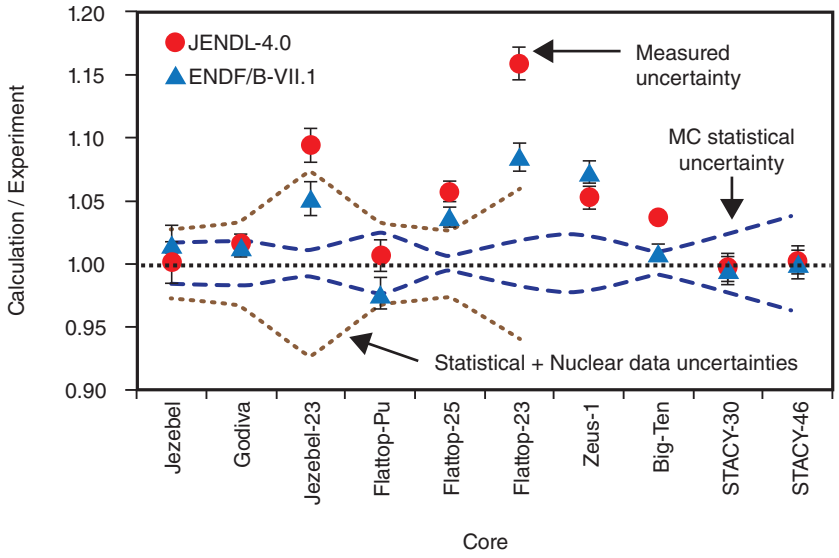

Fig.4-3 Comparison of calculated and measured values
Measured α values at a delayed critical condition and calculated α values with the MVP code are shown for various critical assemblies (Table 4-1). ● and ▲ show the results obtained with the nuclear data library JENDL-4.0 developed at JAEA and the U.S. library ENDF/B-VII.1, respectively; the error bars denote experimental uncertainties. The uncertainties induced by nuclear data are estimated for the six assemblies.

Table 4-1 Critical assemblies for which reactor kinetics parameters have been calculated

Core	Reactor type	Fuel
Jezebel	Fast	Pu
Godiva	Fast	High enriched U
Jezebel-23	Fast	U-233
Flattop-Pu	Fast	Pu
Flattop-25	Fast	High enriched U

Core	Reactor type	Fuel
Flattop-23	Fast	U-233
Zeus-1	Fast	High enriched U
Big-Ten	Fast	Enriched U (10%)
STACY-30	Thermal	Low enriched U
STACY-46	Thermal	Low enriched U

The Monte Carlo (MC) method used for reactor analysis simulates the behavior of neutrons in a reactor to calculate nuclear reactor parameters. This method can model the calculation geometry very accurately, compared with the deterministic method conventionally used for reactor design calculations. In addition, the cross-section data, which represent the probability of the interaction between a neutron and a nucleus, can be addressed continuously as a function of energy. In other words, the MC method enables us to perform highly accurate calculations with almost no approximations.

The MC method has great advantages, but one cannot calculate all the parameters necessary for nuclear reactor analysis. The parameters that one cannot calculate to date using the MC method are the reactor kinetics parameters, the effective delayed neutron fraction, and the neutron-generation time. These are nuclear safety parameters directly related to reactor power variation. Thus, these parameters must be calculated as accurately as possible because small changes in them significantly affect the reactor power.

We have developed a novel method to for calculating the reactor kinetics parameters with the MC method. The difficulty lies in defining the parameters, which is done using the ratio of adjoint-weighted values. The novel method does not calculate adjoint-weighted values but does exactly calculate the parameters with the differential coefficient of the effective multiplication factor. To verify the novel method, we have implemented it into our MC code MVP and have compared the α value under a delayed critical condition for various critical assemblies (Table 4-1). Fig.4-3 shows a comparison between the calculated and experimental α values. The α value at the delayed critical condition is defined by the effective delayed neutron fraction divided by the neutron generation time and multiplied by −1; the α value is a nuclear reactor parameter that can be measured with critical experiments. The calculated values agree fairly well with the measured ones within the MC statistical and nuclear-data-induced uncertainties; there are some calculated values that significantly differ from the measured ones.

The outcome of this research enables us to calculate the reactor kinetics parameters. It is expected that the novel method can provide reference values for the parameters for nuclear systems including fuel debris and innovative reactors of new types.

Reference

Nagaya, Y., Calculation of Reactor Kinetics Parameters with Monte Carlo Differential Operator Sampling, Annals of Nuclear Energy, vol.82, 2015, p.226–229.

4–2 Combining Two Nondestructive Elemental Analysis

— Development of Elemental Analysis by using an Intense Pulsed Neutron Beam —

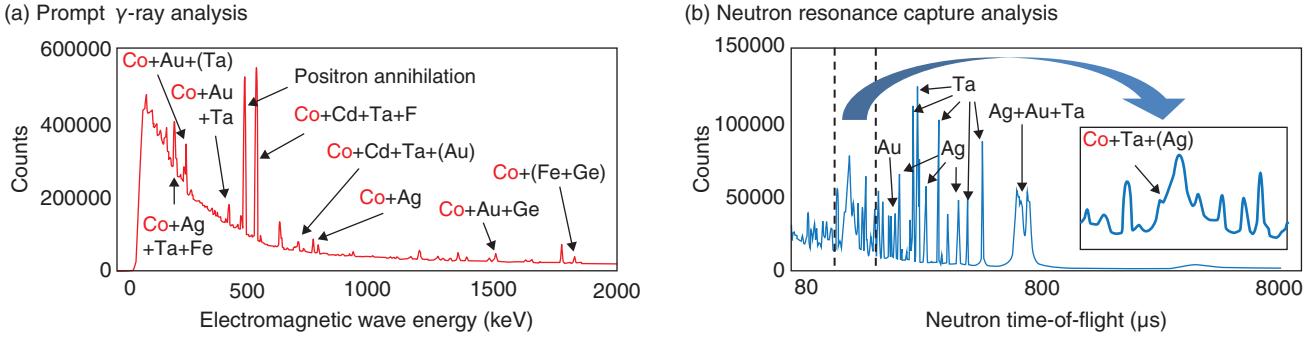

Fig.4-4 Spectra obtained by conventional methods
(a) and (b) are the mixed sample spectra obtained by PGA and TOF, respectively. The Co peaks in both PGA and TOF are interfered with by unresolved γ-rays from other elements in the mixed sample.

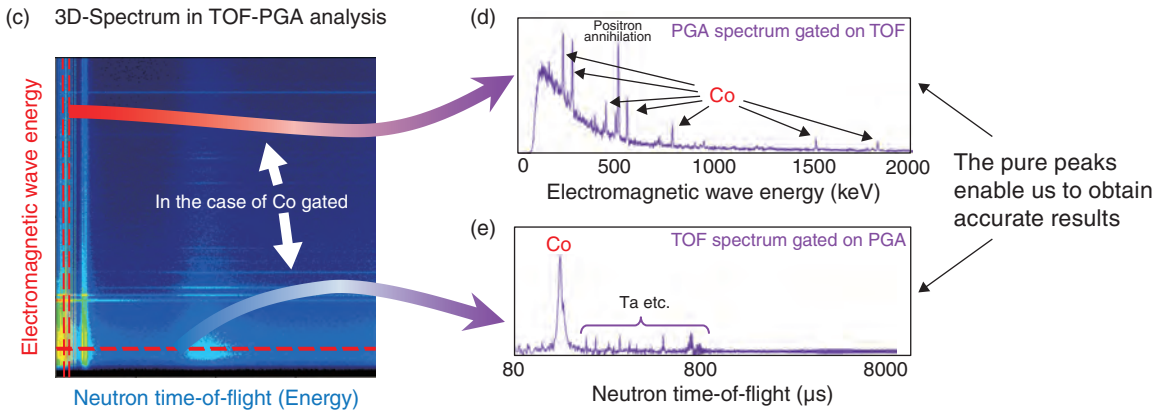

Fig.4-5 Spectra obtained by TOF-PGA
(c) shows the 3D-spectrum obtained by TOF-PGA. The correlation between the PGA and TOF methods enables us to eliminate the overlapping γ-rays in the Co peak and to obtain a pure or almost pure Co peak. Therefore, we can accurately quantify Co using TOF-PGA.

Nondestructive analysis allows us to reuse a specimen as it is after a measurement and yields analytical results with little or no extra work, such as chemical separation processes. Thus, nondestructive analysis is preferred in fundamental research and applied technology, both of which are often used to investigate scientifically important or high-value specimens. However, qualitative information from nondestructive analysis is not enough in some cases, especially for samples that have complex elemental compositions (Fig.4-4). Therefore, a technological breakthrough in nondestructive analysis is needed in many fields of scientific research and industry.

Prompt γ-ray analysis (PGA) and time-of-flight elemental analysis (TOF) are known as rapid and efficient nondestructive analytical tools. The TOF method is formally called neutron resonance capture analysis. In both the PGA and TOF methods, a sample is irradiated with a neutron beam and γ-rays are emitted from neutron-capture reactions. Thus, these two methods are similar. PGA requires the use of a germanium (Ge) detector with a high γ-ray energy resolution, even though it has a relatively slow response time. On the other hand, a scintillation detector, such as C_6D_6, is usually used in TOF due to its good time resolution. If PGA and TOF could simultaneously be conducted with one detector, synergy is expected as well as simultaneous acquisition of PGA and TOF spectra. Specifically, the simultaneous measurement can be used to quantify element concentrations in samples that neither the TOF nor PGA methods can be applied to.

The Accurate Neutron-Nucleus Reaction Measurement Instrument (ANNRI) is located at beamline No. 04 at the Materials and Life Science Experimental Facility (MLF) of the Japan Proton Accelerator Research Complex (J-PARC). We developed a new analytical method (TOF-PGA) that combines PGA and TOF by using an intense pulsed neutron beam at ANNRI, a Ge detector system with a high detection efficiency, a high-speed data-acquisition system, and effective neutron shields. This method offers correlation between the PGA and TOF methods; thus, the TOF-PGA spectrum has three dimensions. Analysis of this spectrum by gating on the PGA (or TOF) peaks enables elimination, or at least significant suppression, of overlapping γ-ray events and provides correspondingly more accurate results (Fig.4-5).

The TOF-PGA method will be an irreplaceable tool for many fields, including radioactive waste management, cosmochemistry, archeology, geochemistry, and environmental science.

Reference

Toh, Y. et al., Synergistic Effect of Combining Two Nondestructive Analytical Methods for Multielemental Analysis, Analytical Chemistry, vol.86, issue 24, 2014, p.12030–12036.

4–3 Predicting Corrosion Behavior in Nitric Acid Solution

— Simulation of Intergranular Corrosion of Stainless Steel using the Cellular Automata Method —

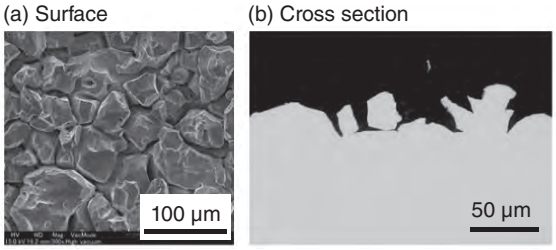

Fig.4-6 Intergranular corrosion of stainless steel in a nitric acid solution
(a) Stainless steel in high-temperature condensed nitric acid solution shows the morphology of an IG corrosion surface. (b) The IG corrosion surface looks bumpy in a cross-sectional image.

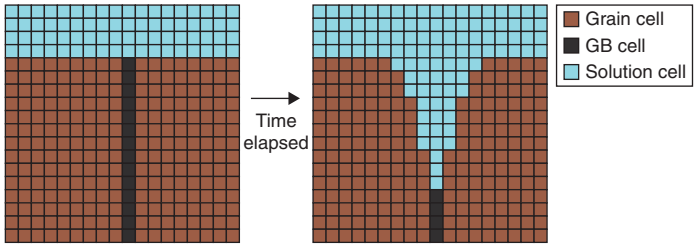

Fig.4-7 Schematic of an intergranular corrosion model using the cellular automata method
In the model, the system is divided into lattice cells and those cells are designated grain, GB, and solution cells. IG corrosion behavior can be simulated by calculating the time sequence of cell exchanges using the cellular automata method.

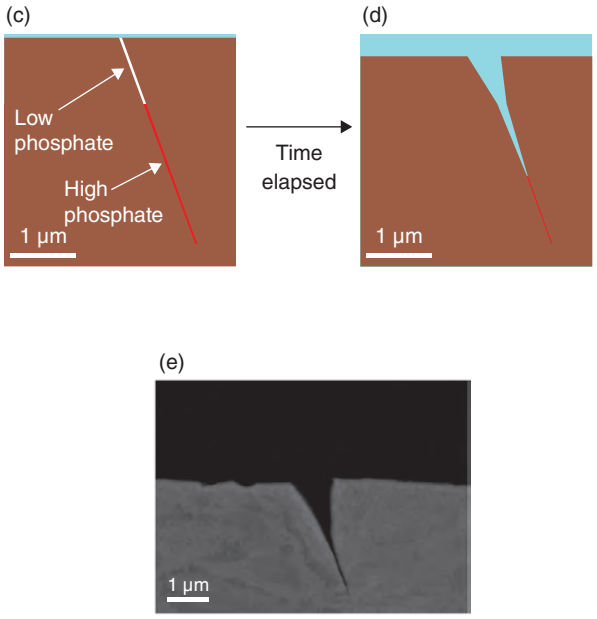

Fig.4-8 Intergranular corrosion behavior considering the concentration of phosphide
Simulation results are shown in (c) and (d). The width of IG corrosion becomes narrow in the phosphide-rich GB region. From comparison between the simulation result (d) and the experimental result (e), complicated IG corrosion shapes can be simulated using the developed model.

Nuclear fuel reprocessing plants contain high-temperature condensed nitric acid (HNO_3) solution for dissolution of spent nuclear fuel, and austenitic stainless steels are used as a main material for spent nuclear reprocessing systems. In such a highly oxidizing environment, stainless steel shows the morphology of an intergranular (IG) corrosion surface, as shown in Fig.4-6. It is known that grain dropping occurs with IG corrosion development, accelerating the corrosion rate. To maintain the safety of the system, it is important to understand the IG corrosion behavior. Although one of the causes of IG corrosion is the existence of impurities in steel, such as carbon and phosphorus, it is not clear that there is a cause-and-effect relation between impurity and IG corrosion behavior.

In this study, we developed a new IG corrosion simulation model using a cellular automata method to clarify the influence of impurity in stainless steels on IG corrosion behavior. A cellular automaton is a discrete model wherein a system is divided into lattice cells and those cells are set to some states and wherein time evolution is implemented according to some fixed rule defined in each specified cell. Using the developed model, we can simulate not only simple but also complicated IG corrosion shapes by applying grain, grain boundary (GB), and solution states into grids of cells, as shown in Fig.4-7. In the study, we conducted IG corrosion simulation of stainless steel with several concentrations of impurity around the GBs, and the results of the simulation had similar shapes to those of IG corrosion tests of extra-high-purity stainless steel with small amounts of phosphorus impurities, as shown in Fig.4-8. These results indicate that the existence of impurities in stainless steels affects the complicated IG corrosion shapes of stainless steels in HNO_3 solution, and concentrated phosphate around the GBs accelerates the IG corrosion rate.

We can conduct several kinds of IG corrosion simulations, such as grain-dropping, using the developed model. This model promises to shed light upon the mechanisms behind various corrosion phenomena by simulating those corrosion shapes and weight losses.

Reference

Igarashi, T. et al., Simulations of Intergranular Corrosion Feature for Stainless Steel using Cellular Automata Method, Zairyo to Kankyo (Corrosion Engineering of Japan), vol.63, no.7, 2014, p.431-437 (in Japanese).

4–4 Vacancies Studied by Positron Annihilation Lifetime and Hydrogen Adsorption
— Hydrogen Embrittlement under Elastic Stress of High-Strength Steel —

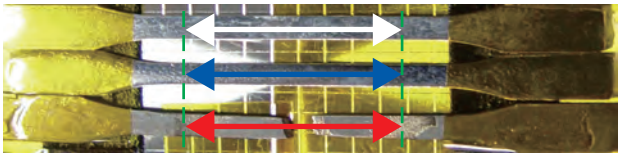

Fig.4-9 Specimens for positron annihilation lifetime measurements
Every arrow indicates the measured area for each specimen. The color of every arrow corresponds to the color of the plots in Fig.4-10.

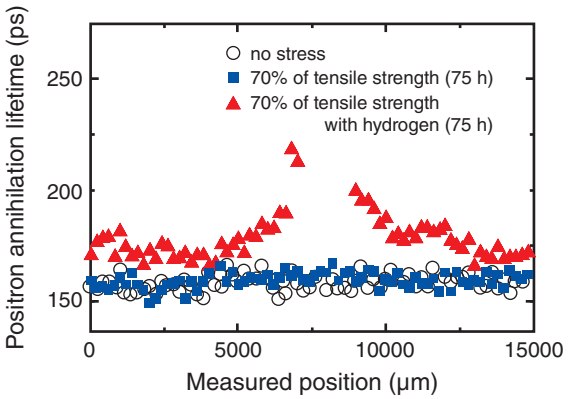

Fig.4-10 Results obtained by positron annihilation lifetime
The results are shown with ○: no stress; ■: 75 h elastic stress without hydrogen; and ▲: 75 h elastic stress with hydrogen (fractured). Long lifetimes near the fracture surface are caused by large holes (vacancy clusters) assembled from small holes (vacancies).

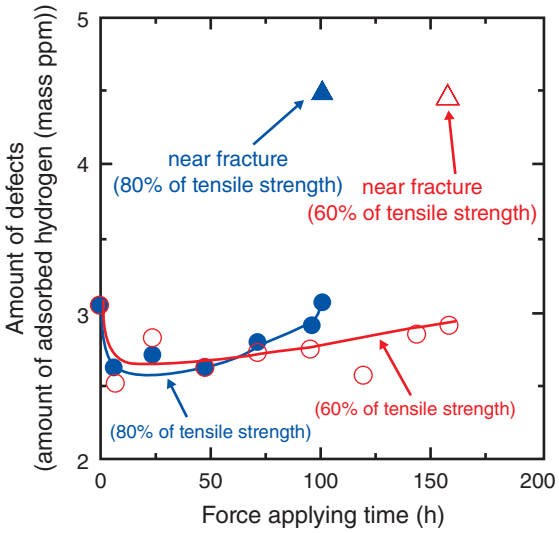

Fig.4-11 Results obtained by hydrogen adsorption
Force-application time-dependence of the amount of defects (amount of hydrogen adsorption) is shown. ●, ○ were measured at the central parts (about 30 mm) of the specimens and ▲, △ were measured near the fracture surface (about 1 mm). The reason why these specimens took a longer time to fracture than the specimen indicated in Fig.4-10 is probably the different shape of the specimens.

High-strength steel (tempered martensitic steel), which is also used as steel plates for automobiles, is not usually destroyed by weak forces as it is without deformation. However, it will fracture in about 100 h when a large amount of hydrogen is present. This brittleness caused by hydrogen is called hydrogen embrittlement, but the elucidation of the mechanism has not progressed. One reason for this is that there have been no reliable experiments concerning the behavior of hydrogen. The arrangement of atoms in the steel (crystalline structure) changes along the process to destruction. For example, creases on the plane of the lined up atoms (dislocations) or holes of missing atoms (vacancies) can form. These are generally called defects. Here, there are two methods used for the measurement of defects: one is to measure the time until positron annihilation with one of the electrons in the steel occurs which is called positron annihilation lifetime spectroscopy, and the other is a measurement of the quantity of hydrogen adsorbed in the steel which is called thermal desorption spectroscopy. The studies using these techniques were conducted by the National Institute of Advanced Industrial Science and Technology (AIST) and Sophia University.

The positron efficiently finds a defect and the time until annihilation (lifetime) of the positron is longer in a larger vacant space. As a result, the lifetime is longer in a vacancy than in a dislocation, and longer still in a large hole, i.e., gathered vacancies (vacancy cluster). The steel specimens (Fig.4-9) loaded with 70% tensile strength for 75 h with and without hydrogen were evaluated by the positron annihilation lifetime. As shown in Fig.4-10, the positron annihilation lifetime was longer only with hydrogen, probably because of vacancy formation. In addition, the positron annihilation lifetime is longer still in the vicinity of the broken part because larger vacancy clusters might be formed there.

On the other hand, although hydrogen will easily go out of defect-free steel samples, if defects exist, they attract hydrogen that will not come out easily. Hydrogen adsorbed in dislocations and vacancies comes out at higher temperatures, and the amount of desorbed hydrogen shows the amount of defects in the steel. As shown in Fig.4-11, reduction of defects due to the disappearance of originally existing dislocations is observed at the early stage, and then, the number of defects monotonically increases until fracture.

This study indicates that fracture phenomenon due to hydrogen embrittlement is dominated by the formation of defects such as vacancies. For this study, a “Sawamura Award” was awarded by the Iron and Steel Institute of Japan, and the “Six major results of 2013 from Nanotechnology Platform Japan and Best research support award 2014” was awarded by the Ministry of Education, Culture, Sports, Science and Technology of Japan (MEXT).

Reference

Doshida, T., Hirade, T. et al., Enhanced Lattice Defect Formation Associated with Hydrogen and Hydrogen Embrittlement under Elastic Stress of a Tempered Martensitic Steel, ISIJ International, vol.52, no.2, 2012, p.198–207.

4–5 Toward the Evaluation of Minor Actinide Transmutation Fuel Behavior
— Preparation of a High-Purity Curium Sample at the Milligram Scale —

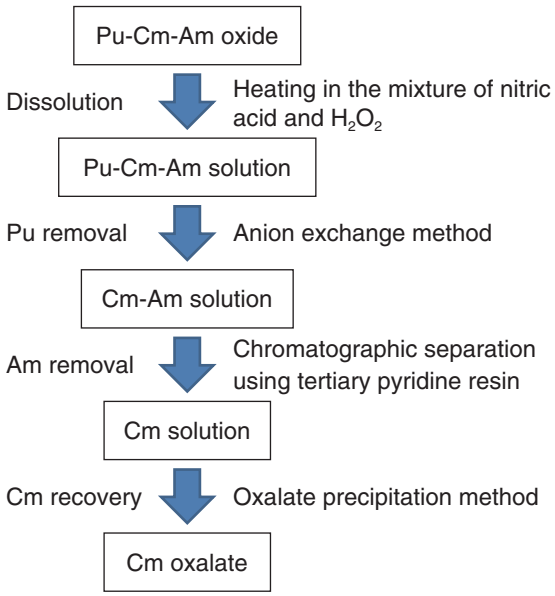

Fig.4-12 Outline of the method for preparing a high-purity curium sample from aged ^{244}Cm oxide samples
A 20% ^{244}Cm–80% ^{240}Pu oxide sample containing an ^{243}Am impurity (about 1%) was dissolved in the mixture of nitric acid and H_2O_2 with heating. A high-purity Cm oxalate sample was prepared from a Cm solution purified by the removal of Pu with an anion exchange method and the removal of Am with chromatographic separation using tertiary pyridine resin.

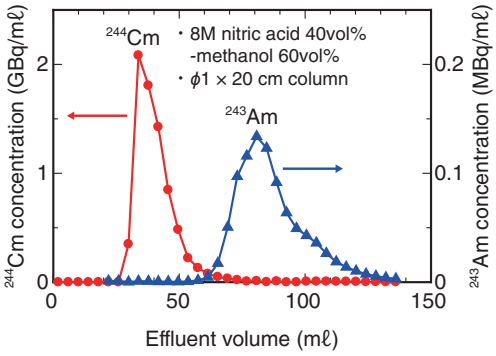

Fig.4-13 Chromatographic separation of Am and Cm using tertiary pyridine resin
After a Cm–Am solution was fed into a chromatography column packed with the tertiary pyridine resin (developed and manufactured by the Tokyo Institute of Technology), effluent from the column with the flow of 8M nitric acid/methanol mixed solution was collected in fractions. Separation of Am and Cm occurred because of a difference in their affinities to tertiary pyridine resin.

Fig.4-14 The Cm oxalate sample that we prepared
Cm oxalate precipitate (about 10 mg) was prepared by mixing the purified Cm solution with the oxalic acid.

Research and development of technologies for partitioning and transmutation is active in many countries including Japan. These technologies aim at reducing the burden of waste disposal by partitioning elements such as fission products and minor actinides (MA: neptunium (Np), americium (Am), curium (Cm)), which are classified as high-level wastes in the current nuclear fuel cycle, and by transmuting long-lived nuclides including MA into stable or short-lived ones. Transmutation of the long-lived nuclides is proposed to be achieved using commercial fast reactors or dedicated transmuters such as accelerator-driven systems (ADS) wherein fuels or targets containing long-lived nuclides are used.

To develop the fuels for MA transmutation, it is necessary to evaluate their behavior based on the thermochemical and mechanical properties of MA compounds. Our studies on MA compounds had been limited to those on Np and Am because of the difficulty of preparing Cm samples at mg scale with the high purity necessary for the abovementioned studies and of handling such samples. The most widely available isotope ^{244}Cm is highly radioactive and decays to plutonium-240 (^{240}Pu) almost immediately because the half-life of ^{244}Cm is 18.1 years.

We developed a method for preparing high-purity Cm samples from aged ^{244}Cm oxide samples. Removal of Pu and Am is necessary to obtain high-purity Cm samples from the starting material, a typical composition of which is 20% ^{244}Cm–80% ^{240}Pu oxide and which contains ^{243}Am impurities (about 1%) (Fig.4-12). This method comprises four steps: dissolving the starting material in a mixture of nitric acid and H_2O_2 (oxidizing agent) with heating; removal of Pu by an anion exchange method; removal of Am by chromatographic separation using tertiary pyridine resin and a nitric acid/methanol mixed solution (Fig.4-13); and precipitation of Cm oxalate from the high-purity Cm solution (Fig.4-14).

We have prepared the oxide and nitride samples using the obtained high-purity Cm oxalates and have successfully measured their thermochemical properties. The method for preparing high-purity Cm samples, which will be used for the evaluation of MA transmutation fuel behavior, was established.

This study contains the results of “Basic actinide chemistry and physics research in close cooperation with hot laboratories” conducted under the Strategic Promotion Program for Basic Nuclear Research by the Ministry of Education, Culture, Sports, Science and Technology of Japan (MEXT).

Reference

Hayashi, H. et al., Separation and Recovery of Cm from Cm–Pu Mixed Oxide Samples Containing Am Impurity, Journal of Radioanalytical and Nuclear Chemistry, vol.296, issue 3, 2013, p.1275–1286.

4–6 Simple, Low-Cost, Highly Efficient Treatment Technology for Radioactive Wastewater

— Uranium Removal from Decontamination Wastewater using an "Emulsion Flow Method" —

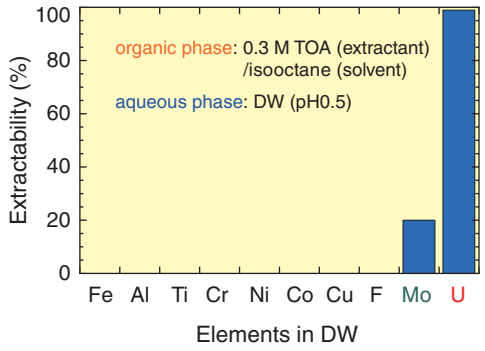

Fig.4-15 Selective extraction of U from decontamination wastewater
Using an adequate extractant—tri-octylamine (TOA) in this case—U is selectively removed from aqueous solutions that contain various metal ions.

Fig.4-16 Recovery of suspended particulate matter in decontamination wastewater
Particulate components suspended in the water are recovered and removed by accumulation at the water/oil interface.

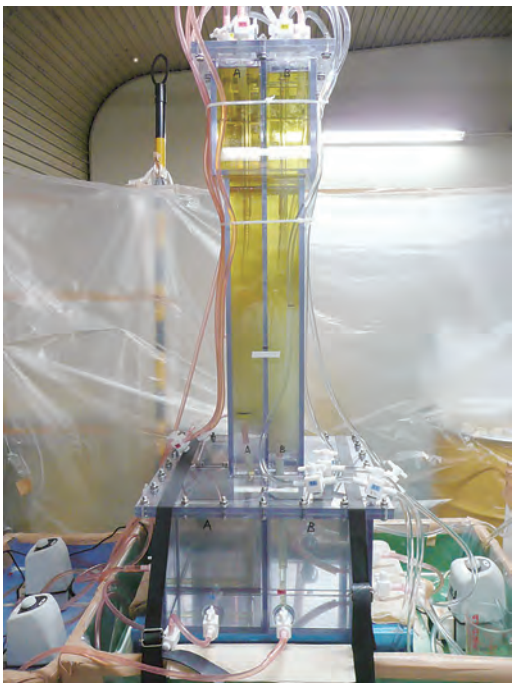

Fig.4-17 Removal experiment for U in decontamination wastewater
A purification experiment of uranium-containing wastewater, generated from the decontamination of a facility or apparatus at the Ningyo-toge Environmental Engineering Center, is shown. The yellow coloration of the organic phase is due to the extraction of U.

At the Ningyo-toge Environmental Engineering Center, a large quantity of uranium-containing wastewater has been generated from the decontamination of facilities or apparatuses. The decontamination wastewater (DW) is treated by coagulation-precipitation processes to form radioactive sludge, into which the uranium (U) in DW passes. A selective removal of U from DW is required to reduce the U content of the sludge and to dispose it of more easily. Uranium-removal methods using ion exchange resin or chelate resin have been previously considered, but they have challenges of low processing speed and high cost.

We here introduce a simple, safe, and low-cost liquid-liquid extraction method using a newly developed "emulsion flow" (EF) extractor, wherein a flow of emulsified phases, referred to as EF, is originated by spraying fine droplets of extractant-containing organic phases into aqueous phases. The distinguishing features of the EF method are high extractability due to sufficient mixing of the organic and aqueous phases and high processing speed due to the high separation ability of the emulsified phases in the EF apparatus. Using an adequate extractant, U can be selectively extracted from DW that contains various metal ions (Fig.4-15). The EF method is also applied to collecting and removing suspended solids (SS) by accumulating them at a water/oil interface (Fig.4-16). The use of the EF method allows the treatment of DW with higher speed (more than tenfold) and higher efficiency at a low cost (less than one fifth) compared with conventional techniques using ion exchange resin and the like.

An experiment using an EF extractor with about half the size of the practical scale (Fig.4-17) was conducted to treat actual DW generated at the Ningyo-toge Environmental Engineering Center with a speed of 60–90 ℓ/h. As a result, we succeeded in promptly removing U in DW (3 Bq/cm^3) below the effluent standard level (0.0022 Bq/cm^3) and in recovering SS in the wastewaters into the recovery part of the extractor. It was also found that connecting three EF extractors would permit the selective removal of more than 99.9% of U from DW.

The EF method is expected to be widely applicable for the treatment of domestic uranium-containing wastewaters. This new technology has received much attention not only in the nuclear field but also in many industrial fields because of its usefulness for purifying industrial wastewaters or recovering rare metals from them.

This study received the 47th Award for Distinguished Technology in FY 2014 from the Atomic Energy Society of Japan (AESJ).

Reference

Nagano, T. et al., Continuous Extraction of Uranium from Actual Uranium-Containing Liquid Wastes using an "Emulsion Flow" Extractor, Nippon Genshiryoku Gakkai Wabun Ronbunshi (Transactions of the Atomic Energy Society of Japan), vol.12, no.4, 2013, p.277-285 (in Japanese).

4–7 Rapid and Reliable Analysis of Impurities in Uranium Ore

— Mass Spectrometric Characterization of Impurities Based on Solid Sample Introduction —

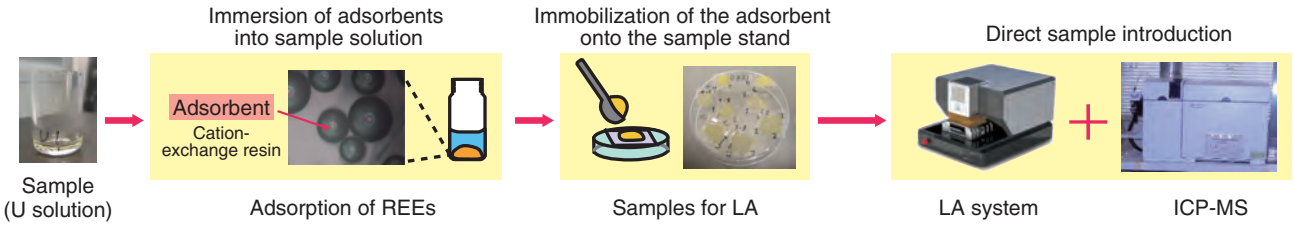

Fig.4-18 Simplified sample preparation achieved by laser ablation technology for ultratrace analysis of rare earth elements
ICP-MS is commonly used for the determination of trace amounts of REEs. Liquid sample introduction, which is typical in ICP-MS analysis, involves a cumbersome dissolving process before measurement. In the proposed method, direct introduction of samples via an LA system achieves the rapid analysis of REEs.

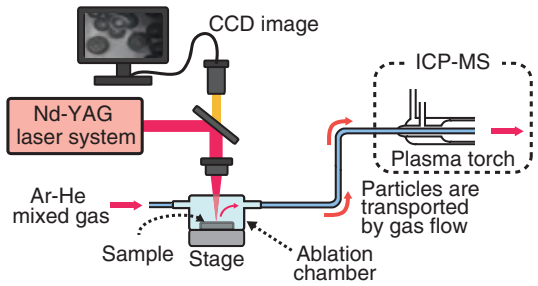

Fig.4-19 Basic principle of the LA system
Particles generated by ablating the sample surface are effectively transported to a plasma torch by an Ar-He mixed gas flow, which leads to the direct measurement of solid samples.

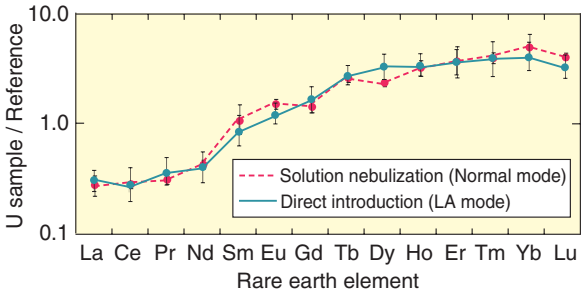

Fig.4-20 REE pattern obtained by laser ablation ICP-MS
The REE pattern obtained through LA-ICP-MS analysis of the U sample exhibited close agreement with that obtained through the nebulization ICP-MS of the REE-purified solution.

Rare earth elements (REEs) comprising Sc, Y, and 15 lanthanides behave as a coherent group over geological and industrial processes, showing a distinctive pattern unique to their origin. The REE patterns found in uranium (U) ores and their refined products can be a reliable indicator of the origin attribution of U. This is a remarkable property in terms of the regulation of nuclear materials. In this study, a rapid and reliable analytical technique based on inductively coupled plasma mass spectrometry (ICP-MS) combined with a solid sample introduction system was developed for obtaining REE patterns.

ICP-MS has been a promising technique for determination of ultratrace amounts of REEs. However, interferences caused by isobars and molecular ions that have the same mass-to-charge ratio as a target isotope can be a definite factor in misleading measured values. In the determination of REEs, barium (Ba) may cause interferences by forming several barium oxides (e.g., $^{135}Ba^{16}O$ to ^{151}Eu) within the plasma. The formation of such oxides is effectively attenuated by the direct introduction of a solid sample using laser ablation (LA) technology. Liquid sample introduction, which is typical in ICP-MS analysis, may induce the formation of oxides in the plasma. Ba in the sample solution can be combined with ^{16}O of H_2O molecules in an aqueous solution. In the developed method, ultratrace levels of the REE in a U-bearing sample solution (U standard solution) were adsorbed into cation-exchange resin particles to concentrate the REE into a solid phase and to remove U along with other coexisting elements. Then, the REEs adsorbed in the resin particles were directly measured with LA-ICP-MS, resulting in an efficient and interference-free measurement (Fig.4-18). In the LA mode, fine particles generated by evaporating the sample surface were efficiently transported by an Argon (Ar)-Helium (He) mixed gas flow (Fig.4-19). The REE pattern obtained through LA-ICP-MS analysis of the U-bearing sample agreed within uncertainty with that obtained through the conventional technique based on the nebulization of the REE-purified solution (Fig.4-20).

The developed method is applicable to the fingerprinting of nuclear materials, or nuclear forensic analysis, providing practical information for specifying interdicted nuclear materials.

Reference

Asai, S. et al., LA–ICP–MS of Rare Earth Elements Concentrated in Cation–Exchange Resin Particles for Origin Attribution of Uranium Ore Concentrate, Talanta, vol.135, 2015, p.41–49.

4–8 Revised Database for Spent Nuclear Fuel Reprocessing

— Handbook on Process and Chemistry of Nuclear Fuel Reprocessing, 3rd Edition —

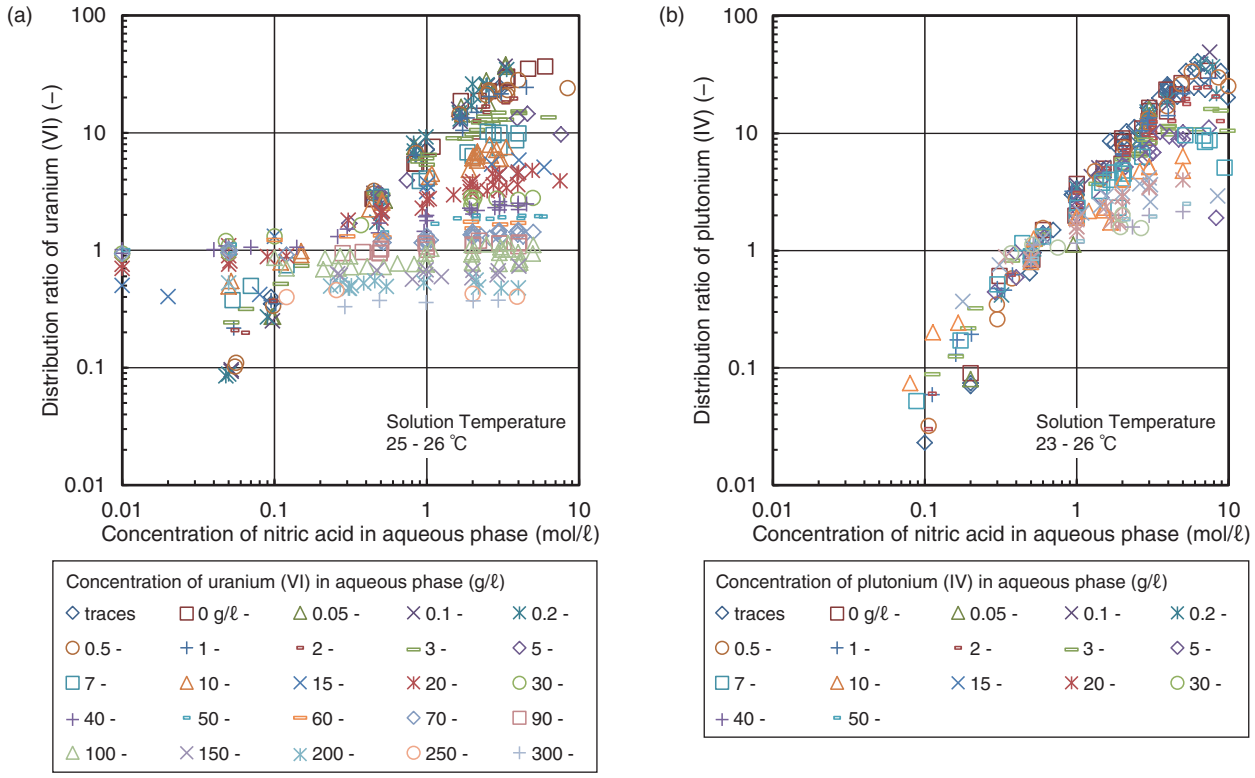

Fig.4-21 Summary of distribution ratios of (a) uranium (VI) and (b) plutonium (IV) in nitric acid/30vol% tributylphosphate-hydrocarbon diluent system
Distribution data of several important elements in reprocessing were arranged and visualized so as to easily understand their dependence on the concentration of nitric acid and metal elements.

PUREX is well-known as a reprocessing method for spent nuclear fuel discharged from nuclear power plants. In Rokkasho-mura, a large reprocessing plant is now being prepared to start commercial operation.

In the reprocessing of high burn-up fuel or spent mixed-oxides fuel, which is anticipated in the near future, large amounts of fission products and plutonium would complicate the process; therefore, we have to investigate the influences of several processes, such as fuel dissolution, solvent extraction, and high-level liquid waste (HLLW) treatment.

We published the 1st and 2nd editions of the “Handbook on Process and Chemistry of Nuclear Fuel Reprocessing” in 2001 and 2008, respectively. They included results from literature surveys and PUREX experiments conducted in the Nuclear Fuel Cycle Safety Engineering Research Facility (NUCEF) of JAEA. In March 2015, the 3rd edition was published, aiming at improved reliability and greater usefulness. On the editing committee, specialists in reprocessing from domestic universities, industry, and JAEA discussed the usefulness of this book, especially for students and young researchers and engineers.

In this edition, we have summarized more technical information from a careful literature survey and lessons learned from the recent nuclear accident; we have also included some properties of radioactive materials for the estimation of processes in the abnormal state.

In the opening section, an outline of PUREX is inserted as assistance to beginners. More information is also incorporated, for example, on the compositions of solid depositions, undissolved residue, and HLLW, as well as the volatility of some compounds and the flash points of organic solvents at high temperature, distribution ratios in solvent extraction of uranium (VI) and plutonium (IV) (Fig.4-21), and experimental results in fast reactor fuel reprocessing.

Huge technical knowledge and operational experiences in aqueous reprocessing have been accumulated in the world. We think it is important that they be transmitted steadily to the next generation for promoting the nuclear fuel cycle. It is expected that this handbook will be widely utilized for future research and development.

Reference

Committee of Handbook on Process and Chemistry of Nuclear Fuel Reprocessing, Handbook on Process and Chemistry of Nuclear Fuel Reprocessing 3rd Edition, JAEA-Review 2015-002, 2015, 726p. (in Japanese).

4–9 Improved Capability for Atmospheric Dispersion Simulation
— Enhancement of Prediction Performance of WSPEEDI-II for Middle-Range Scale Dispersion using Krypton-85 Measurement Data —

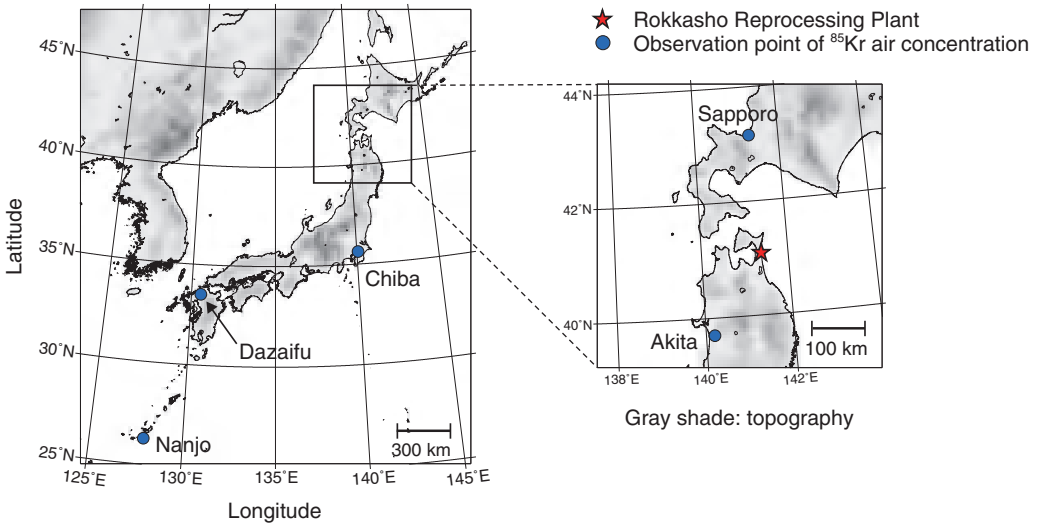

Fig.4-22 Calculation areas and observation points of air concentration of ^{85}Kr
Atmospheric dispersion simulations were conducted using the ^{85}Kr release data provided by Japan Nuclear Fuel Limited for the area including the whole of Japan (Left) and that around RRP (Right) with spatial resolutions of 18 and 6 km, respectively. Observation of the ^{85}Kr air concentrations was performed by the Japan Chemical Analysis Center.

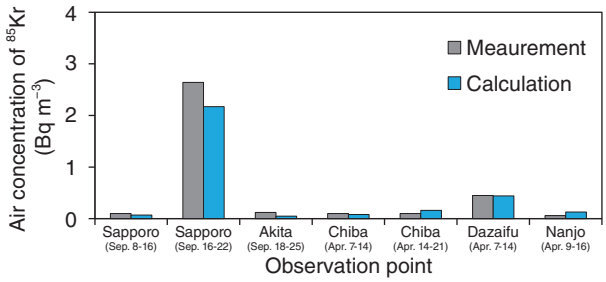

Fig.4-23 Simulation result of the air concentration of ^{85}Kr by WSPEEDI-II
Measured weekly mean surface air concentrations of ^{85}Kr were reproduced by calculation with the modified GFD. Observation periods in 2008 are listed in the brackets following the names of observation points. The measurements show the increases from the background levels.

When radioactive materials are discharged into the atmosphere due to nuclear accidents, atmospheric dispersion simulations are very important for the understanding of the distributions of released radioactive materials and planning of environmental monitoring and countermeasures for the radiation protection of the public. Simulations are conducted over a wide-range of areas from the immediate vicinities of accident sites to regions far distant from them, depending on the magnitudes of the accidents. Then, model parameters that can appropriately simulate various phenomena depending on the scale of the objective area are important for precise simulations. Diffusive effects due to wind turbulence are typically expressed by diffusion coefficients in atmospheric dispersion models. The horizontal diffusion coefficient by Gifford (1982) (hereafter, GFD) is usually used for long-range dispersion with a horizontal distance of several thousand km. However, there have been few verification studies of GFD for middle-range scale dispersions over distances of several hundred km.

In this study, we verified the performance of the second Worldwide version of System for Prediction of Environmental Emergency Dose Information (WSPEEDI-II) for middle-range scale dispersion by dispersion analysis of krypton-85 (^{85}Kr), which was released in test operations at the Rokkasho Reprocessing Plant (RRP) in Aomori Prefecture, Japan using GFD. Air concentrations of ^{85}Kr were observed at several sites in Japan to understand the background level (Fig.4-22). The observation detected the ^{85}Kr discharged from RRP at locations 200–2000 km away. Since ^{85}Kr is a nonreactive gas with a half-life of 10.76 years and the release point is known, the observation data are particularly useful for the verification of diffusion processes.

WSPEEDI-II reproduced weekly mean surface air concentrations of ^{85}Kr with errors ranging between 0.5 and 2 times as much as the measurements. However, from a sensitivity analysis of the horizontal grid distances (resolution) of the meteorological model ranging from 2 to 54 km (used for local- to global-scale simulations), it was found that as the simulated grid resolution became higher, the calculated concentrations became lower than the results using the 54 km resolution. It is believed that the concentrations around the distribution center were underestimated because diffusive effects explicitly represented by grid-resolved wind fields may have been considered redundantly by GFD when using meteorological fields with relatively high grid resolutions. On the basis of the sensitivity analysis, an empirical modification method for GFD according to the grid resolution was proposed. This method improved the reproducibility of concentrations in the middle-range scale, and the result showed the usefulness and validity of this method (Fig.4-23). Using the diffusion coefficients modified by this method, the problem of calculated concentrations varying depending on the selected grid-resolution was remedied, and dispersion simulations that are consistent from local- to global-scales became possible.

Reference

Terada, H. et al., Validation of a Lagrangian Atmospheric Dispersion Model Against Middle–Range Scale Measurements of ^{85}Kr Concentration in Japan, Journal of Nuclear Science and Technology, vol.50, issue 12, 2013, p.1198–1212.

4–10 Tracking Pollutants in the Pacific Ocean

— Drift Simulation of Tsunami Debris due to the Great East Japan Earthquake —

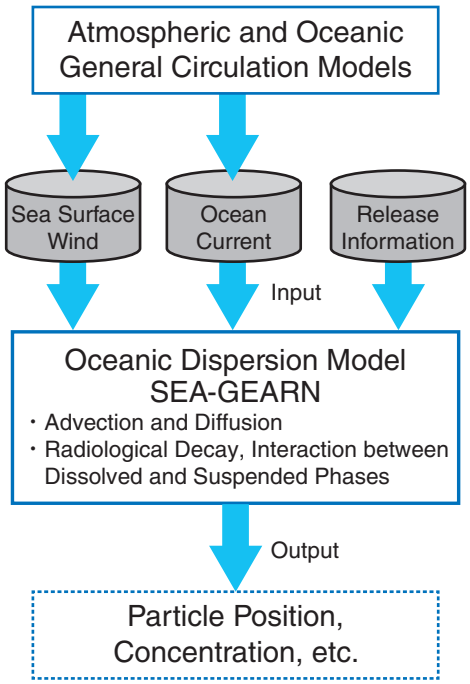

Fig.4-24 Schematic of SEA-GEARN
SEA-GEARN calculates advection and diffusion by ocean current and radiological decay by inputting data of sea surface wind and ocean currents that have been calculated by atmospheric and oceanic general circulation models. It outputs the positions of particles assumed to be radionuclides, tsunami debris, and the like, as well as the concentrations of radionuclides.

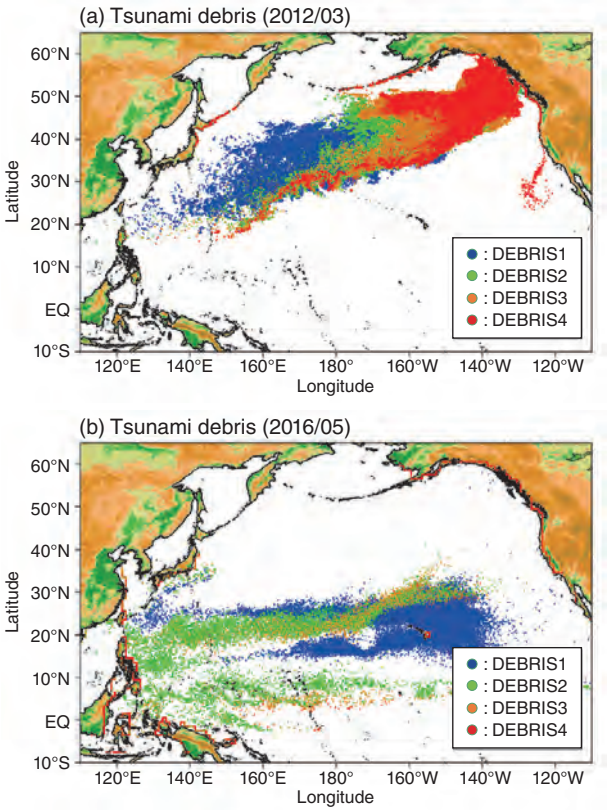

Fig.4-25 Distribution of tsunami debris in (a) March 2012 and (b) May 2016
DEBRIS 1 is fully submerged debris. The ratios of the volume above the sea surface to that below are 1:1, 2:1, and 4:1 for DEBRIS 2, 3, and 4, respectively.

We are developing an oceanic dispersion model called SEA-GEARN (Fig.4-24) to assess the effects of pollutants such as radionuclides on the marine environment. We implemented drift simulations of tsunami debris such as lumber and plastic products flushed out due to the tsunami accompanying the Great East Japan Earthquake using SEA-GEARN in cooperation with domestic institutes. Tsunami debris will drift in the Pacific Ocean for a long time, probably damaging marine ecosystems or the coastal environment. Therefore, understanding the distribution of tsunami debris is important to assess its effect on the marine environment and prevent marine pollution in advance.

The Japan Aerospace Exploration Agency analyzed satellite images obtained by an advanced land-observing satellite called Daichi, which enabled us to determine the initial release points and duration for the drift simulation. We implemented the hindcast simulation from March 2011 to September 2013 using sea surface wind and ocean current data calculated by an ocean data assimilation system, which synthesizes a model and observations, developed at the Meteorological Research Institute of the Japan Meteorological Agency. This was done to assess the past distribution of tsunami debris. The forecast simulation was further implemented from October 2013 to June 2016 with sea surface wind and ocean current data forecasted by the Japan Agency for Marine-Earth Science and Technology. Actual tsunami debris comprised various items such as lumber and plastic products. A part of the tsunami debris above the sea surface was directly driven by wind on the sea surface. Therefore, tsunami debris were divided into four types according to the ratio of the volume above the sea surface to that below in the drift simulation.

It was suggested that tsunami debris flushed out from the Tohoku district was mainly transported southeastward after the earthquake and then transported eastward by the Kuroshio Extension in the North Pacific (Fig.4-25(a)). The distribution of tsunami debris in the hindcast simulation well agreed with the shipboard sighting information compiled by the Japanese government. The hindcast simulation also demonstrated tsunami debris reported by the news such as a fishing boat seen off the Canadian coast in March 2012. According to the forecast simulation, it was suggested that tsunami debris off the west coast of the United States would be mainly transported southwestward and distributed in the southern North Pacific (Fig.4-25(b)). It was remarkable that tsunami debris would be concentrated around the Hawaiian Islands. In the future, we plan to refine the future distribution of tsunami debris by ensemble drift simulations with several different types of sea surface wind and ocean current data.

The present study was sponsored by the Ministry of the Environment.

Reference

Kawamura, H. et al., Drift Simulation of Tsunami Debris in the North Pacific, Global Environmental Research, vol.18, no.1, 2014, p.81–96.

4–11 Development of the Particle and Heavy Ion Transport Code System, PHITS
— Simulating the Motion of All Radiations in One Computational Code —

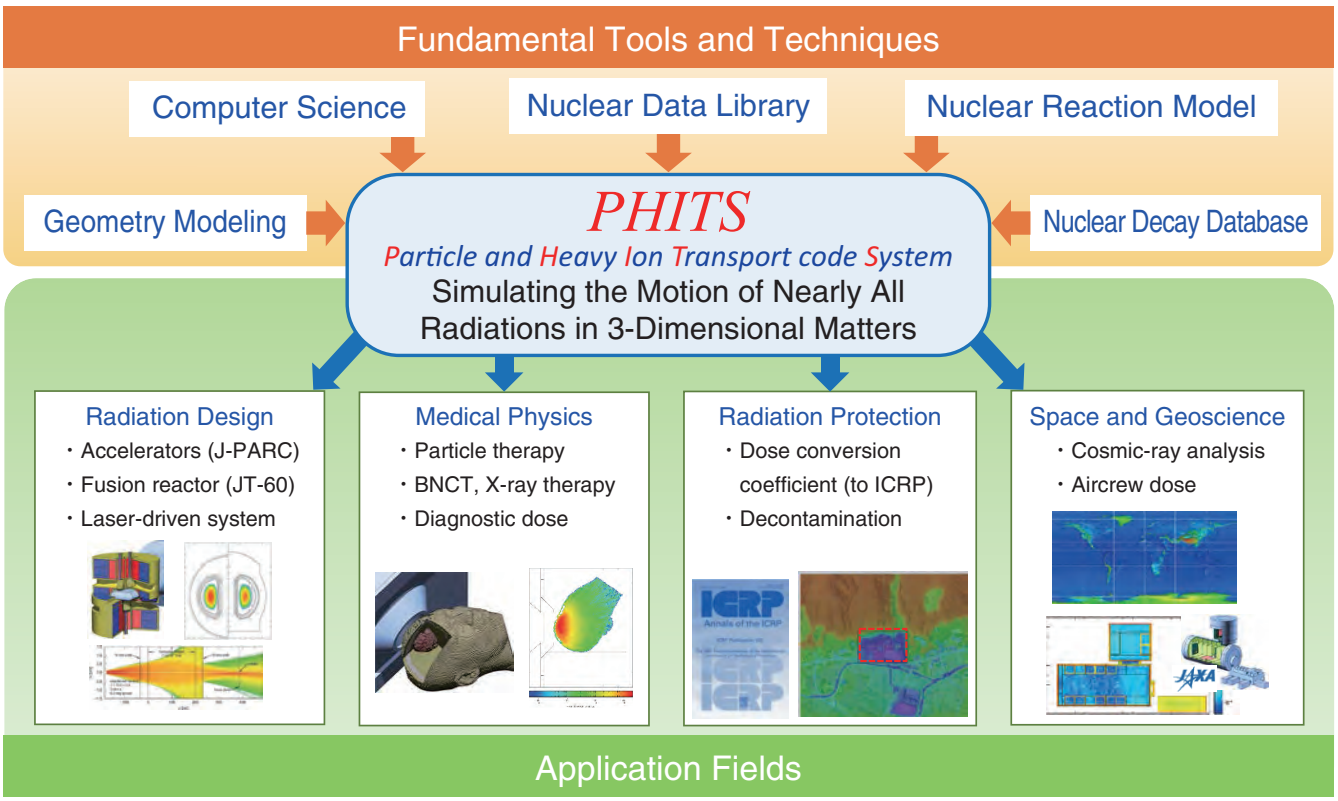

Fig.4-26 Overview and applications of the PHITS code

Radiations travel through matter in complicated ways by inducing ionization and nuclear reactions. Thus, it is very important to precisely simulate the motion of radiation when designing the shielding of nuclear reactors and accelerators as well as when planning treatment during radiation therapy. Several particle transport simulation codes have been developed in Japan, but they have been insufficient for use in various purposes because of their limited functions.

We therefore developed a new general purpose particle transport simulation code by combining and improving a number of related techniques and tools developed in Japan, under collaboration with various institutes (Fig.4-26). The code was designated as PHITS: the Particle and Heavy Ion Transport code System. The basic features of PHITS are as follows.

(1) PHITS can simulate the transport of nearly all radiations over a wide energy range, including low-energy neutrons and photons that are important for nuclear technology as well as high-energy protons and heavy ions that are important for accelerator design, medical physics, and space applications.
(2) PHITS contains high-reliability nuclear reaction models and nuclear data libraries that can well reproduce experimental data.
(3) PHITS has two kinds of parallel execution functions that can be utilized not only on super computers but also on conventional PCs such as Windows® and Mac PCs.
(4) PHITS is easy to setup and use owing to its semi-automatic installer and user-friendly interface. In addition, we have frequently organized PHITS tutorials, including that held in Paris in 2013 and have established a hospitable user-support system.

Owing to these features, PHITS has been used in various applications such as design of radiation facilities, medical physics, radiation protection research, and space and geosciences. The number of PHITS users has continuously increased and reached up to 1600 in Japan and a few hundred outside Japan within 5 years after its first release.

For more detailed information, please visit its website: http://phits.jaea.go.jp.

Reference

Sato, T. et al., Particle and Heavy Ion Transport Code System, PHITS, Version 2.52, Journal of Nuclear Science and Technology, vol.50, issue 9, 2013, p.913–923.

5 Quantum Beam Science Research

Quantum Beam Science and Technology Researches and Research Sites
— R&D using Quantum Beam Facilities and Fundamental Technologies —

"Quantum beam" is a generic term for neutron beams, ion beams, electron beams, high-intensity lasers, and synchrotron X-rays that are generated from accelerators, high-intensity laser facilities, and research reactors. Recently, quantum beam technology has been extensively developed, with the most advanced manufacturing and observations being conducted using highly controlled quantum beams.

There are several large quantum beam facilities such as Japan Proton Accelerator Research Complex (J-PARC), Takasaki Ion Accelerators for Advanced Radiation Application (TIARA), Japan Atomic Energy Agency (JAEA) Kansai Advanced Relativistic ENgineering (J-KAREN), Super Photon ring-8 GeV (SPring-8) beamlines, and Japan Research Reactor-3 (JRR-3) at JAEA. We have produced numerous results from these facilities. In this chapter, we introduce representative research results on "quantum beam" science and technology.

1. Development of Beam Technologies for Quantum Beam Facilities

(1) Technological Development at J-PARC

J-PARC comprises a series of three proton accelerators, namely, the LINear ACcelerator (LINAC), 3 GeV Rapid Cycling Synchrotron (RCS), and 50 GeV synchrotron, and three experimental facilities. The facilities include the Materials and Life Science Experimental Facility (MLF) for a wide range of research fields using neutron and/or muon beams, the Hadron Experimental Facility for nuclear and particle physics experiments using K-mesons and other particles, and the Neutrino Experimental Facility for the T2K particle physics experiment using neutrinos. All these experimental facilities are open to users from across the globe.

To realize operations with a 1 MW beam, the expected performance of LINAC and RCS needed to be improved by means of such as a beam current upgrade and beam loss reduction in FY 2014. At LINAC, the radio-frequency-driven negative hydrogen ion source and the Radio Frequency Quadrupole (RFQ) LINAC were replaced (Fig.5-1), resulting in the peak current being upgraded from 30 mA to 50 mA. In January, 2015, a 1 MW equivalent proton beam pulse was successfully accelerated at RCS and delivered to the neutron source target of MLF for the first time. At MLF, steady operation with injection of a 300 kW proton beam has been continued since the last fiscal year, and the beam power has been increased up to 400 kW since March, 2015. As for a suite of neutron instruments, the energy-resolved neutron imaging system, which has superior performance to the non-destructive inspection of materials, was made available for the user program.

Users conducted 422 experiments at 19 neutron and 2 muon beamlines for a wide range of research fields, including materials science, magnetism and strongly correlated electron systems, soft materials, fundamental physics, electronic properties of matter, and hydrogen in matter and general applications. In this chapter, outcomes from MLF (Topics 5-12, 5-13, and 5-14) are presented.

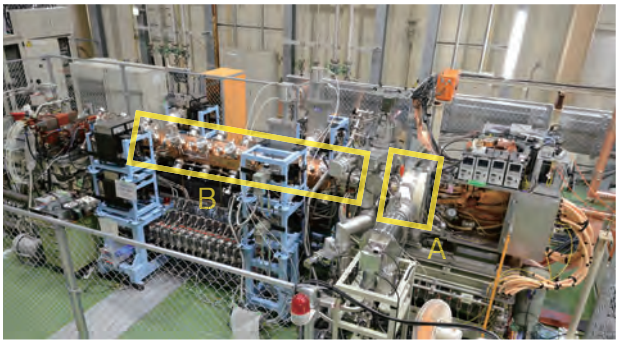

Fig.5-1 First acceleration stage of LINAC
Radio-frequency-driven negative hydrogen ion source (A) and Radio frequency quadrupole LINAC (B).

(2) Technological Development at TIARA

TIARA comprises four ion accelerators. Together with an electron accelerator and gamma-ray irradiation facilities, the TIARA accelerators are available to researchers in JAEA and other organizations for R&D activities on new functional and environmentally friendly materials, biotechnology, the radiation effects of materials, and quantum beam analysis. Practical technological developments currently in progress involve microbeam formation, single ion hits, techniques for large-area uniform irradiation, efficient beam transmission and acceleration (Fig.5-2 and Topic 5-15) at the cyclotron, three-dimensional in-air PIXE analysis, and a three-dimensional microfabrication technique at the electrostatic accelerators.

To make such advanced beams available to many researchers in a wide range of research and development fields, an emphasis was placed upon shortening the beam conditioning time in FY 2014. By developing methods to correct off-axis beam transport, it now takes about 1 h to form a uniform beam with an area of 10 × 10 cm^2, a process which formerly took 3 h. Now that the time required to conduct beam experiments has been drastically reduced, more and more users from not only JAEA but also from other organizations may participate in the R&D activities on new functional and environmentally friendly materials, biotechnology, and so forth.

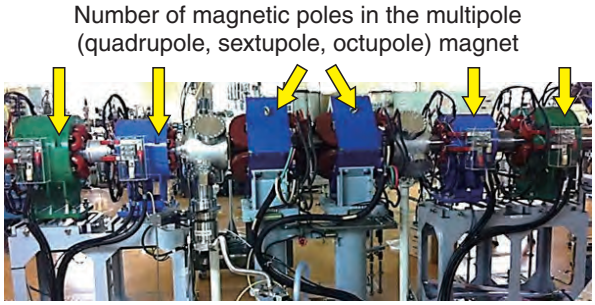

Fig.5-2 Multi-pole magnet system to enable large-area uniform irradiation in TIARA
Various types of multi-pole (quadrupole, sextupole, and octupole) magnets are installed to adjust the beam profile.

(3) Kansai Photon Science Institute

In the Kizu District, we are eagerly engaged in R&D activities concerning lasers. For instance, we are developing high-quality lasers and studying the use of electron beams, ion beams, and X-rays generated by high-intensity short-pulse lasers. FY 2014 marked the final stage of the upgrade of the J-KAREN laser (Fig.5-3), where the peak power was increased up to 1.2 PW with a 0.1 Hz repetition-rate to obtain a high-energy ion beam.

In the Harima District, we have been developing and improving a state-of-the-art analytical technique for expressing the functional and reaction mechanisms of materials. For this purpose, we employ four JAEA synchrotron radiation beamlines at SPring-8. These beamlines are also applied to nanotechnology, energy, and environmental studies, including a decontamination technique for revitalization at Fukushima.

Furthermore, external researchers are being supported as part of the Nanotechnology Platform Project entrusted to us by MEXT. Roughly 30% of all user times was provided for external use in FY 2014.

Fig.5-3 JAEA Kansai Advanced Relativistic ENgineering (J-KAREN) laser system
Upgraded components are shown in the area surrounded by dotted lines.

2. Advanced R&D on Quantum Beam Science and Technology

JAEA's abovementioned large quantum beam facilities have been employed in diverse science and technology fields.

By controlling the beam parameters, quantum beams can be used to probe atomic- or molecular-level information. Quantum beams can further investigate materials at nanometer scales (i.e., at the atomic or molecular level) because they interact with the material's constituent atoms to change their configuration, composition, and electronic state. In medical applications, these beams are used for radiotherapy, which focuses a beam onto cancer cells (Fig.5-4).

We have been developing new beam sources and enhancing the beam intensities. These improvements will help clarify unknown phenomena and extend the applicability of quantum beams. In addition, quantum beam "probes" have yielded notable results in materials science, environmental and energy research, medicine, and biotechnology, which are related to life sustainability and green innovations (Fig.5-5).

In this chapter, we introduce our recent research outcomes on advanced beam technology (Topics 5-1 and 5-2) and the application of quantum beams to the abovementioned fields (Topics 5-3, 5-4, 5-5, 5-6, 5-7, 5-8, 5-9, 5-10, 5-11, and 5-16).

We are also contributing to the recovery from the accident at the Fukushima Daiichi Nuclear Power Station of Tokyo Electric Power Company, Incorporated. For example, we have been developing advanced decontamination techniques utilizing quantum beams (Chapter 1, Topic 1-8).

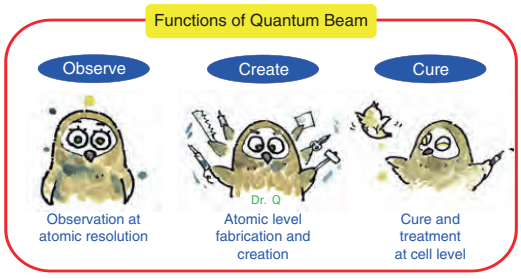

Fig.5-4 Characteristics of quantum beams

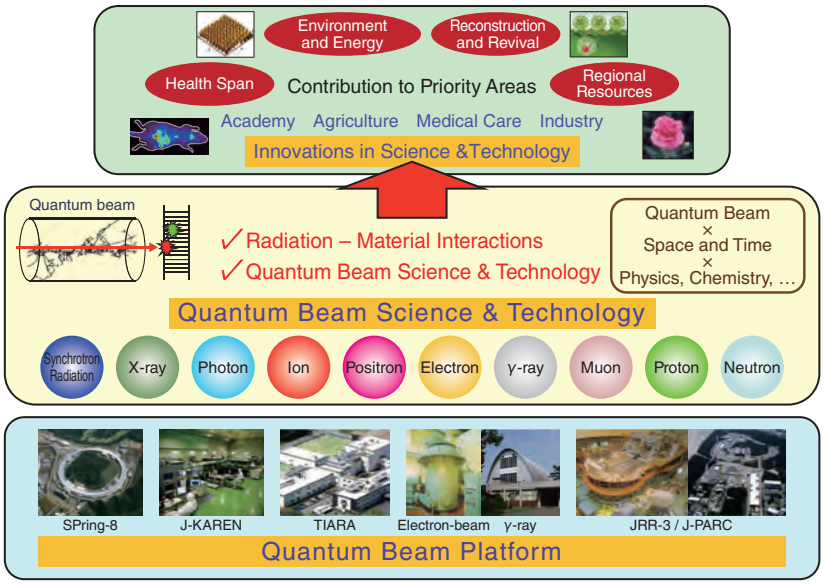

Fig.5-5 Quantum beam facilities and research system for quantum beam science and technology at JAEA

5–1 Instantaneous Generation and Acceleration of Fully-Stripped Fe Ions in GeV
— Toward the Application of the Laser-Driven Heavy Ion Accelerator —

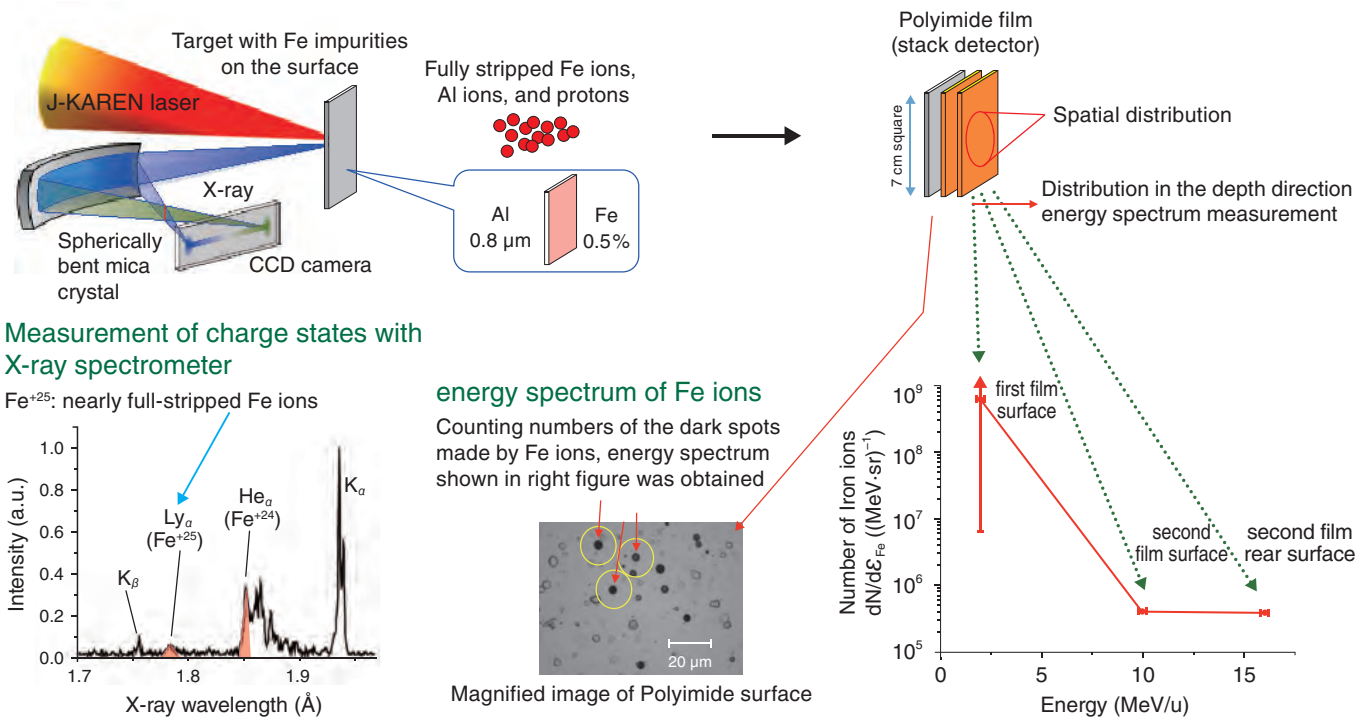

Fig.5-6 Experimental set-up and results of the highly charged Fe ion-acceleration
A J-KAREN laser with 200 TW laser power was irradiated onto a 0.8-μm-thick Al target with 0.5% Fe impurities. Observing the accelerated Fe ions with a Polyimide stack detector and an X-ray spectrometer, almost fully stripped Fe ions (Fe^{+25}) with 16 MeV/u were obtained.

A laser-driven ion acceleration scheme can provide an acceleration field with a much higher gradient than the conventional method.

At Kansai Photon Science Institute (KPSI), a J-KAREN laser system can provide strong laser pulses with a power of 10^{15} W. The intensity of such laser pulses can be as high as 10^{21} Wcm^{-2}, if focused on a ~1 μm focal spot. The electric field strength of the laser at the focal spot corresponds to ~100 TV/m. The atoms in the target material irradiated by such laser pulses are instantaneously highly charged. The electrons stripped away from those atoms are accelerated forward and away from the target. As a result, an extremely high-gradient acceleration field is established at the rear side of the target. The field can even efficiently ionize high-Z atoms and can simultaneously accelerate them toward high energy. This laser-driven ion acceleration scheme is more efficient for high-Z elements.

We have performed experiments using laser pulses with an energy of 8 J, duration of 35 fs (full width at half maximum, FWHM), wavelength of 0.8 μm, and typical contrast of 10^{10}. These pulses were focused onto a target with a peak intensity of 10^{21} Wcm^{-2}. The target was a 0.8-μm-thick aluminum (Al) foil. On its surface, the foil had impurities, mainly comprising iron (Fe). In terms of atomic number density, the Fe-to-Al content ratio was 0.5%. The Fe ions are detectable by Polyimide film, whose response was calibrated in advance with the ion beam from a conventional accelerator. After the laser shot, the Polyimide films were etched to reveal the pits, corresponding to the Polyimide breakdown produced by individual ions. We counted all the pits that originated under Fe ion bombardments and obtained the energy spectrum of the Fe, as shown in Fig.5-6. Based on the depth of the pits inside the stack detector, the ion energy was calculated using the PHITS code. The calculation shows that more than 10^6 Fe ions per shot were extracted from the target with energies from 0.56 to 0.89 GeV. The ion energy surpassed previous experimental results.

The charge state of Fe ions can be inferred from X-ray spectra, recorded by a focusing spectrometer with spatial resolution (FSSR) that is equipped with a spherically bent mica crystal and a back-illuminated CCD camera. The resulting X-ray spectrum reveals Fe^{+25} carrying only one electron and Fe^{+24} carrying two electrons, as shown in Fig.5-6.

We demonstrated the acceleration of GeV highly charged Fe ions from a micron-thick Al foil with an Fe impurity on its surface using a femtosecond 200 TW laser having an 8 J pulse energy.

The usage of laser-driven ion acceleration schemes in existing radio-isotope facilities and heavy ion accelerators can provide a complementary radio isotope source to facilitate measurements of the properties of hitherto inaccessible exotic nuclei.

Reference

Nishiuchi, M. et al., Acceleration of Highly Charged GeV Fe Ions from a Low–Z Substrate by Intense Femtosecond Laser, Physics of Plasmas, vol.22, issue 3, 2015, p.033107–1–033107–8.

5–2 Transmission Nuclear Resonance Fluorescence Assay of a Spent Fuel Canister
— Demonstrating Feasibility in a Realistic Scenario —

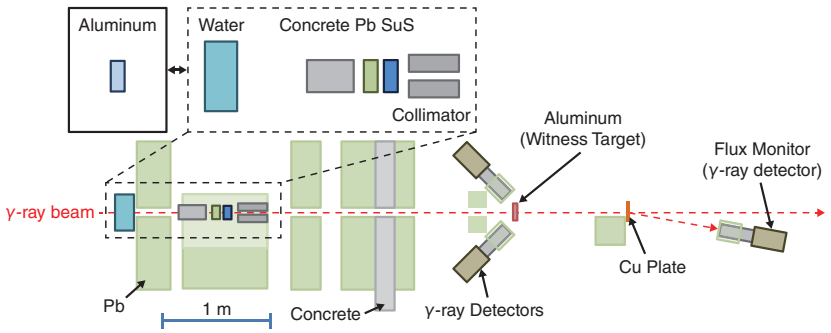

Fig.5-7 Diagram of the TMI-2 transmission nuclear resonance fluorescence experiment
In the experiment, the beam first traversed water, concrete, lead, and stainless steel absorption targets, and then continued to the aluminum witness target, where scattered NRF γ-rays were measured by four detectors. The γ-ray beam flux was determined by measuring the Compton scattering off of a Cu plate. A measurement was also done by changing the absorption target to a single aluminum target.

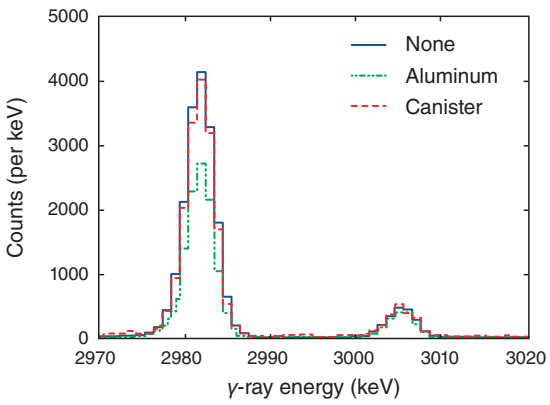

Fig.5-8 ^{27}Al nuclear resonance fluorescence peaks
The NRF peak areas in ^{27}Al measured at the witness station decrease in proportion to the amount of aluminum in the absorption target.

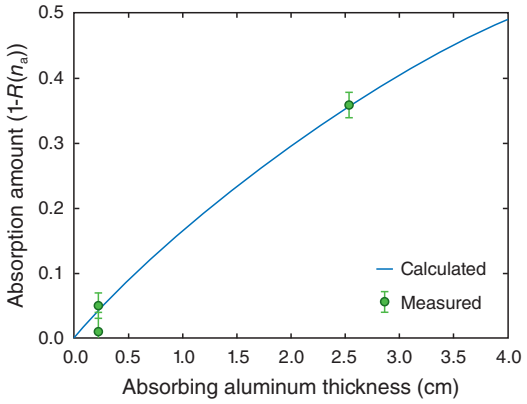

Fig.5-9 Absorption amount for the 2982 keV state
The 2982 keV state's calculated (——) and measured (●) absorption amounts (1-$R(n_a)$) for the following absorbers: canister, concrete (both 0.2 cm aluminum thickness), and aluminum (2.5 cm).

Transmission nuclear resonance fluorescence (NRF) is a promising method for precision non-destructive assay (NDA) of ^{239}Pu in spent fuel stored inside a canister. This method may be needed to assay the melted fuel from the TEPCO's Fukushima Daiichi NPS if the fuel were immediately placed in such a canister, an action that would minimize the possibility of future re-contamination. The Three Mile Island Unit 2 (TMI-2) canister, which was used to store the melted fuel from the Three Mile Island NPS, is one possible candidate. To demonstrate the feasibility of using transmission NRF to assay material inside of a TMI-2 canister, an experiment was conducted at the HIγS facility at Duke University in North Carolina, USA (Fig.5-7).

With transmission NRF, the decrease in NRF scattering from a ^{239}Pu witness target (normalized by flux), or, in other words, the absorption amount, $R(n_a)$, is proportional to the amount of ^{239}Pu through which the γ-ray beam is transmitted. This proportionality is guaranteed because of the resonant absorption nature of NRF. In the demonstration experiment, ^{27}Al was used in place of ^{239}Pu because of their similar NRF properties. The absorption amounts due to aluminum in a simulant TMI-2 canister and in other absorption targets were measured at a γ-ray energy of 2980 keV.

The flux normalized NRF spectra displayed resonant absorption (Fig.5-8), verifying assay feasibility. The measured absorption amount in each case was consistent with the expected absorption amount (Fig.5-9). This agreement demonstrates that overlapping resonances from competing isotopes in the TMI-2 canister should not interfere with the assay.

Reference

Angell, C. T. et al., Demonstration of a Transmission Nuclear Resonance Fluorescence Measurement for a Realistic Radioactive Waste Canister Scenario, Nuclear Instruments and Methods in Physics Research B, vol.347, 2015, p.11–19.

5–3 Extraction of Atomic-Level Magnetism using Synchrotron Radiation

— Element-Specific Magnetization Measurements by Soft X-ray Magnetic Circular Dichroism —

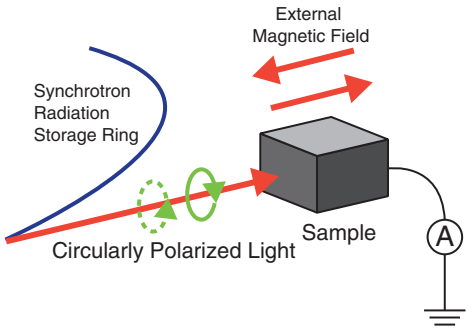

Fig.5-10 Schematic of XMCD measurements
The sample is magnetized by an external magnetic field. The left- or right-polarized light irradiates the samples along the directions parallel and antiparallel to the magnetization of the sample. The XMCD is defined as the difference between absorption coefficients of the left- and right-polarized light.

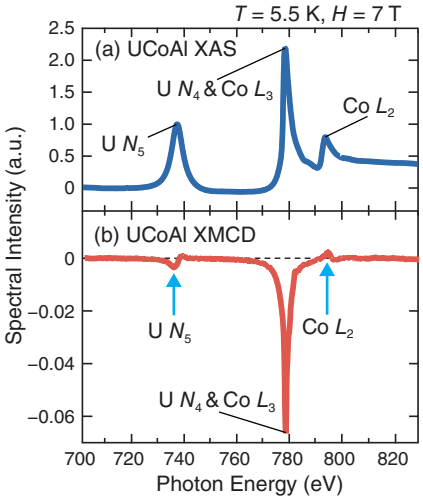

Fig.5-11 Experimental spectra of UCoAl at the U 4d-5f ($N_{4,5}$) and Co 2p-3d ($L_{2,3}$) absorption edges
(a) XAS spectrum. (b) XMCD spectrum. These spectra were taken at 5.5 K and 7 T. See text below for →.

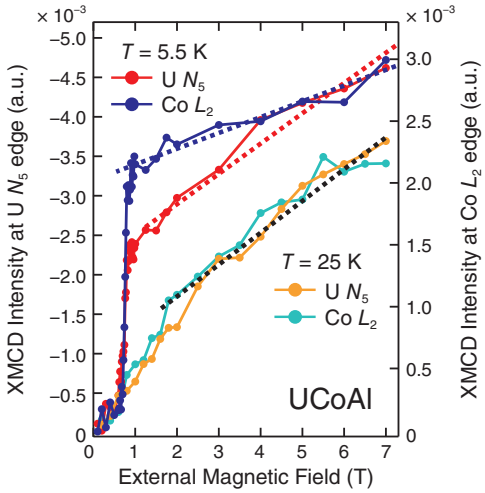

Fig.5-12 H-dependence of the XMCD intensity at the U and Co sites
These plots indicate the H-dependence of the magnetic moments at each site (→ in Fig.5-11(b)). The temperature of the sample was maintained at 5.5 K and 25 K.

Magnetism is derived from magnetic elements such as transition metal, rare-earth, and actinide elements. It is difficult to utilize actinide elements as practical devices due to radioactivity; however, actinide compounds show a variety of magnetic properties that are very attractive in the solid-state physics.

UCoAl is composed by two magnetic elements (uranium (U) and cobalt (Co)) and a nonmagnetic element (aluminum (Al)). The compound shows a metamagnetic transition (MT) from paramagnetic to ferromagnetic states at low temperature (T) when an external magnetic field (H) is applied. To understand the mechanism of the MT, grasping the magnetic behavior at the U and Co sites separately is important.

X-ray magnetic circular dichroism (XMCD) is defined as the difference in the X-ray absorption (XAS) coefficients for left and right circularly polarized light (Fig.5-10). In principle, XMCD is an element- and electronic-orbital-specific magnetic probe. In addition, the XMCD intensity is proportional to the magnitude of the magnetic moment at a target site.

Single crystals of UCoAl were grown in Advanced Science Research Center. The XMCD experiments were conducted at beamline BL23SU of SPring-8. Fig.5-11 shows XAS and XMCD spectra at the U 4d-5f ($N_{4,5}$) and Co 2p-3d ($L_{2,3}$) absorption edges. Since the peaks at the U N_4 and Co L_3 edges overlap each other, the magnetic information from the U and Co sites is mixed in this peak. We can separately extract the magnetic information at the U and Co sites from the peaks at 735 eV (U N_5) and 795 eV (Co L_2), respectively (→ in Fig.5-11(b)).

Fig.5-12 shows the H-dependence of the XMCD intensity at the U and Co sites measured at 5.5 K and 25 K. At 25 K, similar H-dependence is observed at the both sites (▬▬). At 5.5 K, MT is clearly observed at 0.7 T. Then, above 0.7 T, the increase ratio (slope) of the magnetic moment against H at the Co site (▬▬) becomes smaller than that at the U site (▬▬). In other words, the slope at the Co site shows stronger T-dependence than that at the U site. Although it has been believed until now that the magnetic properties of UCoAl are dominated by the U site, the present results suggest that the contribution of the Co site plays an important role in the magnetic behavior of this compound. The element-specific magnetic information from the XMCD experiment is valuable for understanding the mechanism of ferromagnetism in U compounds.

Reference

Takeda, Y. et al., Separation of Magnetic Properties at Uranium and Cobalt Sites in UCoAl using Soft X–Ray Magnetic Circular Dichroism, Physical Review B, vol.88, issue 7, 2013, p.075108–1–075108–6.

5–4 Electron Dynamics Unveiled by Combined Use of Three Quantum Beams

— An Inelastic Scattering Study of Spin and Charge Excitations in Superconducting Cuprates —

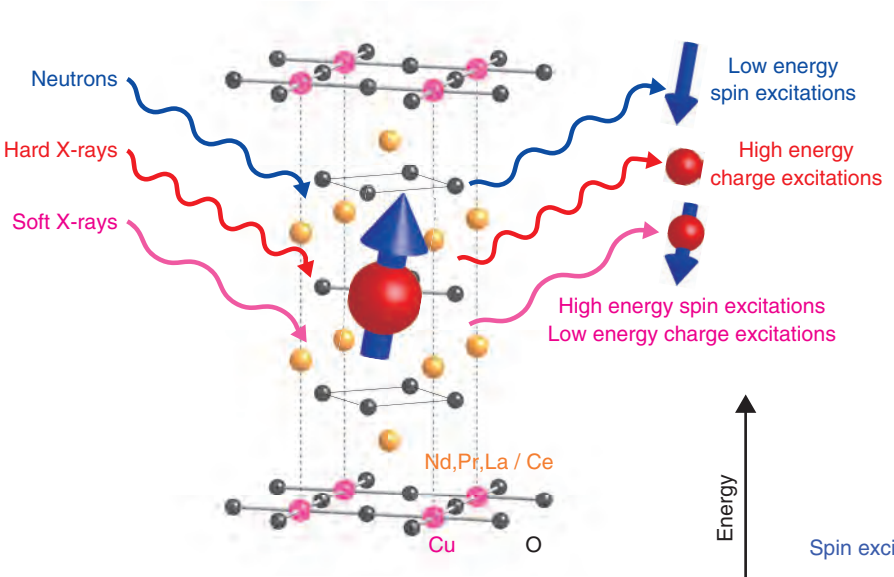

Fig.5-13 Role of quantum beams for measuring electron dynamics
Inelastic scattering of three quantum beams was used to observe the charge (●) and spin (➡) excitations of an electron. The background figure shows the crystal structure of the electron-doped copper oxides superconductor $(Nd,Pr,La)_{2-x}Ce_xCuO_4$ studied in this work.

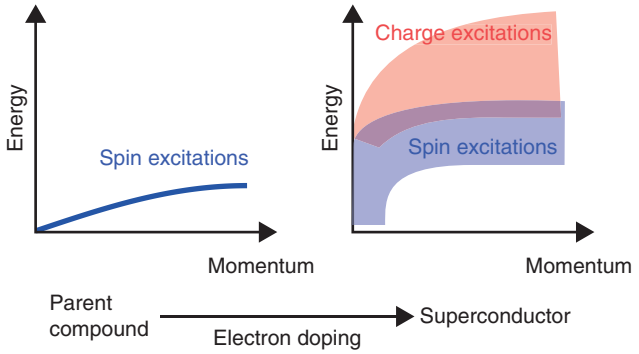

Fig.5-14 Schematic of the experimental results
Spin excitations are observed in the parent compound (left). In the electron-doped superconductor, spin excitations shift to higher energies, accompanied by a broadening of the width. In addition, charge excitations appear above the spin excitations (right).

Superconducting cuprates have the highest transition temperature of superconductivity found so far, and they have attracted great interest since their discovery more than a quarter century ago. The parent compound of superconducting cuprates is an antiferromagnetic insulator, where the up and down spins of an electron align alternatively. Superconductivity occurs when either electrons or holes are doped to the parent compound as mobile charge carriers. Therefore, doping evolution of spin and charge excitations should be clarified for a definitive understanding of the electron dynamics in cuprates, and the differences or similarities between electron- and hole-doped compounds have been a central issue in the study of superconducting cuprates.

As shown in Fig.5-13, we utilized three quantum beams (neutrons at J-PARC, soft X-rays at the ESRF, and hard X-rays at SPring-8) for inelastic scattering experiments in this study. We observed spin and charge excitations in a wide energy-momentum space and comprehensively clarified the electron dynamics of the electron-doped superconducting cuprate $(Nd,Pr,La)_{2-x}Ce_xCuO_4$. Fig.5-14 shows the experimental result schematically. In the parent compound, spin excitations with sinusoidal dispersion were observed and ascribed to the spin-wave in the antiferromagnetic insulator. Charge excitations were missing because the material possesses insulating character. When electrons were doped, the spin excitations shifted to higher energy and their peak width broadened. Such doping evolution of the spin excitations exhibited a striking contrast to the hole-doped cuprates, where the spectral distribution of the spin excitations also broadened but kept its energy position almost unchanged upon doping. Furthermore, in the electron-doped compound, we found charge excitations above the spin excitations. The charge excitations had been theoretically predicted, and the spectral weights of the spin and charge excitations partially overlapped with each other in the same energy region. The high-energy shift of the spin excitations and their mixture with the charge excitations indicate that the electron dynamics of the electron-doped cuprates had a highly itinerant character.

These findings impose constraints on theoretical models, and an adequate description of electronic excitations in electron- and hole-doped cuprates is a prerequisite for the complete understanding of the superconductivity. Incidentally, our work is the first to demonstrate that the complementary use of X-rays and neutrons is very effective in inelastic scattering for studying electron dynamics.

Reference

Ishii, K. et al., High–Energy Spin and Charge Excitations in Electron–Doped Copper Oxide Superconductors, Nature Communications, vol.5, 2014, p.3714–1–3714–8.

5–5 Elucidation of the Site-Occupancy of Hydrogen Atoms in Iron
— In situ Neutron Diffraction under High Pressure and High Temperature —

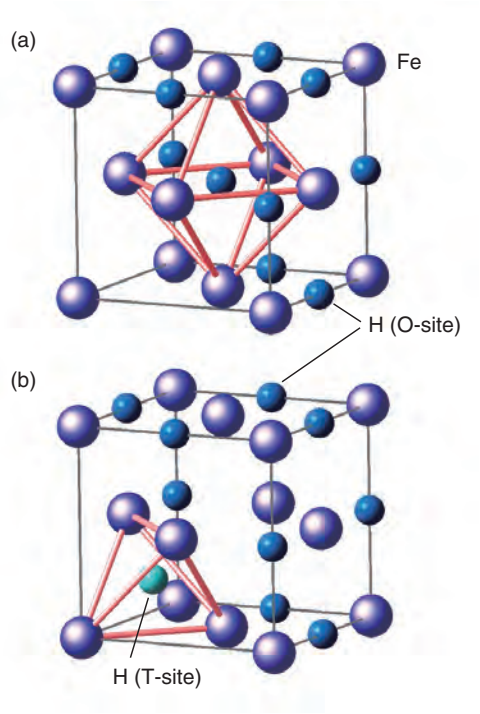

Fig.5-15 Structural models of FeD_x with an fcc metal lattice
The H atoms are accommodated in (a) the only O-site and (b) both the O- and T-sites. Frames colored in red show typical T- and O-sites.

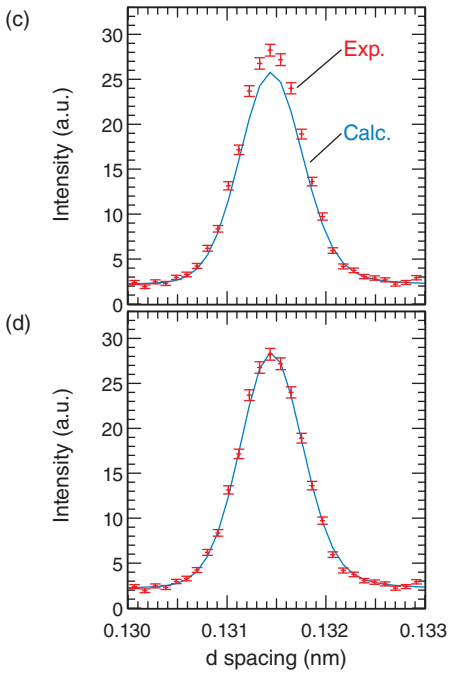

Fig.5-16 *In situ* neutron diffraction profile at 988 K, 6.3 GPa
A typical diffraction peak is shown. Red crosses are the experimental results; the cyan curve is the fitting result using the fcc structural model with the D atoms occupying (c) only the O-site and (d) both the O- and T-sites.

The hydrogen (H) occupation state in a metal lattice provides important information concerning some properties of metal hydrides, such as their stability. It is well-known that slightly dissolved H atoms induce changes in the mechanical properties of a metal. In addition, the crystal structure and physical properties are changed by high concentrations of H atoms in a metal lattice. The high H-concentration state in an iron (Fe) metal lattice is realized only at a high H_2 pressure of several GPa. Hence, it is difficult to experimentally determine the H-occupation state. In this study, we have investigated the H-occupation state of a face-centered cubic (fcc) iron deuteride (FeD_x) using *in situ* neutron diffraction measurement.

The high-pressure neutron diffractometer (PLANET) constructed at the Materials and Life Science Experimental Facility in J-PARC enables us to perform *in situ* neutron diffraction experiments at a pressure of several GPa and temperature of several hundred K. Based on the high-pressure reaction cell for the *in situ* synchrotron radiation X-ray diffraction experiment, we developed such a device for the *in situ* neutron diffraction experiment. The neutron diffraction profile of the deuteride is generally suitable for neutron structural analysis rather than that of the hydride; hence, we performed the *in situ* neutron diffraction experiment on the formation process of FeD_x instead of FeH_x.

At high pressure and high temperature, the Fe metal exhibited fcc structure, which has two interstitial sites available for accommodating H atoms: octahedral (O) and tetrahedral (T) sites (Fig.5-15). We succeeded in observing the formation of fcc-FeD_x. It is believed that D atoms occupy only the O-sites in the fcc-FeD_x; however, the refinement of the neutron-diffraction profile measured at 988 K and 6.3 GPa showed a misfit for some reflection peaks (Fig.5-16(c)). Hence, another structural model was applied for the analysis; the D atoms were accommodated in both the O- and T-sites. Using this model, the profile was well-reproduced and the refined occupancies of the D atoms in the O- and T-sites were 0.532(9) and 0.056(5), respectively (Fig.5-16(d)). We discovered that the D atoms slightly occupied the T-sites of the fcc-Fe. This result provides important information for understanding certain properties of Fe infused with dissolved H atoms.

This study was partly supported by Japan Society for the Promotion of Science (JSPS) KAKENHI Grant-in-Aid for Scientific Research (A) (No.24241032).

Reference

Machida, A. et al., Site Occupancy of Interstitial Deuterium Atoms in Face–Centered Cubic Iron, Nature Communications, vol.5, 2014, p.5063–1–5063–6.

5–6 Remarkably High Fuel Cell Performance of Graft-Type Polymer Electrolyte Membranes
— Origin of High Proton Conductivity Revealed by Hierarchical Structure Analysis —

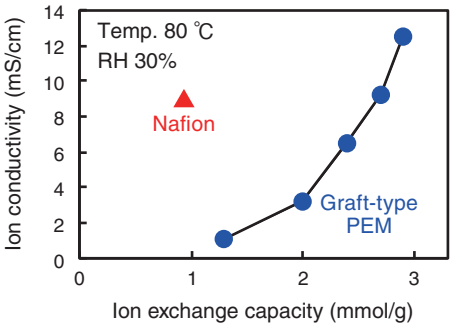

Fig.5-17 Ion conductivity of graft-type PEMs
The ion conductivity of graft-type PEMs increased with the ion-exchange capacity (IEC) and reached a maximum value of 13 mS/cm at an IEC of 2.9 mmol/g.

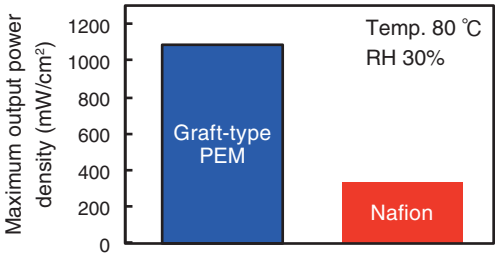

Fig.5-18 Performance of fuel cells using graft-type PEMs
A fuel cell using graft-type PEMs exhibited a maximum output power density of 1085 mW/cm^2, which is about three times higher than that of Nafion.

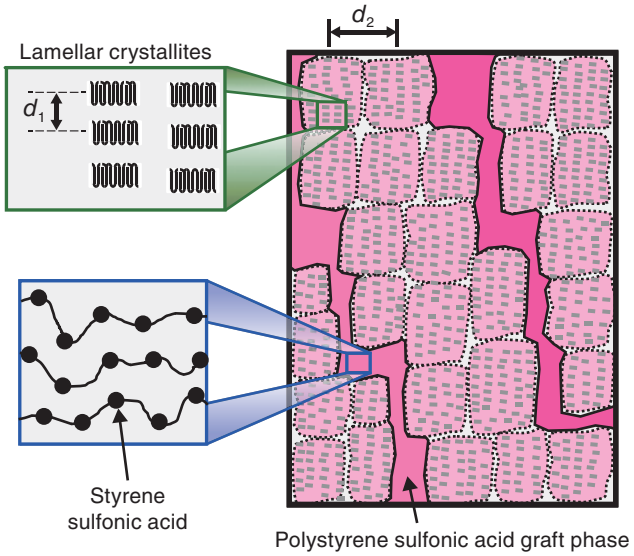

Fig.5-19 Hierarchical structure of the graft-type PEM
The lamellar spacing in the ETFE crystals (d_1) and the spacing between the crystalline phases (d_2) were measured by the SAXS method. It was found that the proton-conductive polystyrene sulfonic acid graft phases were formed in the interstitial regions between the crystallites. This would enhance the proton conductivity, thereby increasing the output power density of the fuel cell even under high temperature and low RH conditions.

Polymer electrolyte fuel cells (PEFCs) are expected to be the next generation of power sources for vehicles. The vital component of PEFC is the proton-conductive polymer electrolyte membranes (PEMs). In recent years, PEMs with high proton conductivity under high temperature and low relative humidity (RH) conditions have been required. Our group has developed PEMs using a radiation-induced grafting method. The main advantage of this method is to control the ion exchange capacity (IEC) of the PEMs by changing the grafting condition.

The PEMs were prepared by the radiation-induced grafting of styrene into ethylene-*co*-tetrafluoroethylene (ETFE) films and subsequent sulfonation. At 80 °C under 30%RH, the proton conductivity of the graft-type PEMs increased with IEC and reached a maximum value of 13 mS/cm (Fig.5-17). This is far higher than the conductivity of Nafion® 212, which is currently the most representative PEM for PEFC.

The PEFC was fabricated using the graft-type PEM with an IEC of 2.4 mmol/g. Even at 80 °C under 30%RH, the maximum output power density was 1085 mW/cm^2, which was three times higher than the case of Nafion (Fig.5-18).

To examine the origin of this high PEFC performance, the hierarchical structure of the graft-type PEMs was investigated by a small-angle X-ray-scattering (SAXS) method. The obtained SAXS profile showed two characteristic peaks at correlation distances of d_1 = 19–29 nm and d_2 = 225–300 nm. The former and latter peaks probably correspond to the lamellar spacing in the ETFE crystals and the spacing between the crystallites, respectively (Fig.5-19). The d_2 value increased with IEC but decreased in the IEC range above 2.4 mmol/g. This result could have been caused by the phase separation phenomenon in the PEM. As shown in Fig.5-19, in high-IEC PEMs, the polystyrene sulfonic acid (PSSA) graft phases were likely formed in the interstitial regions between the crystallites. By phase separation from the PSSA grafts, the crystallites would gather with each other, leading to the reduction of d_2. The graft phases between the crystallites functioned as an ion channel, enhancing the proton conductivity even under high temperature and low RH conditions.

Reference
Tran, D. T., Sawada, S. et al., Hierarchical Structure–Property Relationships in Graft–Type Fluorinated Polymer Electrolyte Membranes using Small– and Ultrasmall–Angle X–Ray Scattering Analysis, Macromolecules, vol.47, issue 7, 2014, p.2373–2383.

5–7 Observation of Residual Stresses in Structural Steel by X-ray and Neutron Diffraction
— Contribution to the Reliability Improvement of Mechanical Components and Structures —

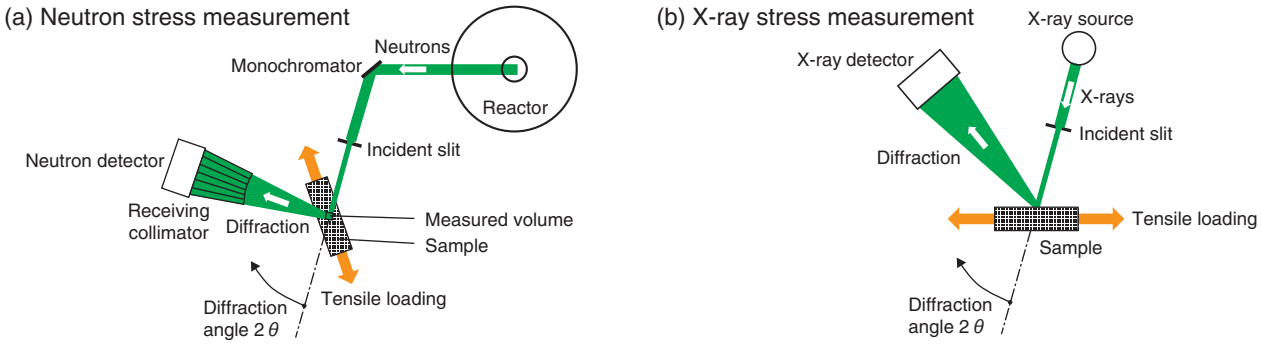

Fig.5-20 Experimental set-up for residual stress measurement under tensile loading
(a) Neutron beams irradiate the sample and are detected by a neutron detector. Residual stress is determined from the measured diffraction angle, 2θ. The measured volume is defined by an incident slit and a receiving radial collimator. The sample position is scanned step-by-step, and then, 3D-distributions of residual stress in the sample are obtained.
(b) The principle of X-ray stress measurement is the same as that with neutrons; however, X-rays diffract in the surface layer; therefore, the surface stresses are measured by X-rays.

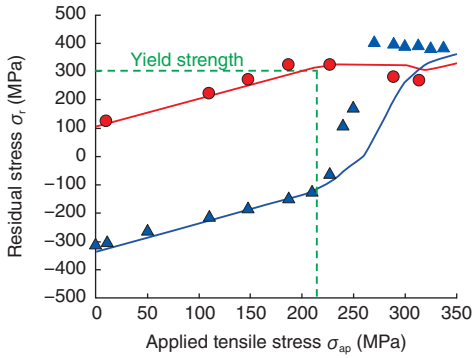

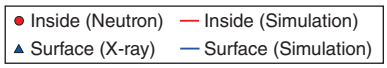

Fig.5-21 Relaxation behaviors of residual stress under tensile loading
The surface and interior residual stresses of the peened sample were measured using X-ray and neutron diffraction, respectively, under tensile loading. Computer simulations by a finite element method were also performed. The interior residual stress reaches the yield strength under an applied load of about 220 MPa. Redistribution of the residual stress is caused by the yielding. This results in the relaxation of surface compressive residual stress.

Compressive residual stresses can prevent "cracking", which is a typical fracture mode of mechanical components and structures caused by fatigue and stress corrosion. The compressive residual stress is introduced in the surface layer of components by surface treatment techniques such as peening and low-plasticity varnishing. However, the compressive residual stress may be relaxed due to external mechanical and/or thermal loadings to which the component in service is subjected. If relaxation occurs, the cracking-prevention effects are reduced and the risk of accidental failure of the component is increased. Therefore, understanding the residual stress relaxation process is quite important for evaluating the strength reliability of mechanical components and structures.

Residual stresses in the surface are measured by an X-ray diffraction method. If we use neutrons instead of X-rays on the diffraction method, residual stresses deep inside the materials can be measured to a depth of several centimeters because of the quite large penetration depth of neutrons. Therefore, the complementary use of neutron and X-ray diffraction can provide decisive evidence for understanding the residual stress relaxation process.

Fig.5-20 shows the setup for neutron stress measurements at JAEA's JRR-3 research reactor. Compressive residual stresses were introduced on a steel sample by a peening technique. Tensile loads were applied to the sample step-by-step on the diffractometer. The measured residual stress behaviors are shown in Fig.5-21. Both surface and interior residual stresses increased with the applied tensile stress. When the applied stress was about 220 MPa, the interior residual stress (● plots) reached the yield strength of the sample and the relaxation of the surface compressive residual stress (▲ plots) started. This fact means that the relaxation of the surface compressive residual stress under tensile loading was caused by yielding inside the sample. Therefore, the surface compressive residual stress relaxation started prior to the plastic deformation of the surface under tensile loading.

As a next step of this study, we have been investigating compressive residual stress relaxation behaviors due to thermal loading. The strength reliability and performance of mechanical components and structures are expected to be improved by using this information in the residual stress relaxation.

This study was partly supported by Japan Society for the Promotion of Science (JSPS) KAKENHI Grant-in-Aid Scientific Research (B) (No.23360061).

Reference

Akita, K. et al., Relaxation Behavior of Laser–Peening Residual Stress under Tensile Loading Investigated by X–Ray and Neutron Diffraction, Mechanical Engineering Journal, vol.1, no.4, 2014, p.14–00183–1–14–00183–8.

5–8 Understanding the Mechanism behind Gene Expression by Flexibility in DNA Structure

— Observation of Base-Sequence-Dependent DNA Dynamics by Quasi-Elastic Neutron Scattering —

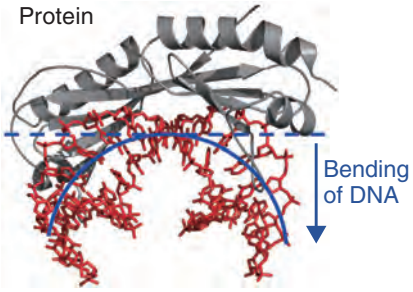

Fig.5-22 Bending of DNA by protein binding
The dotted line indicates the stable DNA conformation, but this conformation accommodates bending depending on base sequences.

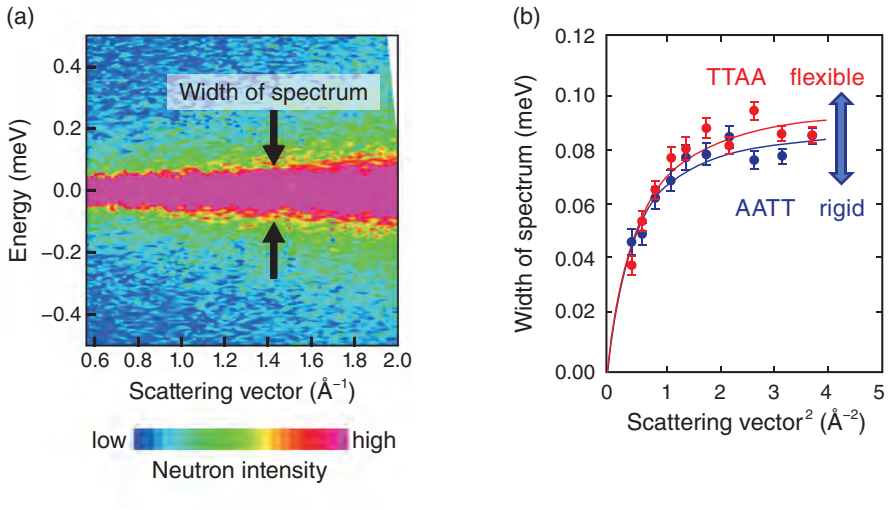

Fig.5-23 (a) Quasi-elastic neutron spectrum of DNA and (b) width of spectrum
(a) Neutron quasi-elastic scattering spectrum as a function of scattering vector and energy. (b) By analyzing the width of the spectrum, we understand the softness of the molecules.

The genomes (DNA sequences) of many organisms have been obtained, and a research base for analyzing and predicting biological function from a genome has been established. However, during the process of gene expression, amino acids and bases interact with each other to form a complex tertiary structure of protein and DNA, and a clear correspondence between gene sequence and biological function cannot necessarily be seen. Recent studies have shown that not only is direct interaction between protein and DNA (known as “direct recognition”) important for the information contained with a genome but also is “indirect recognition”, which is an easy transformation of the sequence-dependent DNA structure (Fig.5-22). Because analysis of fluctuations in the sequence-dependent DNA structure under indirect recognition is important, it is necessary to experimentally demonstrate that the dynamics of DNA can be observed directly by experiment.

In this study, we performed quasi-elastic neutron scattering experiments using the AMATERAS instrument at J-PARC/MLF to study the dynamics of two kinds of DNA sequences: 5’CGCGAATTCGCG3’ (AATT) and 5’CGCGTTAACGCG3’(TTAA). These sequences were predicted to be rigid and flexible, respectively, by analysis of a systematic molecular dynamics simulation. We successfully acquired the neutron spectrum to the required precision (Fig.5-23). Having analyzed the quasi-elastic neutron scattering data in detail, it was found that the width of the spectrum was wider with TTAA than with AATT. Thus, this width constitutes a dynamic index by which to observe the difference in the softness of the structure. This result demonstrates agreement with the molecular dynamics simulation and supports the importance of the indirect interaction of DNA flexibility in the recognition of DNA, as has been proposed based on simulations and statistical analyses of crystal structures.

This result demonstrates that DNA sequences should include not only the string of bases but also information about DNA flexibility. We expect that the discovered structural property of DNA in this study will contribute to both elucidation of the mechanism controlling the “on–off switch” of gene-expression and basic research on gene therapy and regenerative medicine guided by cytodifferentiation.

This study was partly supported by the Ministry of Education, Culture, Sports, Science and Technology of Japan (MEXT) KAKENHI Grant-in-Aid for Scientific Research (No.18031042).

Reference

Nakagawa, H. et al., Local Dynamics Coupled to Hydration Water Determines DNA–Sequence–Dependent Deformability, Physical Review E, vol.90, issue 2, 2014, p.022723–1–022723–11.

5-9 Discovery of "Aggregated DNA Lesions" by Ionizing Radiation

— Evidence for "Clustered DNA Damage" as a Basis for Heavy Ion Beam Cancer Therapy —

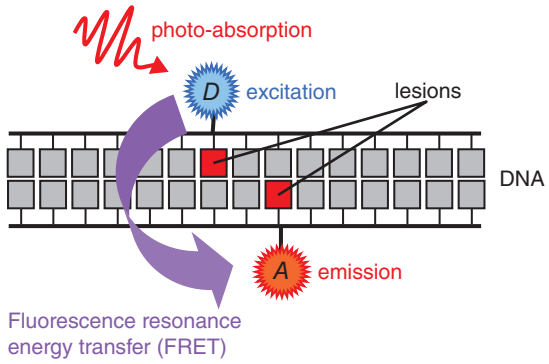

Fig.5-24 Principle of clustered DNA damage detection using FRET
The damaged DNA labeled with fluorophores *D* and *A* is excited by photons for *D* excitation. If an excited *D* is near an *A*, the energy of *D* will be transferred to *A*, followed by emission from *A* (FRET). The total quantity of energy gives the distance between *D* and *A*, and the corresponding distance between the lesions.

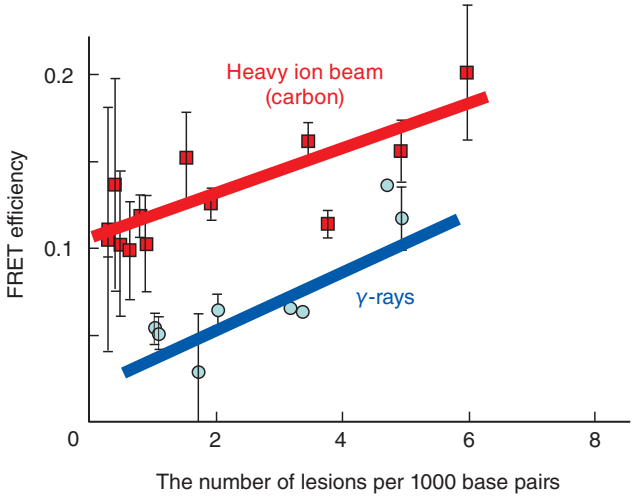

Fig.5-25 Results of the FRET experiments for irradiated DNA
The X-axis expresses the average number of lesions per 1000 base pairs in DNA, which is proportional to absorbed dose of radiation. The Y-axis is the FRET efficiency. The higher the FRET efficiency, the higher the degree of aggregation of lesions. This figure shows that more aggregated lesions (clustered DNA damage) are produced due to a carbon ion beam than due to ^{60}Co γ-rays.

Ionizing radiation exists widely in the environment as well as in space and injures our genomic DNA. Fortunately, cells have evolved mechanisms to protect genomic information by repairing this DNA. However, if a living organism is heavily irradiated all at once, the injured DNA cannot be repaired. On the other hand, the biological effects of radiation are useful to cancer therapy as they can cause irreparable DNA damage to cancer cells. Thus, we must ask: what is the irreparable DNA damage?

So far, more than a hundred DNA lesions produced by radiation have been characterized and each one is known to be repairable, which implies that an isolated lesion on DNA is unlikely to constitute irreparable damage. We considered the distance between lesions to be a key factor for the reparability. It is well-known that repair of artificially clustered DNA damage (defined as a DNA model with two close lesions) is prone to fail in a cell. To begin with, there has not been decisive evidence for the existence of clustered damage or enough knowledge about the chemical structures involved. Thus, we have developed new methodology for investigating the substance of clustered DNA damage. We here focused on a photophysical phenomenon, "fluorescence resonance energy transfer (FRET)". If there are "aggregated" lesions labeled with fluorophores (*D* - *A*), the probability of the excited *D* energy transfer to *A* (FRET efficiency) increases (Fig.5-24). Fig.5-25 shows the results of FRET experiments of DNA irradiated with ^{60}Co γ-rays and carbon ion beams. The higher FRET efficiency for the γ-rays (—) than that for the carbon ion beam (—) indicates that clustered DNA damage was more likely to be produced by the carbon ion beam than by γ-rays. Moreover, it seems that the data points for FRET efficiency near zero dose were around 0.10 in the carbon ion beam, which suggests that such a beam can produce clustered DNA damage sites in a track. This will be a basis for effective heavy ion beam cancer therapy. New findings of clustered DNA damage obtained in the future using the FRET technique will be useful for radiation protection in space as well as for medical applications.

Reference

Akamatsu, K. et al., Localization Estimation of Ionizing Radiation–Induced Abasic Sites in DNA in the Solid State using Fluorescence Resonance Energy Transfer, Radiation Research, vol.183, issue 1, 2015, p.105–113.

5–10 Toward Reduction of Adverse Effects in Cancer Radiotherapy
— Finding the Characteristics of the Radiation-Induced Bystander Effect —

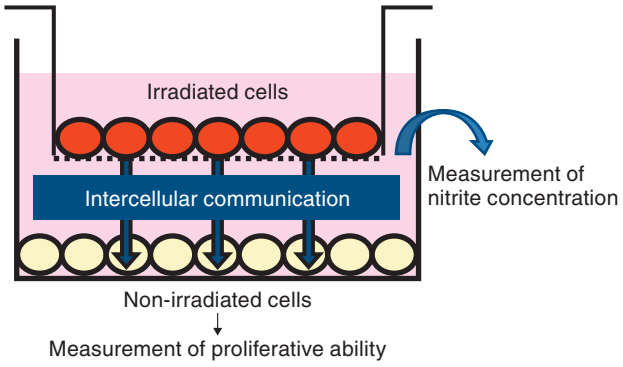

Fig.5-26 Detection of bystander effect
Cells irradiated with γ-rays or a carbon ion beam (top) and non-irradiated cells (bottom) were co-cultured on and below a porous membrane, respectively, to share a culture medium in a vessel. After co-culture, the proliferative abilities of non-irradiated cells and concentrations of nitrite in the medium, derived from biosynthesized nitric oxide (NO) radicals, were measured.

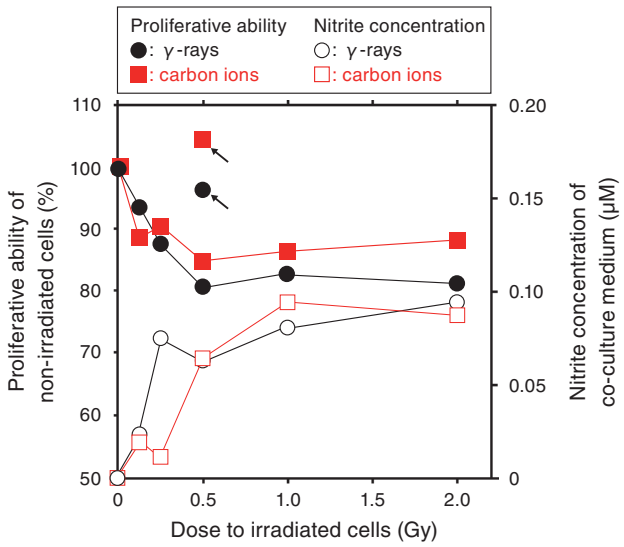

Fig.5-27 Decrease in the proliferative abilities of non-irradiated cells and increase in nitrite concentrations in the co-culture medium
↖ indicate the proliferative abilities of non-irradiated cells under the condition where NO radicals were scavenged.

The bystander effect refers to the phenomenon whereby non-irradiated cells close to irradiated ones mimic the same radiation effects due to intercellular communication.

In this study, we irradiated normal human lung fibroblast WI-38 cells with γ-rays or a carbon ion beam at the Takasaki Advanced Radiation Research Institute, co-cultured the irradiated cells with non-irradiated cells, and measured the proliferative abilities of the non-irradiated cells (Fig.5-26).

As a result, we found that the proliferative abilities of non-irradiated cells decreased in dose-dependent and radiation quality-independent manners (Fig.5-27). The proliferative abilities of non-irradiated cells, however, did not decrease when NO radicals were scavenged from the co-culture medium using the specific scavenger 2-(4-Carboxyphenyl)-4,4,5,5-tetramethylimidazoline-1-oxyl-3-oxide (carboxy-PTIO), indicating that NO radicals are necessary for the induction of the bystander effect. We thus measured the concentrations of nitrite, derived from biosynthesized NO radicals, in the co-culture medium to partly elucidate the molecular mechanism of the bystander effect (Fig.5-26). There was a negative relation between the increase in the concentration of nitrite and the decrease in the proliferative abilities of non-irradiated cells (Fig.5-27). It is assumed that stress-responsive transcription factors such as the nuclear factor κB and downstream NO synthase may have been activated.

Recently, heavy ion radiotherapy has been considered as a minimally invasive form of radiotherapy because of its intensive energy deposition in the tumor region. Undesirable exposure to the normal tissue between the skin and tumor is, however, inevitable, even in the case of heavy ion radiotherapy. Our findings partly elucidated the molecular mechanism of the bystander effect that may modify this adverse effect. In the future, development of new drugs effective in scavenging NO radicals or suppressing their biosynthesis is expected for reduction of the adverse effects of cancer radiotherapy.

The present study was partly supported by Japan Society for the Promotion of Science (JSPS) KAKENHI Grant-in-Aid for Young Scientists (B) (No.25740019).

Reference

Yokota, Y. et al., The Bystander Cell–Killing Effect Mediated by Nitric Oxide in Normal Human Fibroblasts Varies with Irradiation Dose but not with Radiation Quality, International Journal of Radiation Biology, vol.91, issue 5, 2015, p.383–388.

5–11 Why Can Common Reed Grow in Salt Water?

— Visualization of Sodium Exclusion from the Root using a Positron-Emitting Tracer Imaging System —

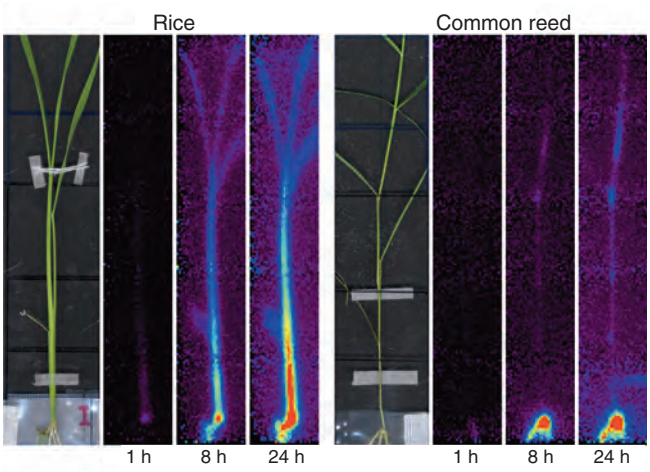

Fig.5-28 Sodium distribution after feeding ^{22}Na into the nutrient solution
^{22}Na moved to the upper shoot in a rice plant (left), whereas ^{22}Na was accumulated in the shoot base in a common reed (right). Red and blue colors indicate high and low ^{22}Na concentration, respectively.

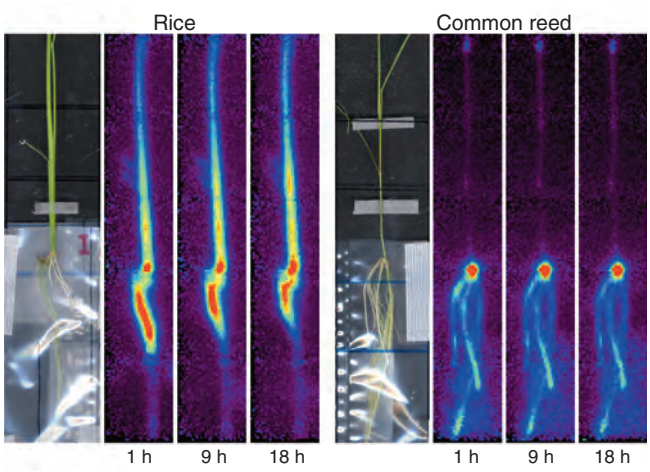

Fig.5-29 Sodium distribution after removing ^{22}Na from the nutrient solution
^{22}Na continuously moved upward in the root of the rice plant (left), whereas ^{22}Na was excluded downward in the root of the common reed (right).

Sodium is not an essential element for most plant species but is a toxic element. Therefore, the growth of rice is often inhibited in paddy fields that have suffered seawater by a tsunami or a typhoon. On the other hand, the common reed, which is classified to the same family as rice, has the ability to withstand a high sodium ion (Na^+) concentration (i.e., it has a high salt tolerance), and therefore, it can grow in the wetlands of brackish water near river mouths, where freshwater and seawater mix.

A previous study of the mechanism behind salt tolerance in common reeds reported that the Na^+ concentration in the fluid through the xylem is lower in the shoot than in the root. Since the xylem is the tissue that transports water and solutes including Na^+ from the root to the shoot, this result suggests that the common reed has the ability to retrieve Na^+ from the xylem in the region between the root and the shoot. However, there has been no direct evidence of this ability. Thus, in this study, we have tried to directly observe the Na^+ movement in an intact common reed using a positron-emitting tracer imaging system (PETIS) that can noninvasively visualize the movement of various radioactive tracers.

Common reeds and rice plants were cultivated in a nutrient solution containing Na^+ at a high concentration (approximately one-tenth that of seawater). After ^{22}Na, a radioactive tracer of sodium, was fed into the solution, we observed the ^{22}Na movement from the solution to the shoot for 24 h using PETIS. We found that ^{22}Na was continuously transported to the upper shoot in the rice plants, whereas it was strongly accumulated in the shoot base but not transported to the upper shoot in common reed plants (Fig.5-28). Furthermore, we replaced the original solution with a fresh nutrient solution without ^{22}Na and traced the ^{22}Na movement inside the plants for 18 h. Using the serial PETIS images (Fig.5-29), we quantitatively analyzed time-course changes of ^{22}Na in small consecutive compartments set along the plant axis. As a result, ^{22}Na ions in the root of the rice plant moved continuously upward, but in contrast, those in the common reed moved downward to the root tip. These results indicate that the common reed has the ability to exclude Na^+ downward from the shoot base and consequently maintains low Na^+ concentration in its shoot.

In this study, we elucidated the common reed-specific mechanism of Na^+ exclusion, and we are now exploring the genes involved in Na^+ retrieval from the xylem and Na^+ exclusion from the root. We expect to produce a salt-tolerant rice plant by introducing the genes of the common reed in the future.

This study was partially supported by the Tokyo University of Agriculture Grant-in-Aid for Advanced Study Projects and the Japan Society for the Promotion of Science (JSPS) KAKENHI Grants-in-Aid for Scientific Research (B) (No.18658028, 21380049).

Reference

Fujimaki, S., Suzui, N. et al., Base to Tip and Long–Distance Transport of Sodium in the Root of Common Reed [*Phragmites australis* (Cav.) Trin. ex Steud.] at Steady State under Constant High–Salt Conditions, Plant and Cell Physiology, vol.56, issue 5, 2015, p.943–950.

5–12 Two-Dimensional Neutron Measurement with High Sensitivity and High Precision
— Development of a Novel Gas-Based Two-Dimensional Neutron Detector System —

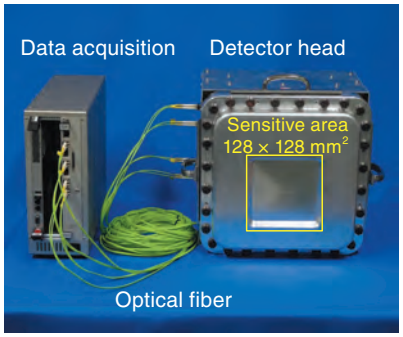

Fig.5-30 The developed gas-based two-dimensional neutron detector system using individual line readout and optical signal transmission
The detector head is connected to the data acquisition device via optical fibers. The optical fiber enables long-distance signal transmission and electrical insulation between the two components.

(a) Counting rate

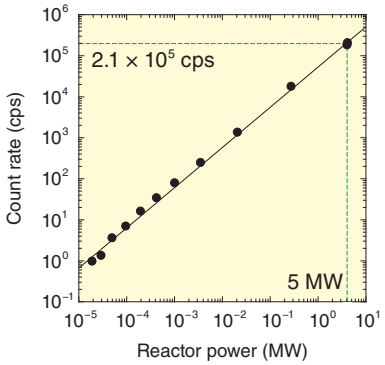

(b) Spatial resolution

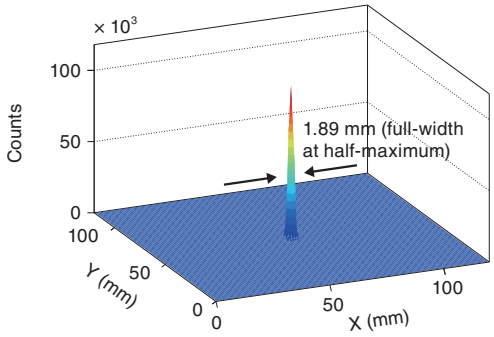

Fig.5-31 Experimental results for (a) counting rate and (b) spatial resolution using neutrons
The capability of a counting rate as high as 210 kcps was confirmed using a continuous neutron beam from a reactor. The detector had a spatial resolution of less than 1.89 mm (FWHM) using a collimated neutron beam with a size of 1.0 mm².

We have developed a He-3 gas-based, two-dimensional neutron detector system for use in neutron scattering experiments using high-intensity pulsed neutrons at J-PARC. Fig.5-30 shows a photograph of the developed detector system. This system exhibits superior performance, including a counting rate greater than several hundred kilo-counts per second (kcps), an average spatial resolution of less than 2.0 mm (full-width at half-maximum, FWHM) with a standard deviation of 0.85 mm in the sensitive region, and a thermal neutron detection efficiency of 80%.

In general, a two-dimensional neutron detector has many signal lines along the vertical and horizontal axes, and the signal lines along each axis are usually connected together to conduct signal processing. The detector we have developed employs an individual readout method, and the signal of each line is individually amplified, shaped, and discriminated by front-end electronics. A short response time and high spatial resolution can be obtained using this method. Although it is necessary to increase the gas pressure to achieve higher detection efficiency, increasing this pressure decreases the amplitude of the output neutron signal, and consequently, discrimination between the neutron and background signals becomes difficult. Therefore, we developed a high-density multiwire detector element, a pressure vessel, multichannel front-end electronics, and optical signal transmission devices specifically for our individual-readout detector system. These devices enabled the detector system to achieve high detection efficiency, short response time, and high spatial resolution. The optical signal transmission could also be used to establish long-distance transmission between the detector head and the data acquisition device without any electrical noise.

The developed detector has a neutron-sensitive area of 128 × 128 mm² and a pixel size of 0.5 × 0.5 mm². As shown in Fig.5-31, this system exhibits an average spatial resolution of less than 1.9 mm (FWHM) in the sensitive region and a counting rate greater than 200 kcps, whereas commercially available neutron detectors have pixel sizes of 2.5 × 2.5 mm² and exhibit counting rates of a few kcps and detection efficiencies of 50%. The thermal neutron detection efficiency of our detector is estimated to be more than 80% with a gas condition of 0.8 MPa.

The developed detector will contribute significantly to high-performance neutron scattering instruments at J-PARC. In particular, for neutron reflectivity measurements, the detector will enable not only specular reflectivity measurements but also off-specular reflectivity measurements such as those involved in grazing-incidence small-angle neutron scattering.

Reference

Toh, K. et al., Development of Two–Dimensional Multiwire–Type Neutron Detector System with Individual Line Readout and Optical Signal Transmission, Nuclear Instruments and Methods in Physics Research A, vol.726, 2013, p.169–174.

5–13 Toward an Understanding of the Role of "Water" in the Earth's Mantle

— Development of a High Pressure, High Temperature Apparatus for Neutron Diffraction at J-PARC —

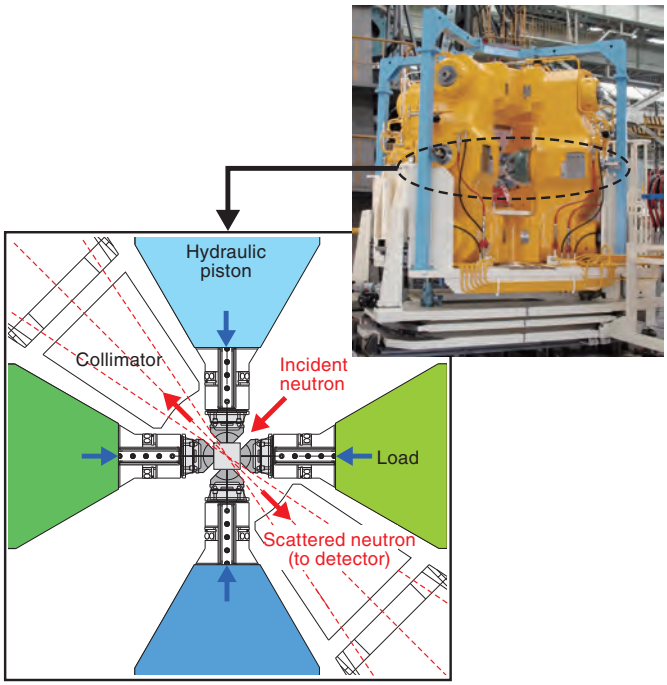

Fig.5-32 Six-axis multi-anvil press "ATSUHIME"
To achieve the extreme conditions of Earth's deep interior, we have developed a six-axis multi-anvil press. A high pressure condition is generated by applying the load with six hydraulic pistons. Neutrons scattered by the sample are detected through the "window" of the press (– – –).

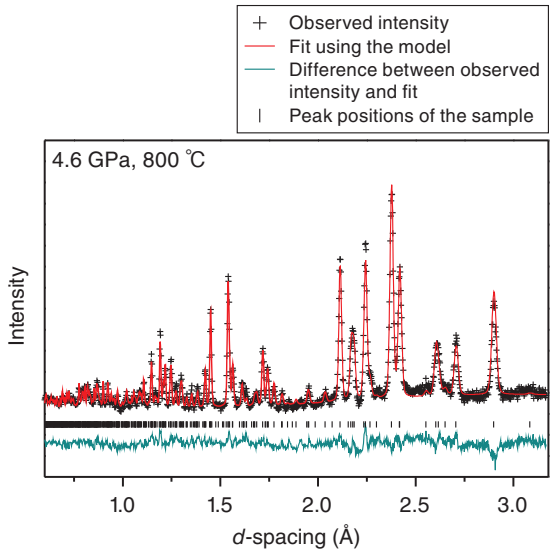

Fig.5-33 Neutron diffraction pattern of the hydrous mineral lawsonite
The neutron diffraction pattern of lawsonite, which is the main carrier of hydrogen in descending oceanic plates, is first obtained at high pressure and high temperature. Hydrogen positions are refined by fitting the observed data (+) with a structural model (——).

The physical properties and structures of minerals and magma change significantly under the high pressure and high temperature conditions in the Earth's interior. *In situ* observation at the extreme condition is thus important for discussions of the Earth's structure and its evolution. Neutron diffraction is a powerful probe for locating hydrogen positions *in situ*, which are difficult to determine by X-ray scattering.

A high pressure condition is achieved by applying force to the sample cell, while high temperature is achieved using a resistive heater in the cell. A conventional multi-anvil press applies a load to a pair of opposed guide blocks using a hydraulic piston. However, when it comes to applying neutrons, this guide block is unfavorable because it limits the "window" for detecting neutrons scattered from the sample. Moreover, the allowable pressure and temperature was limited below 7 GPa and 1000 °C due to insufficient thermal insulation of the small sample cell.

To overcome these problems, we have developed a six-axis multi-anvil press "ATSUHIME" (Fig.5-32). This press comprises six orthogonally aligned hydraulic pistons. The design without guide blocks allows us to enlarge the "window" for neutron scattering and to place the collimation devices near the sample.

The press has been installed in the PLANET beamline at the MLF, J-PARC. We succeeded in conducting *in situ* experiments at 16 GPa and 1000 °C, corresponding to the conditions of the Earth's mantle transition zone where water plays an important role. Thanks to the collimators, high-quality diffraction patterns are available without any parasitic scattering from the high pressure cell (Fig.5-33).

This press constitutes a new tool for understanding the role of water in the deep Earth using neutron scattering.

This study was supported by Japan Society for the Promotion of Science (JSPS) KAKENHI Grant-in-Aid for Scientific Research on Innovative Areas (No.19GS0205), and the Ministry of Education, Culture, Sports, Science and Technology of Japan (MEXT) KAKENHI Grant-in-Aid for Creative Scientific Research (No.20103001).

Reference

Sano–Furukawa, A. et al., Six–Axis Multi–Anvil Press for High–Pressure, High–Temperature Neutron Diffraction Experiments, Review of Scientific Instruments, vol.85, issue 11, 2014, p.113905–1–113905–8.

5–14 Neutron Diffraction Study of Phase Transformations in Steels

— Effect of Partial Quenching on Phase Transformation in Nano-Bainite Steel —

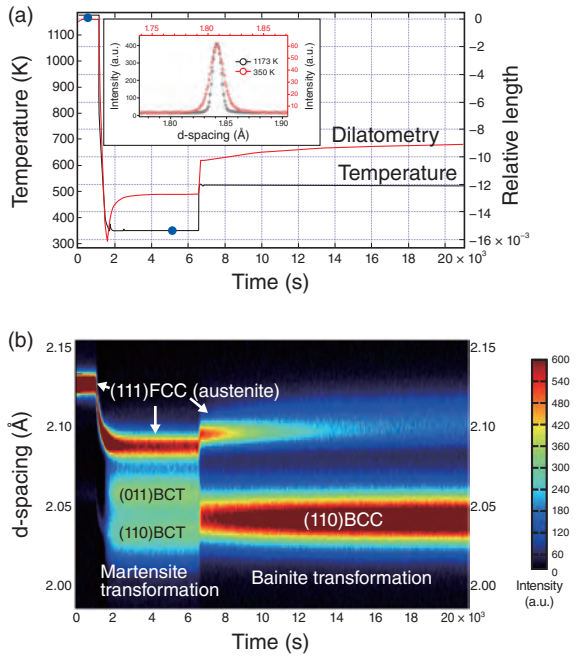

Fig.5-34 Experimental results of QB treatment
(a) Heat treatment route, dilatometry curve, and comparison of (200) peaks of austenite; (b) Diffraction profiles evolution.

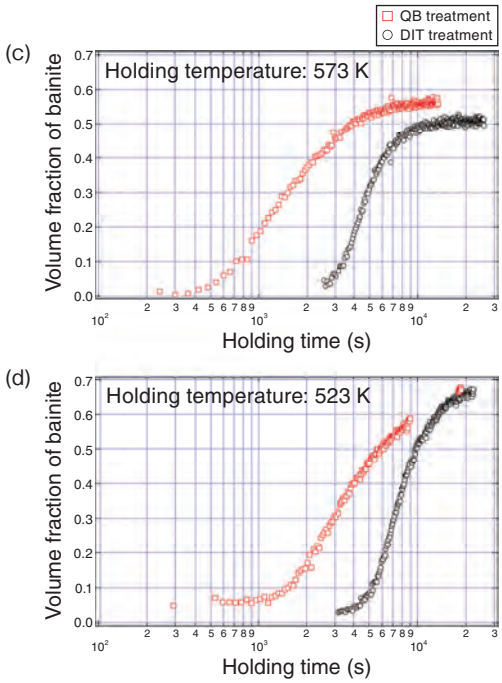

Fig.5-35 Comparison of bainite transformation kinetics between DIT and QB treatment at isothermal temperatures of (c) 573 K or (d) 523 K
In the same holding time, more bainite volume fraction can be obtained in QB treatment than that of DIT treatment, indicating bainite transformation was accelerated by QB treatment.

Nano-bainite steels were designed through alloying to form a bainite structure in the low temperature region of 473–673 K after austenization. These steels with a microstructure comprising nanoscaled laths/plates of bainitic ferrite and carbon-enriched film austenite have been found to exhibit a tensile strength greater than 2 GPa and a fracture toughness of 30 MPa·m$^{1/2}$. However, their extremely slow bainite transformation speed has hindered their engineering applications. Therefore, accelerating the bainite transformation is a necessary issue for further applications of these steels.

To achieve the above demand, we focused on a partial quenching and bainite transformation (QB) treatment. An *in situ* neutron diffraction technique was employed to clarify the effect of partial quenching on the following bainite transformation. The *in situ* neutron diffraction experiments were performed using the engineering neutron diffractometer, TAKUMI, at the J-PARC. The chemical composition of the steel used in this study was Fe–0.79C–1.98Mn–1.51Si–0.98Cr–0.24Mo–1.06Al–1.58Co (wt%). The obtained diffraction profiles were analyzed by the Z-Rietveld code to determine the phase fraction and lattice parameter of each constituent. The convolutional multiple whole profile (CMWP) method was employed for profile analysis to determine the dislocation density and substructure.

The heat treatment route and the corresponding dilatometry curve are shown in Fig.5-34. When the specimen was cooled from 1173 K to 350 K, the austenite phase (face-centered cubic, fcc) transformed into the martensite phase (body-centered tetragonal, bct). After reheating and holding the specimen at 523 K, the behavior of the growing of bcc (body-centered cubic) peaks together with the decrease of the intensity of the austenite peaks implied the operation of a bainite transformation. Fig.5-35 shows a comparison of the kinetics for a direct isothermal bainite transformation (DIT) and for the QB treatments at 573 K and 523 K, respectively. As can be seen, the bainite transformation occurs more quickly under QB treatment than it did under DIT. A comparison of the austensite diffraction peaks around the martensite transformation (collected at the time marked by blue points in the heat-treatment route in Fig.5-34(a)) shows that an apparent peak broadening occurred after the martensite transformation. The CMWP analysis showed that high-density dislocations were introduced into austenite through the progress of the martensite transformation. The dislocations introduced in austenite by accommodating the shape strain of the martensite transformation are believed to have assisted in following bainite transformation.

The *in situ* neutron diffraction technique is useful for the observation of the structure change in steel during heat treatment, which is difficult for conventional methods. In the future, neutron diffraction technique is expected to play an important role in the studies of steels.

Reference

Gong, W. et al., Effect of Prior Martensite on Bainite Transformation in Nanobainite Steel, Acta Materialia, vol.85, 2015, p.243–249.

5–15 Large-Area Uniform Ion Irradiation without Beam Scanning

— Making the Beam Profile Uniform using Nonlinear Force —

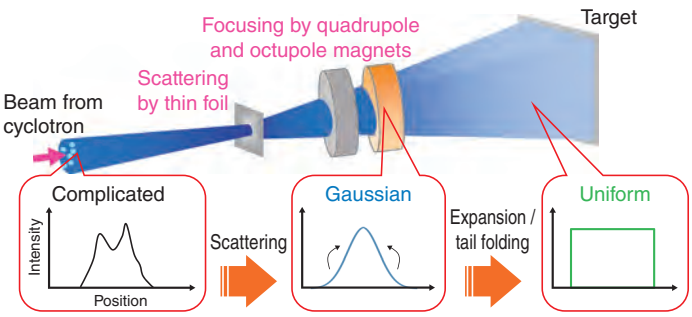

Fig.5-36 Formation procedure of a large-area uniform beam at the TIARA cyclotron
First, the transverse intensity distribution of a beam extracted from the cyclotron is transformed into a Gaussian distribution by means of scattering at thin foil. Then, the beam is focused nonlinearly by a combination of quadrupole and octupole magnets, and finally, the intensity distribution is made uniform on the target.

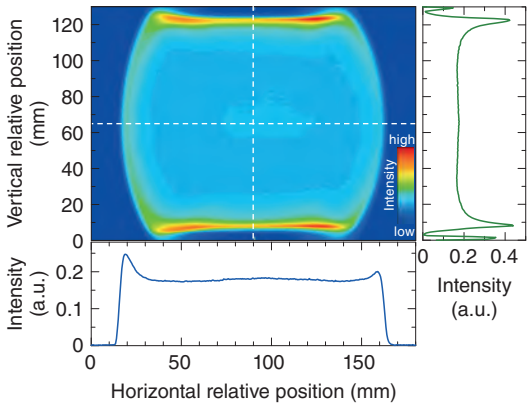

Fig.5-37 Measurement result of the intensity distribution of a large-area uniform beam
The two-dimensional intensity distribution was obtained from the coloration of a radiochromic film irradiated with a 520 MeV Ar large-area uniform beam. The right and lower graphs show the cross-sectional distribution along the central axis (------).

It is necessary to uniformly irradiate a large-area sample or many samples with a beam for research and development, and industrial applications using ion beams. We have developed a large-area uniform ion irradiation technique, which is different from a conventional beam scanning technique, to advance quantum beam science research at the cyclotron in TIARA (Takasaki Ion Accelerators for Advanced Radiation Application). This technique is based on the principle that the tail of a beam with a Gaussian intensity distribution can be folded back inside by the nonlinear force produced with octupole magnets and eventually the distribution can be made uniform. This enables advanced uniform irradiation such as short-time and ultralow fluence irradiation, which is difficult or inefficient with the conventional method, since the beam has a large-area uniform intensity distribution.

To realize the formation and irradiation of such a uniform beam, the behavior of ion beams in the magnetic field has been theoretically analyzed and numerically simulated, so as to determine the proper beam transport condition and field gradients of octupole magnets. Then, the formation procedure of the uniform beam was experimentally established as follows.

As shown in Fig.5-36, first the complicated intensity distribution of a beam extracted from the cyclotron is transformed into a Gaussian distribution, which is a prerequisite for uniform-beam formation, by scattering the beam with thin foil. Then, the beam is focused nonlinearly by a combination of quadrupole and octupole magnets.

In beam scattering, the optimum condition of a foil material and its thickness was determined to reduce the beam energy loss that affects the beam utilization. In the beam formation, we achieved the beam optics by which the aspect ratio of the beam profile could be significantly changed. In this way, the formation and irradiation of a large-area uniform beam were realized using various ions species, from protons to xenon. A typical example of a uniform beam is shown in Fig.5-37. The intensity distribution of the beam was obtained by irradiating a radiochromic film, which exhibits a color change due to radiation exposure. The uniformity (standard deviation of the fluence variation) was 7% in the central area of 120 cm^2.

Such uniform beams have been applied to quantum beam science research. A radiation degradation test of space-use solar cells is ongoing, since the uniform beam irradiation can be made closer to the radiation field in the actual space environment. Moreover, the chemical modification of fluorine polymers is studied using short-time and in-air irradiation.

In the future, available ion species for uniform irradiation will be increased and the quality of the beam will be improved for industrial applications.

Reference

Yuri, Y. et al., Transformation of the Beam Intensity Distribution and Formation of a Uniform Ion Beam by Means of Nonlinear Focusing, Plasma and Fusion Research, vol.9, 2014, p.4406106–1–4406106–4.

5–16 Innovative Structural Health-Monitoring for a High Temperature Piping System
— How to Use a Strain Gauge Processed by Femtosecond Laser Pulses —

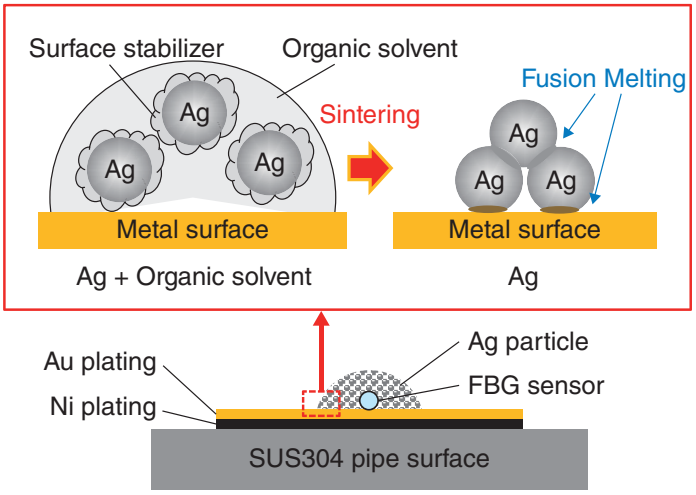

Fig.5-38 Adhesion mechanism for an optical fiber on the surface of a stainless steel plate (nano-sized silver particle adhesive)
Nano-sized silver particles covered by stabilizer maintain a clean surface. After the decomposition of the stabilizer, each particle shows a low melting temperature on its point of contact. Melting at the contact point generates metal joints, making three-dimensional networks.

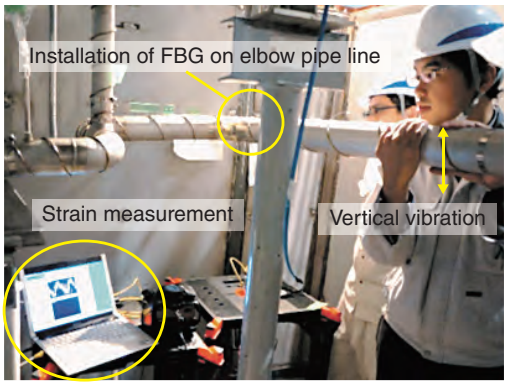

Fig.5-39 Installation of heat-resistant FBG sensors in a Sodium Engineering Research Facility
Heat shocks and seismic vibrations frequently attack the elbows of coolant loops in nuclear power plants. We have successfully installed several FBG sensors for structural health monitoring.

Metal gradually loses elasticity in neutron irradiation environments such as nuclear power reactors or high energy proton accelerators. Thus, it is not useful to tighten assemblies with bolts and nuts; only welding on metal can work well.

However, when the metal is melted and then recoagulated, the excellent performance of the inherent metal tends to be lost. In particular, in the case where repetitive strain is applied to the welding joints, the risk of the fracture drastically increases. Therefore, structural health-monitoring is always requested to observe distortion in such welding parts.

At this time, commercially available strain gauges cannot be used in the high temperature condition. We have succeeded in developing a point-by-point method along an optical fiber core using femtosecond laser processing at the laboratory of the Sensing System Group Kansai Photon Science Institute, generating periodic index-modulation for heat-resistant internal construction. This internal construction is known as a Fiber Bragg Grating (FBG) applicable to the high temperature condition. The periodic index modulation along the optical fiber core represents the characteristic reflection peak wavelength. By placing the optical fiber in close contact with the pipeline, we can know the deformation to monitor the reflection peak shift of the FBG.

The most important issue facing the installation of the FBG sensor on the pipeline is a fine metal particle-based adhesive. The mechanism is shown in Fig.5-38. Adhesive force was activated under 200 °C and can be effective up to 900 °C. Nano-sized silver adhesive was used here. Melting at the contact points between each particle effectively generated countless metal joints. Three-dimensional networks by joined nano-sized silver particles occupied the gaps between the optical fiber and the stainless steel. We developed all the adhesion techniques ourselves and proved the principle of applying them on a Sodium Engineering Research Facility, which is shown in Fig.5-39. The facility was constructed at Shiraki district in Tsuruga City in March 2015.

Reference

Nishimura, A. et al., Demonstration of Heat Resistant Fiber Bragg Grating Sensors Based on Femtosecond Laser Processing for Vibration Monitoring and Temperature Change, Journal of Laser Micro/Nanoengineering, vol.9, no.3, 2014, p.221–224.

6 HTGR Hydrogen and Heat Application Research

Research and Development of HTGR, Hydrogen Production, and Heat Application Technologies

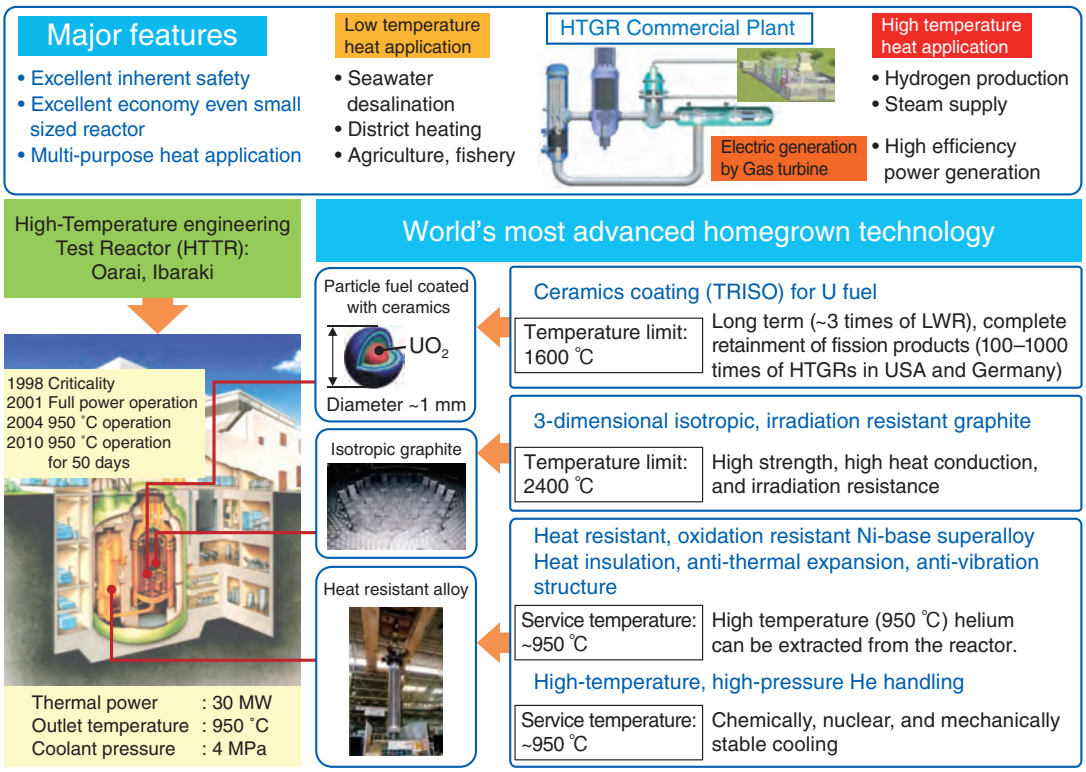

Fig.6-1 Outline of HTGR; features, heat utilization, major specifications, and technologies of HTTR
HTGR is a He gas-cooled and graphite-moderated thermal-neutron reactor that can meet various heat application requirements such as hydrogen production, power generation, and so forth. In particular, it is strongly expected to regain the public's trust in nuclear power due to its inherent safety.

To remedy the fragility of our country's energy supply–demand structure arising from excessive dependence on fossil fuel resources from abroad whilst simultaneously reducing greenhouse gas emissions, it is effective to use nuclear energy not only for power generation but also for various heat applications. The Strategic Energy Plan, Large-boned Policy, and Japan Revitalization Strategy, decided by the cabinet in 2014, list the promotion of research and development of a high-temperature gas-cooled reactor (HTGR) as a national policy because such reactors have the excellent inherent safety and meet the energy demand for various industries. Reflecting on the social situation, the HTGR conference has been developing a strategy to commercialize the HTGR.

An HTGR can supply heat at a temperature of 950 °C using inert helium (He) gas as a coolant. Three other cutting-edge Japanese technologies that make it feasible to obtain such high temperatures in HTGR have been developed in JAEA as follows: (1) a fabrication technology for ceramic-coated fuel particles to contain radioactive fission products within the bodies of the particles; (2) a fabrication technology for isotropic and irradiation-resistant graphite blocks; and (3) a manufacturing technology for heat- and oxidation-resistant super-alloy. Using these major technologies, as well as knowledge of high-temperature structural design and the like, we generated a temperature of 950 °C from the High-Temperature engineering Test Reactor (HTTR) in 2004 for the first time in the world, and demonstrated a stable supply of heat from this reactor over a 50-day operation at 950 °C in 2010 (Fig.6-1).

It is feasible to prevent accidental overheating and oxidation of fuel-coating layers and explosive gas generation by physical phenomena without any engineered safety features. The inherent safety ensures no harmful release of radionuclides to general public and environment in any accident.

A fuel with a burnup targeted at 160 GWd/t has been developed to increase economy and reduce waste by HTGR (Topic 6-1). Furthermore, fuel using 93%-enriched uranium (U) has been researched to reduce the potential radiotoxicity of the spent fuel (Topic 6-2). As for the hydrogen production and heat application technology, chemical reactors made of industrial materials for Iodine-Sulfur (IS) process to produce hydrogen by water-splitting have been developed (Topic 6-3), and a design study has been performed to develop a sea water desalination system utilizing waste from a He gas turbine system (Topic 6-4). The safety-evaluation technology has been developed using HTTR to connect heat application systems manufactured by general industry standards to HTGR (Topic 6-5). We are preparing to resume operation of HTTR, which has been stopped since the Great East Japan Earthquake.

6–1 To Achieve the First Practical Commercial High-Temperature Gas-Cooled Reactor Fuel in the World

— Collaborative Research with the Republic of Kazakhstan Regarding the Irradiation-Performance of High-Burnup Fuel —

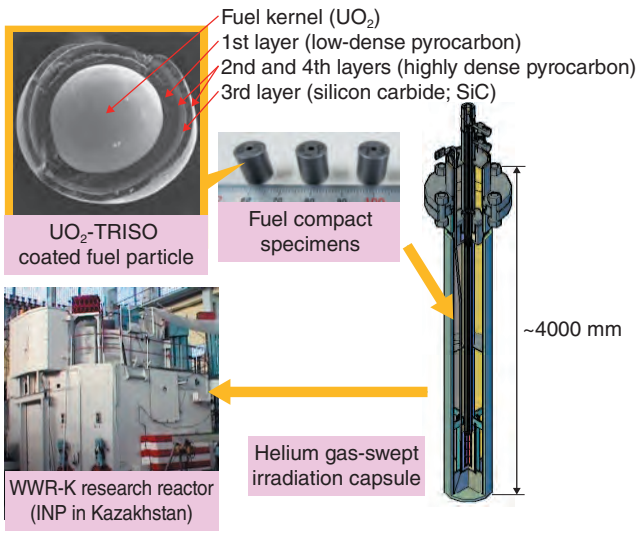

Fig.6-2 Capsule-irradiation test at the Institute of Nuclear Physics (INP) of the Republic of Kazakhstan
To examine the irradiation performance of the newly designed UO_2-TRISO coated fuel particles, fuel specimens fabricated by Nuclear Fuel Industries, Ltd. were irradiated by neutrons in a metallic capsule under an HTGR-simulated helium condition.

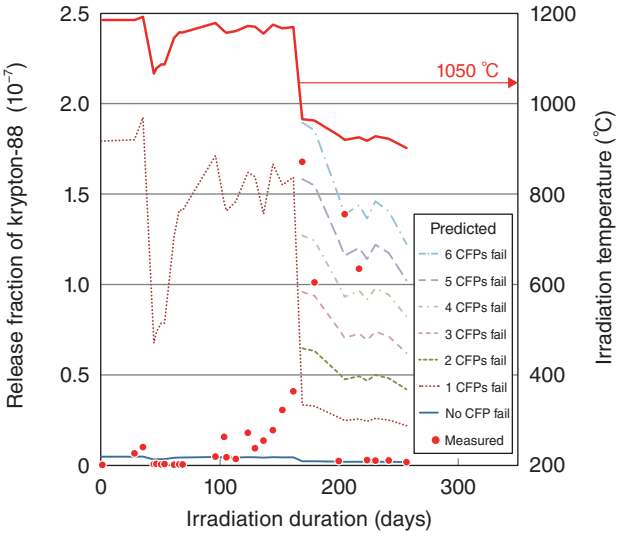

Fig.6-3 Evaluation results of the intactness of coated fuel particles by the release fraction of krypton-88 during neutron irradiation
Although the measured fission gas release increased as the irradiation temperature decreased, it corresponded to the failure of the as-fabricated coated fuel particles (of which there were at most 6), and the high irradiation performance of new fuel was confirmed.

A fuel with a maximum burnup targeted at 160 GWd/t is being developed to increase the economy of and to reduce waste by the practical high-temperature gas-cooled reactor (HTGR). During past investigations, a burnup of around 100 GWd/t has been obtained by researchers in Germany and the United States, corresponding to the average burnup of practical HTGR fuel. In Japan, we have obtained irradiation data for burnups up to 90 GWd/t through the High Temperature Engineering Test Reactor (HTTR) project. However, highly qualified fuels fabricated by a commercial fuel plant were not used in this precursor research. We have newly designed a high-burnup fuel and fabricated it in collaboration with Nuclear Fuel Industries, Ltd. Then, to obtain irradiation data for the new fuel, an irradiation test was conducted at the WWR-K research reactor at the Institute of Nuclear Physics (INP) of the Republic of Kazakhstan, where the HTGR is being developed as a national project. The irradiation test was started in October, 2012 and finished successfully in February 2015. The irradiation temperature was set to 1050±100 °C with a duration of 400 days, with 100 GWd/t being the target burnup. An irradiation capsule was designed and manufactured by INP and loaded at the WWR-K research reactor (Fig.6-2). INP measured krypton-88 as a fission gas (which is not influenced by the precursor nuclide) that is released into the swept-gas of the irradiation capsule to examine the integrity of the fuel during irradiation. To confirm the integrity of the coated fuel particle during irradiation, we evaluated an additional failure fraction of the particle by means of a fission gas-release model developed through the HTTR operation.

Fig.6-3 shows the result of a comparison of the measured release fraction of krypton-88 and the predicted one after 260 days (with a burnup of approximately 70 GWd/t). It was indicated that the measured release fraction was at the same level as that from the initial failure (i.e., the small amount of as-fabricated failure) of the coated fuel particles. Finally, an irradiation test was successfully performed at a burnup of 90 GWd/t by February, 2015, and it was confirmed for the first time that a highly qualified HTGR fuel, which is fabricated using a commercial fuel plant, showed good integrity under a high burnup corresponding to that of a practical HTGR. This has advantages for the development of a further extended-burnup HTGR fuel targeted at 160 GWd/t in the future.

For the next step, the irradiation properties of the fuel will be examined in detail by burnup measurement and the like through post-irradiation examination.

Reference

Ueta, S. et al., Irradiation Performance of HTGR Fuel in WWR–K Research Reactor, Proceedings of 7th International Topical Meeting on High Temperature Reactor Technology (HTR 2014), Weihai, China, 2014, paper HTR2014–31213, 7p., in USB Flash Drive.

6–2 Solutions for Problems of Waste with the Safety, Sustainability, and Economy
— Development of Nuclear Systems using HTGR —

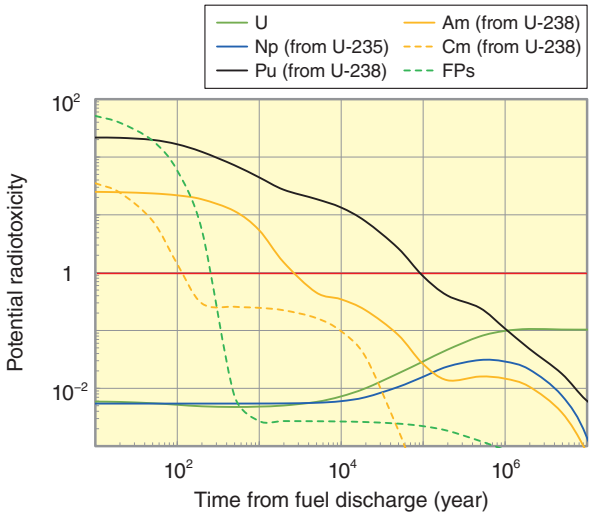

Fig.6-4 Potential radiotoxicity in spent fuels of light water reactors
The cooling time needed for the potential radiotoxicity of Pu to decline below that of natural U (——) is 100 thousand years, and that for Am is 3 thousand years. Np and Cm, which need shorter cooling times than those of fission products (FPs), are not problematic. With reprocessing, Pu is not problematic because it can be recovered and excluded.

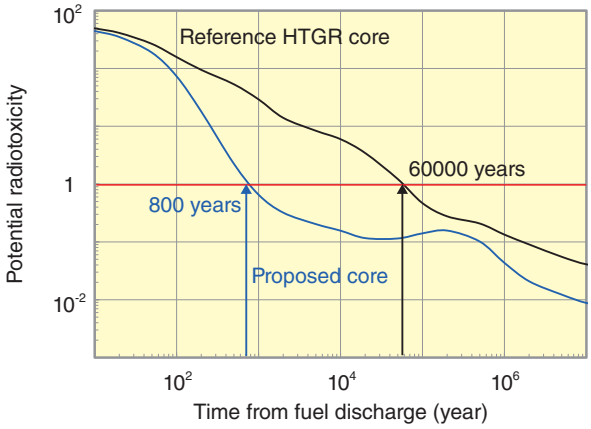

Fig.6-5 Potential radiotoxicity in spent fuels of a reference HTGR core and the proposed core (all nuclides)
In reference HTGR, the cooling time necessary for the potential radiotoxicity to decay below than that of natural U is about 60 thousand years. In the proposed core, the cooling time is 800 years because the amount of U-238 in the fuel is reduced. If laser uranium-enrichment technology is developed, the cooling time can be reduced to about 500 years by higher U enrichment.

The spent fuels (SFs) discharged from nuclear reactors are reprocessed, and high-level radioactive wastes (HLWs) are disposed of in a deep geological repository. The public exposure must be limited to below that of the natural environment. However, the Science Council of Japan has showed a new criterion whereby the total amount of radioactivity in HLWs should be controlled, and has recommended research into nuclear transmutation.

We have performed research on reducing radiotoxicity-generation using the high temperature gas-cooled reactor (HTGR) (which has outstanding inherent safety features and can supply both electricity and high temperatures) without nuclear transmutation.

In general, the toxicity hazard from radioactive nuclides is expressed in the potential radiotoxicity. Thus, it is supposed that a hazard must be controlled by managing the total amount of radiotoxicity. HLWs should be managed until the potential radiotoxicity decays below that of natural uranium (U).

Fig.6-4 shows the potential radiotoxicities of the SFs of light water reactors (LWRs). In particular, the radiotoxicity of plutonium (Pu) and americium (Am) is significant. These radionuclides are generated from U-238. The toxicity generation can be inhibited if the fuel contains only the fissile nuclide U-235. We propose the use of highly enriched U (HEU) with 93% enrichment, which is producible by practical means. To enhance proliferation resistance, the fuel is solidified by yttria-stabilized zirconia (YSZ), which is chemically inert, and fabricated as a coated particle fuel (CPF).

Fig.6-5 shows the potential radiotoxicities of the SFs of the reference HTGR core and the proposed U–YSZ-solidified CPF core. The cooling time necessary for the toxicity to decay below that of natural U is drastically reduced to about 800 years, over which time humanity could realistically manage the SFs.

The resistance of CPF against ground water is one million years, and the erosion rate of YSZ is 1/100 of that of vitrified wastes. The HTGR CPF with a YSZ kernel is suitable for direct disposal. The proposed core does not need any innovative technology to be developed. Cost-evaluation shows that the increase in the electricity-generation cost is within 5%.

Next, the sustainability of this system has been investigated. U exists inexhaustibly in the seawater, with an amount corresponding to the 70-million-year demand of electricity-generation. As the recovery cost has been evaluated to be about twice the present market price, the increase rate of electricity-generation cost using seawater U is only 6%. HTGR can achieve high economic efficiency with the simplicity of a direct gas turbine system. Even with the cost increase due to the proposed core and utilization of seawater U, the electricity-generation cost of HTGR will be cheaper than that of the LWR.

References

Fukaya, Y. et al., Study on Reduction of Potential Radiotoxicity for Spent Fuel by using HTGR, Nippon Genshiryoku Gakkai Wabun Ronbunshi (Transactions of the Atomic Energy Society of Japan), vol.14, no.3, 2015, p.189-201 (in Japanese).
Fukaya, Y. et al., Sustainability and Economy of Energy Supply with HTGR Fueled by Uranium from Seawater, Proceedings of 2014 International Congress on Advances in Nuclear Power Plants (ICAPP 2014), Charlotte, North Carolina, USA, 2014, paper 14299, 7p., in CD-ROM.

6–3 Development of a Chemical Reactor Made of Industrial Structural Materials for a Hydrogen Production Process — Ceramic Sulfuric Acid Decomposer Resisting a Very Harsh Environment —

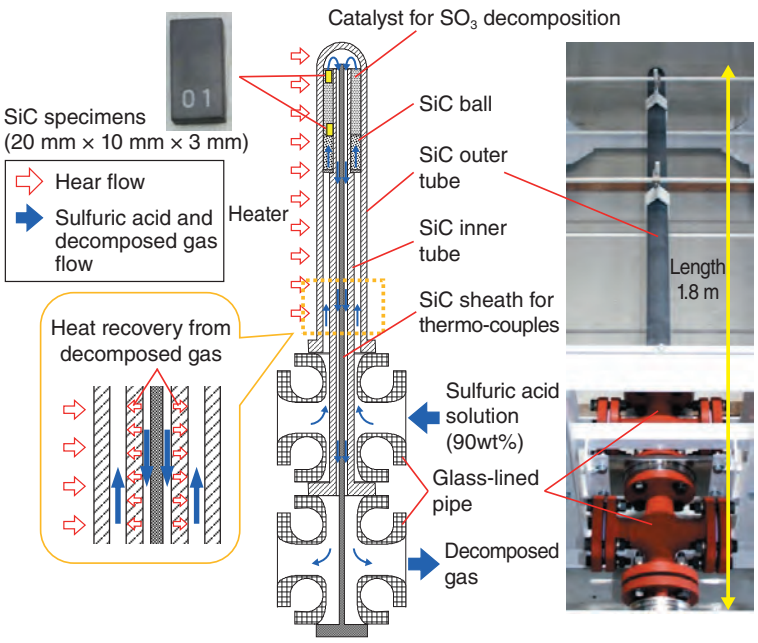

Fig.6-6 Overview of sulfuric acid decomposer made of SiC ceramics
A sulfuric acid decomposer was assembled with industrial structural materials of SiC ceramics and glass-lined steels. The decomposer has multiple functions: sulfuric acid evaporation, decomposition reaction, and heat recovery.

width 18.5 m × depth 5 m × height 8.1 m

Fig.6-7 Hydrogen-production test facility with total process components
We constructed a hydrogen-production test facility including all process components made of industrial structural materials to verify the integrity of the components and to demonstrate continuous hydrogen-production ability.

Table 6-1 Corrosion rates of SiC ceramics in a sulfuric acid decomposition reaction environment
We evaluated the corrosion resistance of SiC ceramics by weight change through an exposure test over about 100 h. Since the corrosion rate is less than 0.05 mm/year, SiC has excellent corrosion resistance.

SiC Specimens No.	Corrosion rate (mm/year)
01	0.062
02	0.057
03	0.052
04	0.067

A thermochemical iodine–sulfur process (IS process) is considered to be a promising hydrogen-production technology using the thermal energy produced by high-temperature gas-cooled reactors. The process splits water into hydrogen and oxygen by combining the chemical reactions of iodine and sulfur. Since it contains aggressive chemicals like sulfuric acid, one of the key tasks for realizing the process is the development of chemical reactor components made of industrial structural materials with heat- and corrosion-resistance abilities. We developed such a chemical reactor made of silicon carbide (SiC) ceramics to serve in a very harsh environment of sulfuric acid decomposition that no metallic material can resist.

SiC is known as a superior corrosion-resistant material, even under a sulfuric acid boiling condition around 300 °C. However, information is limited concerning the corrosion-resistance behavior under higher-temperature sulfuric acid decomposition conditions around 850 °C. SiC generally shows good corrosion resistance due to a stable oxide layer formed on the surface, but it is corroded by high-temperature steam. The subject environment of a sulfuric acid decomposition reaction is more complicated, as it not only has high temperature but also has a complicated corrosive environment including oxygen, steam, sulfur dioxide (SO_2), and sulfur trioxide (SO_3).

We adapted SiC ceramics to fabricate a sulfuric acid decomposer and evaluated the corrosion resistance of the SiC material under the reaction condition. As shown in Fig.6-6, the structure of the decomposer is simple; its design is achieved by coaxially assembling three SiC tubes and setting them on a manifold of glass-lined pipes. Sulfuric acid evaporates and decomposes into water, oxygen, and SO_2 in the top region of the catalyst bed. This structure makes it possible to perform heat recovery from high-temperature decomposed gas flowing in an inner flow channel to the low-temperature sulfuric acid flowing in an outer channel. Moreover, no sealing area is provided in the high-temperature region.

We evaluated SiC corrosion resistance in the sulfuric acid decomposition environment. SiC specimens were placed in the SO_3 decomposition catalyst bed. An exposure test of SiC to the environment was conducted for about 100 h to determine the corrosion rates from the weight changes of the specimens. No significant corrosion was observed from change in surface appearances. The determined corrosion rates were 0.05–0.07 mm/year, which are classified as perfect corrosion resistance, less than 0.05 mm/year, as shown in Table 6-1.

We then constructed a hydrogen production test facility that applies this type of decomposer, and all other plant components are made of industrial structural materials (Fig.6-7). Tests using the facility were launched to verify components' integrity and to demonstrate the ability to produce hydrogen continuously.

Reference

Kubo, S., Noguchi, H. et al., Research and Development on Chemical Reactors Made of Industrial Structural Materials and Hydriodic Acid Concentration Technique for Thermochemical Hydrogen Production IS Process, JAEA-Technology 2015-028, 2015, 32p. (in Japanese).

6–4 Toward the Establishment of Various Heat Application Systems using the HTGR

— Investigation of Water Production Cost with Desalination using HTGR Waste Heat —

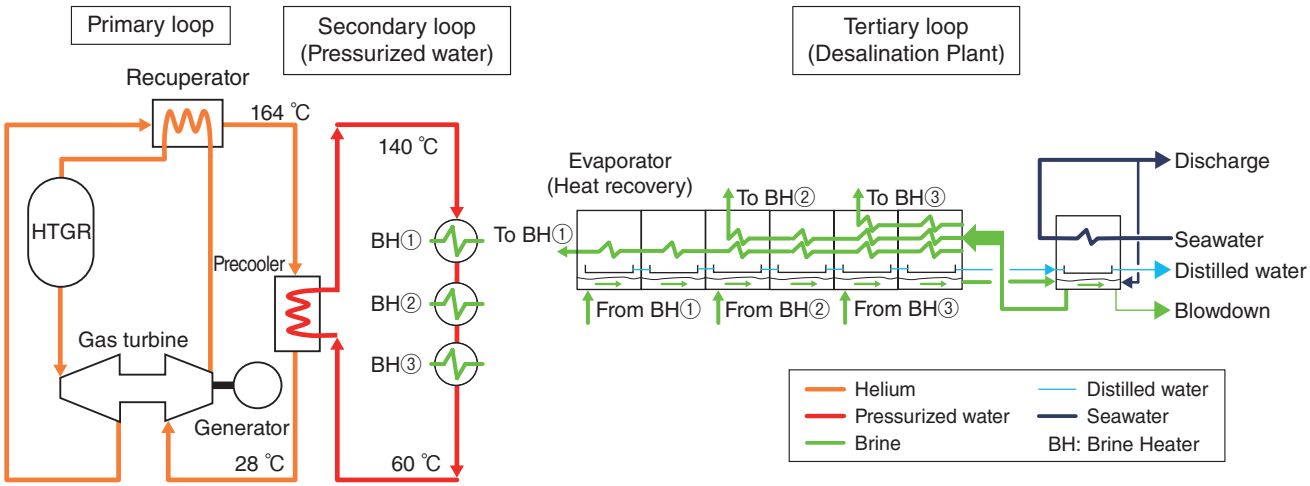

Fig.6-8 Flow diagram of the HTGR desalination system
We proposed an incremental heat-loaded desalination system with multiple brine heaters using the HTGR. The optimum number of brine heaters was determined to be three by considering the balance between performance ratio and water-production cost.

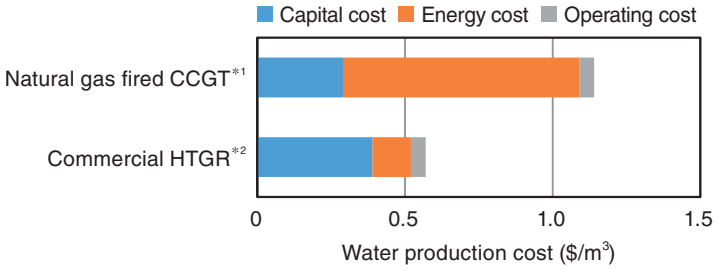

*1 CCGT: Combined Cycle Gas Turbine plant
*2 HTGR: High-temperature Gas-cooled Reactor

Fig.6-9 Cost evaluation of water production with a conventional gas-fired desalination plant and a commercial HTGR plant
It was found that the water production cost was reduced by over 50% compared with conventional desalination despite the increase of capital cost because the energy cost was reduced by utilizing waste heat.

High-temperature gas-cooled reactors (HTGRs) produce not only electricity but also intense heat usable for a variety of applications. We have proposed a commercial HTGR called GTHTR300. With a 600 MWt thermal power, the GTHTR300 generates about 300 MWe of electricity using a helium gas turbine while rejecting about 300 MWt in waste heat from the precooler of the gas turbine system. In this study, a new proposal for an HTGR desalination system and its water-production cost were investigated to evaluate the economics of heat utilization from an HTGR.

Multistage flash (MSF) was selected as the desalination method. Since it is applicable to the temperature range (approximately 160 °C) of HTGR waste heat and offers the greatest maturity and reliability in the world. In MSF, a seawater stream is sequentially heated in the evaporators and the brine heaters and then returned to the flash chamber in the evaporators. The heated brine undergoes flash evaporation by regulating the pressure in the evaporator chambers, and the vaporized water is condensed on the heat-transfer tubes and collected as product water.

The waste heat of an HTGR is supplied through the secondary pressurized water loop and brine heaters. However, a conventional single brine-heater MSF can achieve a quite low performance ratio because of the narrow temperature range of sensible waste heat from the gas turbine system. We therefore proposed the concept of a multiple-brine heater MSF system (Fig.6-8). It was found that the performance ratio of the new MSF increases with the number of brine heaters used. On the other hand, the increase in the number of brine heaters leads to increase in the construction cost. A trade-off study between the performance ratio and the construction cost indicated that the optimum number of brine heaters was three. Based on this finding, the components and plant layout were designed, and the water production cost was estimated. The comparison of the water-production cost between the conventional MSF system with a typical natural gas-fired combined cycle gas turbine plant and the newly proposed multiple-brine heater MSF with GTHTR300 is shown in Fig.6-9. The water-production cost of the multiple-brine heater MSF using the waste heat of the GTHTR300 is reduced by over 50%. The result of this study demonstrates yet another economical advantage of HTGRs for heat applications.

Reference

Kamiji, Y. et al., Flowsheet Study of a Multistage Flash Desalination System for Cogeneration with High Temperature Gas-Cooled Reactor, Proceedings of 22nd International Conference on Nuclear Engineering (ICONE 22), Prague, Czech Republic, 2014, ICONE22-30142, 5p., in DVD-ROM.

6–5 For Supplying HTGR Heat to Non-Nuclear Industry
— Development of Safety Analysis Techniques for Cogeneration HTGR —

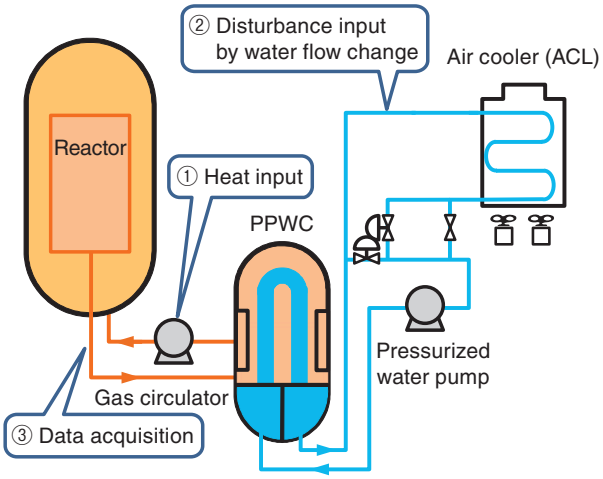

Fig.6-10 Fluctuation test of the reactor inlet temperature by the heat input of the gas circulators
In this test, the helium gas was heated up to 120 °C by the compression heat of the gas circulators. The reactor inlet temperature was changed by controlling the pressurized water flow passing the air cooler. The temperature change was maximal at about 30 °C in the test.

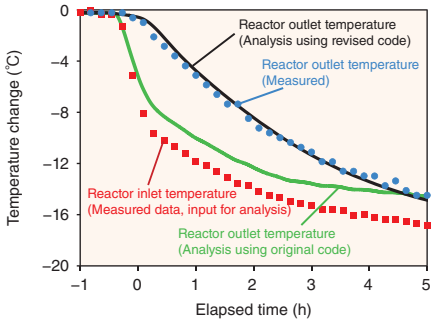

Fig.6-11 Measured and numerical results for the fluctuation of core inlet temperature
The numerical result (——) without the effect of heat-transfer promotion is different from the measured data (●●●). On the other hand, the result of the analysis considering the effect of heat-transfer promotion (——) shows a good agreement with the measured data (●●●).

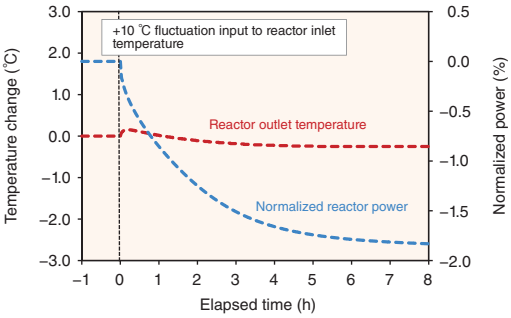

Fig.6-12 Numerical results of the fluctuation of the core inlet temperature under full power
At the full-power condition, the reactor inlet temperature was changed by +10 °C. The effect on heat transfer promotion was investigated using the validated code. The fluctuation of the reactor outlet temperature was extremely small, below +0.2 °C.

We have conducted research and development toward industrial use of the high-temperature gas-cooled reactor (HTGR). Toward the realization of nuclear heat application systems, it is important to ensure reactor safety as well as to not treat nuclear heat application systems as an extension of a nuclear plant from an economic point of view. One of the key requirements is to maintain a normal operation condition for the reactor during every possible operation condition in nuclear heat applications.

A safety analysis code has been evaluated by test results acquired using the high-temperature test engineering reactor (HTTR). However, a pre-investigation found that both the heat capacity of graphite and the heat transfer-promotion by metallic components such as side-shielding blocks had inhibitory effects upon the fluctuation of the reactor outlet-temperature. Therefore, a fluctuation test by non-nuclear heating was conducted. An outline of the thermal load fluctuation tests is shown in Fig.6-10. In this test, it was found that the heat capacities of the graphite components and the fin effect by the metallic components of the side shielding blocks inhibited the fluctuation of the reactor outlet temperature. The results are shown in Fig.6-11. The validated code was applied to the evaluation of a postulated abnormal event in the nuclear heat applications to be connected to the HTTR.

In addition, with the validated code, the transient behavior of the main parameters was investigated under full power conditions. The evaluation quantities such as reactor power and reactor outlet temperature did not exceed the evaluation criteria (+7 °C), as shown in Fig.6-12. As a conclusion, it was validated that the nuclear heat application system is feasible to be constructed under non-nuclear regulations by showing that stable reactor operation can be continued even though temperature transients are induced by abnormal conditions in nuclear heat applications.

In addition, HTTR is under review for a new research reactor's safety regulatory requirements. The test also confirmed the integrity of the reactor system and was useful for operator training.

Reference

Honda, Y. et al., Validation of System Analysis Code with HTTR Thermal Load Fluctuation Test Data (Non-Nuclear Heating) and Evaluation of Reactor Temperature Behavior during Upsets in Hydrogen Production Plant, JAEA-Technology 2015-012, 2015, 17p. (in Japanese).

R&D of Fast Reactor Cycle Technology

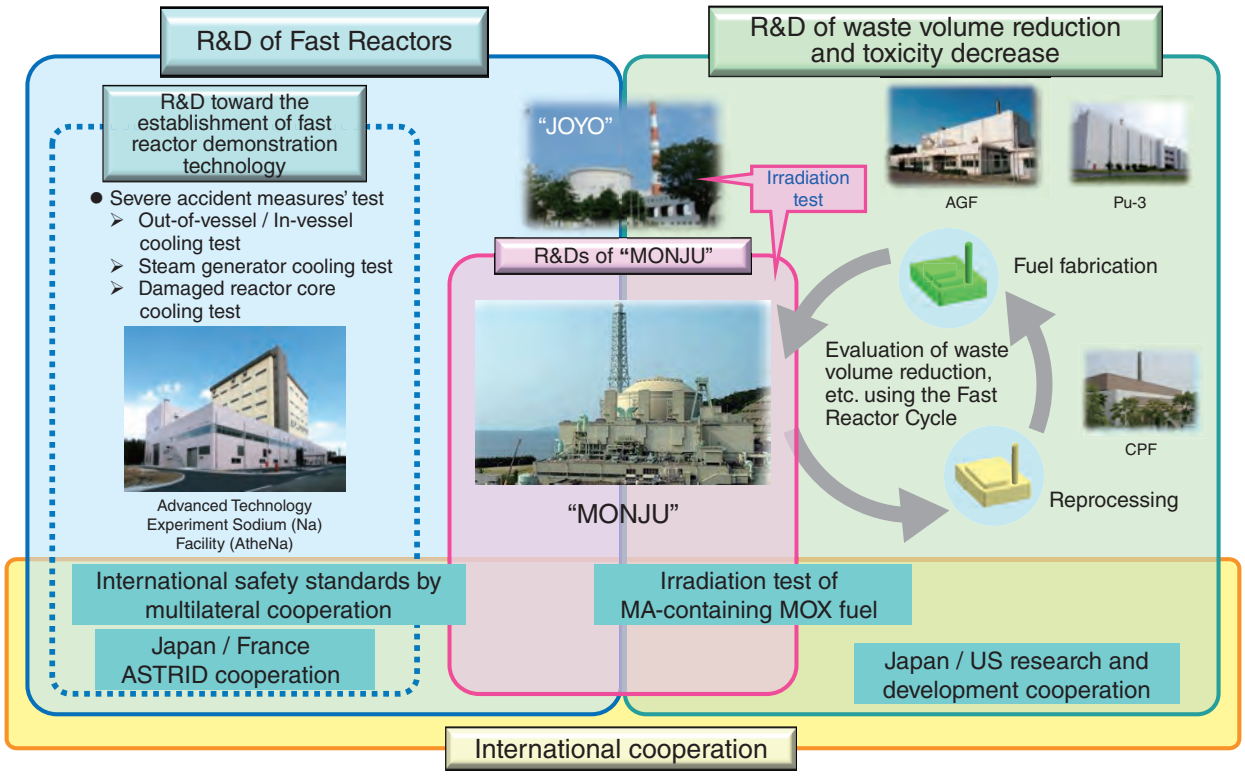

Fig.7-1 Overview of the research and development of fast reactor cycle technology
In accordance with the 3rd Medium- and Long-term Goals established by Governmental authorities in "the 4th Strategic Energy Plan", as of 2015 we are conducting R&D on the subjects of waste volume reduction and toxicity decrease, "MONJU", and the establishment of a fast reactor demonstration technology, with international cooperation.

Fast reactor cycle technology is essential for the establishment of the nuclear fuel cycle from the perspective of our nation's energy security and global warming, and "the 4th Strategic Energy Plan", which was approved by the Cabinet in April 2014, has clearly stated that research and development (R&D) on the technology is a challenge that should be addressed. Based on the 3rd Medium- and Long-term Goals established in this plan, as of 2015 we are conducting R&D on waste volume reduction and toxicity decrease, the prototype fast breeder reactor "MONJU", and the establishment of a fast reactor demonstration technology, with international cooperation (Fig.7-1).

"MONJU" is positioned to be an international research center for technological development such as reduction of the amount and toxicity level of radioactive waste, and is focused on making efforts to overcome challenges such as responding to new regulatory requirements.

We are conducting the R&D necessary for the establishment of the fast reactor demonstration technology using the results obtained by R&D on "MONJU" as well as participation in the international project for the demonstration phase of the French reactor "Advanced Sodium Technological Reactor for Industrial Demonstration (ASTRID)".

For the volume reduction and toxicity decrease of radioactive waste, we promote a separation and recovery technology for minor actinides (MA) and the performance evaluation of MA-containing fuel while leveraging international networks, which are major technological development challenges for nuclear transmutation using fast reactors to reduce of the amount of radioactive waste as well as the long-term remaining toxicity level.

In this chapter, we will introduce our R&D achievements toward strengthening the safety of fast reactors, reducing the volume of radioactive waste, decreasing toxicity, and building the fast reactors "MONJU" and "JOYO".

With the aim of resumption of the experimental sodium-cooled fast reactor (SFR) "JOYO", the restoration work involving in-vessel repair for the radioactive, large, and damaged components applying maintenance techniques was completed, and the success of this work has been a remarkable achievement throughout the world (Topic 7-1).

A dynamic test of an elbow for SFRs was performed based on the knowledge that stress could be easily concentrated into the elbows in piping (Topic 7-2).

The flow field was measured by particle image velocimetry (PIV) in the subchannel around the wrapping wire, which is provided in the fuel subassemblies of SFRs (Topic 7-3).

A high-precision numerical simulation method has been developed for gas entrainment at a gas-liquid interface (Topic 7-4).

Safety-related research was performed on the decay heat and radiation effects of adsorbents containing organic compounds that are used in extraction chromatography technology (Topic 7-5).

Oxygen chemical diffusion coefficients were measured for Am-containing PuO_2 using the latest technology (Topic 7-6).

Thermal-hydraulic phenomena were analyzed for the upper plenum in the "MONJU" reactor to develop a thermal-hydraulic analysis technology for the interior components of SFRs (Topic 7-7).

7–1 Demonstration of the In-Vessel Repair Technology within the Fast Reactor "JOYO"

— Replacement of a Large Structure and Retrieval of a Deformed Test Subassembly —

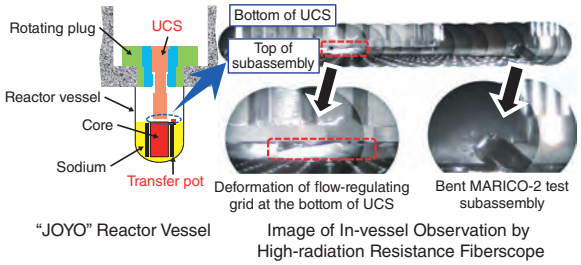

Fig.7-2 Occurrence of an obstacle in the reactor vessel
In the "JOYO" reactor vessel, the lower part of the upper core structure was damaged and the MARICO-2 test subassembly was bent and extruded from a transfer pot. In the area where the UCS makes contact with the MARICO-2 test subassembly, the operation of a rotating plug (UCS was installed in the rotating plug) for fuel-exchange work had to be restricted.

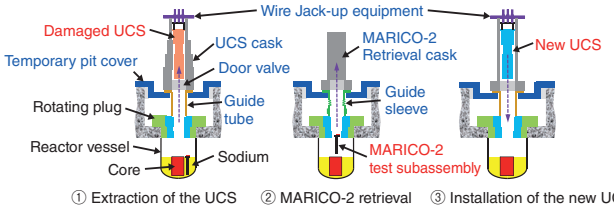

Fig.7-3 Flow of the UCS replacement and MARICO-2 test subassembly retrieval work
The first step is the extraction of the damaged UCS. The second step is retrieving the MARICO-2 test subassembly from the UCS removal hole. The final step is the installation of a new UCS. These objects, which have very high surface dose rates above 100 Sv/h, were handled in this work.

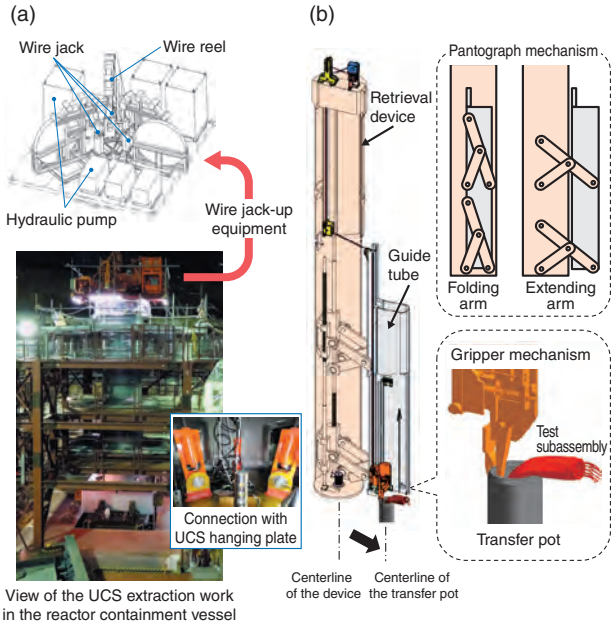

Fig.7-4 An example of a result of technological development
Jack-up equipment for replacement of the UCS and the MARICO-2 test subassembly retrieval device must be able to handle the damaged components by remote operation. This technology has been accumulated and practiced for a long time in the history of "JOYO" and is reflected in the development and operation of the equipment.

The experimental fast reactor "JOYO" needed restoration work including the replacement of the upper core structure (UCS) and retrieval of the bent test subassembly of the material test rig with temperature control (MARICO-2) due to a failure in the disconnecting and unloading work of the MARICO-2 test subassembly in 2007 (Fig.7-2). About 5300 man-days were spent on this restoration work and it was completed in December 2014. The maximum individual dose and the collective effective dose were controlled to be very low, approximately 0.25 mSv and 1.6 man-mSv, respectively.

The restoration work was conducted as shown in Fig.7-3. "JOYO" is a sodium-cooled fast reactor (SFR) in service, and hence, the equipment used for the task had to be capable of withstanding high temperatures (sodium temperature is around 200 °C) and high doses of radiation (components are highly radioactive due to high neutron flux) and it was required to maintain the argon cover gas boundary. Various techniques were developed throughout the study, and the following are introduced as representative examples: (1) UCS jack-up equipment for replacement and (2) MARICO-2 test subassembly retrieval device. In the process of development, mock-up tests were conducted to confirm the functions of the equipment and device in the manufacturer's factory. The data and knowledge obtained by the tests supported the implementation of various techniques and operation methods.

(1) Since exchanging the UCS during the lifetime of the reactor had not been considered during its design, the UCS jack-up equipment has a very precise monitoring capability to check the levelness of the UCS and the applied load to avoid mechanical interference with the surrounding structure and to detect contact and load abnormality quickly on the assumption that there is not much clearance. Furthermore, the state of the UCS could not be observed visually because the UCS with a high dose had to be jacked-up into a large, thick iron cask, as shown in Fig.7-4(a). Hence, this equipment has a stop system interlocked with the load monitoring.

(2) The MARICO-2 test subassembly retrieval device was installed in a removal hole for the UCS. The location of a gripper is adjusted by a remotely operated pantograph mechanism, as shown in Fig.7-4(b). The MARICO-2 test subassembly is gripped and lifted up with the transfer pot by the retrieval device. In the design of this device, temperature-resistant materials were selected and the change in size of this long mechanism due to thermal expansion was carefully considered. Moreover, multiple countermeasures were taken to prevent accidental fall of the transfer pot in the retrieval operation.

When performing maintenance and repair work in an SFR, unique technical developments different from those for a light water reactor are required due to the abovementioned environmental conditions. Considering this, the success of this restoration work involving in-vessel repair for the radioactive, large, and damaged components applying SFR maintenance techniques is a remarkable achievement throughout the world. The knowledge and experience gained from this project will be useful for upgrading the maintenance and repair technology for SFRs in the future.

References

Ashida, T. et al., Inspection and Repair Techniques in Reactor Vessel of the Experimental Fast Reactor Joyo – Investigation and Design for Retrieval Device of Bent MARICO-2 Test Subassembly –, JAEA-Technology 2012-047, 2013, 106p. (in Japanese).
Ito, H., Takamatsu, M. et al., Inspection and Repair Techniques in the Reactor Vessel of the Experimental Fast Reactor Joyo – Development of Repair Techniques for UCS Replacement of Joyo (II) –, JAEA-Technology 2014-024, 2014, 28p. (in Japanese).

7–2 Approach for Advanced Seismic Assessment Technologies for Sodium-Cooled Fast Reactors
— Behavior of Piping for Sodium-Cooled Fast Reactors under High-Level Seismic Loads —

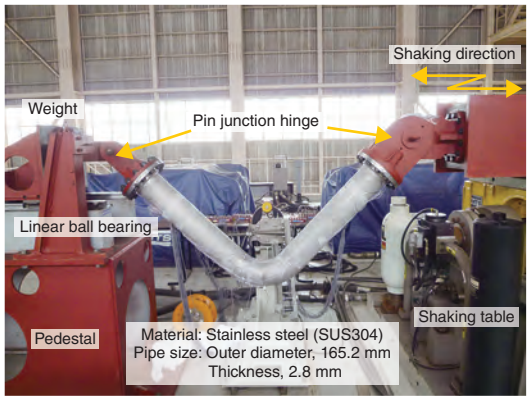

Fig.7-5 Test setup for a dynamic failure test of the elbow
An earthquake was simulated using a shaking table. The excitation of the shaking table imposed an inertial load on the elbow.

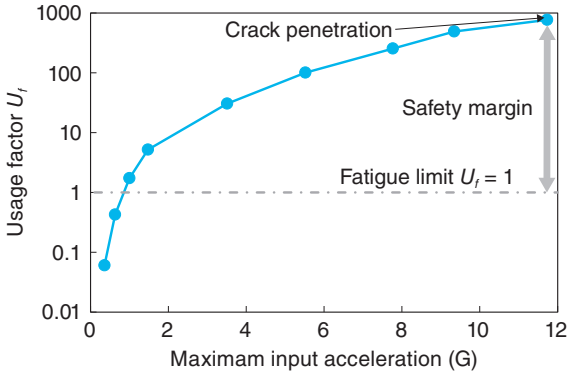

Fig.7-7 Fatigue evaluation based on a design code for piping
The fatigue life of the test specimen was evaluated based on the design code of the piping. The calculated total usage factor significantly exceeded unity. From this result, it was confirmed that the conventional fatigue evaluation method for piping has a large safety margin.

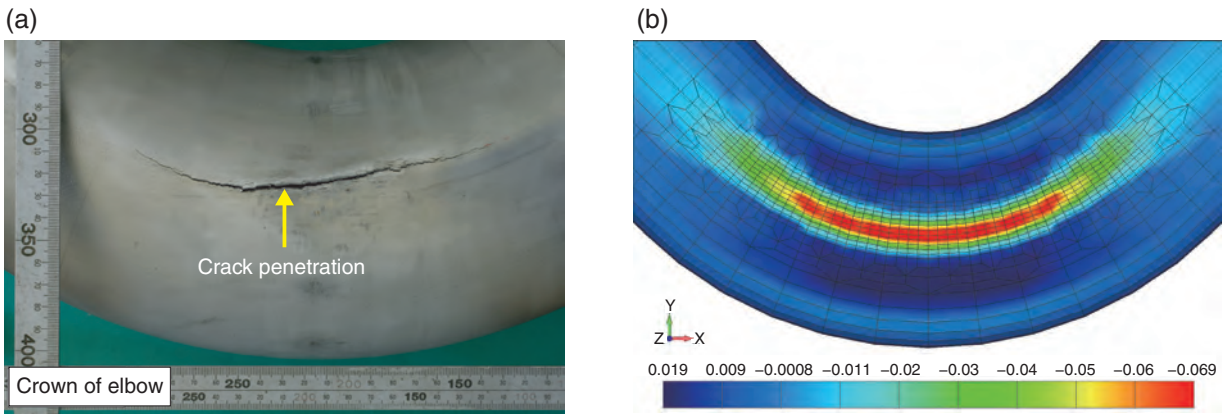

Fig.7-6 Comparison between (a) the test observation at the crown part of the elbow and (b) the analytical result using finite element analysis
(a) A crack in the axial direction was observed at the crown part of the elbow. (b) The test result was reproduced well by finite element analysis.

To ensure the seismic integrity of nuclear power plants, both confirming the ultimate strength under a high-level earthquake beyond the design condition and clarifying the design safety margin up to ultimate strength have been focused as important issues. In this study, a dynamic test of an elbow for a sodium-cooled fast reactor was performed based on the knowledge that stress is easily concentrated into elbows in piping.

In the test, using a pin junction, one end of the elbow was fixed to a shaking table and a weight was fixed at the other end of the elbow (Fig.7-5). Excitation of the shaking table imposed an in-plane bending moment on the elbow by the inertial load of the weight. The results showed that the elbow did not fail under an earthquake of the level for which it was designed. After the confirmation, the excitation level was scaled up and the test was continued to confirm the ultimate behavior of the elbow. High-level excitation significantly exceeding the design level was needed to cause the elbow to fail in the test. Finally, a crack in the axial direction was observed at both sides of the crown part of the elbow (Fig.7-6(a)). It was confirmed from the test that the failure mode of the elbow was low cycle fatigue with crack initiation, propagation, and through-wall penetration. No structural instability such as collapse was observed. Moreover, it was confirmed that finite element analysis can be used to reproduce the failure behavior of the elbow (Fig.7-6(b)).

Fatigue evaluation of the test based on the design code for piping was performed to clarify the safety margin included in the design fatigue evaluation method. The calculated usage factor (a usage factor shows the state of fatigue damage of a structure, with a usage factor of 1 being defined as fatigue failure of the structure) was significantly beyond unity when the elbow actually failed (Fig.7-7). This result indicates that the conventional method of evaluating fatigue in piping has a large safety margin.

Reference

Watakabe, T. et al., Study on Ultimate Strength of Thin–Wall Piping Components for Fast Breeder Reactors under Seismic Loading, Transactions of 22nd International Conference on Structural Mechanics in Reactor Technology (SMiRT–22), San Francisco, California, USA, 2013, p.1575–1584.

7–3 Visualizing the Coolant Flow in the Fuel Assembly
— Achieving Highly Accurate PIV Measurement through Index Matching —

(a) Photo of the test apparatus

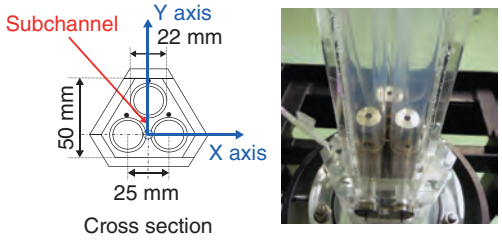

(b) Measurement position

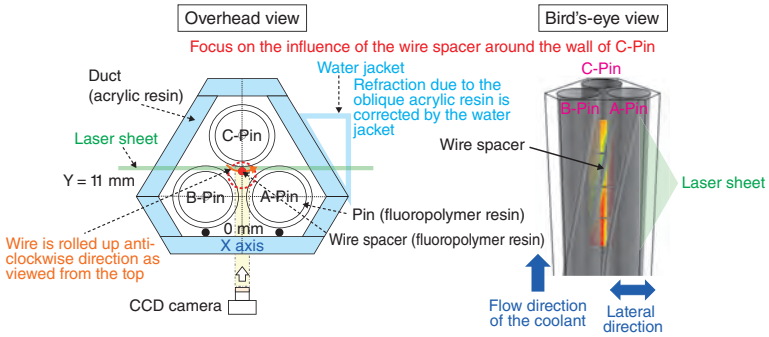

Fig.7-8 Three-pin bundle water experiment system
The distortion of a laser through the pin and wire were eliminated by fabricating them from clear fluoropolymer resin with a refractive index close to that of water (index matching). As a result, highly accurate visualization of flow in the narrow complex flow path has been achieved.

(c) The average flow velocity distribution in 6 s

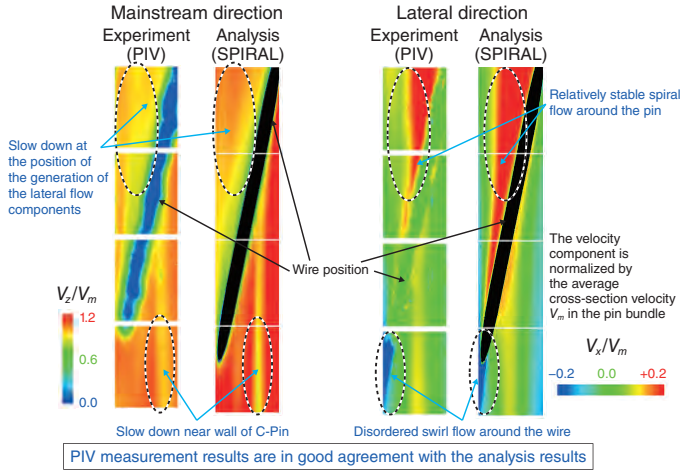

(d) Mesh division of SPIRAL analysis

	Mesh division
Circumferential direction of Pin	96 divide
Radial direction of Pin	18 divide
Total count	890496 elements

Fig.7-9 Comparison between PIV measurement results and analytical results
The average flow velocity obtained by PIV measurement was in good agreement with the analytical results of SPIRAL (finite element mesh code) over 6 s in the flow direction and the lateral direction (which was normalized by the *Vm*-averaged cross-section flow rate) near the wire.

Fuel pins are generally densely arranged in equilateral triangles in the fuel subassemblies of sodium-cooled fast reactors. The spiral wire spacers are adopted to maintain gaps in the fuel pins and to ensure cooling because they can be relatively flexible to deformation of fuel pins caused by neutron irradiation. However, the coolant flow path between the fuel pins might become a narrow, complex shape due to the installation of the wire spacer. Then, the fuel pin could be damaged if a mismatch between the output and the flow rate occurred by some event such as deformation of the coolant flow path for the high burn-up. To evaluate the structural integrity of the fuel pins, it is important to clarify the flow field in this narrow and complex flow path. However, no techniques have been developed for visualizing such a narrow and complex area to obtain the verification data of the analysis codes in past studies.

The flow field was measured by particle image velocimetry (PIV) in the subchannel around the wrapping wire of the three-pin bundle water model (Fig.7-8(a)), which simulated the simplest system of the fuel pins (Fig.7-8(b)) in this study.

The test section comprised an irregular hexagonal acrylic duct tube and fluoropolymer resin pins that had nearly the same refractive index as that of water and had a high light-transmission rate. This refractive index matching enabled us to visualize the inner subchannel through the outer pins with a high degree of accuracy.

As a result, two types of characterized flow field data (the flow velocity distribution and fluctuation intensity) were successfully obtained. One is a relatively stable spiral flow around the pin and the other is a disordered swirl flow around the wire. As an example, the experimental (Fig.7-9(c)) and analytical results obtained by SPIRAL (a finite element analysis code) (Fig.7-9(d)) for the flow velocity distribution near the wire wound on the C-Pin are compared. The two results are in good agreement, and are hence considered to have verified the efficacy of this code.

Verification and validation (V&V) research has focused on the development of a safety assessment analysis code for nuclear power facilities, especially in recent years. Standardization of V&V has been underway in Japan and overseas.

In this way, the results of this study contribute to the promotion of fast reactor development by helping to validate analysis codes as basic technology and to the establishment of a standard for V&V.

Reference

Nishimura, M. et al., Study on Flow in the Subchannels of Pin Bundle with Wrapping Wire, Proceedings of 9th Korea–Japan Symposium on Nuclear Thermal Hydraulics and Safety (NTHAS–9), Buyeo, Korea, 2014, paper N9P0087, 7p., in CD–ROM.

7–4 Physics-Based Simulation of Interfacial Dynamic Motion

— Development of a Mechanistic Evaluation Method for Gas Entrainment Phenomena in a Fast Reactor —

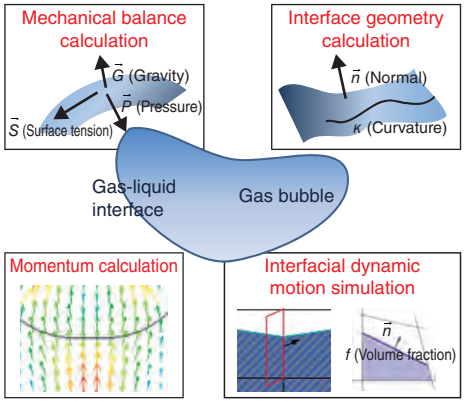

Fig.7-10 Conceptual diagram of a high-precision simulation method
In our study, various physical behaviors at a gas-liquid interface are modeled.

Table 7-1 Numerical error in a slotted-disk revolution problem
The numerical error in the slotted-disk problem is calculated as the discrepancy in the disk shape before and after one full revolution. The present method provides high simulation accuracy even on an unstructured mesh where the numerical error tends to be large due to mesh distortion.

Simulation Method	Mesh	Numerical error
Conventional		
SOLA-VOF	Structured	9.62×10^{-2}
PLIC	Structured	1.09×10^{-2}
Parker-Youngs	Unstructured	1.23×10^{-2}
Present	Unstructured	0.95×10^{-2}

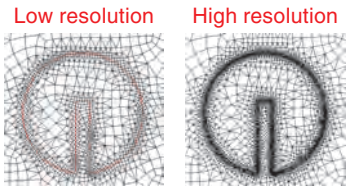

Fig.7-11 Reproduction of a slotted-disk shape with an adaptive mesh scheme
The shape of the slotted-disk can be reproduced well with an adaptive mesh scheme that automatically refines the computational cells near an interface.

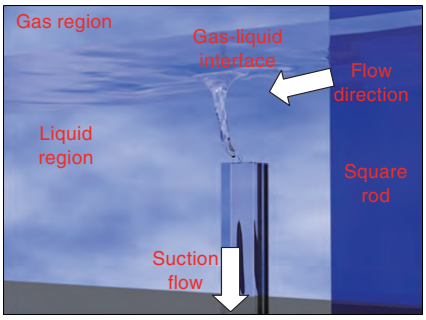

Fig.7-12 Simulation result of gas entrainment due to interface elongation along the vortex core
We have simulated the onset of the gas entrainment caused by an intensified vortex in the wake flow behind a square rod.

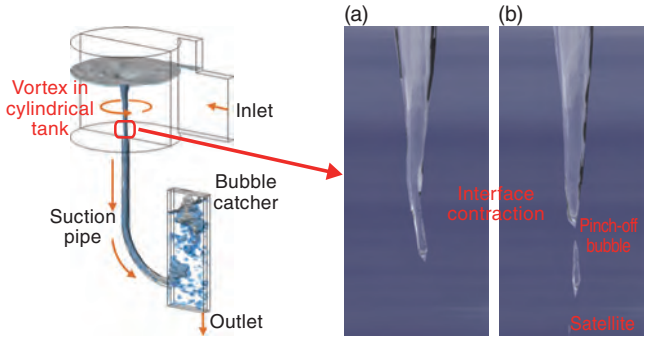

Fig.7-13 Simulation result of bubble pinch-off
The bubble pinch-off at the tip of an elongated interface is well simulated, and the dynamic interfacial motion is evaluated on the basis of the simulation result.

Thanks to significant advances in computer performance and numerical simulation techniques, numerical simulations of complicated nonlinear phenomena can be performed in recent years. Therefore, we are developing specialized simulation codes to address several thermal-hydraulics issues in sodium-cooled fast reactors (SFRs). One most important issue is the gas entrainment (GE) at the cover gas-coolant interface, wherein a highly intensified vortex induces interface elongation along the vortex core and the bubble pinch-off (entrainment) occurs at the tip of the elongated interface. The entrained gas bubbles may cause disturbances in the reactor power or degradation of the heat exchanger efficiency, and therefore, the occurrence of GE should be suppressed in SFRs. Therefore, we are developing a high-precision numerical simulation method for gas-liquid two-phase flows to evaluate the GE occurrences in SFRs and to enhance the safety of SFRs by establishing a GE-free design.

There are various simulation models for gas-liquid two-phase flows. Among them, we have chosen the volume-of-fluid method, a well-used interface-tracking method, to accurately simulate the interfacial dynamic motion. In addition, the unstructured mesh scheme is employed to treat exact structural geometry in numerical simulations. Fig.7-10 shows the conceptual diagram of our high-precision simulation method for gas-liquid two-phase flows wherein various physical behaviors, e.g., the interfacial shape change, are modeled accurately on the basis of rigorous conservation equations. Such an accurate model can perfectly eliminate unphysical behaviors, e.g., the spurious current observed in conventional simulation results. More importantly, the grid convergence of the numerical solution is achieved by our method. As a result, it is shown in Table 7-1 and Fig.7-11 that our high-precision simulation method provides at least 20%–30% smaller numerical error than the conventional simulation codes for the well-known slotted-disk revolution problem.

The GE phenomena in elemental experiments are also simulated, as shown in Figs.7-12 and 7-13. The simulation results show that the interface elongation along the vortex core (Fig.7-13(a)) is well reproduced and that the bubble pinch-off at the tip of the interface (Fig.7-13(b)) can be evaluated. In addition, the entrained gas flow rate in the simulation result agrees well with the experimental data, that is, we can achieve a simulation-based evaluation of the GE phenomena in SFRs.

Reference

Ito, K. et al., A High–Precision Calculation Method for Interface Normal and Curvature on an Unstructured Grid, Journal of Computational Physics, vol.273, 2014, p.38–53.

7–5 Safety Study of Extraction Chromatography Technology for a Partitioning Process
— Behavior of Heat, Hydrogen Gas, and Degradation Products in a Separation Column —

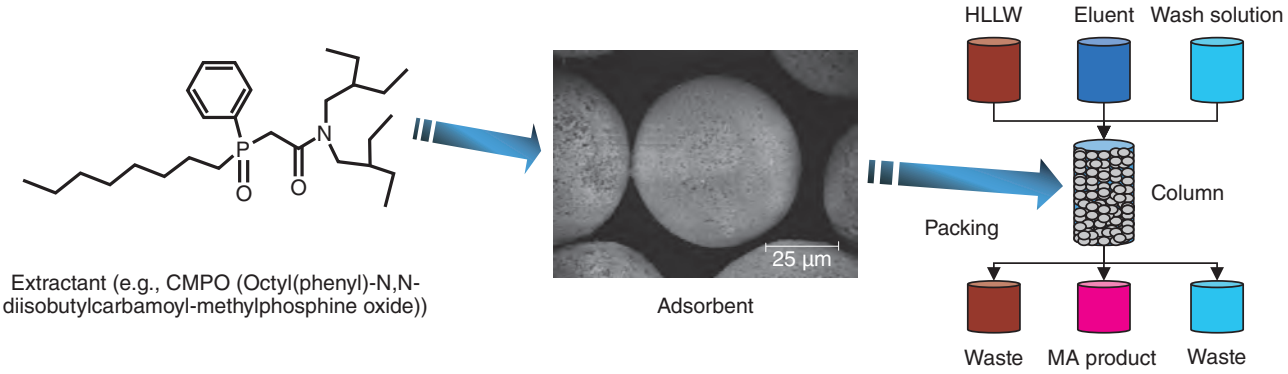

Fig.7-14 Extraction chromatography technology for MA partitioning
MAs in high-level liquid waste are extracted by an extractant impregnated into adsorbents. MAs are recovered through adsorption/elution reactions inside the packed column.

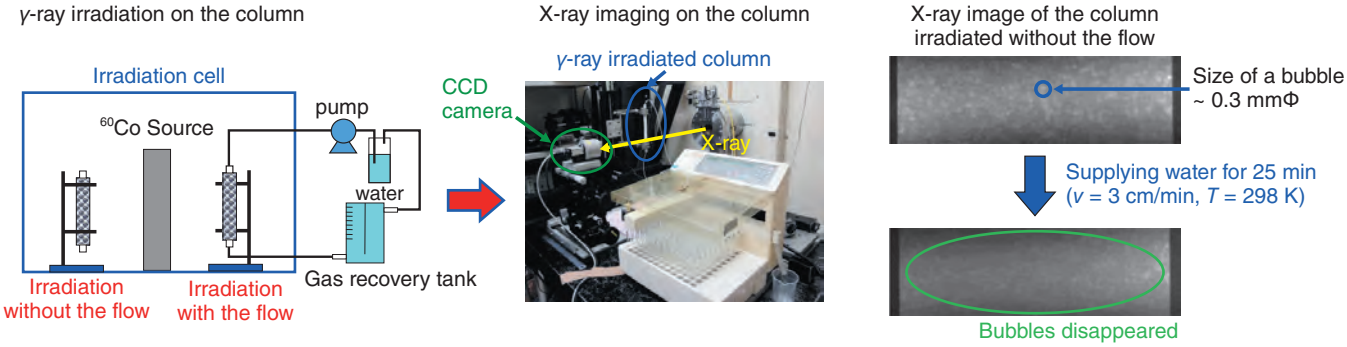

Fig.7-15 *γ*-ray irradiation and X-ray imaging of the column
X-ray imaging experiments on a *γ*-ray irradiated column reveal the distribution of bubbles generated inside the column by irradiation.

Partitioning and transmutation technology, which is used for the recovery process of actinides or long-lived fission products from spent nuclear fuel and transmutation processes of those nuclides by neutron irradiation, is expected to reduce the volume and potential hazard of nuclear waste. We are developing extraction chromatography technology for the recovery of minor actinides (MAs).

This technology employs silica-based adsorbents, and MAs in high-level liquid waste are selectively recovered in a product solution using a chromatographic operation (Fig.7-14).

Since the radioactive elements are treated by adsorbents containing organic compounds, generation and accumulation of decay heat, hydrogen gas, and degradation products of the organic compounds inside the packed column may be unavoidable. Those phenomena cause a potential risk of lead fire or explosion; thus, we have been focusing on the safety of the extraction chromatography system to prevent hazardous accidents.

The behavior of gas inside the extraction chromatography column was investigated through X-ray imaging on the *γ*-ray irradiated column and computational fluid dynamics (CFD) simulation. Although gas is generated by radiolysis and accumulated inside the packed column after the operation is ceased, the supply of a coolant has been revealed to be an effective means of discharging this gas (Fig.7-15). CFD simulation shows that decay heat accumulating due to the stopping of the flow was simultaneously discharged with the gas. Continuous flow is essential for preventing the accumulation of heat and hydrogen gas, and the equipment for feeding coolant must be effective in the case of irregular stoppages of the operation caused by accidents with the pumps.

Degradation products produced by the radiolysis of organic compounds were analyzed in the irradiated adsorbents using *γ*-rays or He^{2+} ion beams by the GC/MS, NMR, and FT-IR methods. Chemical species with low flash or ignition points were not confirmed. It was found that the radiolysis of the organic compounds should not cause fire or explosions. Further investigations of the degradation mechanism of the adsorbents should be undertaken to secure the safety of the extraction chromatography technology.

Reference

Watanabe, S. et al., Safety Operation of Chromatography Column System with Discharging Hydrogen Radiolytically Generated, Proceedings of 2015 International Congress on Advances in Nuclear Power Plants (ICAPP 2015), Nice, France, 2015, paper 15241, 8p., in CD-ROM.

7–6 Quantification of Oxygen Behavior in Nuclear Fuel
— Measurement of Oxygen Diffusion Coefficients in the Mixed Oxide Fuel —

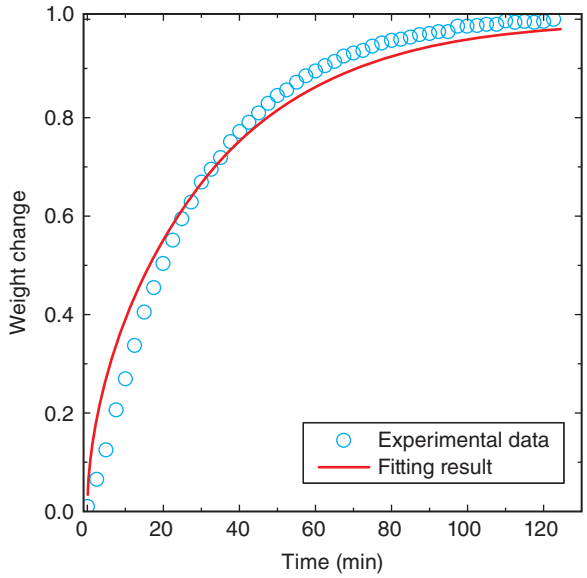

Fig.7-16 Measurement data and fitting results
○ indicates that the weight change of Am-containing PuO_2 at 1500 °C. —— indicates a nonlinear curve-fitting result.

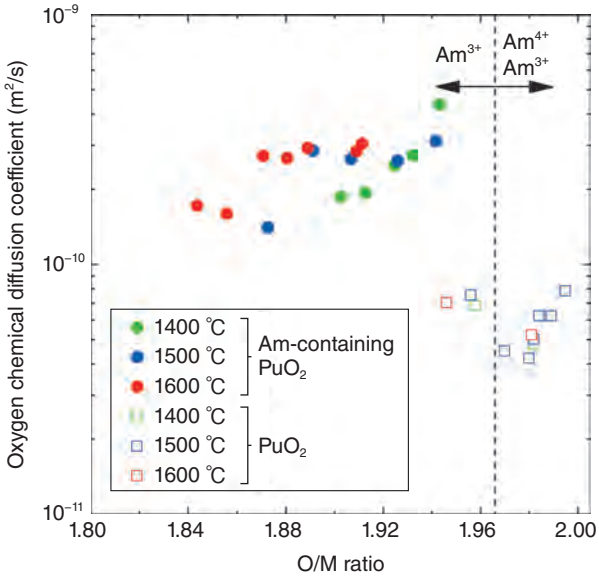

Fig.7-17 Relation between the oxygen chemical diffusion coefficient and the O/M ratio
The oxygen chemical diffusion coefficients of Am-containing PuO_2 slightly decreased with the O/M ratio. All Am ions were present in the trivalent state (Am^{3+}) in the region below O/M ratio = 1.964. This value is indicated by a ------ .

We have performed R&D on oxide fuel containing large amounts of minor actinides (MAs) including Neptunium (Np) and Americium (Am) as a step toward volume reduction and mitigation of the degree of harmfulness of radioactive waste. MAs have a significant effect on the physical and chemical properties of oxide fuel. The Am influences the stability of fission products as well as the fuel behavior, such as fuel-clad chemical interaction (FCCI), during irradiation processes, because it increases the oxygen potential of the fuel. To understand the physical and chemical properties of Am-containing oxide fuel in more detail, it is necessary to precisely measure the oxygen chemical diffusion coefficient, which is an important property in fuel fabrication and evaluation of irradiation behavior.

In this study, we obtained the oxygen chemical diffusion coefficients of the Am-containing PuO_2 using the latest technology. The specimen's weight changed due to oxygen-release into the atmosphere through its surface in the reduction atmosphere. This weight-change was analyzed using a nonlinear curve-fitting method to obtain the oxygen chemical diffusion coefficient (Fig.7-16).

Fig.7-17 shows the oxygen to metal (Pu, Am) ratio (O/M ratio)-dependence of the obtained oxygen chemical diffusion coefficients in the temperature range from 1400 °C to 1600 °C. The oxygen chemical diffusion coefficients of Am-containing PuO_2 were greater than those of PuO_2 and did not have a clear temperature dependence.

Although the oxygen chemical diffusion coefficients of PuO_2 depended on the O/M ratio, those of Am-containing PuO_2 did not have the same trend as PuO_2. From the results of Fig.7-17, it was found that the oxygen chemical diffusion coefficients of Am-containing PuO_2 were plotted in the region where all Am ions were present in the trivalent state. In addition, those of Am-containing PuO_2 were greater than those of PuO_2. Therefore, it seems that the increase of the oxygen chemical diffusion coefficient was caused by the presence of the trivalent Am ion.

We are going to conduct this test under a wide range of temperatures and O/M ratios to clarify the mechanism by which Am affects the oxygen chemical diffusion coefficient.

Reference

Watanabe, M. et al., Oxygen Chemical Diffusion Coefficients of (Pu, Am) O_2 Fuels, NEA/NSC/R(2015)2, 2015, p.376–380.

7–7 Improvement of the Thermal-Hydraulic Analysis Technique for the Coolant in FBR Components

— Evaluation of the Coolant Thermal-Hydraulics of the "MONJU" Reactor Upper Plenum using an Analytical Model —

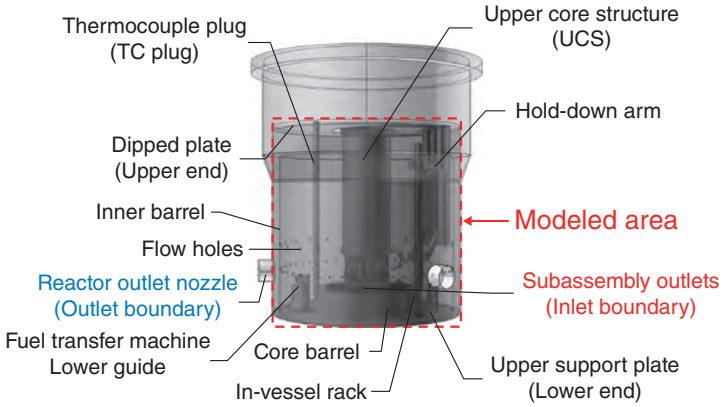

Fig.7-18 Overview of the reactor upper plenum
The structures such as the hold-down arm and the upper core structure (UCS) are installed even during operation. In this test, the sodium temperature distribution was measured by thermocouples on the thermocouple plug (TC plug).

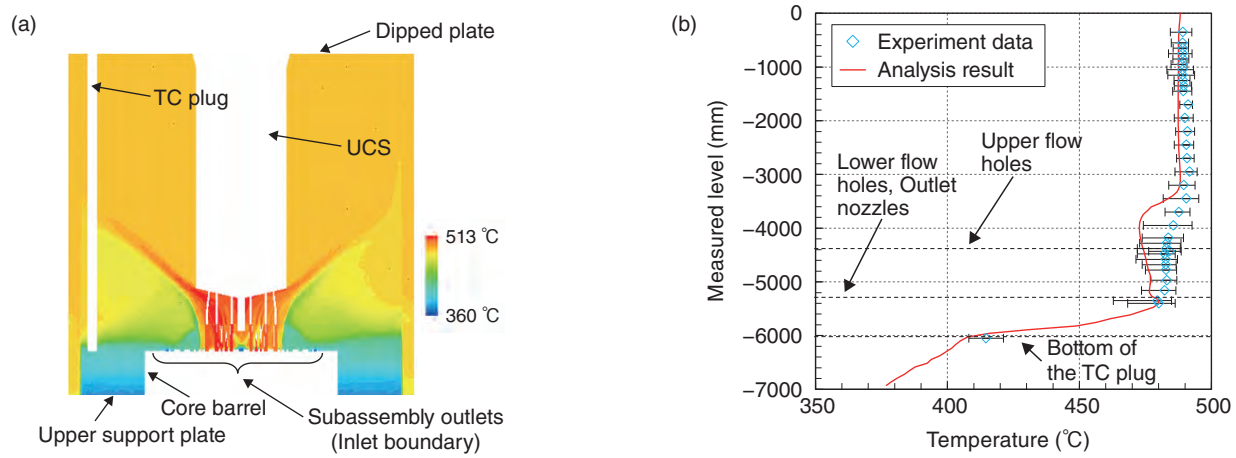

Fig.7-19 Analytical results of the temperature distribution
In (a), lower temperature sodium stagnated over the upper support plate. In (b), the analysis results were compared with the temperature measured along the TC plug. The analysis results agreed well with the measured data within the error bars.

In fast breeder reactors (FBRs), thermal-hydraulic phenomena such as thermal stratification may cause unacceptable sodium temperature distributions under certain conditions, resulting in significant thermal stress in the components. Therefore, it is very important to evaluate thermal-hydraulics in detail. However, performing the test with a model of the same size is unrealistic because such testing would require unrealistic cost and time. Hence, an analytical method for predicting the spatial sodium temperature distribution with good accuracy should be developed. The system start-up tests under a 40% rated power operation condition were conducted in the Japanese prototype FBR, "MONJU".

There is a large volume in the upper plenum of the reactor vessel (RV), as shown in Fig.7-18. The sodium temperature distribution in the vertical direction of the upper plenum was measured with the TC plug (Fig.7-19(b)) in these tests. Since various structures such as the UCS and the hold-down arm are installed in the plenum even under operation, the sodium thermal-hydraulic behavior is complicated. In this study, we developed a three-dimensional analysis model to accurately evaluate the thermal-hydraulics. Since the present calculation condition is steady state, the heat capacity of the structures is negligible. Therefore, we modeled only the shape of every structure except for the inner barrel in the plenum. However, the inner barrel is so thin that thermal conduction is non-negligible, and hence, it was modeled as a solid material. The RV is covered by a thermal insulator, and the amount of heat released from the RV was estimated to be very small. Therefore, the RV wall was modeled as being adiabatic. The flow rates and outlet temperatures of all subassemblies were estimated based on the measured total flow rate of the primary heat transport system, and they were set as the inlet boundary conditions of this analytical model. The measured data were compared with the analytical results for the validation. The analytical results and the measured temperature are shown in Fig.7-19. The range of error bars is twice the standard deviation of the observed temperature fluctuation. From the analysis result, it was found that the lower temperature sodium stagnated over the upper support plate (Fig.7-19(a)), and the analytical results agreed well with the measured data (Fig.7-19(b)). Thus, it is estimated that the present analysis model is applicable for predicting the thermal-hydraulics of the RV upper plenum under the present conditions.

We are going to perform analyses of the plant trip test from the 40%-rated operational conditions to validate the present analytical model and evaluate the thermal stratification behavior as a future subject.

Reference

Honda, K. et al., An Investigation of Thermal–Hydraulics Behavior of MONJU Reactor Upper Plenum under 40%–Rated Steady State, Proceedings of 10th International Topical Meeting on Nuclear Thermal–Hydraulics, Operation and Safety (NUTHOS–10), Ginowan, Japan, 2014, NUTHOS10–1114, 12p., in USB Flash Drive.

8 Research and Development Related to the Backend of the Nuclear Fuel Cycle and the Reprocessing of Spent Nuclear Fuel

Progress in the Decommissioning of Nuclear Facilities and the Treatment and Disposal of Radioactive Waste

Safe and efficient decommissioning of our nuclear facilities and treatment and disposal of radioactive wastes are important issues to consider in our research and development (R&D) activities. We are currently setting up systems to accomplish these goals and are also developing the related technologies (Fig.8-1).

Furthermore, we will be responsible for disposing of radioactive waste generated not only from our research facilities but also from universities, industrial facilities, and other sites.

R&D for the decommissioning of nuclear facilities

We have developed an engineering system for decommissioning and an evaluation system for clearance. It is important to assess the applicability of these systems to the decommissioning of our nuclear facilities such as the Fugen Nuclear Power Plant.

In the Fugen Nuclear Power Plant, to properly operate the clearance system, the target nuclides for evaluation were selected and a method for evaluating their radioactive concentrations was established (Topic 8-1).

The Ningyo-toge Environmental Engineering Center has been managing the Ningyo-toge Uranium Mine, now out of service for mining, in accordance with the mine safety law.

For the remediation of the Yotsugi Mill Tailings Pond multi-layered capping was constructed to reduce rainwater penetration to lower the burden of water treatment and to reduce radon exhalation and dose rates. Only natural materials have been used for the capping for long-term stability after remediation. As for the structure, multi-layered capping wherein each layer has a different purpose was adopted. At present, the monitoring of several items including the concentration rates of elements in the water has been continued to verify the effectiveness of the capping (Topic 8-2).

R&D for characterization of radioactive waste

For safe disposal of radioactive wastes, it is necessary to understand their nuclide compositions. Therefore, we developed related techniques to enable reasonable and effective analysis.

To reduce the radiation exposure of operators during an analytical procedure, a simple and rapid analytical method with capillary electrophoresis has been developed to measure the concentration of neodymium (Nd) contained in the radioactive waste.

According to this analytical method, Nd was separated from various coexisting elements and detected (Topic 8-3).

Disposal of low-level radioactive waste

Before radioactive wastes are disposed of, their radioactivity concentrations must be confirmed to be less than acceptance criteria for some important radioactive nuclides.

Therefore, appropriate evaluation methods for 16 radioactive nuclides in metal wastes generated from Japan Power Demonstration Reactor (JPDR) dismantling were established as a combination of the Scaling Factor method (SF method), the mean activity concentration method, and the theoretical method (Topic 8-4).

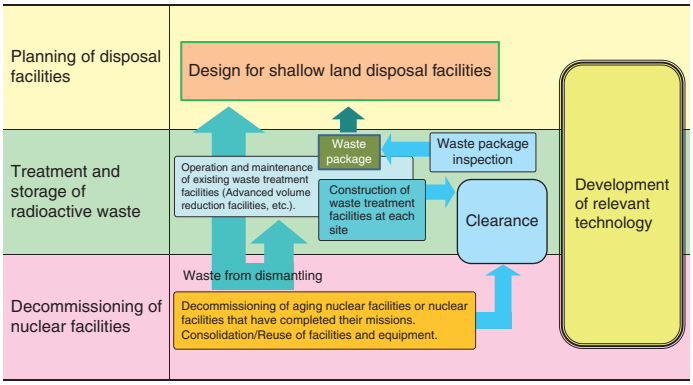

Fig.8-1 Outline of measures for the decommissioning of nuclear facilities and the treatment and disposal of radioactive waste
We are establishing systems to decommission nuclear facilities and manage radioactive waste. In addition, we are developing related technologies (e.g., decommissioning, treatment, and disposal) and constructing radioactive waste treatment and disposal facilities.

R&D to Improve Technology and Reliability of Geological Disposal in Japan

Geological disposal is one option for long-term isolation of high-level radioactive waste (HLW) produced during nuclear power generation from human environments. This is a critical issue with which the present generation must sensibly deal and it will remain crucial despite any revision of the national nuclear energy policy. In Japan, spent fuel from power reactors is reprocessed to extract reusable uranium (U) and plutonium (Pu) for power generation. The liquids separated from the spent fuel during chemical reprocessing are solidified into a stable glass form. Under the Japanese disposal concept, vitrified wastes are then encapsulated in a thick steel overpack surrounded by highly compacted bentonite and placed in a stable geological environment at more than 300 m below the surface (Fig.8-2). Implementing geological disposal of HLW is a long-term project that will last over 100 years. The project begins with site selection and continues to repository construction and operation, which will be followed by backfill for repository closure. It is thus of great importance to proceed efficiently with the project as a national responsibility by continuously improving its sound technical basis and applying

these attitudes to implementation, regulatory activities, and, most importantly, enhancement of public confidence. To this end, we have made and will continue to make steady progress in R&D in various fields, including geoscience, repository engineering, and safety assessment, to improve the technologies used for reliable geological disposal in Japan.

At present, our R&D focuses specifically on projects at two underground research laboratories (URLs)—one at Mizunami, which researches crystalline rocks, and the other at Horonobe, which researches sedimentary formations (Fig.8-3). At the end of 2014, excavation of galleries at a depth of 500 m at Mizunami had been finished, and preparation of research galleries at a depth of 350 m at Horonobe had been completed. Multidisciplinary investigations are ongoing, because the reliability of various investigative techniques should be tested and verified before the site characterization program begins (Topics 8-5, 8-6, 8-7, and 8-8). In addition, studies on tectonics, volcanic and faulting activities, and the like are in progress to evaluate the long-term stability of geological environments in Japan (Topic 8-9). The Toki Research Institute of Isotope Geology and Geochronology (TRIGGER) was established in November 2014 for the development of dating techniques using advanced equipment for isotope geology and geochronology. In parallel with such geoscientific efforts, we are conducting an extensive study to assess the performance of the disposal system, of engineered barrier systems, and of the long-term chemistry and migration of radionuclides at Tokai to expand our knowledge base for geological disposal

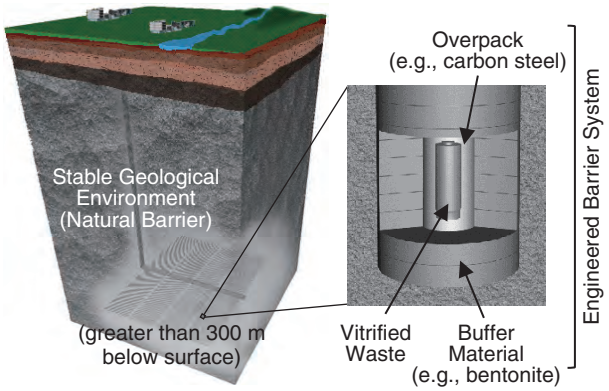

Fig.8-2 Schematic view of the basic concept for the geological disposal of high-level radioactive waste (HLW) in Japan

(Topics 8-10, 8-11, and 8-12). These studies exploit data and information about geological environments that were obtained through geoscientific research at both URLs. The prototype knowledge management system that was developed in 2010 is being improved to systematically provide and transfer multiple associated R&D results to both implementers and regulators and to ensure their safety. Furthermore, the results of the R&D activities have been summarized as an unconventional web-based report (CoolRepH26), which has been available on Japan Atomic Research Agency (JAEA)'s public website since March 2015.

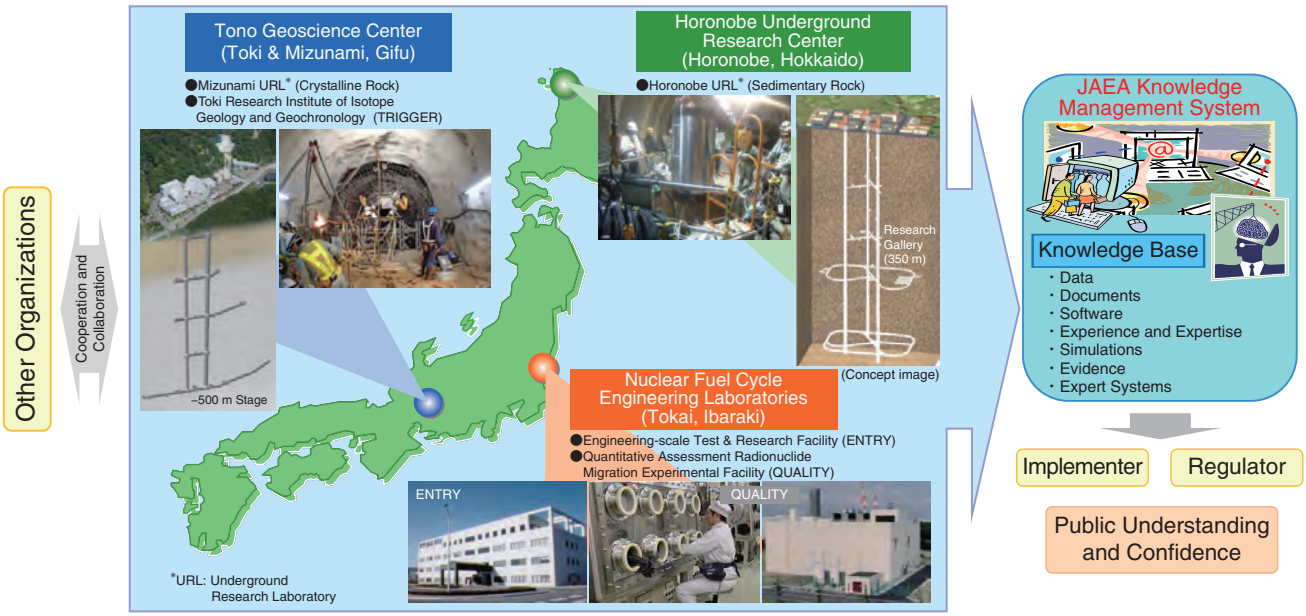

Fig.8-3 System for implementing JAEA R&D activities

Implementing Safety Measures at the TRP and Enhancing Reprocessing Technologies

After the Great East Japan Earthquake and the accident at the Fukushima Daiichi Nuclear Power Station of Tokyo Electric Power Company, Incorporated, various emergency safety measures were implemented at the Tokai Reprocessing Plant (TRP).

To reduce the probability of hazards at the TRP, efforts have been focused on solidifying and stabilizing the highly active liquid waste (HALW) at the Tokai Vitrification Facility and the Pu solution at the Plutonium Conversion Development Facility as soon as possible.

Vitrification of all the stored HALW is estimated to require two decades. Thus, an advanced glass melter is under development to make steady progress on the solidification and stabilization of the HALW.

For low-level radioactive effluents, a cement-based solidification method accompanying a nitrate-ion decomposition process has been developed to reduce the environmental impact.

As an effort to improve reprocessing technologies, the rate constant of Pu extraction has been studied using a microchip. The results obtained in this study indicate that the microchip can be an effective tool for studying the Pu rate constant as well as analyzing radioactive elements (Topic 8-13).

8–1 Toward the Application of a Clearance System to the Fugen Nuclear Power Plant

— Establishment of an Evaluation Method for Radioactive Concentration on the Contamination of a Turbine System —

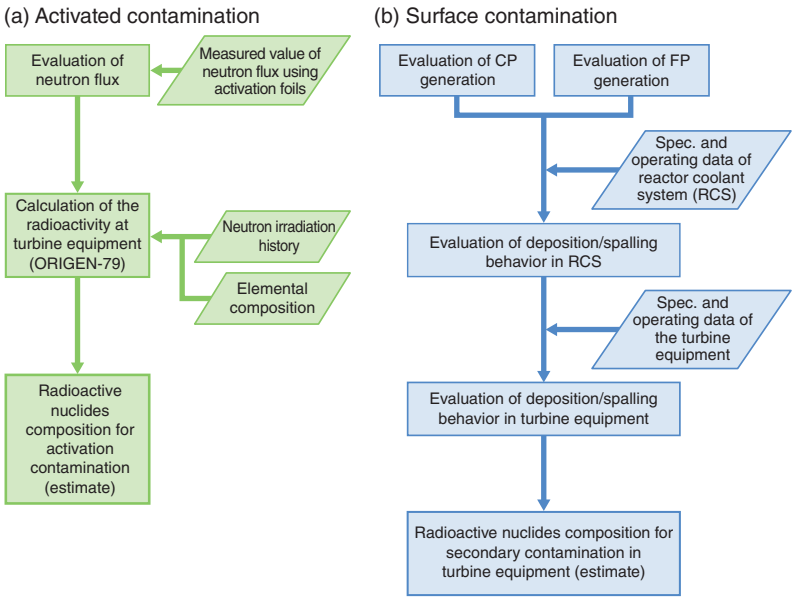

Fig.8-4 Flow diagram for evaluating contamination
We set the evaluation method for both activated contamination and surface contamination with consideration of the characteristics of the turbine system.

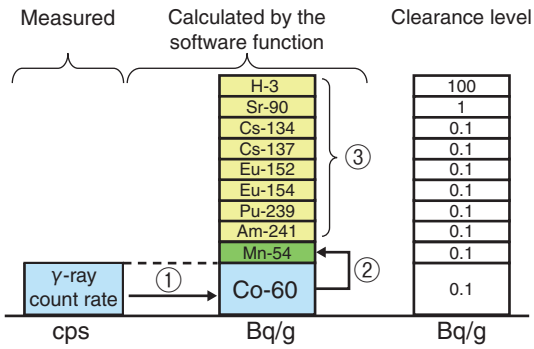

① Co-60 is directly measured by the clearance monitor.

② The radioactive concentration of Mn-54 is evaluated by multiplying the ratio of Mn-54/Co-60 by the measured radioactive concentration of Co-60.

③ Other 8 nuclides (H-3, Sr-90, Cs-134, Cs-137, Eu-152, Eu-154, Pu-239, and Am-241) are evaluated as the average value of the sample data including detector limit data.

Fig.8-5 Evaluation of Nuclide Concentration
We set the evaluation method for the radioactive concentration using the procedure shown from ① to ③ .

At the Fugen Nuclear Power Plant (NPP), we plan to conduct appropriate classification of the waste according to the contamination level of the material of the plant to reduce the amount of radioactive waste and to rationally and efficiently promote dismantling work. For this reason, we are going to apply the clearance system to the material generated by the dismantling of the turbine system to reduce the radioactive waste amount as much as possible.

To properly operate the clearance system, the target nuclides for evaluation need to be selected accurately and a method for evaluating their radioactive concentration should be established.

To select the target nuclides for evaluation, we investigated both activated contamination and surface contamination with consideration of the plant characteristics.

For evaluating the activated contamination, we selected the main steam pipe, where neutron flux is the highest in the turbine system, as evaluation point considering the effect of activation by neutrons induced by the β-decay of N-17, which exists to a slight degree in the steam. Then, taking the neutron spectrum at this point, we calculated the estimated radioactivity for activated contamination in the turbine system using the calculation code "ORIGEN-79" (Fig.8-4(a)).

For evaluating the surface contamination, we regarded radioactive corrosion products (CP) and fission products (FP) as the origin of the contamination and the standardized migration behavior of CP and FP, and calculated the estimated radioactivity for surface contamination in the turbine system (Fig.8-4(b)).

As a result, we have selected 10 significant nuclides, including H-3, Mn-54, Co-60, Sr-90, Cs-134, Cs-137, Eu-152, Eu-154, Pu-239, and Am-241 as the target nuclides for evaluation based on the calculated radioactivity.

Then, to carry the clearance material out of "Fugen", we need to establish an evaluation method for the radioactive concentration to judge reasonably and surely whether the radioactive concentration of the dismantled material in them is less than the clearance level.

As a result of measurements on actual contamination and so on and because "Fugen" has a very low degree of contamination outside of the reactor core, we can detect only Co-60 and Mn-54 in the turbine system. Co-60 is the primary nuclide of "Fugen" and Mn-54 correlates with Co-60.

The other eight nuclides were not detected in the turbine system. Therefore, we set the method of evaluating the radioactive concentration conservatively for such nuclides, i.e., calculating the average radioactive concentration including the detection limit in the measurements.

As a result, we were able to set the method for properly evaluating the radioactive concentrations in turbine system (Fig.8-5).

In the near future, using this evaluation method, we plan to start the application of the clearance system to the dismantled equipment of the Fugen NPP.

Reference

Hayashi, H. et al., Application of Measurement and Evaluation Method on the Clearance System of the Fugen NPP for Dismantled Equipment of Turbine System, Proceedings of 23rd International Conference on Nuclear Engineering (ICONE 23), Chiba, Japan, 2015, ICONE23–1488, 7p., in DVD–ROM.

8–2 Remediation of Mill Tailings Pond in a Closed Uranium Mine
— Capping Construction using Natural Material for Long-Term Stability —

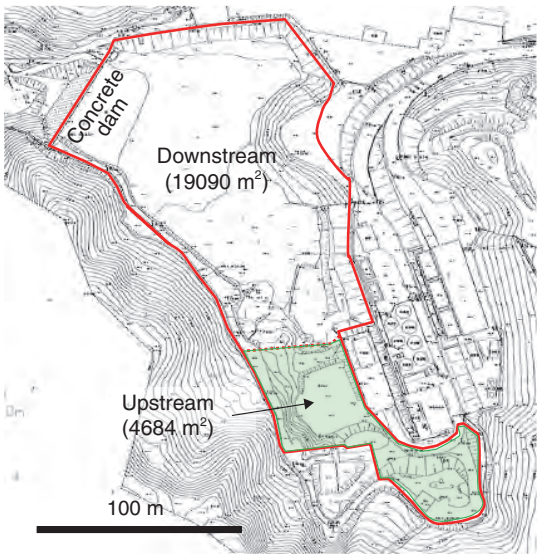

Fig.8-6 Yotsugi Mill Tailings Pond
The Pond is composed of "Upstream" (green-colored part) and "Downstream" areas. Mill tailings are deposited behind the concrete dam.

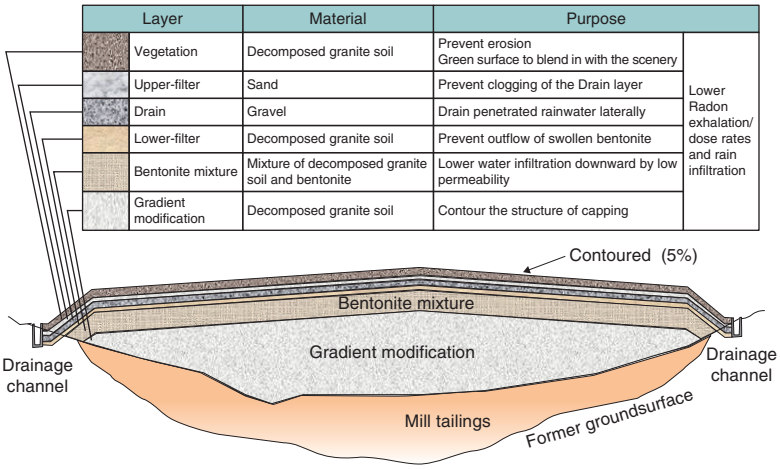

Fig.8-7 Structure and material of the capping constructed "Upstream"
Multi-layered capping was adopted wherein each layer has a respective material and purpose. It has convex shape to drain penetrated rainwater.

Ningyo-toge Environmental Engineering Center has been managing the Ningyo-toge Uranium Mine, now out of service for mining, in accordance with the Mine Safety Law. In parallel, the center has been conducting remediation activities to ensure the radiation protection from the exposure pathways to humans in the future and to prevent the occurrence of mining pollution.

Remediation has been planned not only to ensure safety required by the Mine Safety Law but to make it most appropriate technologically and economically. Among mine-related facilities subject to remediation, the highest priority has been placed on the Yotsugi Mill Tailings Pond, which is located upstream of the Yoshii-gawa River, one of the largest rivers in the Okayama Prefecture.

As part of the Pond, a concrete dam was directly constructed on geologically stable basement rock. Behind the dam, mill tailings generated through mining activities have been deposited. Moreover, mine water generated from former mine-mouths has been temporally impounded so that the Pond can be used as a buffer reservoir before being transferred to the Water Treatment Facility.

For the remediation of the Pond, a multi-layered capping was constructed "Upstream" between FY 2011 and FY 2012, wherein mill tailings were dominated by sand-grained material and not submerged. Its purpose was to reduce rainwater penetration to lower the burden of water treatment and to reduce radon exhalation and dose rates below 1 mSv/year without background (Fig.8-6).

Only natural materials have been used for the capping for long-term stability after remediation. As for the structure, a multi-layered capping was adopted with each layer having a separate purpose (Fig.8-7). Among the layers, the Bentonite mixture layer is mainly composed of bentonite, which is a kind of clay mineral that has a swelling property when soaked in water. It is expected that the layer should lower the degree of rainwater penetration from its surface downward and exhalation of radon gas generated from the mill tailings upward.

Above the Bentonite mixture layer, a "Drain layer" is set using gravel to drain penetrated rainwater laterally into a newly constructed drainage channel around the Pond. In addition, the structure of whole capping was composed with a convex shape with a north–south ridge to reduce the water amount that flows into the mill tailings to minimize the burden on the Water Treatment Facility.

At present, monitoring is being continued to verify the effectiveness of the capping in terms of several items, including settlement amount, drainage water amount, concentration rate of elements in the water, and dose rate. The monitoring will be continued to accumulate data for the abovementioned items, and the data is to be used for future remediation of the "Downstream" area, with revision of its specifications if necessary.

Reference

Saito, H. et al., Remediation Strategy, Capping Construction and Ongoing Monitoring for the Mill Tailings Pond, Ningyo-toge Uranium Mine, Japan, Proceedings of 15th International Conference on Environmental Remediation and Radioactive Waste Management (ICEM 2013), Brussels, Belgium, 2013, ICEM2013-96021, 4p., in CD-ROM.

8–3 Rapid Understanding of Nuclide Composition in Radioactive Wastes
— Development of an Analytical Method with Capillary Electrophoresis —

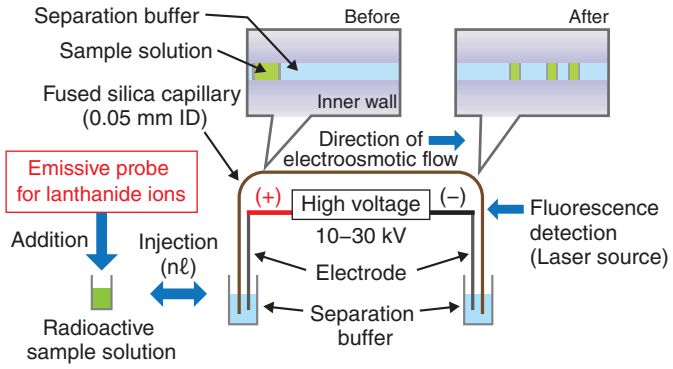

Fig.8-8 Development of a simple and rapid analytical method with CE
CE is a high-performance separation technique using differences in electrophoretic speed due to ionic charge and size in a capillary tube with a small internal diameter. This method needs a very small sample volume and compact equipment.

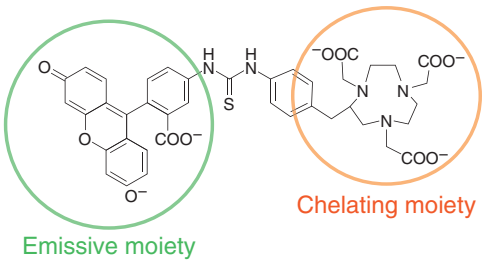

Fig.8-9 Emissive probe L for a Nd ion
The probe L has an emissive moiety for improving sensitivity and a cyclic hexadentate chelating moiety for connecting with Nd ions.

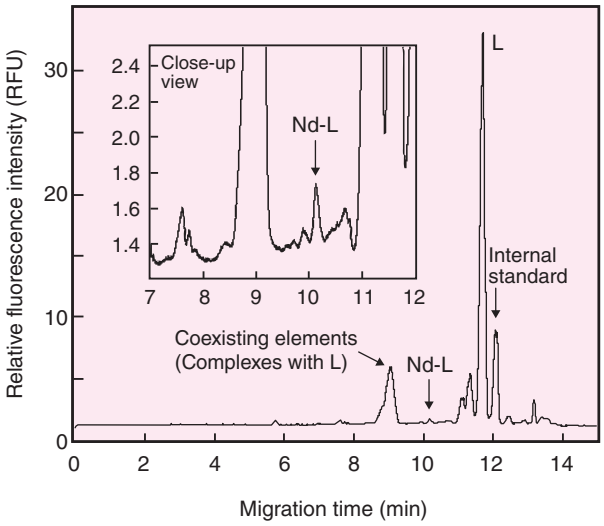

Fig.8-10 Typical electropherogram of a Nd complex with probe L
A successful separation and detection of Nd was performed using the emissive probe L in a spent nuclear fuel sample composed of various coexisting elements. The Nd-L shows a Nd complex with probe L.

For safe disposal of radioactive waste, it is necessary to understand their nuclide compositions. It has been suggested that the nuclide composition in contaminated wastes generated from spent nuclear fuel reprocessing facilities can be estimated from the concentration of neodymium (Nd) related to the burnup (degree of fuel consumption). For the analysis of the Nd in spent nuclear fuel samples, it has to be separated from various other coexisting elements, especially lanthanides (Ln) with similar chemical properties and the large excess of uranium (U) in the sample. To reduce the radiation exposure of operators during the analytical procedure, a simple and rapid analytical method with capillary electrophoresis (CE) has been developed (Fig.8-8); however, the conventional CE method using absorbance detection has a sensitivity that is too low.

This study focuses on the CE-laser-induced fluorescent detection method (CE-LIF) to drastically improve the sensitivity. Emissive probes for detecting Ln ions, especially Nd ions, suitable for CE-LIF were developed. The emissive probes designed for CE-LIF are composed of an emissive moiety for improving sensitivity, a chelating moiety for connecting with Ln ions, and a spacer between them. The chelating moiety, which is most important, is required for high selectivity of Ln as compared with U. In this study, a cyclic hexadentate probe is synthesized (Fig.8-9). We find that each Ln complex with the probe moved at a different electrophoretic speed by reaction with hydroxide ions in the separation buffer. A suitable pH of the separation buffer enabled a successful detection and separation of Nd in a spent nuclear fuel sample (Fig.8-10). This method with small sample volume and a short analytical time (about ten minutes) has great potential to be applied to analysis of radioactive waste samples for reducing the radiation exposure of operators.

This study was accomplished as part of a collaborative research with Saitama University, entitled “Separation and Detection System for Actinide Ions by Capillary Electrophoresis using Novel fluorescent Probes”.

Reference

Haraga, T. et al., Application of Capillary Electrophoresis with Laser–Induced Fluorescence Detection for the Determination of Trace Neodymium in Spent Nuclear Fuel using Complexation with an Emissive Macrocyclic Polyaminocarboxylate Probe, Analytical Sciences, vol.30, no.7, 2014, p.773–776.

8–4 Development of Reasonable Confirmation Methods Concerning Radioactive Wastes

— Study of Evaluation Methods to Determine the Radioactivity Concentrations of Radioactive Wastes Generated by Research Reactors —

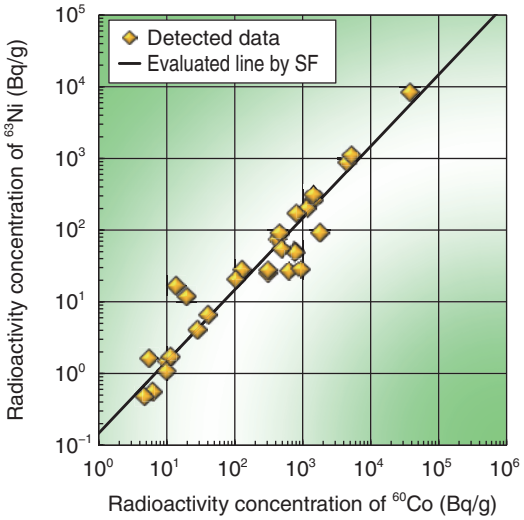

Fig.8-11 Application example of the SF method for ^{63}Ni
The radioactivity concentration of ^{63}Ni measured by radiochemical analysis of metal wastes generated from JPDR was shown to have good linear correlation with that of ^{60}Co, which uses the same production mechanism. From this result, the SF method was adopted into the confirmation system for ^{63}Ni.

Table 8-1 Evaluation methods for radioactive wastes generated from JPDR dismantling
Appropriate evaluation methods for 16 radioactive nuclides in metal wastes generated from JPDR dismantling were established as a combination of the SF method, the mean activity concentration method, and the theoretical method.

Nuclides *1		Evaluation methods	Nuclides *1		Evaluation methods
^{3}H	β-rays	The mean radioactivity concentration method *2	^{94}Nb	γ-rays	Scaling Factor Method
^{14}C	β-rays	The mean radioactivity concentration method *2	^{99}Tc	β-rays	The mean radioactivity concentration method *2
^{36}Cl	β-rays	The mean radioactivity concentration method *2	^{108m}Ag	γ-rays	γ-rays measurement
^{59}Ni	X-rays	The theoretical method	^{137}Cs	γ-rays	γ-rays measurement
^{60}Co	γ-rays	γ-rays measurement	^{152}Eu	γ-rays	The mean radioactivity concentration method *2
^{63}Ni	β-rays	Scaling Factor Method	^{154}Eu	γ-rays	The mean radioactivity concentration method *2
^{90}Sr	β-rays	The mean radioactivity concentration method *2	^{166m}Ho	γ-rays	The mean radioactivity concentration method *2
^{93}Mo	X-rays	The mean radioactivity concentration method *2	Total α	α-rays	The mean radioactivity concentration method *2

*1 Nuclides with main released radiation
*2 Determine by a constant like mean radioactivity concentration

We are planning to establish a business for the disposal of radioactive wastes generated from research, industrial, and medical facilities. Before radioactive wastes can be disposed, the radioactivity concentrations in these wastes must be confirmed to be less than the acceptance criteria for some important radioactive nuclides. However, because α- or β-ray-emitting nuclides are difficult to measure (DTM) from outside of radioactive waste packages, a great deal of effort is placed upon radiochemical analysis of waste samples because of chemical treatments like dissolving waste samples in acid before measurement.

In the case of radioactive nuclides with same production mechanism and transport behavior in a nuclear reactor, the radioactive concentrations among these radioactive nuclides are expected to correlate with each other. The scaling factor (SF) method is a technique for evaluating the radioactivity concentrations of DTM nuclides using the ratios of radioactivity concentrations between DTM nuclides and γ-ray emitting nuclides such as Cobalt-60 (^{60}Co) or Cesium-137 (^{137}Cs), which are measurable from outside of radioactive waste packages. Therefore, applications of the SF or other methods have been studied for 16 important nuclides such as Tritium (^{3}H), Carbon-14 (^{14}C), and Nickel-63 (^{63}Ni) (which were selected based on the safety assessment of the disposal facility) in radioactive metal wastes generated from the dismantling of the Japan Power Demonstration Reactor (JPDR), because a large amount of these wastes are stored in the Nuclear Science Research Institute. In this study, an example of the application of the SF method for ^{63}Ni has been described.

Combination of the radioactive nuclides under consideration was the focus of the study on the applications of the SF method. Radioactive nuclides are produced by neutron activation of corrosion products, which are transported through the reactor core, and the products of nuclear fission. ^{63}Ni and ^{60}Co are produced by neutron activation, and the transport behavior of ^{63}Ni is similar to that of ^{60}Co because they have the same physicochemical characteristics in the reactor cooling water. From the results of the radiochemical analysis of metal wastes, a good correlation between the radioactivity concentration of ^{63}Ni and that of ^{60}Co was confirmed (Fig.8-11). Therefore, it was found that the SF method can be applied for ^{63}Ni.

On the other hand, because the transport behaviors of volatile DTM nuclides such as ^{3}H or ^{14}C are not similar to those of ^{60}Co or ^{137}Cs, the SF method cannot be applied to them. For these kinds of DTM nuclides, other evaluation methods were applied to determine their concentrations from the mean radioactivity concentrations. Similarly, no detected nuclides were applied to determine their concentrations from the mean detection limits of a detector.

From these results, appropriate evaluation methods for 16 radioactive nuclides in metal wastes generated from JPDR dismantling were established as a combination of the SF, the mean activity concentration, and the theoretical methods (Table 8-1). Based on this result, studies of evaluation methods are planned for radioactive wastes generated from other research reactors.

Reference

Tsuji, T. et al., Study on the Evaluation Methods to Determine the Radioactivity Concentration in Low-Level Radioactive Wastes Generated from JPDR Facilities – Part 2 –, JAEA-Technology 2015-009, 2015, 46p. (in Japanese).

8–5 Hydrochemical Disturbances in Groundwater during the Construction and Operation of the Mizunami Underground Research Laboratory
— Variation of Groundwater Chemistry in the Last Decade —

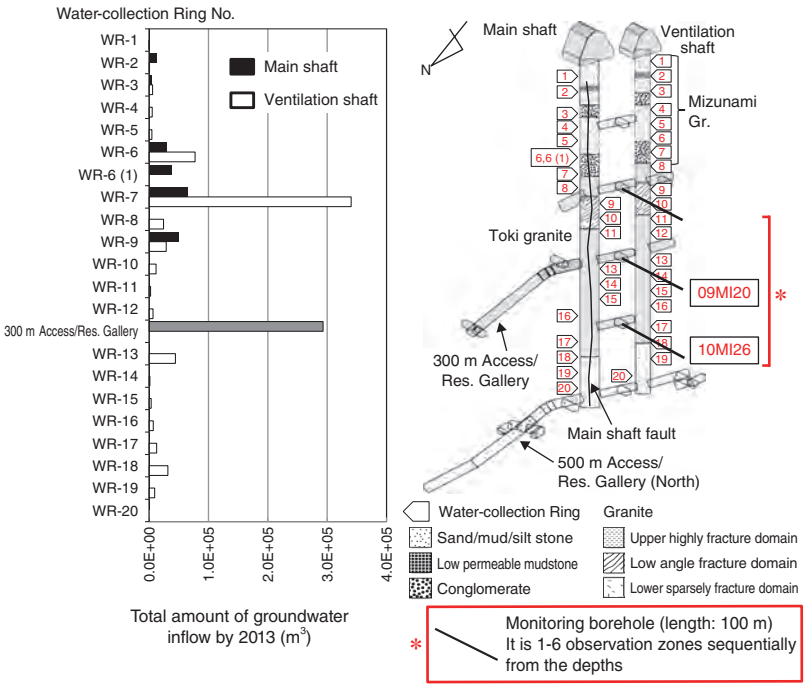

Fig.8-12 Groundwater inflow into the gallery and the monitoring point of hydraulic pressure/chemistry
Water pressure and chemistry were observed regularly in monitoring boreholes at various depths. Groundwater inflow depends upon the geological condition. It tends to increase at the conglomerate layer of a sedimentary rock and the fracture zone of granite.

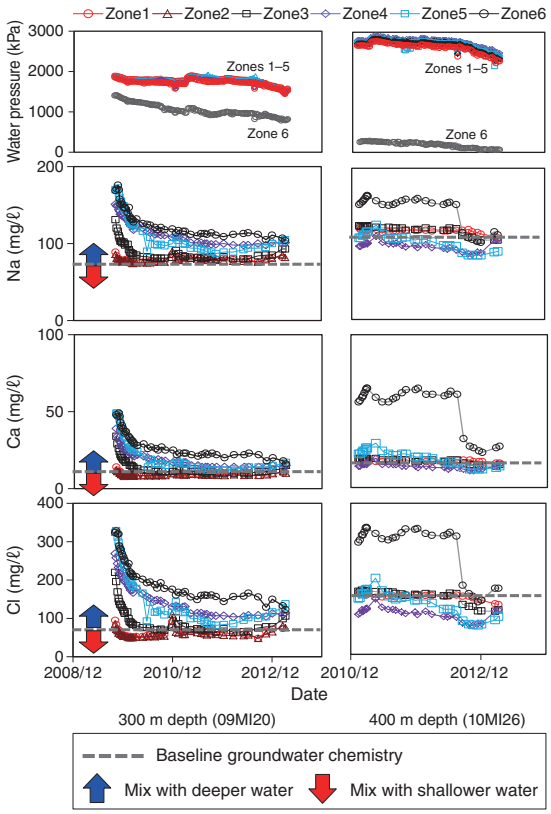

Fig.8-13 Changes of water pressure and chemistry with time at depths of 300 m and 400 m
Groundwater chemistry has been changing according to the distance from gallery in response to the drawdown.

The construction and operation of a large underground facility, such as a repository of high-level radioactive waste, probably changes the groundwater environment, possibly impacting the suitability of the selected disposal site. This study identifies the hydrochemical changes in groundwater up to depths of 500 m in response to 10 years of construction and operation of the Mizunami Underground Research Laboratory (MIU).

Geology, geological structure, and the baseline of groundwater pressure/chemistry had been identified by borehole investigation from ground surface prior to the excavation of the gallery. Groundwater inflow at these depths was measured (Fig.8-12). Hydrochemical change around the gallery was observed at monitoring boreholes of various depths (Fig.8-12).

Groundwater drawdown was observed below the mudstone layer at a depth of about 50 m. The groundwater level, at a range of approximately 100 m from the gallery, was lowered by 150 m from the baseline condition in March 2015. Moreover, a change in the groundwater chemistry due to hydraulic drawdown has also been identified (Fig.8-13). Based on the observation results and multivariate statistical analysis, the following fundamental insights regarding the impact of an underground facility upon the geological environment have been obtained.

- The hydrochemical disturbances during facility construction and operation are caused by the upconing of deep groundwater around the deepest part of the shaft and gallery and by the infiltration of shallow groundwater according to groundwater drawdown.
- Hydrogeological structures, such as low-permeability clay layers and faults with an abundance of clay materials suppress the hydraulic impact, whereas the impact occurs intensely in permeable conglomerates and fracture zones.

Designs and plans for underground facility layouts that take hydrogeological structures into consideration aim to enable comprehensive management that minimizes the hydrochemical impact.

We continue to observe the long-term hydrochemical change around the facility and start a drift-closure experiment to understand hydrochemical recovery processes from the disturbed groundwater condition.

Reference

Iwatsuki, T. et al., Hydrochemical Disturbances Measured in Groundwater during the Construction and Operation of a Large-Scale Underground Facility in Deep Crystalline Rock in Japan, Environmental Earth Sciences, vol.74, issue 4, 2015, p.3041–3057.

8–6 Reduction of Groundwater Inflow in the Deep Underground

— Countermeasures Taken during the Construction of the Mizunami Underground Research Laboratory —

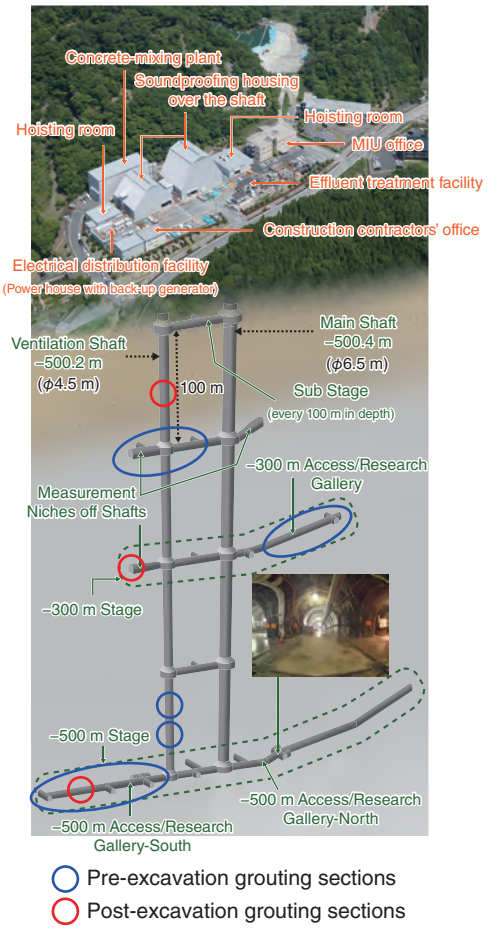

Fig.8-14 Layout of the Mizunami Underground Research Laboratory
Pre- and post- excavation grouting was performed for some sections.

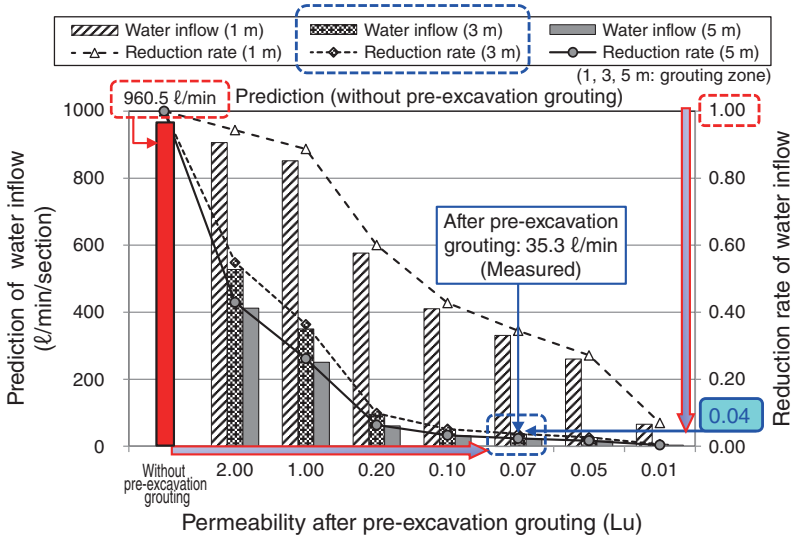

Fig.8-15 Estimated water inflow depending on the pre-excavation grouting in the –500 m Access/Research Gallery-South
The water inflow measured in the 16 m section decreased sufficiently from 960.5 (estimated water inflow) to 35.3 ℓ/min (4%).

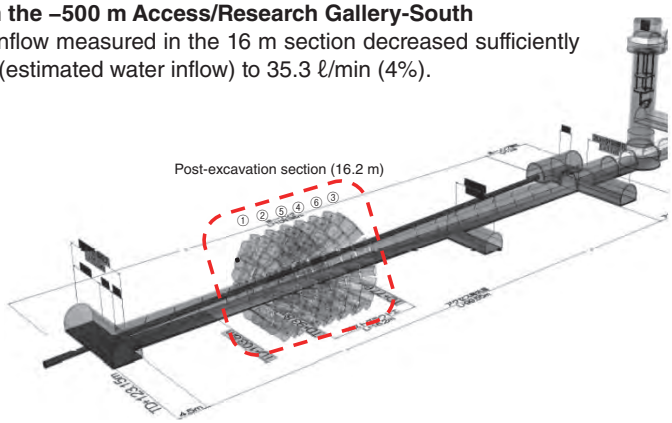

Fig.8-16 Layout of the post-excavation grouting section in the –500 m Access/Research Gallery-South
We selected a 16 m section among the pre-excavation grouted sections.

Tono Geoscience Center is managing a geoscientific research and development (R&D) project, namely the "Mizunami Underground Research Laboratory" (MIU) Project. The MIU Project was launched as a generic underground research laboratory in a crystalline rock environment under an R&D program to establish a scientific and technical basis for geological disposal of high-level radioactive waste (HLW). MIU has clearly been distinguished from any actual disposal facilities. MIU is the first Underground Research Laboratory in Japan. The results will be utilized to provide basic information for the final HLW geological disposal project and to draw up national safety regulation standards.

To mitigate potential excess groundwater inflow, pre-excavation grouting of open fractures in the rock mass was performed (Fig.8-14; pre-excavation grouting was conducted before the excavation at −200 m, −300 m, −400 to −460 m, and −500 m depths). In planning the construction, the targeted reduction in water inflow was established by theoretical analysis of the groundwater flow in terms of the bedrock conditions. Actual inflows indicate that pre-excavation grouting was successful and the targets were achieved. Thus, the results indicate that the methodology is effective in reducing water inflow and is applicable deep underground and under high-groundwater pressure conditions (Fig.8-15).

Then, post-excavation grouting work with six fans was conducted at a 16 m section of the pre-excavation grouting area for further reducing the inflow at the −500 m Access/Research Gallery-South in order to develop an appropriate post-excavation grouting design method in the deep underground (Fig.8-16). Pre- and post-excavation grouting measures were successful in reducing groundwater inflow at the −500 m Access/Research Gallery-South. These waterproofing experiences must be fruitful for advancing the present grouting technology in the deep underground. Therefore, it can be suggested that there is still more potential to reduce the water inflow.

Reference
Sato, T., Mikake, S. et al., Status of Grouting to Reduce Groundwater Inflow into Deep Shafts and Galleries in the Mizunami Underground Research Laboratory, Japan, Proceedings of 8th Asian Rock Mechanics Symposium (ARMS–8), Sapporo, Japan, 2014, 10p., in USB Flash Drive.

8–7 Evaluation of the Mass Transport Characteristics in Rock Masses

— Case Study Based on In situ and Laboratory Tests using Fractured Sedimentary Rock at the Horonobe URL —

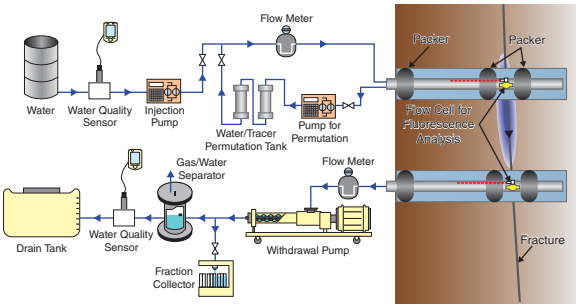

Fig.8-17 Schematic view of the *in situ* dipole tracer migration test
A tracer solution from the injection borehole migrates to the withdrawal borehole through the fracture. Mass-transport characteristics in the fracture are evaluated by the concentration of tracer solutions sampled from the withdrawn borehole.

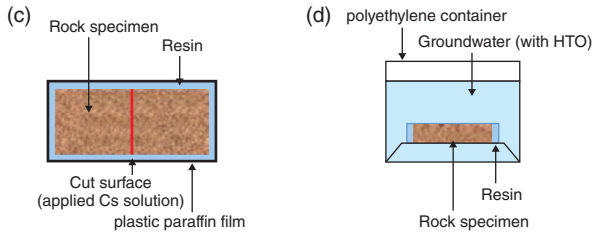

Fig.8-19 Schematic view of non-steady diffusion tests
(c) To determine the diffusivity obtained for Cs, a rock specimen is cut into two specimens and the Cs solution is applied to the cut surface of the specimens. (d) To determine the diffusivity obtained for HTO, a rock specimen is immersed in ground water with HTO.

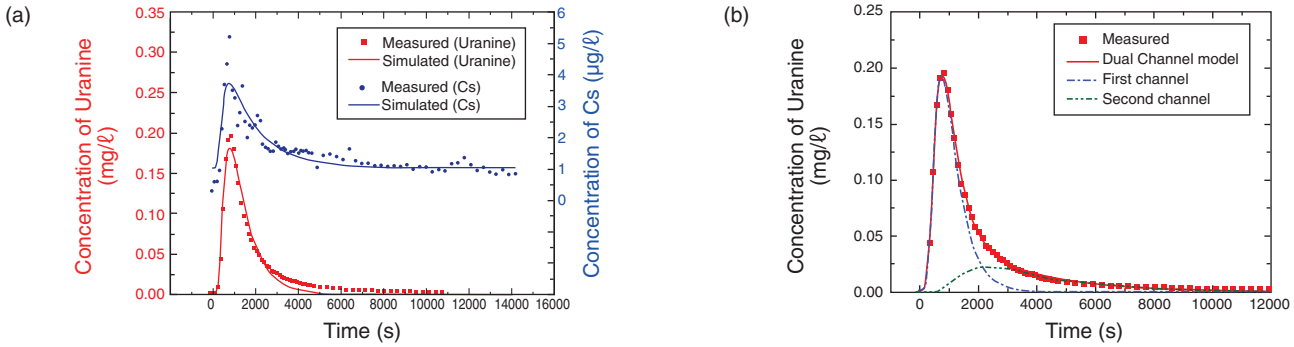

Fig.8-18 Breakthrough curve obtained from the dipole migration tests and fitting curves
The concentration of uranine is better described by the dual channel model (b) than by the single channel model (a). The dispersivity of Cs is greater than that of uranine, and the Wakkanai Formation has higher sorptive properties for Cs than those for uranium because the peak concentration of Cs was much smaller than that of uranine.

Mass transport through fractures and porous media in groundwater is accompanied by dispersion, diffusion, and sorption. It is important for high-level radioactive waste disposal to develop evaluation techniques for the mass transport characteristics. *In situ* and laboratory tests were conducted to evaluate the mass transport of cesium (Cs) and uranine in the Wakkanai Formation consisting of siliceous mudstone, which is porous and fractured rock mass.

In situ dipole tracer migration tests were conducted to elucidate migration processes such as sorption onto the surface of a fracture and flow channel in the fracture at the 250 m gallery of the Horonobe Underground Research Laboratory (URL). A solution using a non-radioactive tracer is injected into the injection borehole, and is then sampled from the withdrawal borehole to determine the tracer concentration to obtain the breakthrough curves (Fig.8-17). The curves shown in Fig.8-18(a) indicate that the peak concentration of Cs is much smaller than that of uranine, suggesting that the Wakkanai Formation has high sorptive properties for Cs. The breakthrough curves also indicate that the Wakkanai Formation has a large dispersivity for Cs. This large dispersivity suggests that a minute amount of Cs ions sorbed onto the fracture are partially desorbed and arrived later. In addition, the result of the *in situ* dipole tracer migration test is well described by the dual-channel model (Fig.8-18(b)) compared with the single-channel model (Fig.8-18(a)), suggesting that two channels of flow exist in the fracture.

A non-steady diffusion test was conducted to elucidate the sorptive properties in the rock matrix of the Wakkanai Formation using rock samples from the Horonobe URL (Fig.8-19). The apparent diffusivities for Cs (2.9×10^{-12} m^2/s) and tritium (HTO) (3.4×10^{-10} m^2/s) were obtained. The sorption coefficient for Cs (488 mℓ/g) was also obtained by the sorption test using powdered rock samples. It was also confirmed that the Wakkanai Formation has high sorptive properties for Cs, as suggested by the results of the *in situ* dipole tracer migration tests. We planned to integrate the data and knowledge obtained from further combined *in situ* and laboratory tests to develop evaluation techniques for the mass transport characteristics with high reliability.

Reference

Tanaka, S. et al., Dipole Tracer Migration and Diffusion Tests in Fractured Sedimentary Rock at Horonobe URL, Proceedings of 23rd International Conference on Nuclear Engineering (ICONE 23), Chiba, Japan, 2015, ICONE23–1860, 6p., in DVD–ROM.

8–8 Predictions of the Transmissivity of Underground Fault Zone Fractures

— Development of a Hydrogeological Investigation Technique for Fault Zones —

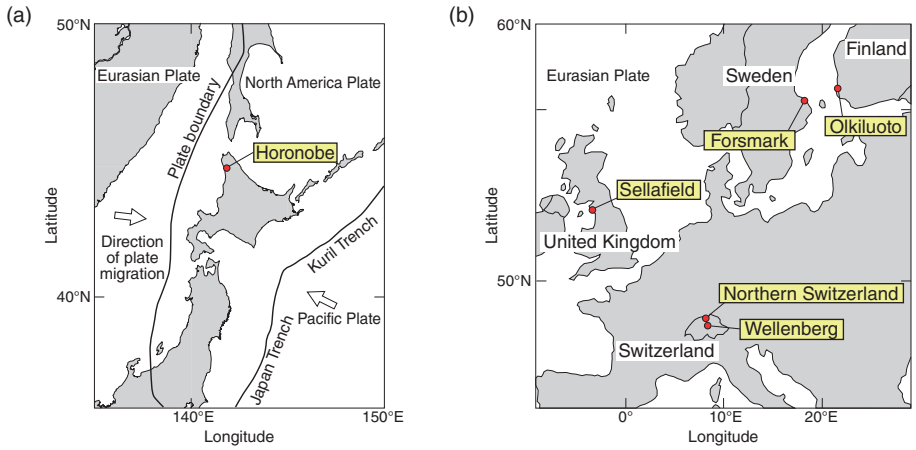

Fig.8-20 Six areas that were studied
The locations of the six studied areas and the names and directions of the migration of related plates are shown.

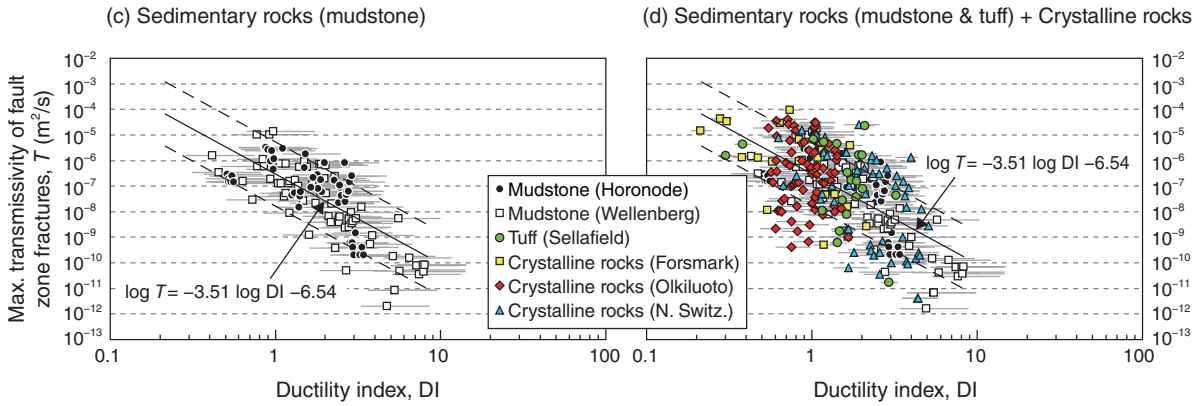

Fig.8-21 Relation between the maximum transmissivities of fault zone fractures and ductility index values
Solid lines show the power law approximation, and the equation is shown in the figures. Broken lines show the standard error (±1.25 in log *T*). Gray horizontal bars show estimation errors.

Spatial and temporal prediction of the transmissivity of underground fault zones based on limited data is an important problem in high-level radioactive waste disposal. To develop the prediction methods, this study compiled various experimental data obtained from areas in Japan and abroad in relation to fault zone transmissivity, and successfully revealed a new relation helpful for the prediction.

Borehole data obtained from six areas (Fig.8-20) in different geological environments, namely, Horonobe (Japan; mudstone), Wellenberg (Switzerland; mudstone), Sellafield (UK; tuff), Forsmark (Sweden; crystalline rocks), Olkiluoto (Finland; crystalline rocks), and Northern Switzerland (crystalline rocks), revealed that the maximum transmissivities of fractures in fault zones are strongly controlled by their ductility index (DI) (Fig.8-21). DI is a new indicator and is defined as the effective mean stress normalized to the tensile strength of the intact rock. The effective mean stress refers to the average stress that is actually loaded into a rock, and the tensile strength refers to rock strength against tensile failure. DI is a parameter that can be spatially and temporally predicated from information such as a geological map and the local tectonic evolution.

The results of this study mean that DI and the relation shown in Fig.8-21 allow for the spatial and temporal prediction of the maximum transmissivities of fault zone fractures in a rock mass. Since the studied fault zones have experienced many fault movements in the past, it can also be suggested that the maximum transmissivities of the fault zone fractures do not irreversibly increase beyond the above relation, even with fault movement.

The finding of this study allows for the spatial and temporal predictions of underground fault zone transmissivity and may prove helpful for various geoscientific/geoengineering problems as well as geological disposal. This finding will be further studied in the Horonobe underground research laboratory by *in situ* tests in the underground (e.g., a hydraulic disturbance test for a fault zone) and laboratory tests, leading to a demonstration of the buffering ability of sedimentary rocks against tectonic movement.

Reference

Ishii, E., Predictions of the Highest Potential Transmissivity of Fractures in Fault Zones from Rock Rheology: Preliminary Results, Journal of Geophysical Research: Solid Earth, vol.120, issue 4, 2015, p.2220–2241.

8–9 Visualization at Depths between 0 and 1000 m Below Sea Level
— Subsurface Geological Mapping of the Japanese Islands —

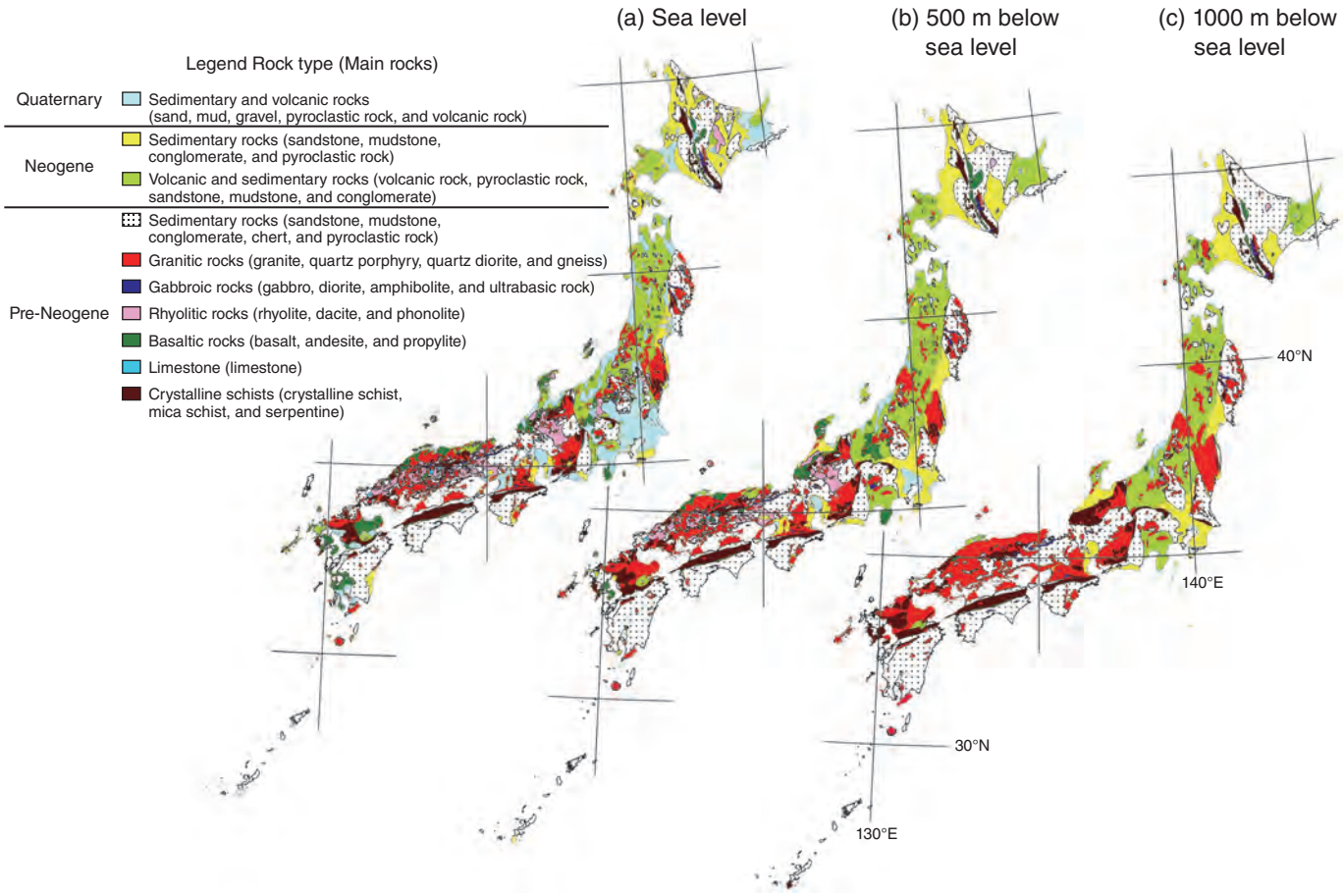

Fig.8-22 Subsurface geological mapping of the Japanese Islands
Horizontal slices at sea level (a), and depths of 500 m (b), and 1000 m (c) below sea level throughout the Japanese Islands showing the distribution of various rock types.

From the viewpoint of utilizing underground space for purposes such as the geological disposal of radioactive waste and carbon dioxide, it is imperative to understand subsurface geological structures.

In general, widely-used conventional methods of subsurface mapping convert subsurface geological information into two-dimensional space. We present the horizontal geological cross sections at depths of 0, 500, and 1000 m below sea level throughout the Japanese Islands. These are extrapolated mainly from geological maps, vertical geological cross sections, and borehole data (Fig.8-22). The data were collected from studies published prior to 2001.

Synthesized borehole data were compiled from a total of 291 sites. The density of borehole data varies widely by region. When data are insufficient, tectonic lines and the granite are mapped vertically in the subsurface. Therefore, it is hard to estimate the subsurface geological structures in the individual region based on these maps in detail. However, these maps are helpful for understanding the subsurface geological outline in the Japanese Islands.

The legend of these maps followed a classification based on a unified legend proposed by the Geological Survey of Japan. Depending on the purpose, it is possible to simplify the display of these maps. For example, in the geological disposal of radioactive waste, rock type is often divided into two categories: sedimentary and crystalline. It is possible to visually recognize a three-dimensional distribution of the two categories in the Japanese Islands.

Improvement of the accuracy of these maps is expected due to recent information.

Reference

Yasue, K., Kobori, K. et al., Subsurface Geological Mapping of the Japanese Islands, Chishitsugaku Zasshi (Journal of the Geological Society of Japan), vol.120, no.12, 2014, p.XIII-XIV.

8–10 Performance Assessment of the Geological Disposal System in Terms of Changes in the Geological Environment
— Radionuclide Migration Analyses Focused on the Difference between Uplift and Erosion Rates —

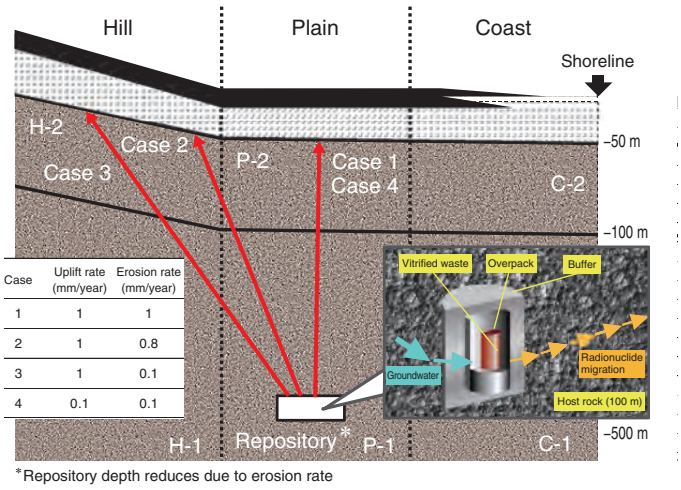

Case	Uplift rate (mm/year)	Erosion rate (mm/year)
1	1	1
2	1	0.8
3	1	0.1
4	0.1	0.1

*Repository depth reduces due to erosion rate

Fig.8-23 Test cases with different uplift and erosion rates
- If the uplift rate is the same as the erosion rate (Cases 1 and 4), the repository location changes from a deep part of the plain (P-1) to a shallow part of the plain (P-2).
- If the uplift rate is larger than the erosion rate (Cases 2 and 3), the repository location changes from a deep part of the plain (P-1) to a shallow part of the mountain (H-2).
- Both uplift and erosion rates were parametrically set based on a conservative erosion rate of 1 mm/year with consideration to uplift throughout Japan over the past 100 thousand years.

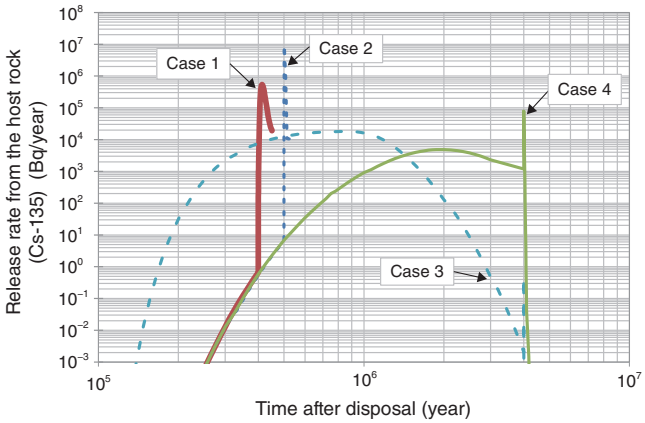

Fig.8-24 Example of release rates from the host rock (Cs-135)
Maximum value and time of occurrence for the release rate of Cs-135 in Cases 1–4. Differences in release rate are due to differences between uplift and erosion rates and geological environmental changes. Moreover, the radionuclide migration parameters differ among cases.

The Japanese archipelago is located in the tectonically active zone around the Pacific Rim. To demonstrate the safety of a geological disposal system, potentially disruptive phenomena such as volcanism, seismicity, fault movement, and uplift/erosion must therefore also be considered for performance assessment of a geological disposal system in Japan. Uplift and erosion generally occur slowly on a regional scale, but they could gradually cause changes in the geological environment of the system whereby a repository might approach the ground surface over a very long time. Changes in the depth of the repository and the regional geography, for example, could have a significant effect on groundwater flow and geochemistry. A method focused on the difference between uplift and erosion rate has therefore been developed to evaluate the effects on the system performance as a consequence of changes in the geological environment.

In a previous study, it was conservatively assumed that the depth of a repository from the ground surface would gradually decrease, resulting in changes in groundwater flow and geochemistry. The analyses of system performance in the study were based on a conservative assumption that the uplift rate would be equal to the erosion rate so that any uplift would be instantly removed by erosion. Under actual conditions, however, it is possible that the uplift rate would exceed the erosion rate.

Thus, the current study has been trying to include this possibility in the analysis of system performance. Here, a depth of 500 m for the repository was assumed in a simple, layered sedimentary rock, and the surface geography was classified into several generic types of hill, plain, and coast, (Fig.8-23). Many parts of Japan have been subject to uplift, and hence, four test cases were defined to understand the effect of the combination of changes in depth and surface geography above the repository with time. Parameters relating to radionuclide migration affected by changes in the geological environment were also defined. Groundwater flow velocity, for example, was initially slow at deep depth, but increased as the repository neared the ground surface. The distribution coefficient for cesium (Cs)-135, which is one of dominant radionuclides in the system performance, also changed as the repository neared the ground surface. Based on such assumptions, the radionuclide migration analyses with the time-dependent parameters were executed in response to the four test cases (Fig.8-23). The relative difference between uplift and erosion rates for each test case had a significant effect upon the release rate of Cs-135 (Fig.8-24). Differences in the release rate of Cs-135 were found to be large due to the increased groundwater flow velocity near the ground surface. This study enables performance assessment with regard to uplift/erosion in a more phenomenological and quantitative manner.

Reference

Ebashi, T. et al., “Relative Rates Method” for Evaluating the Effect of Potential Geological Environmental Change due to Uplift/Erosion to Radionuclide Migration of High–Level Radioactive Waste, Materials Research Society Symposium Proceedings, vol.1665, 2014, p.39–45.

8–11 Mechanical Properties of Mudstone from the Wakkanai Formation

— Strength Affected by the Degree of Saturation and Bedding Plane Orientation —

Table 8-2 Specifications of specimens
Bedding planes in the sample are indicated. The arrows of the Brazilian tension test show the loading directions.

	Loading direction to the bedding plane		Specimen Size
	Perpendicular to the bedding plane	Parallel to the bedding plane	
Uniaxial compression test	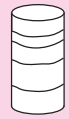	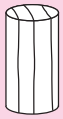	Diameter 25 mm Height 50 mm
Brazilian tension test		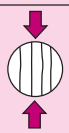	Diameter 25 mm Thickness 13 mm

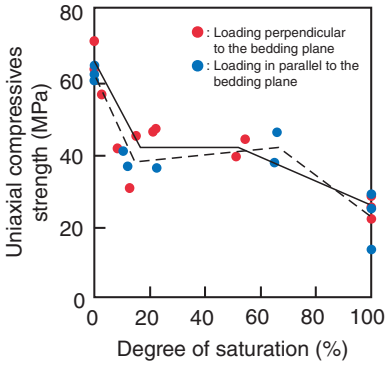

The solid and dashed lines trace the mean uniaxial compressive strength in loading directions perpendicular and parallel to the bedding plane, respectively.

Fig.8-25 Relation between uniaxial compressive strength and degree of saturation
Uniaxial compressive strength has an inverse relation with the degree of saturation. Uniaxial compressive strengths were similar at degrees of saturation of 10% and 60%.

Table 8-3 Results of the Brazilian tension test
Brazilian tensile strength, strength ratio in the loading direction (perpendicular/parallel) to the bedding plane, and strength ratio in the water-containing state (dry state/saturated state).

Loading direction to the bedding plane	Water-content	Brazilian tensile strength (MPa)	Strength ratio (perpendicular/parallel)	Strength ratio (dry state/saturated state)
Perpendicular	Dry state	8.0	1.5 (Dry state)	2.7
	Saturated state	2.9		
Parallel	Dry state	5.2	1.4 (Saturated state)	2.5
	Saturated state	2.1		

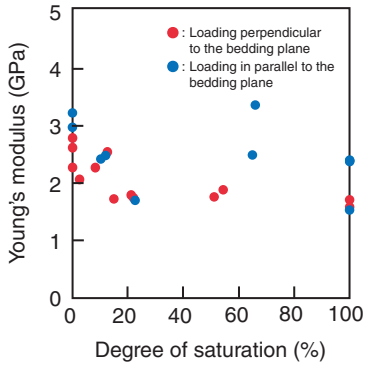

Unlike the uniaxial compressive strength, Young's modulus did not show a correlation with the degree of saturation.

Fig.8-26 Relation between Young's modulus and the degree of saturation
Correlation between the Young's modulus and the degree of saturation was not recognized, although the loading direction parallel to the bedding plane tended to result in a larger Young's modulus.

Part of the research and development (R&D) program on the geological disposal of high-level radioactive waste has been conducted at the Horonobe Underground Research Laboratory (URL). A sample of the siliceous mudstone of the Wakkanai formation obtained from the URL has a high porosity of between 30% and 50%. Mechanical tests confirmed that the volume of the mudstone varies as a function of water saturation and that the moisture content may exert some control on the deformation and destruction behaviors of the mudstone.

The degree of water saturation in a rock mass changes when a gallery is excavated; hence, uniaxial compressive and Brazilian tension tests were performed to investigate the relation between moisture content and the mechanical properties of the rock mass. Furthermore, the mechanical properties of the rock mass in relation to the bedding planes and banded structures in the siliceous mudstone of the Wakkanai formation were also investigated.

Specimens of siliceous mudstone from the Wakkanai formation were obtained at depths of more than 300 m below the ground surface. Two kinds of specimens having loading directions either perpendicular or parallel to the bedding plane were used in uniaxial compression and Brazilian tension tests (Table 8-2).

Both uniaxial compressive strength (Fig.8-25) and Brazilian tensile strength (Table 8-3) were high in the dry state and decreased as the degree of water saturation became higher. Differences in water saturation, however, could not be distinguished in the Young's modulus of stiffness (Fig.8-26). The uniaxial compressive strength and Young's modulus in the compression state (Figs.8-25 and 8-26) were not affected by orientation with respect to the bedding plane. On the other hand, orientation with respect to the bedding plane could be recognized in the Brazilian tensile strength in the tension state (Table 8-3). The strength ratio in the loading direction (perpendicular/parallel) to the bedding plane was 1.4 in the water-saturated state and 1.5 in the dry state. It is believed that the characteristics of intact rock restrict the influence of the bedding plane upon the uniaxial compressive strength and Young's modulus, and the ease of splitting the bedding plane is identified in the Brazilian tensile strength.

It was found that the mechanical characteristics of siliceous mudstone of the Wakkanai formation depended on the degree of saturation. The uniaxial compressive strength and Brazilian tensile strength were high when the degree of water-saturation was low, and the direction of loading was perpendicular to the bedding plane. In the case of sedimentary rock with high porosity and bedding planes, it is important to consider the degree of water saturation of the rock mass and the direction of the bedding plane with respect to gallery excavation.

Reference

Hashiba, K., Sugita, Y. et al., Mechanical Properties of Siliceous Mudstone of the Wakkanai Formation, Genshiryoku Bakkuendo Kenkyu (Journal of Nuclear Fuel Cycle and Environment), vol.21, no.2, 2014, p.75-82 (in Japanese).

8–12 Prediction of Radionuclide Migration in a Buffer Material

— Development of an ISD Model in Compacted Bentonites —

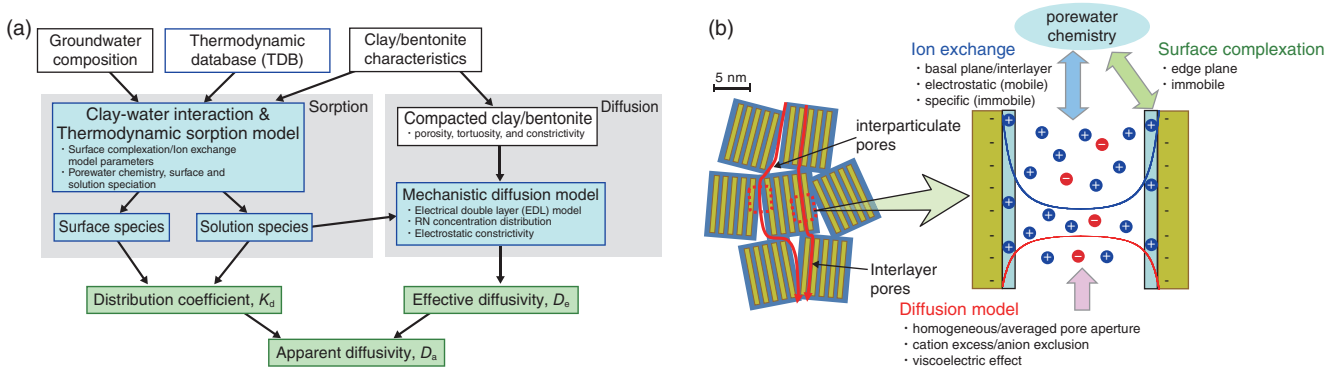

Fig.8-27 Framework and conceptual sketches of the ISD model in compacted bentonite
The ISD model is based on (a) a consistent combination of the clay-water interaction, sorption, and diffusion models; (b) coupling of the thermodynamic sorption model (ion exchange and surface complexation) and the EDL diffusion model in homogeneous pores.

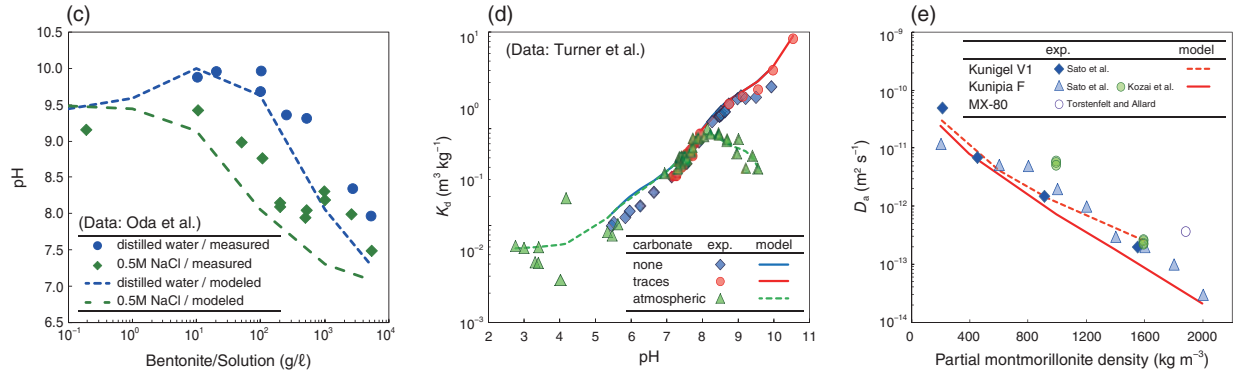

Fig.8-28 Applicability of the ISD model for predicting porewater chemistry, sorption, and diffusion
The ISD model was successfully tested for (c) pH in porewater, (d) K_d of Np(V) under a wide range of conditions, and (e) D_a of Np(V) as a function of partial montmorillonite density.

Sorption and diffusion of radionuclides in compacted bentonite are key processes in the safe geological disposal of radioactive waste. Quantitative understanding of the sorption and diffusion behavior of radionuclides, typically expressed as distribution coefficients (K_d) and effective diffusivities (D_e), are essential for safety assessment (SA). Geochemical variability and uncertainty, as well as their effects upon sorption and diffusion, usually have to be considered for SA. It is not feasible, however, to experimentally determine K_d and D_e values for all possible geochemical conditions. For this purpose, an integrated sorption and diffusion (ISD) model in compacted bentonite with nanoscale complex pore structures has been developed to achieve a consistent combination of the clay–water interaction, sorption, and diffusion models (Fig.8-27).

The basic premise considered in the ISD model was to consistently use the same model design and parameters to describe sorption/diffusion as well as porewater chemistry. A 1-site non-electrostatic surface complexation model in combination with a 1-site ion exchange model was used as the sorption model. The basic model, derived from surface titration data for purified montmorillonite, was parameterized on the basis of published sorption datasets for various radionuclides in dispersed systems, which cover a range of key geochemical conditions. The pH and sorption trends for Np(V) can be quantitatively described by the model considering a full suite of surface species including hydrolytic and carbonate species (Figs.8-28(c) and (d)).

The diffusion model based on the electrical double layer (EDL) describing relative ionic concentrations and viscoelectric effects at the negatively charged clay surface is connected to a simplified homogeneous pore model. The diffusion model component was integrated with the clay–water interaction and sorption models. The ISD model was successfully tested for Np(V) with a complex chemistry (Fig.8-28(e)) using published diffusion data (D_a, D_e) as a function of the partial montmorillonite density. It can therefore be concluded that the ISD model developed here is able to adequately explain the sorption and diffusion behavior of various radionuclides with a complex chemistry in compacted bentonites.

References

Tachi, Y. et al., Integrated Sorption and Diffusion Model for Bentonite. Part 1: Clay–Water Interaction and Sorption Modeling in Dispersed Systems, Journal of Nuclear Science and Technology, vol.51, issue 10, 2014, p.1177–1190.
Tachi, Y. et al., Integrated Sorption and Diffusion Model for Bentonite. Part 2: Porewater Chemistry, Sorption and Diffusion Modeling in Compacted Systems, Journal of Nuclear Science and Technology, vol.51, issue 10, 2014, p.1191–1204.

8–13 Determination of the Plutonium Rate Constant using a Microchannel

— Microchip Initiates New Separation/Analytical Chemistry for Plutonium —

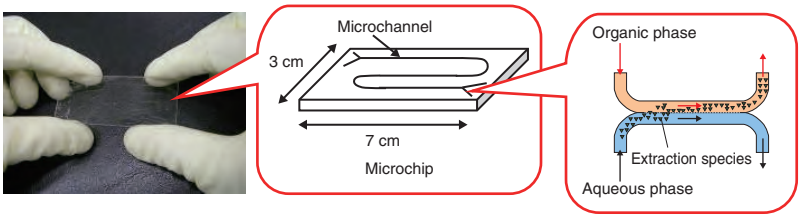

Fig.8-29 The glass microchip used for Pu extraction
The microchannel width is 100 μm and the depth is 40 μm.

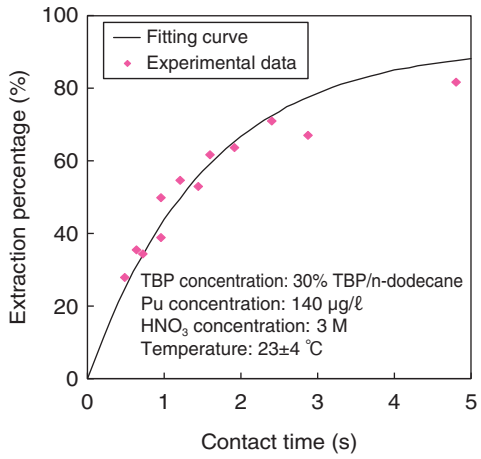

Fig.8-30 Dependence of Pu extraction on the contact time
The Pu-extraction percentage increases with the contact time. The maximum extraction percentage was 82% at a contact time of 4.8 s in this experiment.

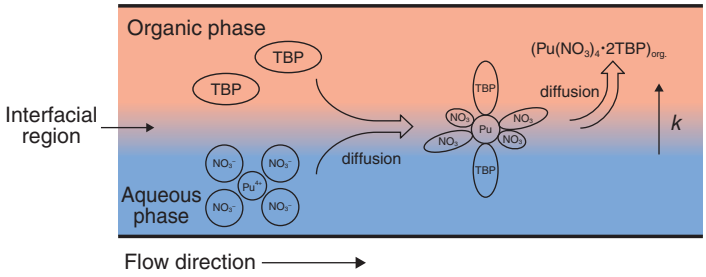

Fig.8-31 The model of Pu extraction in the microchip
The Pu^{4+} in the aqueous phase diffuses into the interfacial region. Then, Pu^{4+} forms a complex with TBP and is extracted into the organic phase, where it diffuses. k is the reaction rate constant of Pu^{4+} and TBP extraction.

The extraction of plutonium (Pu) by tri-*n*-butylphosphate (TBP) is used for spent nuclear fuel reprocessing. It is important to know the rate constant of this extraction system in order to design fast-extraction instruments such as centrifugal extractors. The single-drop method is primarily used to measure rate constants, although the specific interfacial area between the single drop and the surrounding liquid is generally small and limits the reaction. In this study, we used a microchip, which stably provides a large specific interfacial area, to evaluate the rate constant of Pu extraction.

The microchip, as shown in Fig.8-29, is a several cm square glass plate that typically has a few hundred μm channels. Effective extraction is expected in this micro-sized region due to a large interfacial area compared with the sample volume. Moreover, when the aqueous and organic phases contact in the microchip under a certain flow rate, a stable interface can be observed because of the laminar flow.

A solution of 3 M nitric acid including Pu and a solution of 30% TBP diluted with n-dodecane were used as aqueous and organic phases, respectively. These solutions were fed separately into the microchip and the interface between each phase was observed. It was found that a stable interface was formed for flow rates between 5 and 20 $\mu\ell$/min. The Pu extraction percentages at each contact time were obtained by analyzing the Pu concentration of the solution from the microchips. Fig.8-30 depicts the dependence of Pu extraction on the contact time with the time interval below 1 s. To evaluate the rate constant from this data, Pu extraction in microchip was modeled as shown in Fig.8-31. This extraction model was based on the Pu diffusion in the microchannel and the extraction at the interfacial region. A theoretical equation was derived from rate equations according to the model. It was fitted with the data in Fig.8-30 using the least-squares method. Consequently, the rate constant of Pu extraction was evaluated.

The results obtained in this study indicate that the microchip can be an effective experimental tool for studying the Pu rate constant. The data are expected to be used for the design of fast-extraction instruments. Furthermore, applications of microchips to the separation and analysis of radioactive materials are expected because microchip extraction can reduce the radioactive waste and downsize the analytical apparatus.

Reference

Yamamoto, M. et al., Evaluation of Plutonium(IV) Extraction Rate between Nitric Acid and Tri–*n*–butylphosphate Solution using a Glass Chip Microchannel, Journal of Separation Science, vol.38, issue 10, 2015, p.1807–1812.

Toward Practical Use of Fusion Energy

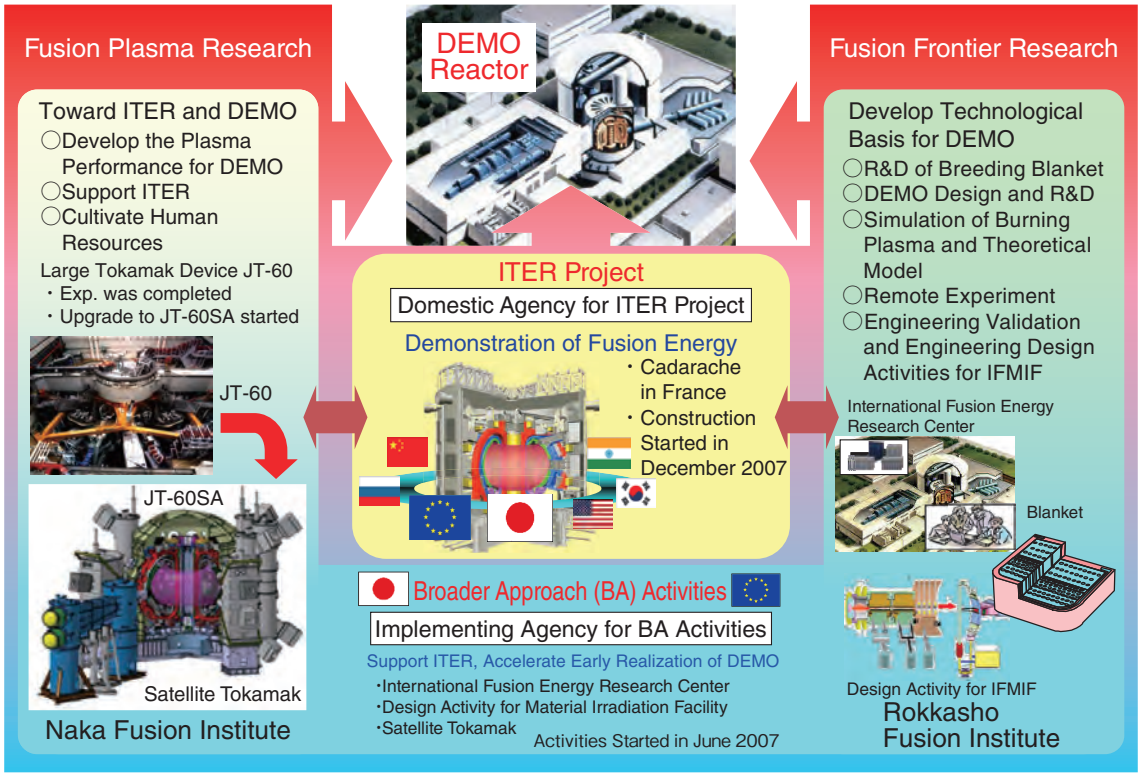

Fig.9-1 Steps involved in the development of the fusion DEMO reactor
Fusion plasma research and fusion frontier research are being pursued to develop a DEMO reactor. Furthermore, international cooperation toward the development of the International Thermonuclear Experimental Reactor (ITER) project and the Broader Approach (BA) activities is being promoted, aiming for the early realization of fusion energy.

Crucial research and development (R&D) on fusion plasma and fusion frontiers is being pursued through intensive international cooperation toward the practical use of fusion energy. For example, the International Thermonuclear Experimental Reactor (ITER) project, Broader Approach (BA) activities, and other collaborations (Fig.9-1), aiming for the early realization of a fusion DEMO reactor, are underway. Fusion plasma research is mainly being advanced at the Naka Fusion Institute, whereas fusion frontier research is mainly being advanced at the Rokkasho Fusion Institute.

ITER Project

The ITER project is an international cooperative project aimed at demonstrating the scientific and technological feasibility of fusion energy through the construction and operation of an experimental reactor. The ITER agreement came into force in October 2007, and the Japan Atomic Energy Agency (JAEA) was designated as the domestic agency for the implementation of the ITER project in Japan. JAEA proceeded with preparing the equipment that Japan agreed to provide and achieved various results in terms of technological development (Topics 9-1, 9-2, and 9-3). In particular, JAEA completed production of its entire quota of superconductors for the toroidal field coil in December 2014.

BA Activities

The BA activities are joint projects by Japan and the European Union to conduct supporting research for ITER and R&D for a DEMO reactor (which is the next step of ITER), aiming for early realization of fusion energy. The BA agreement came into force in June 2007, and JAEA was designated as the implementing agency of the BA activities in Japan.

The BA activities consist of three projects: projects in the International Fusion Energy Research Center (IFERC), the engineering validation and engineering design activities of the International Fusion Materials Irradiation Facility/Engineering Validation and Engineering Design Activities (IFMIF/EVEDA), and the Satellite Tokamak Program (STP). In the STP, the joint construction of JT-60SA by Japan and the European Union has progressed well. Topics 9-4 and 9-5 are results contributing to JT-60SA.

Fusion Plasma Research

The analysis of the JT-60 experimental data was promoted, and inter-machine experiments were conducted in order to achieve high economic efficiency for the fusion reactor by attaining a high plasma pressure. Topic 9-6 is a result that enables the measurement of the temperature and density of plasma with high accuracy.

Fusion Frontier Research

Various R&D activities are being executed by the Rokkasho Fusion Institute, aiming at the construction of a technological basis for the DEMO reactor. Topics 9-7 and 9-8 are results that lead to securing the safety of the fusion reactor. Topic 9-9 is a result that enables fusion fuel to be collected from seawater. Topics 9-10 and 9-11 are results that contribute to the development of a breeding blanket.

9–1 Development of a Fast Power-Modulation Method in Triode Gyrotron

— Demonstration of the ITER Electron Cyclotron Heating and Current Drive System Requirement —

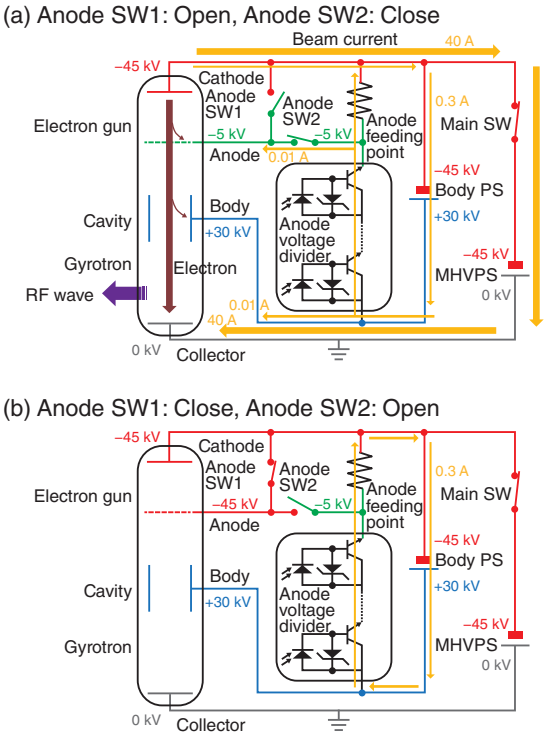

Fig.9-2 Fast power-modulation operation using the double-anode switches method. Circuit states in (a) RF-wave on-phase and (b) RF-wave off-phase are shown
Electron beam current is stopped by shorting the anode and cathode, and then, the RF wave stops.

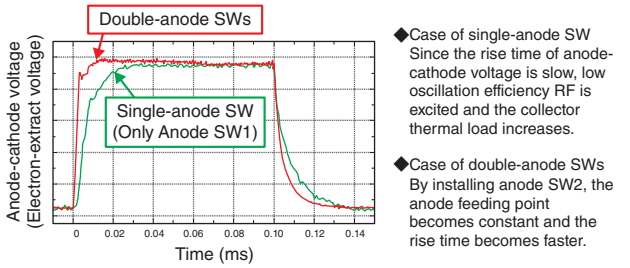

Fig.9-3 Effect of double-anode switches
Oscillation of the unwanted RF wave is minimized by a fast start-up of the electron extraction voltage through the introduction of double-anode SWs.

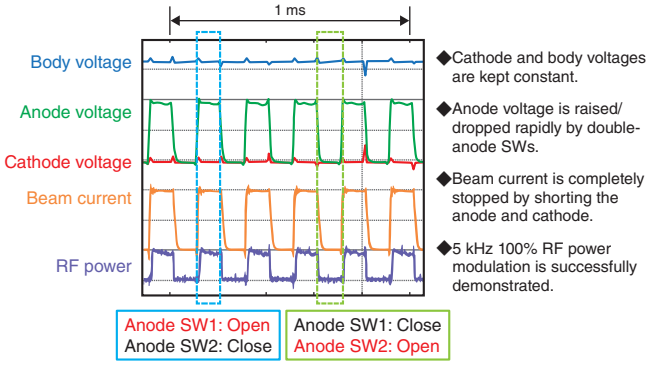

Fig.9-4 Demonstration of 5 kHz full power-modulation
Since the double-anode SWs method is able to stop the beam current, the thermal load to a collector goes to zero.

In the International Thermonuclear Experimental Reactor (ITER), fusion plasmas are controlled and stabilized by applying a 170 GHz radio-frequency (RF) wave with a power of 20 MW. We have already succeeded in developing an ITER gyrotron that simultaneously satisfies the ITER requirements for an output power of 1 MW and an electrical efficiency of 50%. However, a neo-classical tearing mode (NTM) is assumed in ITER plasmas, and it generates magnetic islands that lead to the degradation of the plasma performance. Therefore, synchronized injection of 5 kHz RF waves onto the rotating magnetic islands in the plasma is required for the effective suppression of NTM. In a conventional scenario of fast modulation, power modulation is introduced into an RF wave by the changing acceleration voltage between a cathode voltage at an electron gun and a body voltage at a cavity. However, it is difficult to modulate the cathode voltage fed from a main power supply with a high voltage and large current. Therefore, the modulation of the body voltage is used because the body current is small. This modulation method alternately shifts the oscillation condition from the high-efficiency region to the low-efficiency region. Therefore, the thermal load to a collector increases due to the high-energy electron beam. Hence, variation of power amplitude is limited by up to 50% in the case of the 5 kHz power-modulation.

We have developed a new power-modulation method without the modulation of the acceleration voltage to resolve this limit. The JAEA gyrotron is a triode gyrotron with an energy-recovery mechanism. Electrons are extracted by a voltage between a cathode and an anode in an electron gun and accelerated by a voltage between a cathode and a body, and a spent electron beam is partially recovered by retarding the voltage between a body and a grounded collector. Electron extraction is easily stopped in the triode gyrotron by shorting the anode and cathode. Two fast-switches (SWs) with 1 μs rise/fall time are introduced between the cathode and the anode (anode SW1) and between the anode and the anode feed (anode SW2). Circuits using the double-anode SWs method are shown in Figs.9-2 (a) and (b) in the cases of on-phase and off-phase RF waves, respectively. Fig.9-3 shows the effect of double anode SWs. In the case of a single–anode SW (only Anode SW1), the rise time of the anode–cathode voltage is slow because the anode feeding voltage becomes the cathode voltage if the cathode and anode are shorted. By installing the Anode SW2, the anode feeding voltage can be kept constant and the rise time can be increased. As a result, the beam current is completely controlled by the double anode SWs and a 5 kHz 100% RF power modulation is demonstrated for the first time in the world, as shown in Fig.9-4. This result fulfills the ITER requirement.

Reference

Kajiwara, K. et al., Full High–Power Modulation on a 170 GHz 1 MW ITER Gyrotron with a Triode Magnetron Injection Gun, Nuclear Fusion, vol.53, no.4, 2013, p.043013–1–043013–5.

9–2 Achievements toward the Manufacture of the ITER Divertor
— Development of an ITER Full-Tungsten Full-Scale Prototype Divertor —

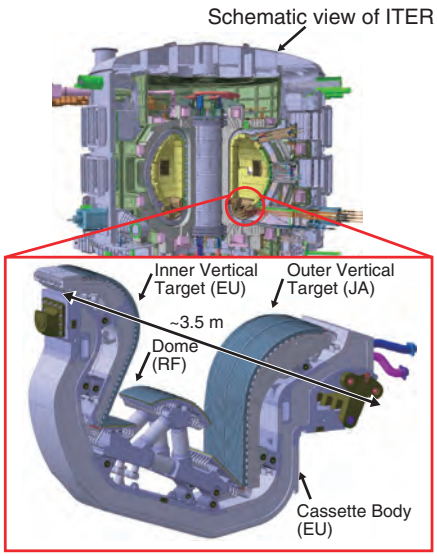

Fig.9-5 Appearance of the ITER divertor (Cassette structure)
The ITER divertor comprises outer vertical targets, inner vertical targets, and domes, which are installed in a cassette body. The total number of divertor cassettes to be installed in a tokamak is 54.

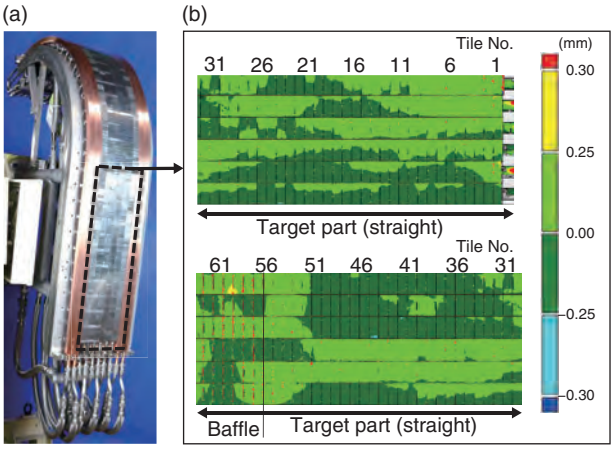

Fig.9-6 Appearance of full-tungsten full-scale prototype plasma-facing units and a result of 3D geometrical measurement
(a) Appearance of six plasma-facing units assembled onto a test frame for high-heat flux testing.
(b) Result of 3D geometrical measurement on the tungsten armor tiles shows that the surface of the target part of the plasma-facing units satisfies the profile tolerance of ±0.3 mm.

JAEA, as the Japan Domestic Agency (JADA), is currently manufacturing various components for the ITER project. The ITER divertor, as shown in Fig.9-5, is intended to neutralize incident impurities and exhaust them from the plasma. These divertor components are provided by three parties (Japan, European Union, and Russian Federation). JADA is going to manufacture one of the high-heat flux components, the so-called “outer vertical targets”.

The plasma-facing units (PFUs) of the ITER divertor are subjected to high-heat flux from plasma. Carbon-fiber-reinforced carbon composite (CFC) materials have been selected as one of the armor materials for the PFUs in the non-nuclear operation phase of the ITER. In 2013, all-tungsten armored PFUs were adopted so as to utilize PFUs in both non-nuclear and nuclear (DD and DT) operational phases, since tungsten is expected to retain less tritium than CFCs. The tungsten armor tiles are metallurgically bonded onto cooling tubes made of copper alloy (CuCrZr) to achieve an adequate heat removal capability. In addition, the geometrical tolerance of the plasma-facing surface of the PFUs is tight enough to avoid the melting of tungsten armor tiles by incident heat flux upon their leading edges. JADA has selected braze technology as a candidate for bonding the tungsten armor tiles to the cooling tubes. High-heat flux tests of prototype PFUs are mandatory for demonstrating the thermal performance and durability of the PFUs and for qualifying the candidate bonding technology in the ITER project. As a first step, JADA has developed full-tungsten, full-scale prototype PFUs, as shown in Fig.9-6(a). Several non-destructive inspections upon the brazed or welded parts of the prototype PFUs have been performed prior to high-heat flux testing. Fig.9-6(b) shows the result of a 3D geometrical measurement on the plasma-facing surface of the prototype PFUs. The target part (straight part), which is subjected to the highest heat flux (~20 MW/m^2) among the divertor components of all prototype PFUs satisfied the required stringent tolerance of ±0.3 mm. Thus, JADA achieved one of the key milestones toward the realization of the ITER divertor.

High-heat flux testing of the prototype PFUs is to be conducted at the ITER Divertor Test Facility (IDTF) by the Russian domestic agency in 2016.

Reference

Ezato, K., Suzuki, S. et al., Progress of ITER Full Tungsten Divertor Technology Qualification in Japan, Fusion Engineering and Design, vols.98–99, 2015, p.1281–1284.

9–3 Cable Twist Pitch Variation in Superconductors for ITER
— Behavior of a Superconducting Cable during Cable Insertion —

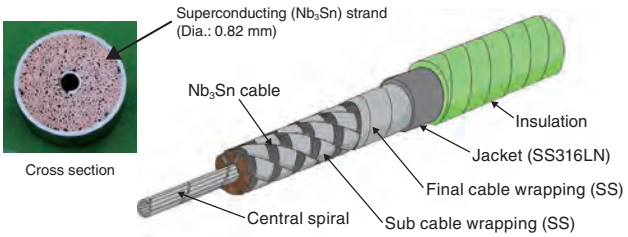

Fig.9-7 Superconductors for the ITER Toroidal Field Coils
A circular, multistage superconducting cable, comprising around 1000 superconducting strands, is inserted into a circular stainless steel jacket.

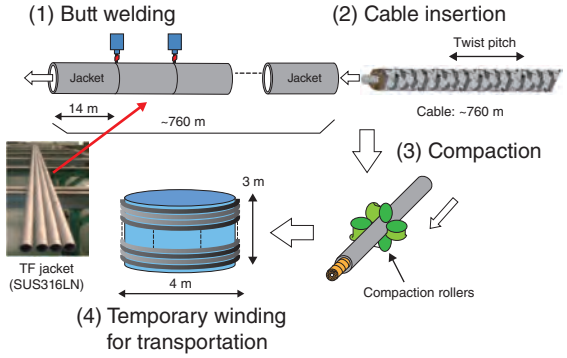

Fig.9-8 Manufacturing procedure for the superconductor
A superconducting cable is inserted into a circular stainless steel jacket assembled by a butt-welding technique, and the jacket is compacted and spooled to a diameter of 4 m.

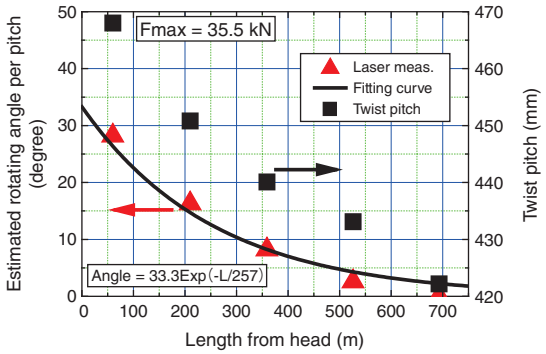

Fig.9-9 Cable twist pitch and estimated rotating angle per one pitch along the entire length
The twist pitch monotonously decreases from head to tail. The rotating angles were estimated from the twist pitches by geometrical analysis using a simple model.

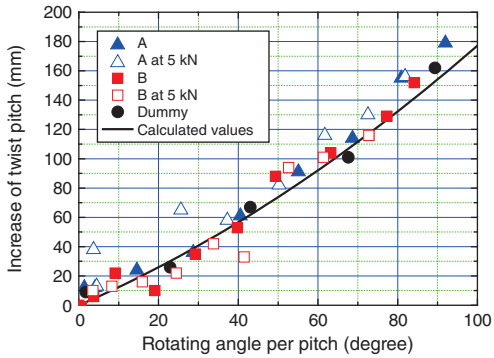

Fig.9-10 Increase of twist pitches versus rotating angle per one pitch
Measured values were obtained during tensile tests of cables (length: 5 m). Calculated values were estimated by geometrical analysis using a simple model.

Around 1000 Nb_3Sn strands with a diameter of 0.82 mm were cabled around the central spiral, as shown in Fig.9-7. The superconducting cables were inserted into the jacket assembled using the automatic Tungsten Inert Gas butt welding technique, as shown in Fig.9-8. The jackets were compacted to the final dimension (43.7 mm) in one step and spooled to a diameter of 4 m. It was observed that the cable pitch of the destructive sample was 474 mm, which is longer than the original pitch (430 mm) at cabling. The cables were manufactured by two suppliers and the cable twist pitches of both cables were elongated. JAEA investigated the cause of the elongation. It was confirmed that the superconducting performance of the conductors with a cable twist pitch below 493 mm is the same as that of conductors with the original twist pitch (430 mm).

The twist pitches of conductors were estimated using the Fourier analysis on the cycles of unevenness (around 0.05 mm) of the outer diameter measured continuously every 20 mm over the entire length (760 m). The twist pitch distribution is shown in Fig.9-9(■). The twist pitch monotonously decreases from head to tail.

To investigate the mechanical behavior of the cables, we performed tensile tests upon them and measured the correlation between increase of their twist pitch and the rotating angle, as shown in Fig.9-10. Calculated values in Fig.9-10(▬) were estimated from the twist pitches by geometrical analysis using a simple model. A good agreement between calculation and measurement is obtained. Therefore, the rotating angle during the cable insertion can be estimated using the increase of twist pitches in Fig.9-9(■) and this correlation. The estimated results are shown in Fig.9-9(▲). The total rotating angle of the cable head during the insertion can be calculated by integration of the rotating angle from head to tail. The obtained angle is 18029°, and the total number of rotations is 50 turns.

A cable rotation measurement was also successfully performed on a 760-m-long cable during the insertion using rotation sensors. The measured value was 51 turns, agreeing with the estimate.

According to these results, it can be concluded that the twist pitch was elongated during the cable insertion due to the pulling load. Since elongation is unavoidable, it is noted that this untwisting behavior of the cable should be considered during the manufacturing of conductors using this method and the manufacturing of the coil (for example terminal fabrication).

Reference

Takahashi, Y. et al., Cable Twist Pitch Variation in Nb_3Sn Conductors for ITER Toroidal Field Coils in Japan, IEEE Transactions on Applied Superconductivity, vol.23, issue 3, 2013, p.4801504–1–4801504–4.

9–4 Production of a Negative Ion Beam with the Largest Current in the World

— Achievement of a 32 A Negative Ion Beam by Improvement of the Beam's Uniformity in the JT-60SA Negative Ion Source —

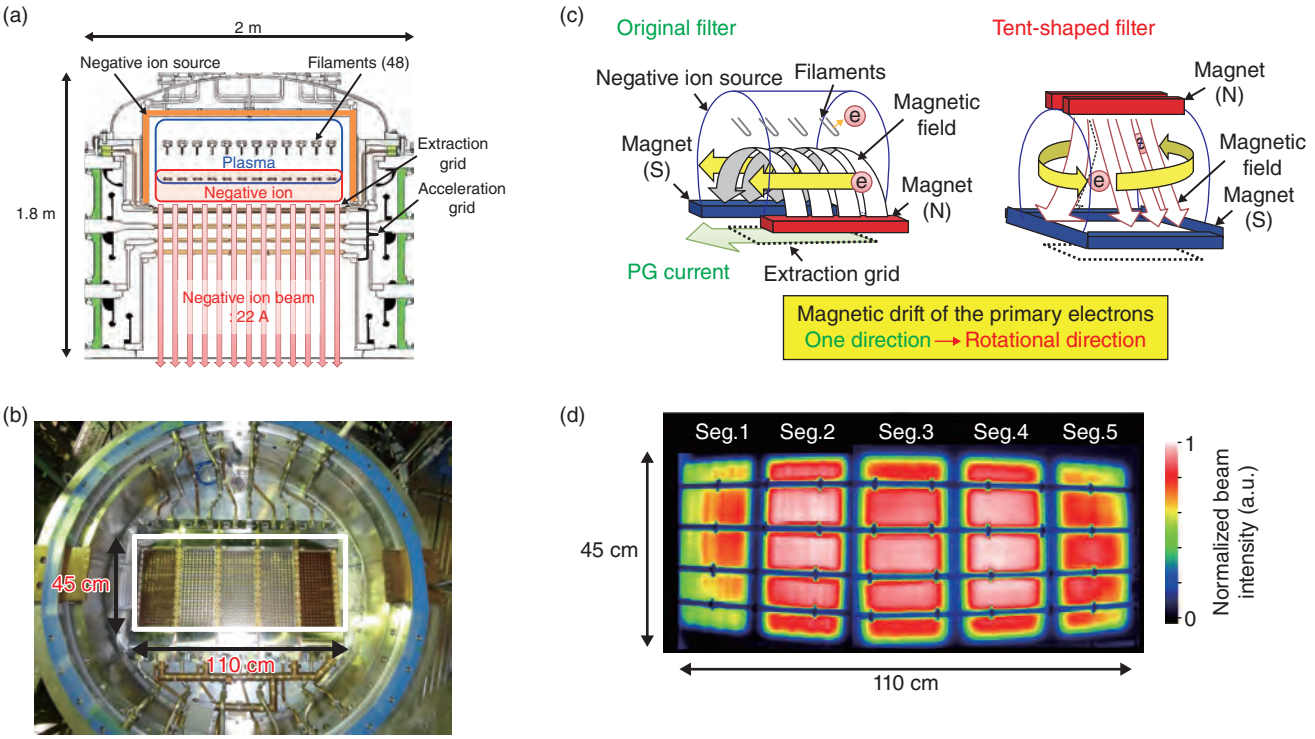

Fig.9-11 JT-60 negative ion source
(a) Cross-sectional view of the JT-60 negative ion source.
(b) Beam extraction grid with the world-largest area of 45 × 110 cm^2.

Fig.9-12 Production of the 32 A H$^-$ negative ion beam
(c) The magnetic field structure and direction of the primary electrons in the original filter and the newly applied tent-shaped filter.
(d) Beam profile of the negative ions produced by the tent-shaped filter.

A negative-ion-based neutral beam injector (N-NBI) is a powerful tool for heating core plasmas and driving plasma currents with high efficiency in fusion machines such as JT-60 Super Advanced (JT-60SA), which is currently under construction. In JT-60SA, the negative ion source for the N-NBI is designed to produce 22 A negative ion beam for 100 s (Fig.9-11(a)) with a large extraction area of 45 × 110 cm^2 (Fig.9-11(b)). One of key issue for such powerful beam production is the improvement of the beam's uniformity because non-uniform beams cause degradation of the beam optics. This leads to the reduction of the beam currents and increase of the local heat load on the extraction/acceleration grids.

We have examined the origin of the non-uniformity of the beams from the JT-60SA negative ion source using an original filter with a transverse magnetic field. As a result, it is experimentally determined that the non-uniform beam production is caused by the localization of the primary electrons emitted from filaments due to drift in the magnetic field. To improve the beam's uniformity, the magnetic structure of the JT-60 negative ion source is modified to a tent-shaped filter (Fig.9-12(c)).

This magnetic structure is expected to allow the primary electrons to rotationally drift in the longitudinal direction. Then, it is found from a trajectory calculation of the primary electrons that their localization can be significantly suppressed by changing the magnetic field filter. By suppressing the localization of the primary electrons, uniform plasma can be successfully produced. As a result, the beam's uniformity is improved from 68% to 83% over the entire extraction area of 45 × 110 cm^2. The improvement of the beam's uniformity leads to the production of 32 A H$^-$ ion beams over the entire extraction area. The obtained beam current fulfills the requirement for JT-60SA (Fig.9-12(d)).

Reference

Yoshida, M. et al., Improvement of Uniformity of the Negative Ion Beams by Tent-Shaped Magnetic Field in the JT-60 Negative Ion Source, Review of Scientific Instruments, vol.85, issue 2, 2014, p.02B314-1-02B314-4.

9–5 Thermal Shields for a Large Superconducting Magnet

— Establishment of a Manufacturing Method for the Thermal Shields for On-Site Assembly —

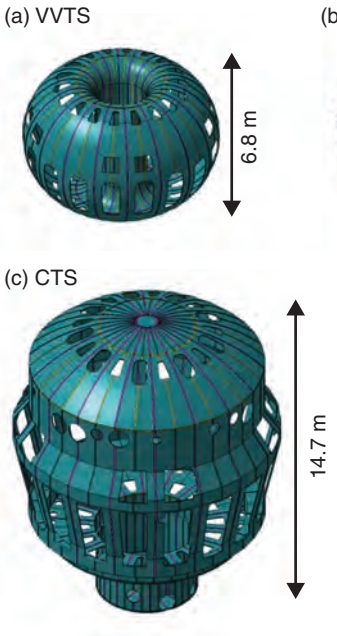

Fig.9-13 Thermal shields (TS) for JT-60SA
VVTS, CTS, and PTS are shown.

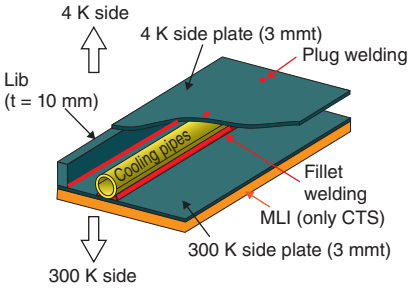

Fig.9-14 Concept of TS
TS comprises two 3-mm-thick stainless steel plates reinforced by ribs and cooling tubes.

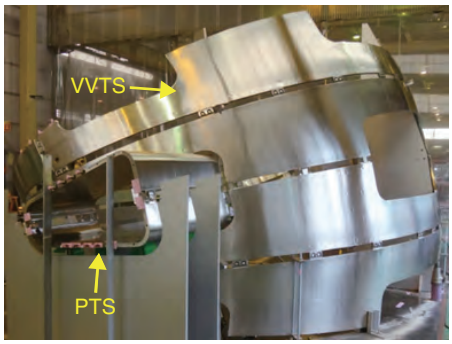

Fig.9-15 Pre-assembly of VVTS
Four sets of VVTSs (10°) are assembled to measure dimensions and to adjust the shape of the coupler.

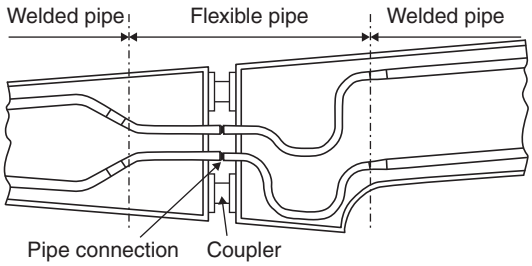

Fig.9-16 Flexible pipe for assembly
The flexible pipe can be moved to adjust the positions of pipe both ends.

JT-60SA is a fully superconducting tokamak device for confining 100 MK plasmas in power-breakeven-equivalent conditions. The superconducting magnet system comprises 18 toroidal field (TF) coils (D-shape), a central solenoid (CS) with four modules, and six equilibrium field (EF) coils (circular shape). The cryostat provides the vacuum environment to stop convective heat transfer to the superconducting magnetic components. The thermal shield (TS) minimizes the heat loads transferred by thermal radiation and conduction from room temperature components to the superconducting magnetic components at 4 K.

The TS comprises three main parts: the vacuum vessel thermal shield (VVTS), the cryostat thermal shield (CTS), and the port thermal shield (PTS), as shown in Fig.9-13. The TS comprises two 3-mm-thick stainless steel plates reinforced by ribs and cooling tubes installed between them, as shown in Fig.9-14. The surface of the plate is polished in the same function as a mirror (emissivity: 0.15). The VVTS has to be divided electrically into 18 toroidal segments and one poloidal segment to avoid excessive eddy current heating. Cooling pipes are connected after each TS (20°) panels are assembled to the already mounted TS on the vacuum vessel of JT-60SA.

Several trials of manufacturing the VVTS are conducted to satisfy the component's tight tolerance (±5 mm at 6.8 m in height). The VVTS, as a thin welded structure, has a large deformation during welding of the pipe and ribs. Shape correction methods of VVTS are established with the mechanical deformation by a jack after pipes and ribs are welded onto the 3 mm plate. Each connecting coupler between the panels is customized to adjust the bolt hale during the preassembly stage (Fig.9-15).

The TS panels are assembled with couplers during on-site assembly. After assembly is complete, cooling pipes are connected by butt welding. The positions of the pipe ends move slightly because the shape of the panel is deformed when the bolt of the coupler is fixed. Thus, each pipe needs flexible parts to adjust the position of the pipe ends within ±2 mm. This flexibility of pipe position is created by the bends of the pipe itself, as shown in Fig.9-16, because bellows cannot fit a space between two plates.

Some VVTSs for the JT-60SA have been manufactured (Fig.9-15) by the shape correction method and the adjustment of pipe position by a flexible pipe. VVTS will be assembled on the vacuum vessel at the Naka site.

Reference

Yoshida, K. et al., Mass Production of Superconducting Magnet Components for JT-60SA, IEEE Transactions on Applied Superconductivity, vol.24, no.3, 2014, p.4200806-1-4200806-6.

9–6 New Method for Plasma Diagnostics to Reduce Noise Effects
— Separation of Two Signals from a Round-Trip Laser —

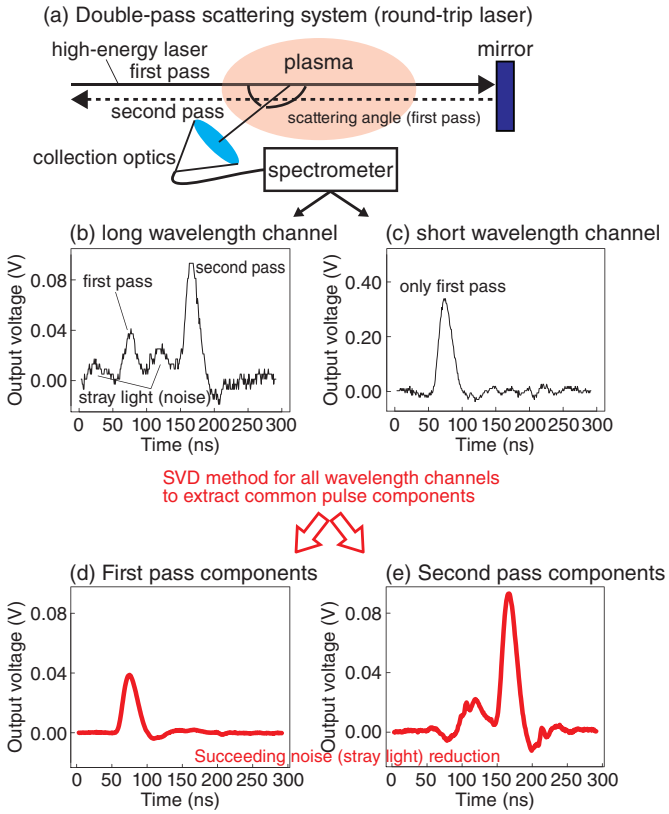

Fig.9-17 Double-pass scattering system and output signals
(a) A laser passes though the plasma twice and generates two time-separated scattered lights. (b) and (c) Typical output signals from a spectrometer (short and long wavelength channels, respectively). (d) and (e) Filtered signals of the first and second passes by the SVD method, respectively.

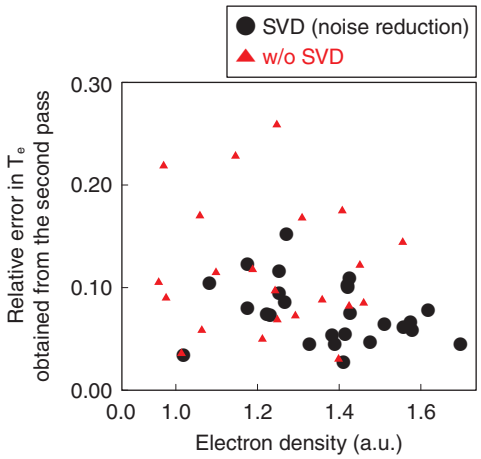

Fig.9-18 Comparison of the relative error in the electron temperature obtained from the second pass in LHD experiments
●: noise filtered using the SVD method. ▲: non-filtered.

When a high-energy laser goes through the plasma, scattered light (Thomson scattering) is generated along the laser path. Electron temperature and density in the plasma can be calculated from the measured spectrum of the scattered light. Recently, double-pass scattering systems, whereby laser beams pass through the plasma twice using a reflection mirror and provide scattered lights twice, have been developed (Fig.9-17(a)) in some fusion experiments. This system is utilized for spectral calibrations and for evaluating discrepancies in electron temperature between the parallel and perpendicular directions about the magnetic field. Analyzing two different spectra generated from the double-pass scattering makes this possible.

However, the double-pass scattering system sometimes suffers from intense stray light, which overlaps with the pure scattered light in the measured signals because of multiple diffuse reflections of the laser on the vacuum windows. Shaping of the overlapped signal is difficult because both components (stray and scattered light) are similar in the frequency space. A noise removal method using singular value decomposition (SVD), which does not use the Fourier analysis, was employed to extract pure scattered signals.

We tested the method using data obtained in the Large Helical Device (LHD) under a collaboration study with the National Institute for Fusion Science. Figs.9-17(b) and (c) present output signals from two wavelength channels in the spectrometer. Strong noise components (presumably stray light) appear in the long wavelength channel (Fig.9-17(b)). Use of the signals from all six wavelength channels enables the effective extraction of pure scattered signals. The extracted components (signals) for the first and second passes are obtained as shown in Figs.9-17(d) and (e), respectively. Fig.9-18 compares relative errors in electron temperature obtained from the noise-reduced signals by the SVD and from the raw signals for many measurements. Use of the former case is effective to ensure good accuracy. This noise reduction method can be used for a JT-60SA Thomson scattering system.

Reference

Tojo, H. et al., Signal Evaluations using Singular Value Decomposition for Thomson Scattering Diagnostics, Review of Scientific Instruments, vol.85, issue 11, 2014, p.11D865–1–11D865–3.

9–7 Study on a LOCA in a Fusion DEMO Reactor

— Activity Toward the Establishment of Safety Design Guidelines for Conceptual Design of a Fusion DEMO Reactor —

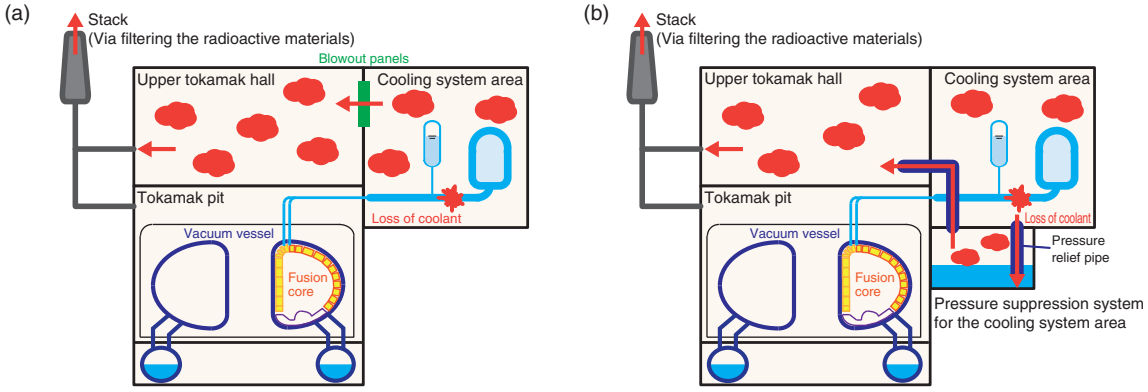

Fig.9-19 Strategies to maintain the integrity of the final confinement barrier for radioactive materials in a loss-of-coolant accident

We compared two confinement strategies: (a) use of the emergency HVAC system and (b) use of the emergency HVAC system and the pressure suppression system for the cooling system area. In the latter case, depressurization due to condensation in the pressure suppression system is expected. ← represent the routes of pressure relief.

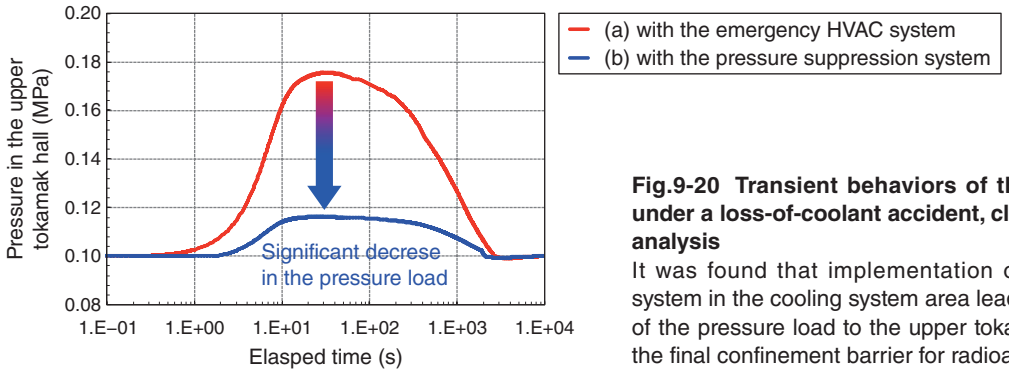

Fig.9-20 Transient behaviors of the fusion DEMO systems under a loss-of-coolant accident, clarified by thermohydraulic analysis

It was found that implementation of a pressure-suppression system in the cooling system area leads to significant suppression of the pressure load to the upper tokamak hall, which constitutes the final confinement barrier for radioactive materials.

Fusion reactors involve radioactive materials like tritium as fusion fuel and radioactive products due to irradiation by fusion neutrons. If an accident occurs, progression of the accident must be prevented and functions for confinement of the radioactive materials must be ensured. Safety research is being conducted now by JAEA, aiming to establish safety design guidelines for the conceptual design of the fusion demonstration (DEMO) reactor. We postulate a variety of accident situations, and analyze the responses of DEMO systems to such accidents. The accident analyses allow us to identify the safety characteristics of the DEMO in accident situations. We are also studying systems for the prevention of accident progression and for mitigation of accident consequences.

Ex-vessel loss-of-coolant accidents (LOCAs) are postulated to be of importance for the safety of the fusion DEMO reactor. Water, which is used for cooling the in-vessel components and electricity generation, is maintained under conditions of a pressure of 15.5 MPa and a temperature of 290–325 °C; these conditions are similar to those of light water nuclear reactors (pressurized water reactors; PWRs). If a cooling pipe is broken, the water generates a large pressure load to the building constituting the final confinement barrier, and the building may suffer breaks. A key issue addressed here is whether the fusion DEMO reactor will need a pressure-tight area like the containment building of PWRs.

We have analyzed the thermohydraulic response of the fusion DEMO reactor to the ex-vessel LOCA and assessed the effectiveness of strategies to mitigate the pressure load on the building. We conservatively assumed a double-ended break of a cooling pipe in the analysis, which is considered to hardly ever occur. We considered two confinement strategies Fig.9-19(a) use of the emergency heating, ventilating, air conditioning (HVAC) system, and Fig.9-19(b) use of the emergency HVAC system and the pressure suppression system for the cooling system area. The results of the thermohydraulic analysis (Fig.9-20) indicate that use of the pressure suppression system for the cooling system area will significantly decrease the pressure load upon the upper tokamak hall, which constitutes the final confinement barrier for radioactive materials and has a large volume for maintenance of in-vessel components. If the strategy (b) is chosen, the volume of the cooling system vault, which is pressure tight, is three times smaller than the typical volume of a PWR containment building.

We have thus found that the integrity of the final confinement barrier can be maintained by a combination of the use of the area for the intrinsic purposes, i.e., maintenance, with proper segregation of the confinement areas. Although the fusion DEMO reactor will need a pressure-tight area, its volume is relatively small. This finding is important for establishing a concept to confine the radioactive materials by the final barrier.

Reference

Nakamura, M. et al., Study of Safety Features and Accident Scenarios in a Fusion DEMO Reactor, Fusion Engineering and Design, vol.89, issues 9–10, 2014, p.2028–2032.

9–8 Toward Dynamic Control of Core Plasma

— Simulation Study on Non-Local Response in Core Plasma —

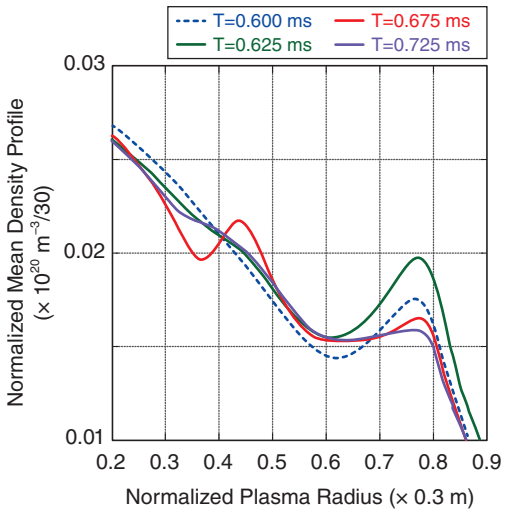

Fig.9-21 Time evolution of the mean density profile
Horizontal axis: normalized plasma radius; vertical axis: normalized mean density profile. A density source is initially applied at the location 0.8 (× 0.3 m) of the plasma radius. Subsequently, the source is turned off and the density profile evolution is followed. At T = 0.675 ms, a non-local response appears near the radial location 0.4 (× 0.3 m) (indicated by ——).

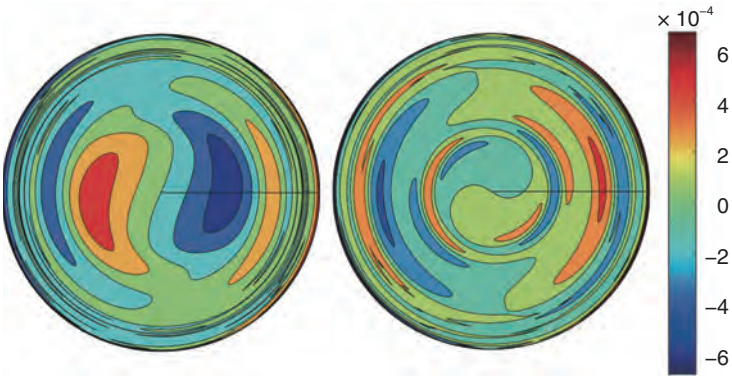

Fig.9-22 Our plot of fluctuating density in a poloidal cross section
Left: fluctuating density in the poloidal cross section (=vertical cross section of the torus) at the time just after the density source is turned off. Right: fluctuating density at the time at which a non-local response appears. At this instant, a spiral structure is formed, which connects the central region of the plasma with its periphery.

For the realization of a tokamak fusion reactor, it is necessary to sustain the burning state. For this purpose, real-time diagnostics with feedback to external profile control should be developed to avoid the degradation of energy confinement and disruptive plasma collapse phenomena. Various control methods have been proposed, such as current profile control through an external current drive and density profile control through pellet injection. A thorough understanding of the plasma response is an important prerequisite for plasma control. In conventional transport codes, the profile evolution was analyzed under the assumption that a steady state is instantaneously realized for all processes that are faster than the collision time. For the dynamic control of plasmas, this assumption should be relaxed.

It has recently been reported that, during pellet injection experiments in tokamaks, an abrupt increase in the electron temperature in the central region simultaneously occurs with a cooling of the plasma edge. This phenomenon occurs on a time scale that is shorter than the collision time and is thought to originate from direct interactions between the central and peripheral regions. To describe such a non-local response, a transport model has recently been proposed, wherein the flux is formulated on the basis of an integral kernel. Such a model can capture transport processes that occur on time scales faster than the collision time. However, direct interactions between the central and peripheral regions of the plasma were not considered.

In this study, the source associated with pellet injection is implemented in a 4-field reduced magnetohydrodynamics (MHD) model, and the transient plasma response is examined. Fig.9-21 shows the time evolution of the mean density profile in a case where the density source is initially applied to the plasma edge and subsequently turned off. ---- represents the density profile just after the source is turned off. It is seen that a non-local profile change appears at a location far away from the source at the moment the density abruptly decreases in the peripheral region. Since the model is normalized by the time that is characteristic for MHD instabilities, it is clear that this phenomenon occurs on a time scale that is much shorter than the collision time. To examine the response in the plasma core, two-dimensional contour plots of the fluctuating density are produced, as shown in Fig.9-22. It is found that the non-local response is accompanied by the formation of a spiral structure. Once this structure forms, it can directly connect the central region with the peripheral one. This may facilitate non-local responses. On this basis, the observed non-local response, the underlying physical mechanism of which has remained obscure so far, can now be understood as a two-dimensional transport phenomenon.

The insights obtained in this study will contribute to the establishment of a physical basis for dynamic control of the ITER and DEMO plasmas as well as non-local transport modeling.

Reference

Yagi, M. et al., Simulation Study of Nonlocal Transport from Edge to Core in Tokamak Plasmas, Contributions to Plasma Physics, vol.54, issues 4–6, 2014, p.363–367.

9–9 Lithium Recovery Technology for Stably Supplying Fuel to Fusion Reactors
— World-First Dialysis Technique for Lithium Recovery from Seawater —

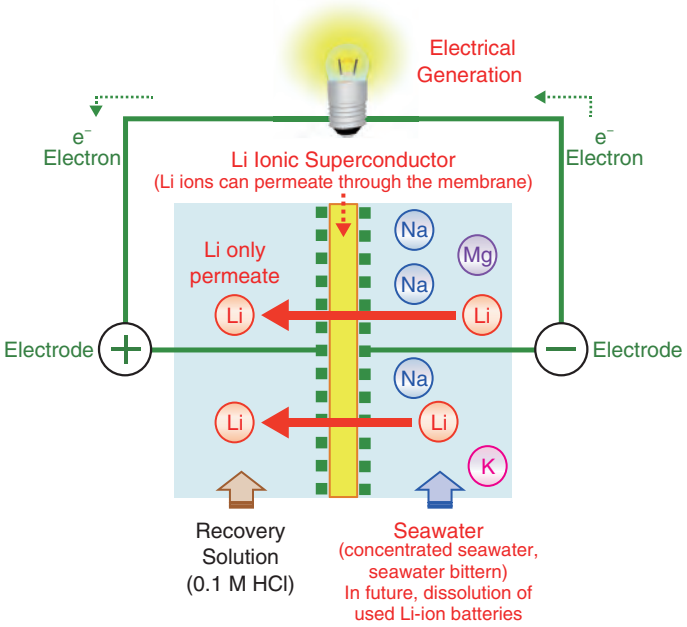

Fig.9-23 Li recovery from seawater by an innovative separation technique
Li only permeates from the negative electrode side to the positive electrode side through a Li ionic superconductor. The principle of this method is similar to that of an ion concentration cell. Although the Li concentration in seawater is very low, only Li ions were successfully recovered from the negative electrode side. Furthermore, electrical power is generated.

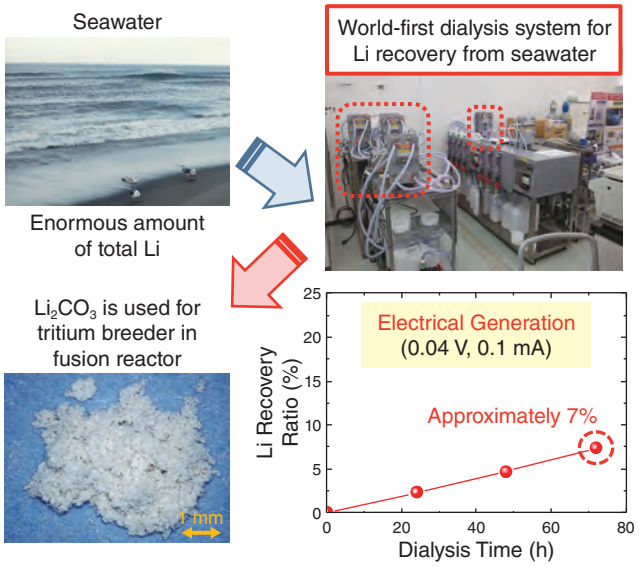

Fig.9-24 Establishment of a Li recovery process for fusion reactors
A Li recovery technique from seawater using a world-first dialysis device has been established. Li becomes selectively concentrated in a Li recovery solution. Then, Li_2CO_3 powder, as a raw tritium breeder for fusion reactors, was fabricated by the chemical reaction of a Li recovery solution (LiCl solution) and a Na_2CO_3 solution.

Fusion reactors need deuterium and tritium as their fuel. Since tritium does not exist in nature, it is necessary to produce tritium in a reactor by neutron irradiation of lithium (Li). Furthermore, Li is rapidly becoming a valuable commodity. As a means of addressing global warming, the world is increasingly turning to the use of large Li-ion batteries in electric vehicles; therefore, there is a growing demand for Li.

Although Li is recovered from salt lakes in South America, the quantity of natural resources in these waters is limited. On the other hand, an enormous fraction of all Li on Earth is known to be present in seawater. The extraction of Li from seawater would allow a large amount of it to be inexpensively acquired. Therefore, Li procurement is a national policy issue worldwide. In particular, Japan relies solely on Li imports from overseas.

Here, we developed a technique for recovering Li from seawater by means of a Li ion superconductor. A potential difference exists between the negative and positive electrodes, even when a voltage is not applied. When a difference in Li concentration between the seawater and the Li recovery solution exists, Li ions flow through the Li ion superconductor. In other words, Li ions can be spontaneously recovered from seawater without the application of outside voltage (Fig.9-23).

Measurements of the Li ion concentration at the positive electrode side as a function of dialysis duration showed that the Li recovery ratio increased to approximately 7% after 72 h with no applied electric voltage. Moreover, other ions in the seawater (Na, Mg, Ca, and K) did not permeate the Li ion superconductor. The recovery solution (LiCl solution) was concentrated after treatment, followed by the addition of an aqueous solution of Na_2CO_3; in this fashion, Li_2CO_3 can be precipitated in an aqueous solution of NaCl (salt water), allowing for the easy extraction of Li_2CO_3 (Fig.9-24).

This world-first recovery technology shows good energy efficiency and is easily scalable. It should be suitable for the industrialized mass production of Li from seawater as well as for the recycling of used Li-ion batteries. In addition, as electricity is also generated in the separation process, a zero emission resource recovery capability is foreseen.

Reference

Hoshino, T., Innovative Lithium Recovery Technique from Seawater by using World-First Dialysis with a Lithium Ionic Superconductor, Desalination, vol.359, 2015, p.59–63.

9–10 Modification of Plasma-Facing Material

— Modification of Vacuum Plasma Sprayed Tungsten Coating by Friction Stir Processing —

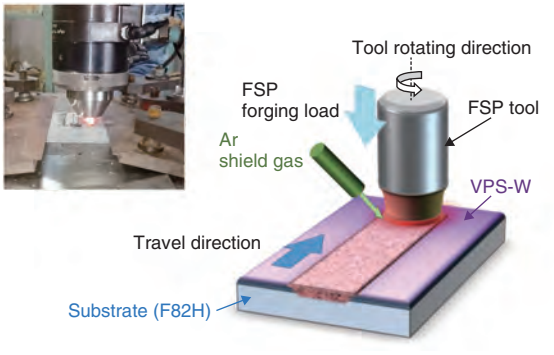

Fig.9-25 General view of friction stir processing
Friction stir processing (FSP) is a modification technology that can eliminate defects and increase the hardness of a material surface by friction heat and plastic flow induced by tool rotation and travel.

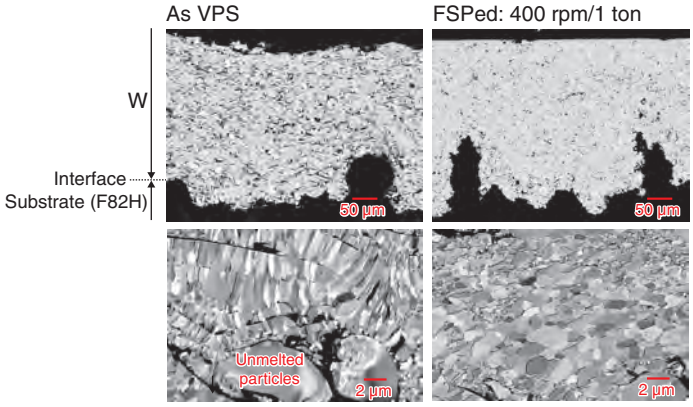

Fig.9-26 SEM observation on VPS-W before and after FSP
The elongated grains in as-VPS-W become finer and more uniform, and the number of interfacial cracks become much less after FSP is applied.

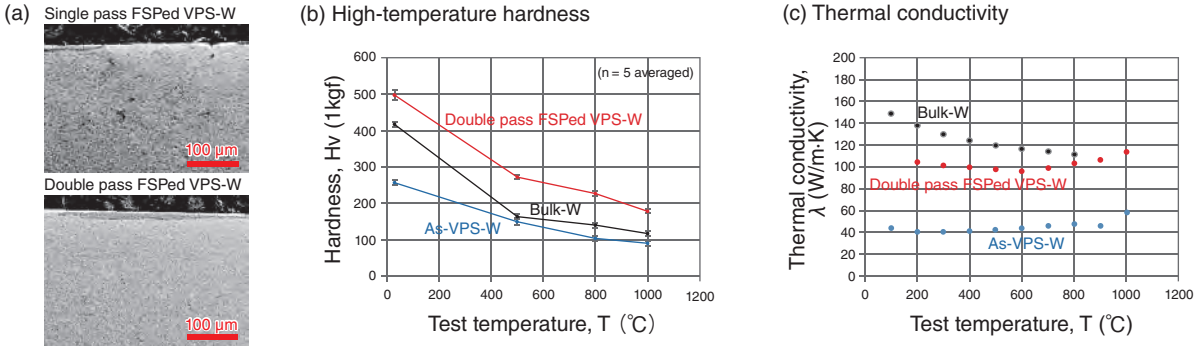

Fig.9-27 Cross-sectional SEM images, temperature dependences of high-temperature hardness, and thermal conductivities of double-pass FSPed VPS-W, as-VPS-W, and bulk-W
Grains become more equiaxed and uniform in the double-pass FSPed VPS-W (a); the FSPed VPS-W is harder than bulk-W and VPS-W in all temperature ranges (b); and the thermal conductivity of the FSPed VPS-W is 80% of that of bulk-W at 200 °C and becomes equivalent to that of bulk-W at 800 °C (c).

Tungsten (W) is the primary candidate for a plasma-facing material in fusion devices, due to its high melting temperature, good thermal conductivity, and low sputtering rate.

The vacuum plasma spray (VPS) technique has been investigated, as it is practical for coating a large area. The issues are that the thermal conductivity of VPS-W is significantly lower and the hardness of VPS-W is much less than those of bulk-W.

Friction stir processing (FSP) is a modification technology that was successfully demonstrated on thermally sprayed cemented carbide layers, which are used as the base materials for cutting tools, dyes, and molds. FSP was applied to VPS-W in this study to solve the issues related to VPS-W (Fig.9-25). The elongated grains in as-VPS-W were found to become finer, equiaxed, and uniform when the VPS-W was FSPed, and the number of interfacial cracks and pores became much less in FSPed VPS-W (Fig.9-26). The remaining gaps between stirred grains in the single-pass FSPed VPS-W were almost gone in double-passed FSPed VPS-W, and grains became more equiaxed and uniform (Fig.9-27(a)). High-temperature hardness tests revealed that the FSPed VPS-W was harder than bulk-W and VPS-W in all temperature ranges and that the thermal conductivity of the FSPed VPS-W is 80% of that of bulk-W at 200 °C and became equivalent at 800 °C (Figs.9-27(b) and (c)).

This study was conducted as collaborative research with Professor Hidetoshi Fujii of the Joining and Welding Research Institute, Osaka University.

Reference

Tanigawa, H. et al., Modification of Vacuum Plasma Sprayed Tungsten Coating on Reduced Activation Ferritic/Martensitic Steels by Friction Stir Processing, Fusion Engineering and Design, vols.98–99, 2015, p.2080–2084.

9–11 Corrosion Inhibition using a Small Amount of Oxygen

— Effect of Dissolved Oxygen on the Corrosion Properties of a Blanket Structural Material —

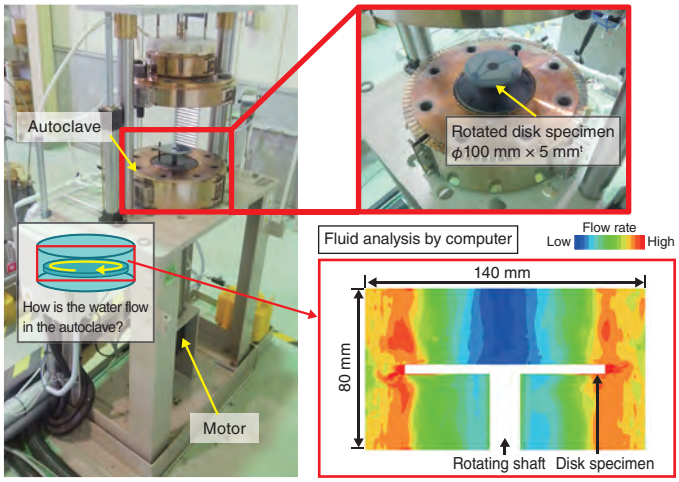

Fig.9-28 Appearance of a corrosion test apparatus for a rotated disc specimen
A rotated disc specimen has been tested in high-temperature pressurized water to investigate the flow-assisted corrosion of structural material for the fusion blanket. The flow speed distribution around the disc specimen has been visualized using computational fluid dynamics.

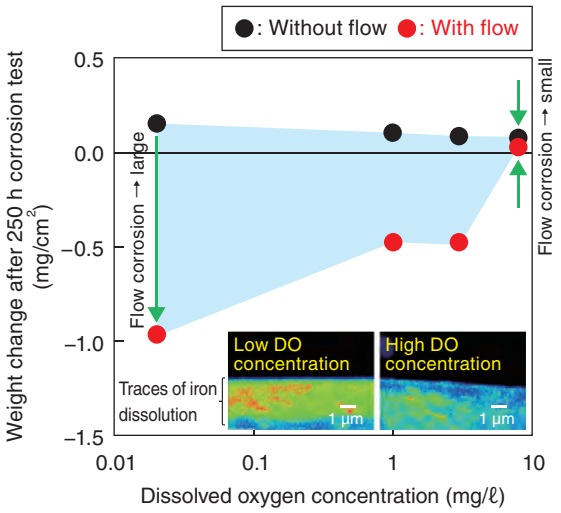

Fig.9-29 Relation between dissolved oxygen concentration and weight change (degree of corrosion) after corrosion test of 250 h
A small amount of oxygen in water (DO) has drastically reduced the effect of flow on corrosion properties ( ). Iron dissolution is hardly observed on the specimen tested at an 8 mg/ℓ DO concentration.

A fusion blanket is a component surrounding fusion plasma and converts fusion energy into thermal energy using high-temperature pressurized water as a coolant. It is important to investigate the corrosion behavior of a structural material for robust design of a blanket. Since the coolant water has a maximum flow rate of 5 m/s, it is worrisome that corrosion will be accelerated by the flow. Therefore, we developed a corrosion test apparatus for a rotated disc specimen to simulate the water flow condition in the blanket (Fig.9-28). We performed the corrosion test in flowing high-temperature water using this apparatus.

Based on the results obtained from the corrosion test under various dissolved oxygen (DO) concentrations (Fig.9-29), all the specimens demonstrated a weight gain after the corrosion test without the water flow. This was caused by oxidation of the specimen. On the contrary, weight loss was observed after corrosion tests under a water flow condition and was significant when DO concentrations were low. By increasing the DO concentration up to 8 mg/ℓ, the weight loss was successfully suppressed and so was the flow-assisted corrosion (in Fig.9-29).

For a clear understanding, a cross-sectional observation of the specimen was conducted. The thick iron-poor layer that formed as a result of the dissolution of iron was observed on the specimen under lower DO concentration, while there was no thick iron-poor layer on it under higher DO concentration. Therefore it is believed that the dissolution of iron caused the weight loss. Based on the microstructural observation of the corrosion product, it was considered that the dissolution of iron was suppressed by forming hematite as corrosion-resistant oxide on the surface of the specimen tested with high-DO water.

Since water flow corrosion was inhibited by inputting a small amount of dissolved oxygen, we obtained an outlook for water conditioning that demonstrates less corrosion. These results contribute to the determination of cooling water conditions for the fusion blanket and bring us one step closer to the realization of a fusion reactor.

Reference

Nakajima, M. et al., Corrosion Properties of F82H in Flowing High Temperature Pressurized Water, Journal of Plasma and Fusion Research SERIES, vol.11, 2015, p.69–72.

Computational Science and Technology as a Common Foundation for Nuclear Research and Development

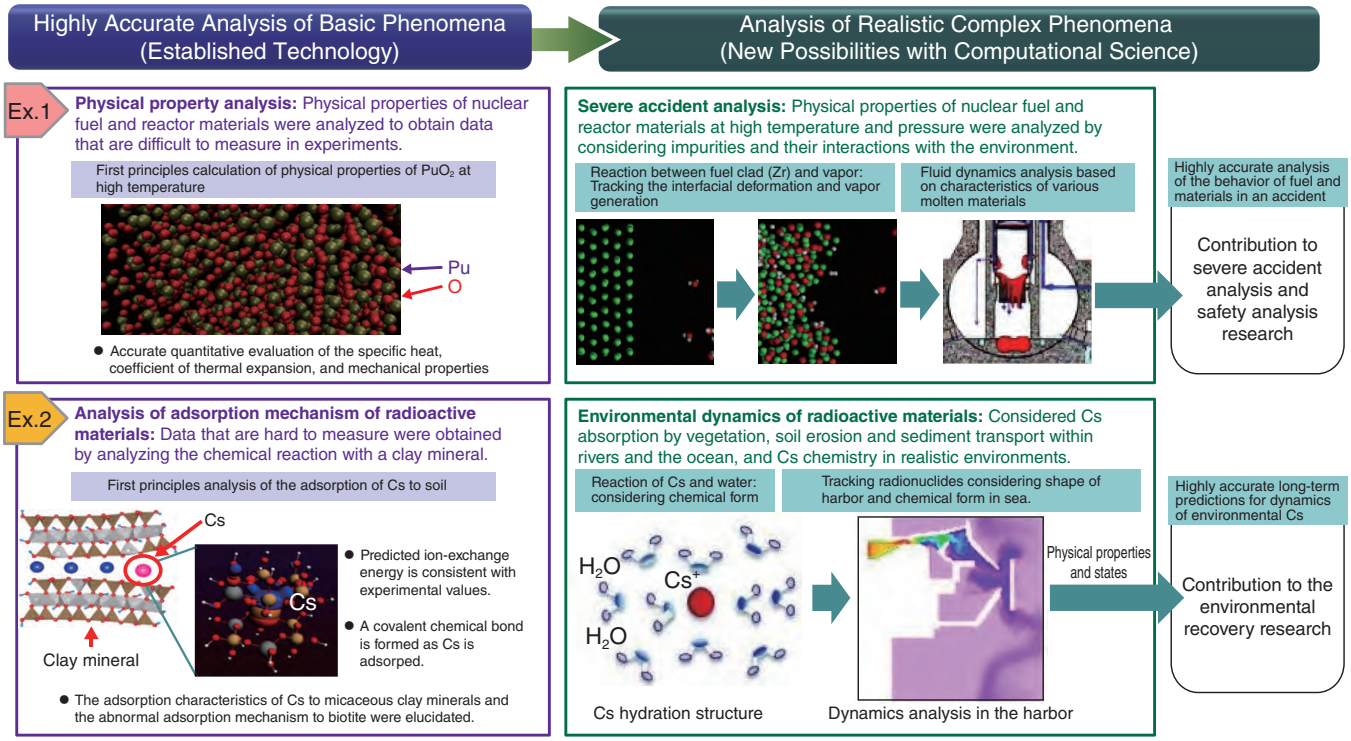

Fig.10-1 Activity with computational science and technology by CCSE
Using both established techniques and knowledge and pursuing new technological developments in computational science, CCSE is contributing to the reconstruction and revitalization for Fukushima.

Computational simulation is indispensable for analyzing the complex problems created by the accident at the Fukushima Daiichi Nuclear Power Station of Tokyo Electric Power Company, Incorporated, such as environmental dynamics of radioactive materials, volume reduction of polluted soil, and severe accident analysis. For example, to understand the kinds and forms of radioactive materials released by severe accidents, simulating the total system, ranging from atom-scale behavior involving impurities in nuclear fuel to wide-area environmental dynamics, is necessary. Since such simulations require large amounts of memory and computing time due to their complexity, employing supercomputers is necessary. The simulation technology for analyzing complex phenomena is the common foundation of nuclear research and development as well as severe accident analysis.

At the Center for Computational Science & e-Systems (CCSE), we were developing the technology needed for highly accurate analysis of the physio-chemical phenomena that underlie the abovementioned complex phenomena and applying it to nuclear fuel and structure analysis. At present, we have expanded the established technology base by incorporating experimental results and observations and are tackling new problems related to the analysis of complex phenomena (Fig.10-1).

To understand why radioactive cesium (Cs) is adsorbed so strongly by clay minerals in soil, we solved a part of the adsorption mechanism by comparing the results of an atomistic simulation with those of observations and experiments (Chapter 1, Topic 1-7). This achievement through the use of computational science contributes to Fukushima reconstruction and revitalization. Other top research achievements include the following contents.

(1) Demonstration that hydrogen in low-temperature iron impedes the movement of defects (dislocations) related to the deformation of reactor materials (Topic 10-1).
(2) Systematic examination of the tolerance of a superconductor to its impurities using a supercomputer (Topic 10-2).
(3) Development of technology to improve numerical analysis by enabling interactive visualization between remote supercomputers and a local personal computer (Topic 10-3).
(4) Progress in technology to analyze the behavior of the total structure of a nuclear facility against earthquakes on the basis of the modeling of the many parts forming the facility and the joints between them (Topic 10-4).

CCSE continues to promote research and development of computational science and to domestically and internationally disseminate its results.

10–1 Search for the Strengthening Elements of Metals

— Strength Prediction of Metal Materials via Quantum Mechanical Computation —

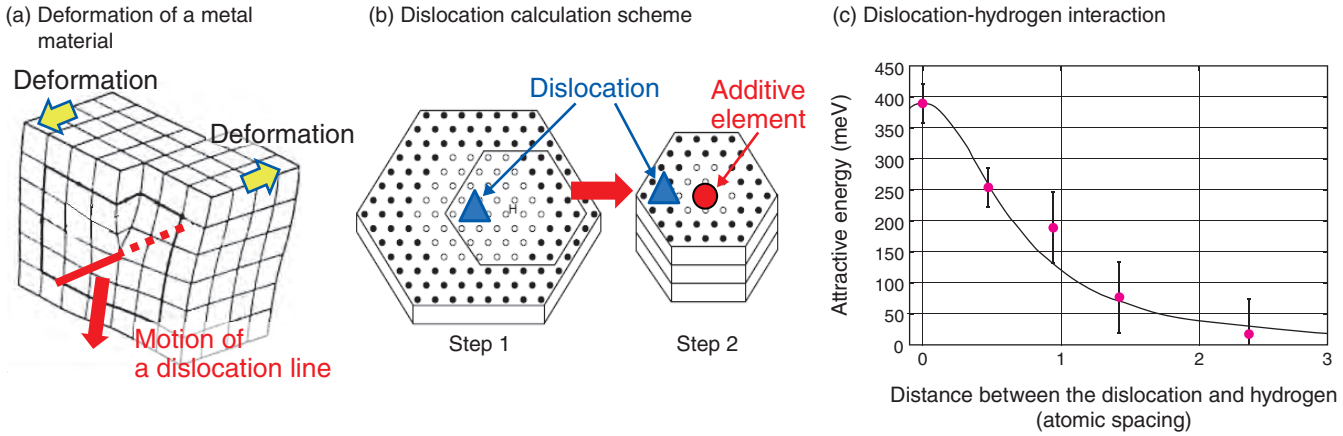

Fig.10-2 Calculation of dislocation and impurity elements
Schematics of the QM calculations of dislocation and additive elements developed in the present study.
(a) The behavior of a dislocation line when a metal material deforms. A half-plane, whose boundary is ▬ ▪ ▬, is introduced to the crystal. The crystal is cut by this plane and atoms located on it are displaced by one atomic spacing. If ▬ ▪ ▬ moves downward, the displacement propagates in the crystal and the crystal deforms.
(b) The numerical scheme to reduce the number of atoms in the calculation of the dislocation and an additive element. First, QM calculation of the dislocation line shown by ▲ is conducted, and then, an additive element (●) is introduced and calculation is performed only for the atoms near the additive element. ○ and ● denote the atoms for which QM calculations have been performed and omitted, respectively.
(c) The attraction between the dislocation and a hydrogen atom, estimated by the present study. The attraction becomes stronger when the dislocation is closer to the hydrogen atom.

Owing to their strength and availability, steels are used for various applications in our civilization, such as automobiles, bridges, and nuclear reactors. Modern steels generally contain more than ten separate elements, and their content rates are optimized for specific purposes based on the results of numerous experiments. For example, it has been found that chromium increases corrosion-resistance and phosphorus degrades the steel. Recently, much attention has been devoted to computational materials design, which considers the effect of various elements based on the simulations and big data analysis, for the accelerated development of new materials.

To predict the effect of various elements on the strength of steels, quantum mechanical (QM) calculations are required. The difference in the number of electrons in different elements greatly changes the behavior of electrons in the material and affects various material properties. Calculation of these effects must account for many electrons. The computational time is proportional to the cube of the number of atoms. Even for current supercomputers, several hundred atoms is the maximum possible scale of calculation. Within this limitation, using ingenious calculation techniques, various material properties have been clarified by QM calculations, such as the effect of additive elements on the force required to break the material. However, owing to the complexity of the process, there have been no QM calculations of the deformation properties of metal materials, which is one of their most important properties. Fig.10-2(a) depicts the deformation process of metal materials. A movement of a dislocation line in a material induces a slip on the atomic plane and the material deforms while the crystal structure remains intact. Since the dislocation line is relatively a large-scale structure, calculation of a dislocation line and additive element requires about one thousand atoms, which is impossible.

To solve this problem, we have invented a multi-scale approach wherein QM calculation of a dislocation line is performed first and then an additive element is included in the calculation. QM calculations are performed only for the atoms close to the additive element. By this method, the number of atoms in the QM calculation is reduced to one-third of the original case, allowing the calculation to be treated by current supercomputers. We have applied this method to investigate the effect of hydrogen atoms on the motion of dislocations in iron and found that there is a strong attraction between the hydrogen atom and dislocation, which prevents deformation of iron at low temperature. We will apply this method to various additive elements used in nuclear reactor materials and accelerate the development of improved nuclear materials.

Reference

Itakura, M. et al., The Effect of Hydrogen Atoms on the Screw Dislocation Mobility in BCC Iron: A First-Principles Study, Acta Materialia, vol.61, issue 18, 2013, p.6857-6867.

10–2 Supercomputer Simulations Solve the Puzzle of Impurity-Robust Superconductors
— Relation between the Relativity of Electrons and Superconductivity —

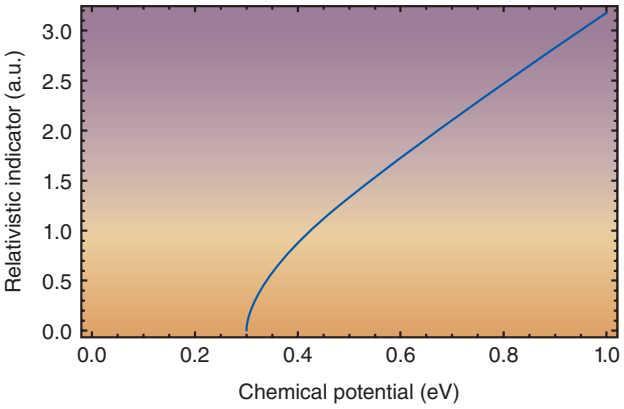

Fig.10-3 Chemical-potential dependence of the "relativistic" parameter (see the main text) in superconductor $Cu_xBi_2Se_3$
Cu-doping level is proportional to chemical potential. Then, electrons become more relativistic in higher doped region.

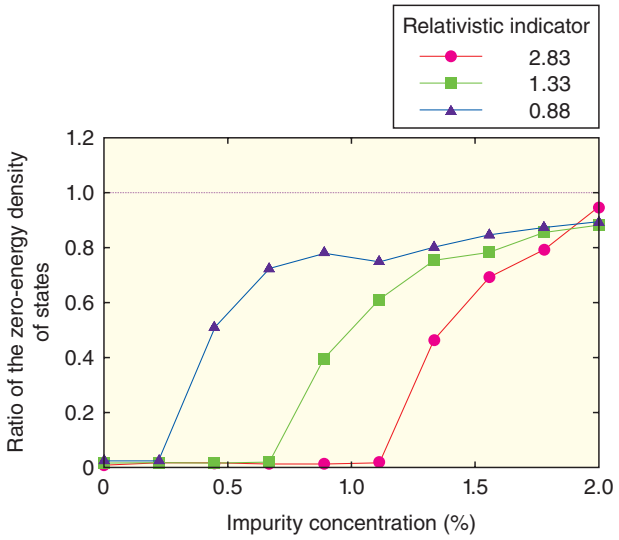

Fig.10-4 Impurity amount dependence on the ratio of the zero-energy density of states in superconducting state to that of the normal one in the superconductor
When the ratio reaches unity, the superconductivity is completely destroyed. The superconductor becomes more robust against non-magnetic impurities as the relativistic parameter increases.

In the materials called superconductors, electrical resistance vanishes at low temperature. So far, potential applications of the superconductors have been intensively studied in nuclear R&D fields. In fact, superconducting coils will be indispensable for nuclear fusion reactors. The superconductors can also produce autonomous devices working in ultimate environment like space.

Recently, so-called topological superconductors have attracted much attention, since entirely new types of devices become possible when using topological superconductors. However, the topological superconductors have been usually regarded to be very fragile against impurities. In other words, with increasing impurity concentration, the superconducting transition temperature decreases, and then any device application does not work. Therefore, we investigated how robust a candidate of topological superconductors, $Cu_xBi_2Se_3$ against impurities. As a result, we theoretically found that a "relativistic" parameter determines the impurity robustness. This "relativistic" parameter comes from the fact that the equation of motion for electrons in $Cu_xBi_2Se_3$ is equivalent to that for relativistic particles. As the speed of electron increases, the superconductivity becomes more robust against impurities. By shifting the chemical potential proportional to Cu-doping, one can adjust the relativistic parameter (Fig.10-3).

In order to confirm this theoretical scenario, we numerically simulated the superconductivity with finite impurity concentration. Then, we developed the code which can solve the equation of motion for electrons in realistic materials on a supercomputer. Consequently, we obtained the result that a superconductor with a large "relativistic" parameter is robust against impurities and that one can control the impurity robustness by Cu-doping (Fig.10-4). Thus, we could show that these kinds of topological superconductors become useful by tuning the "relativistic" parameter.

This study was supported by Japan Society for the Promotion of Science (JSPS) KAKENHI Grant-in-Aid for Young Scientists (B) (No.26800197).

Reference

Nagai, Y. et al., Nonmagnetic Impurity Effects in a Three–Dimensional Topological Superconductor: From *p*– to *s*–Wave Behaviors, Physical Review B, vol.89, issue 21, 2014, p.214506–1–214506–6.

10–3 Visualization of Large-Scale Data Located on a Remote Supercomputer

— Development of a Remote Visualization System Based on Particle-Based Volume Rendering —

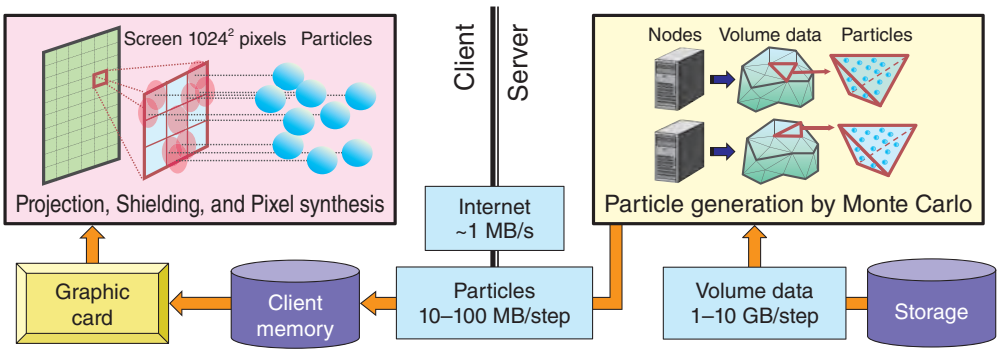

Fig.10-5 Abstract of the remote visualization system
This system compresses a large-scale simulation result into small-scale particle data using a massively parallel process on the server-side and transfers the particle data to a PC on the client-side. This system can minimize the amount of data transfer and enable high-speed remote visualization.

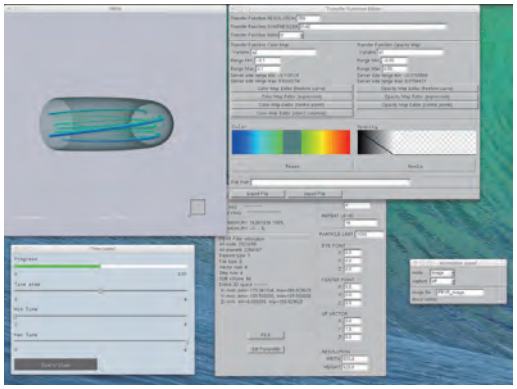

Fig.10-6 Example of the use of the remote visualization system
Users can interactively visualize the large-scale data located on the remote supercomputer using the intuitive interface.

The recent progress of supercomputer technology has resulted in an increase of the simulation scale and the resulting data size. It is difficult to visualize such large-scale data by the conventional offline processing approach because all the resulting data needs to be transferred to a PC on which commodity visualization software has been installed. To resolve this problem, we have developed a remote visualization system based on a visualization method called “particle-based volume rendering”.

This system converts volume data (resulting data) into particle data (Fig.10-5). The conventional visualization technique involves the growth of polygons commensurate with the volume data size. In contrast, our system remarkably compresses the gigabyte-order large-scale volume data into small particle data, whose size is determined by the screen resolution and is typically of the order of 10 megabytes. By focusing on this feature, the particle conversion and rendering processes are separated into a server and a client, respectively, bringing about a distributed visualization model with the least-size data transfer.

The other issue facing the large-scale data visualization is parallel processing. The conventional parallel visualization process subdivides the volume data into numerous sets of sub-volume data. However this requires parallel polygon-sorting against the screen, which increases node communication costs and decreases parallel performance. Our system generates the particle data in parallel and is thus able to combine the entire particle data without such a sorting process. However, it is difficult to maintain a load-balance of the parallel particle generation because of the deviation of the particle distribution. Dynamic load-balance has solved this problem, which is developed to assign a subsequent particle generation to empty cores. This technique has accelerated the particle generation with high parallel efficiency up to 1000 cores.

A comparison of the performance of our system with that of conventional visualization software is conducted by connecting a remote supercomputer and PC via a network. Our system achieved ~30 times faster speed than that of the conventional software and enabled users to interactively visualize the large-scale data located on a remote supercomputer. To disseminate our system to many users within JAEA and beyond, a graphical user interface has been prepared (Fig.10-6) and released as open-source software.

(http://ccse.jaea.go.jp/ja/download/software.html)

Reference

Kawamura, T. et al., Remote Visualization System Based on Particle Based Volume Rendering, Proceedings of SPIE, vol.9397, 2015, p.93970S–1–93970S–8, in CD–ROM.

10–4 Analyzing Structural Soundness using “K” Computer

— Contributing to Infrastructure Maintenance with High Earthquake Resistance through the Structural Analysis of an Assembly —

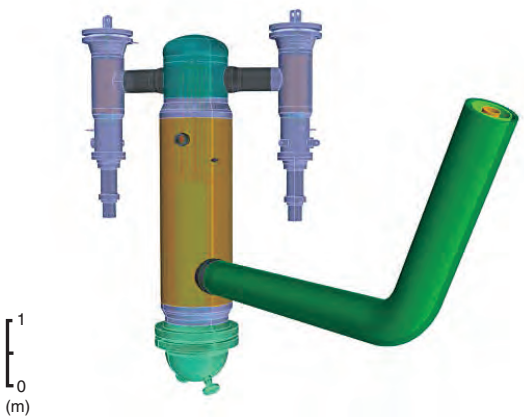

Fig.10-7 Simulation under real conditions
Part of the plant structure under real conditions, represented as a complex three-dimensional structure in graphical form. As indicated by the different component colors, the structure is an assembly of various parts.

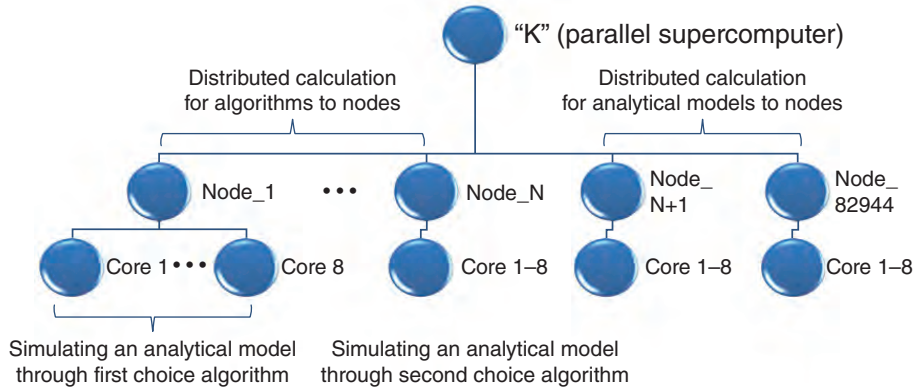

Fig.10-8 Parallel distributed processing for the structural analysis of assemblies
“K” computer is composed of 82944 nodes, each of which has one CPU with eight cores. This allows 663552 (=82944 (CPUs) × 8 (cores)) parallel computations.

The Center for Computational Science and e-Systems (CCSE) has established a principle that can greatly improve the certainty of the structural analysis of an assembly in seismic assessment by utilizing the state-of-the-art supercomputer, “K”.

Most industrial products are composed of multiple parts. When analyzing the soundness of an assembly, empirical knowledge and know-how are required for the handling of part joints. The need to achieve more realistic results for this soundness analysis prompted us to investigate technological developments to simulate the structure under real conditions (Fig.10-7). One of these developments is the “structural analysis of an assembly”.

Recently, the code for the structural analysis of an assembly which was developed by JAEA, was ported onto “K” to enable structures to be simulated under real conditions. In particular, the analysis of the resonance conditions of a structure, which are indispensable for the vibration analysis of an assembly, was performed simultaneously by using several calculation methods for several design proposals on “K”. This not only shortens the calculation time, but also dramatically improves the certainty of the calculation results (Fig.10-8).

However, as conventional supercomputers do not have the computing ability to simultaneously process several huge datasets consisting of details of the many parts of assembled structures, computations are commonly performed by empirically selecting an analysis method. Therefore, based on R&D outcome, the use of “K” computer to compare the results of several calculation methods enabled us to significantly improve the rational analysis by achieving higher simulation accuracy for the first time. In addition, the simulation of an assembly vibration analysis, which used an observed seismic wave as the input wave, also succeeded.

In the future, it is foreseen that this research will contribute to the advancement of seismic infrastructure maintenance. It will be utilized not only in the nuclear field, for example, for light-water and next-generation reactors, but also for industrial applications.

This study is supported by the HPCI Strategic Program “Next-generation seismic simulation of large industrial plants” of the Ministry of Education, Culture, Sports, Science and Technology in Japan (MEXT).

Reference

Nakajima, N., Nishida, A. et al., Structural Analysis for Assembly by Integrating Parts, Proceedings of 22nd International Conference on Nuclear Engineering (ICONE 22), Prague, Czech Republic, 2014, ICONE22–30251, 9p., in DVD–ROM.

Technological Development and Human Capacity Building in the Area of Nuclear Nonproliferation and Nuclear Security to Support the Peaceful Use of Nuclear Energy

The Integrated Support Center for Nuclear Nonproliferation and Nuclear Security (ISCN) has been conducting the following technological and human capacity development activities related to nuclear nonproliferation and nuclear security in cooperation with relevant domestic and overseas organizations (Fig.11-1).

Technological Development for Japanese and International Applications

We have been developing a nondestructive assay technology based on passive γ-ray emission from fission products coexisting with nuclear materials to quantify nuclear materials in fuel debris at the Fukushima Daiichi Nuclear Power Station of Tokyo Electric Power Company, Incorporated and have also been examining safeguard technologies in case spent fuel direct disposal is applied. We have developed some basic technologies for nuclear measurement and detection to enhance nuclear security and improve safeguards. Furthermore, we have developed basic analytical technologies for nuclear forensics. Topic 11-1 shows one of the results of this development, namely, a database called the nuclear forensics library.

Support for Government Policy Formulation Based on Our Expertise

We are conducting research on measures for ensuring nuclear nonproliferation and nuclear security on the backend of the nuclear fuel cycle. To reduce the burden of safeguards upon the direct disposal of the spent fuel, the plutonium concentration and isotopic ratio in spent fuel as well as the difficulty in recovering plutonium from spent fuel were investigated.

Based on the investigation, practical measures for future institutional issues were studied.

Support for Human Capacity Development

Based on the commitments of the Japanese government at the Nuclear Security Summit in April 2010, we established the center, which will contribute to strengthening nuclear security among Asian countries. In FY 2014, approximately 680 participants (approximately 410 participants from Asian states) participated in the seminars and training courses on nuclear security and safeguards.

International Contributions Based on Our Expertise and Experience

To establish a global verification regime for the nuclear tests, we have been provisionally operating the facilities of the international monitoring system of the Comprehensive Nuclear-Test-Ban Treaty (CTBT) as well as a National Data Center (NDC). The Takasaki Radionuclide Station not only continues to conduct particulate monitoring but also was certified by the CTBT organization as the first noble gas station in the coastal states comprising East Asia in December 2014.

Support for JAEA's Transportation and Research Reactor Fuel Duties

We are supporting nuclear transportation conducted by our research and development centers and have coordinated the procurement of fresh fuels and disposal measures of spent fuels for our research reactors. Through these activities, we contribute to Global Threat Reduction Initiative (GTRI), which has been strengthening global nuclear security by promoting the systematic return of highly enriched uranium to the United States.

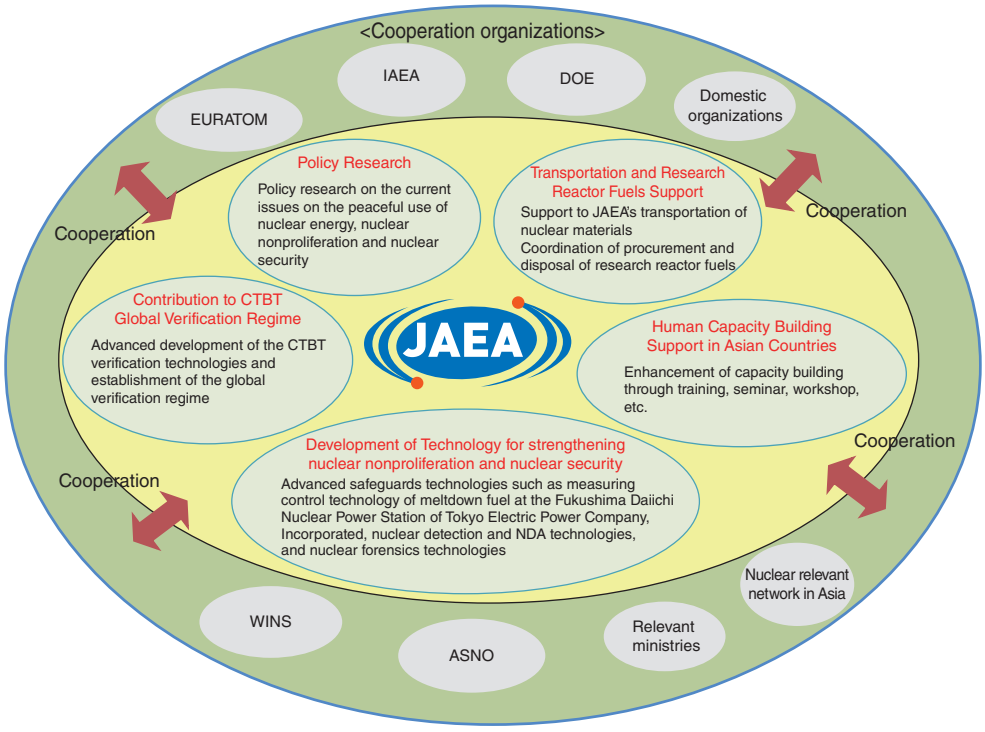

Fig.11-1 JAEA activities toward the development of science and technology for nuclear nonproliferation and nuclear security
We have been playing an active role in international organizations, such as the IAEA, and in technological development in each country to ensure transparency. We are also continuing to develop human capacity to support nuclear nonproliferation and security projects in Asian countries.

11–1 Information Infrastructure for the Identification of Illicit Nuclear and Radioactive Materials

— Development of a Nuclear Forensics Library and Data Analysis Tool for Nuclear Forensics —

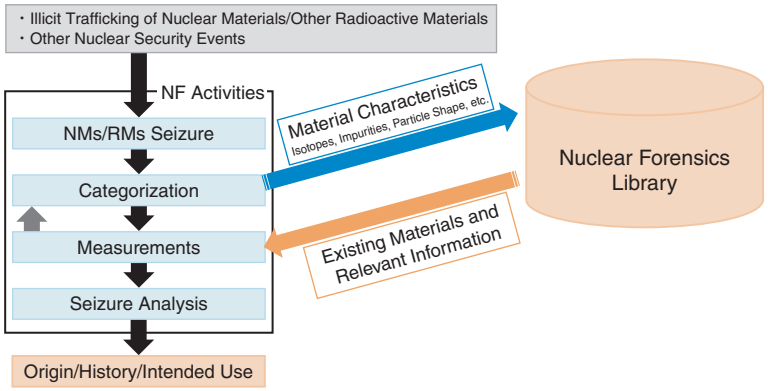

Fig.11-2 Nuclear forensics library and nuclear forensics activities
Development of an NFL is one of the most important elements in nuclear forensics activities.

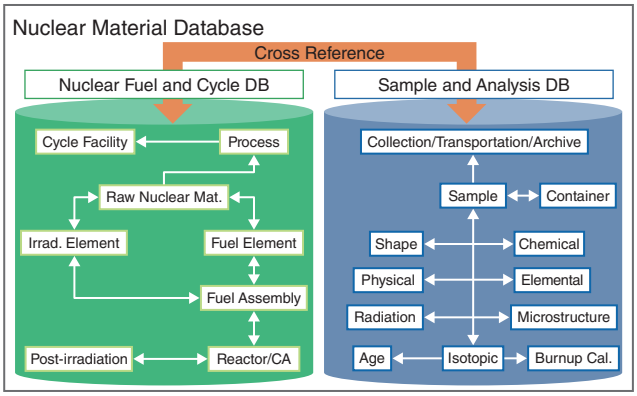

Fig.11-3 Outline of the nuclear material database structure of the nuclear forensics library in JAEA
The nuclear material database has been developed with flexibility based on existing data on various nuclear materials from JAEA.

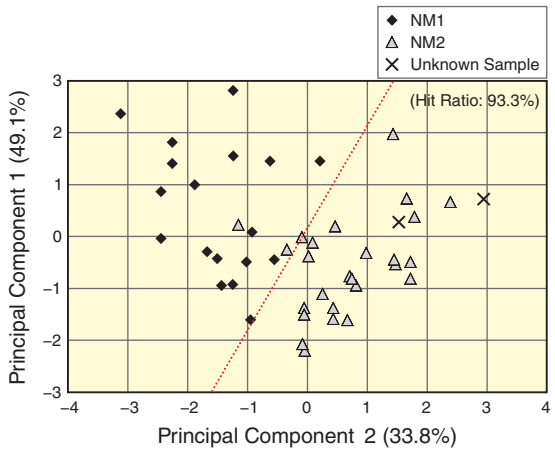

Fig.11-4 Evaluation example of the data analysis tool
An unknown sample was evaluated and compared with the data of two nuclear materials stored in the database by principal component and discrimination analyses. The result shows that the unknown sample is judged as NM2 with ≥90% probability.

Recently, illicit trafficking of nuclear materials and other radioactive materials has been an issue of concern to international society, and many countries have been making efforts to establish the capabilities to perform nuclear forensics activities. A nuclear forensics library (NFL) is generally defined as an organized collection of data and information about nuclear and other radioactive materials produced, used, or stored in the past. When the illicit trafficked nuclear or radioactive materials are detected, they are seized and their physical and chemical characteristics are measured. Then, the measurement data is matched against existing materials registered in the NFL, and suspect materials are identified with their historical information. The final goal of nuclear forensics analysis is to identify the origin, history, and intended use of the seized materials (Fig.11-2). In this context, an NFL is one of the most important elements of nuclear forensics activities.

Currently, the development of NFL has been conducted by some countries and the concept of a national NFL (NNFL) that collects the data of all the materials in a country and that is used during inquiries from other countries, is the most popular concept in current international society. The prototype NNFL project at JAEA also follows this concept. JAEA has continued to develop a prototype of NNFL based on data related to nuclear materials and other radioactive materials that it possessed during past research activities. By the end of last year, the development a nuclear material database (NMDB) with a basic data-handling system (Fig.11-3) was completed and the computational multivariate analysis tools to identify illicit materials were developed (Fig.11-4). Furthermore, JAEA participated in a virtual table top exercise on NNFL hosted by the International Technical Working Group for Nuclear Forensics (ITWG).

The performance of JAEA in the exercise was evaluated as well, and the knowledge, lessons, and experiences obtained through the exercise were applied to the NFL development project at JAEA.

The prototype NNFL will be improved by some development items such as a radioactive material database and a nuclear forensics image analysis tool. In the future, it is expected that the prototype NNFL, the analytical tools, and the knowledge obtained from our development activities could be utilized by responsible national authorities for nuclear forensics after the national nuclear forensics regime is established in Japan.

This study was partly supported by the Ministry of Education, Culture, Sports, Science, and Technology of Japan (MEXT).

Reference

Kimura, Y. et al., Lessons Learned from the International Tabletop Exercise of National Nuclear Forensics Library at JAEA, Journal of Nuclear Materials Management, vol.XLII, no.4, 2014, p.40–45.

Promotion of Collaboration

To make the technologies, patents and other research results, and facilities and equipment of the Japan Atomic Energy Agency (JAEA) widely available to society, we are promoting activities in three areas: “academia-industry collaboration”, “utilization of intellectual property”, and “facility usage”. We are also creating a database of patents and intellectual property information held by the JAEA. The following table is a list of intellectual property (patents in foreign countries) in the fiscal year 2014.

Intellectual Property Held by JAEA
Patent Information

Title	Department	R&D Institutes and Centers	Publication Number	Date of Registration
1 USA				
Method for Detecting Fine Particles in Fluid with X-ray	Nuclear Science and Engineering Center, Sector of Nuclear Science Research	Nuclear Science Research Institute	8744042	Jun. 3, 2014
Image Capturing Apparatus, Image Displaying Method and Recording Medium, Image Displaying Program Being Recorded Thereon	Quantum Beam Science Center, Sector of Nuclear Science Research	Kansai Photon Science Institute	8792000	Jul. 29, 2014
Nondestructive Inspection System using Nuclear Resonance Fluorescence	Quantum Beam Science Center, Sector of Nuclear Science Research	Kansai Photon Science Institute	8804911	Aug. 12, 2014
Neutron Detector and Neutron Image Detector with Scintillator	J-PARC Center, Sector of Nuclear Science Research	Nuclear Science Research Institute	8822943	Sep. 2, 2014
Particle Radiation Monitoring Apparatus, Recording Medium to Retain Particle Radiation Monitoring Program, and Particle Radiation Monitoring Method	Takasaki Advanced Radiation Research Institute, Sector of Nuclear Science Research	Takasaki Advanced Radiation Research Institute	8909495	Dec. 9, 2014
Spectroscopic Apparatus	Quantum Beam Science Center, Sector of Nuclear Science Research	Kansai Photon Science Institute	8983032	Mar. 17, 2015
Composite Optical Fiber and Method of Manufacturing the Same	Quantum Beam Science Center, Sector of Nuclear Science Research	Kansai Photon Science Institute	8983255	Mar. 17, 2015
Pixel-Type Two-Dimensional Image Detector	J-PARC Center, Sector of Nuclear Science Research	Nuclear Science Research Institute	8993973	Mar. 31, 2015
2 UK				
Use of Light Emitting Material	Oarai Research and Development Center, Sector of Fast Reactor Research and Development	Oarai Research and Development Center	1757671	Oct. 8, 2014
3 France				
Particle Detector and Neutron Detector that Use Zinc Sulfide Phosphors	J-PARC Center, Sector of Nuclear Science Research	Nuclear Science Research Institute	503801	Jun. 27, 2014
Use of Light Emitting Material	Oarai Research and Development Center, Sector of Fast Reactor Research and Development	Oarai Research and Development Center	1757671	Oct. 8, 2014
Liquid Alkali Metal Dispersed with Nanoparticles and Method of Manufacturing the Same	Oarai Research and Development Center, Sector of Fast Reactor Research and Development	Oarai Research and Development Center	1151588	Dec. 26, 2014
4 Germany				
Use of Light Emitting Material	Oarai Research and Development Center, Sector of Fast Reactor Research and Development	Oarai Research and Development Center	602005044870.5	Oct. 8, 2014
Material for Nuclear Fusion Reactor Excellent in High Temperature Characteristics Comprising Beryllium Intermetallic Compound	Oarai Research and Development Center, Sector of Nuclear Science Research	Oarai Research and Development Center	1494244	Jan. 7, 2015
5 China				
Polymer Electrolyte Membrane Comprising Alkylether Graft Chain and Method of Producing the Same	Quantum Beam Science Center, Sector of Nuclear Science Research	Takasaki Advanced Radiation Research Institute	ZL201010109458.2	Apr. 9, 2014
Method for Extracting and Separating Rare Earth Elements	Nuclear Science and Engineering Center, Sector of Nuclear Science Research	Nuclear Science Research Institute	ZL201010278408.7	Aug. 27, 2014
Image Capturing Apparatus, Image Displaying Method and Recording Medium, Image Displaying Program Being Recorded Thereon	Quantum Beam Science Center, Sector of Nuclear Science Research	Kansai Photon Science Institute	ZL201010288859.9	Oct. 15, 2014
Composite Optical Fiber and Method of Manufacturing the Same	Quantum Beam Science Center, Sector of Nuclear Science Research	Kansai Photon Science Institute	ZL201180028326.X	Mar. 25, 2015

About the Design of the Cover

The cover is designed with white hexagons similar to the pattern in a tortoise shell, an ancient Japanese symbol of people's wish for longer lives. Coincidentally, this shape is the same as that of core fuel assemblies for both the prototype fast breeder reactor "MONJU" and the high-temperature engineering test reactor "HTTR".

The images on the cover show overview of the JAEA Chart of the Nuclides 2014 (top left) and a map of ambient dose equivalent rates through the eighth vehicle-borne survey (bottom right).

The top left image shows the overview of JAEA Chart of the Nuclides 2014. We have constructed a folding (A4-size) nuclear chart, including the latest experimental (3150 points) and theoretical (1578 points) decay data for nuclear science experts and the general public (Chapter 3, Topic 3-7, p.47).

The bottom right image shows the an example of the map of ambient dose equivalent rates obtained using vehicle-borne surveys (June-August 2014). To make clear decreasing in ambient dose equivalent rate in Fukushima, they were compared and analyzed with other data obtained after the accident (Chapter 1, Topic 1-1, p.13).

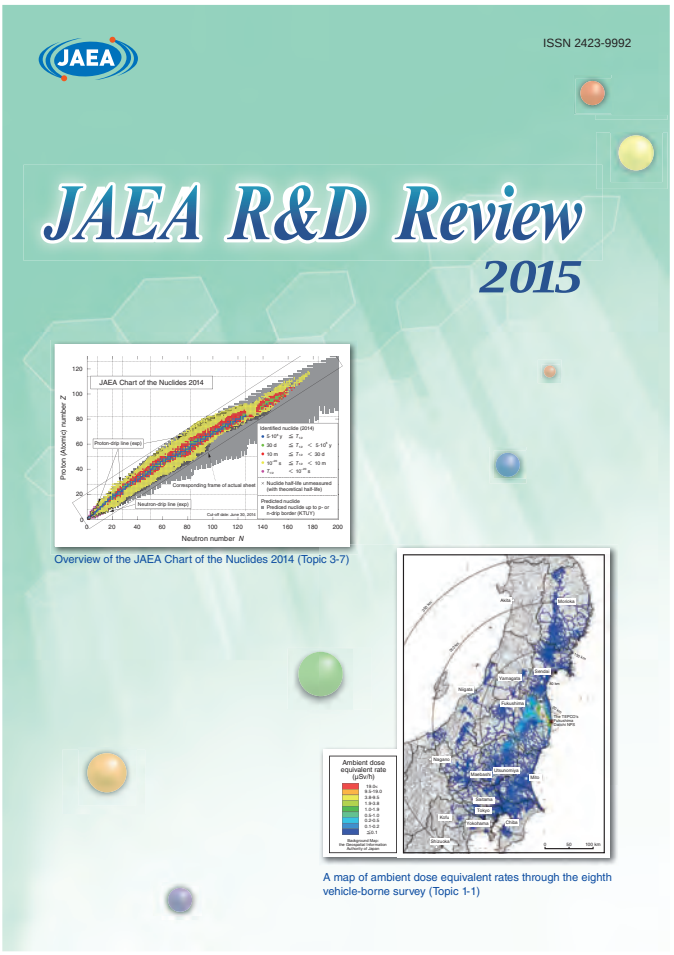

JAEA R&D Review 2015

Published by
Japan Atomic Energy Agency in February 2016

This publication is issued by Japan Atomic Energy Agency (JAEA) on a yearly basis.
Inquiries about availability and/or copyright of the contents in this publication should be addressed to Institutional Repository Section, Intellectual Resources Management and R&D Collaboration Department, Japan Atomic Energy Agency (JAEA).

Address: 2-4 Shirakata, Tokai-mura, Naka-gun, Ibaraki-ken 319-1195, Japan
Phone: +81-29-282-6387, **Facsimile:** +81-29-282-5920, **e-mail:** ird-seika_shi@jaea.go.jp